**Pedro Miguel Cavaco Carrilho dos Santos Inácio**

# Extracellular electrical transducers for recording signals of cells in culture

PhD in Electronic and Telecommunications Engineering

Work done under the supervision of:

**Professor Doutor Henrique Leonel Gomes**

Universidade de Coimbra

Faculdade de Ciências e Tecnologia

Departamento de Engenharia Eletrónica e Computadores

**Doutora Rute Castelo Félix**

Universidade do Algarve

CCMAR − Centro de Ciências do Mar

UAlg FCT

UNIVERSIDADE DO ALGARVE

FACULDADE DE CIÊNCIAS E TECNOLOGIA

2023

**Pedro Miguel Cavaco Carrilho dos Santos Inácio**

# Extracellular electrical transducers for recording signals of cells in culture

PhD in Electronic and Telecommunications Engineering

Work done under the supervision of:

**Professor Doutor Henrique Leonel Gomes**

Universidade de Coimbra

Faculdade de Ciências e Tecnologia

Departamento de Engenharia Eletrónica e Computadores

**Doutora Rute Castelo Félix**

Universidade do Algarve

CCMAR − Centro de Ciências do Mar

UAlg FCT

UNIVERSIDADE DO ALGARVE

FACULDADE DE CIÊNCIAS E TECNOLOGIA

2023

**Declaração de autoria de trabalho e indicação dos direitos de cópia ou copyright**

# Extracellular electrical transducers for recording signals of cells in culture

Declaro ser o autor deste trabalho, que é original e inédito. Autores e trabalhos consultados estão devidamente citados no texto e constam da listagem de referências incluídas.

Pedro Miguel Cavaco Carrilho dos Santos Inácio

Assinatura: _____



.

This work would not have been possible without funding provided by the Portuguese Foundation for Science and Technology (FCT/MCTES), through national funds and when applicable co-funded EU funds by FEDER under the PT 2020 Partnership Agreement, namely, by the project “Implantable organic devices for advanced therapies” under the contract number PTDC/EEI-AUT/5442/2014 – INNOVATE; by the Instituto de Telecomunicações (IT) under the contract numbers UID/Multi/04326/2013, UID/EEA/50008/2019 and UIDB/EEA/50008/ 2020; by the Centro de Ciências do Mar (CCMAR) under the contract numbers UID/Multi/04326/2019 and UIDB/Multi/04326/2020; by the Instituto de Materiais de Aveiro (CICECO) under the contract numbers UIDB/50011/2020 and UIDP/50011/2020; and by the Centro de Investigação em Biomedicina (CBMR) under the contract number UID/BIM/04773/2019. All work was done in Instituto de Telecomunicações (IT) facilities.

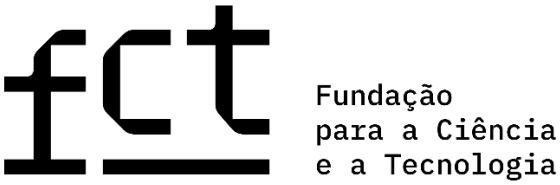



*To my wife Margarida and parents*

*whose love and support have made this project possible.*

# Agradecimentos

Há tantas pessoas que estiveram envolvidas na criação deste trabalho. Alguns estiveram intrinsecamente envolvidos nos detalhes técnicos, enquanto outros forneceram suporte e enriqueceram minha vida de outras maneiras. Se falhar em mencionar o seu nome, peço que compreenda que estou grato por me ter ajudado neste processo quando precisei.

Começo por agradecer ao meu orientador, o Professor Henrique Leonel Gomes, pela sua amizade, entusiasmo, energia motivação e espírito eterno. Ele tem sido um grande mentor, desenvolvendo em mim competências técnicas e a capacidade de pensar de forma crítica e criativa. Este trabalho não teria sido possível sem a sua orientação, sem o seu tremendo apoio, e pela oportunidade única de trabalhar num projeto desafiante e inovador, pelas quais estou profundamente grato.

Agradeço também à minha orientadora associada, a Doutora Rute Castelo Félix, pela sua amizade e entusiasmo. Sua experiência e perceções foram inestimáveis enquanto eu lutava para compreender os aspetos biológicos deste trabalho, pelos quais sou profundamente grato.

Seguidamente, quero agradecer a todos os que de algum modo participaram de forma direta e indiretamente neste trabalho, começando pelos meus colegas de laboratório, a Ana Mestre, Doutor Youssef Elamine, Doutor Leonardo Silva, Rosa Pires, Doutora Sanaz Asgarifar, Tiago Almeida, Fábio Cabrita, André Santos, Lino Gonçalves, Doutor Gabriel Gaàl, Doutor Tiago Carvalho, Rodrigo Santos, Joana Canudo, Doutor João Santos e Doutor Paulo Rocha. Agradeço-vos profundamente o vosso apoio, amizade, partilha, e todos os bons momentos e discussões. Saibam que foi um privilégio trabalhar convosco. Em especial, agradeço à Ana Mestre, Doutor Youssef Elamine e Doutora Sanaz Asgarifar, formámos um bom grupo de trabalho por vários anos e partilhámos muitos bons momentos e laços de amizade!

A todos os Professores e Doutores, nomeadamente, Maria C. R. Medeiros, Peter C. Hubbard, José Bragança, Deborah M. Power, Maria L. Cristiano, Fabio Biscarini, Jorge Morgado, Luís Alcácer, Quirina Ferreira, Ana Charas, Carmen S. R. Freire, Dago de Leeuw, Rui Guerra, Noélia Correia, Peter Stallinga, Ana M. Cavaco, Ana M. R. Costa, João Ventura, Paulo Aguiar, Patrícia A. Madureira, Dr.ª Clara Romero, e Dr. Artur B. Lourenço. Saibam que foi um privilégio trabalhar convosco, e que estou profundamente agradecido por me terem acompanhado e ajudado a concretizar este trabalho através da partilha e apoio dos recursos dos vossos laboratórios, na escrita, e claro, pela vossa amizade, e todos os bons momentos e discussões.

Um agradecimento especial aos coordenadores do Centro de Eletrónica, Optoeletrónica e Telecomunicações (CEOT), o Prof. Rui Guerra e Prof.ª Noélia Correia pelo suporte financeiro através de uma bolsa de investigação dedicada ao grupo de investigação de Sensores e Biologia, e claro, pela vossa amizade, e todos os bons momentos e discussões.

E, finalmente, quero agradecer a toda a minha família, o vosso suporte foi inestimável e decisivo a concluir este trabalho. Estou-vos profundamente grato por partilharem todos os momentos da minha vida.

Primeiro que tudo, à minha querida esposa Margarida, pela sua Doação e Amor incondicional, pelo seu empenho com que me acompanha de forma presente em todas as jornadas da minha vida! Obrigado por me teres transmitido a força e confiança que tanto precisei para concluir este trabalho.

Ao Simba e à Nala, os nossos dois gatos e que são parte da nossa vida e família. Os dois, foram companheiros sem igual todos os dias em que trabalhei neste projeto.

Aos meus Pais, Arminda, António, Odete e Amadeu, que incondicionalmente estão sempre presentes na minha vida, transmitindo me sempre a confiança e apoio que tanto precisei para concluir este trabalho, dando-me Amor, Carinho e Força, e por partilharem todos os momentos da minha vida!

Aos meus irmãos e sobrinhos, pelo vosso apoio e fraterna amizade, dando-me carinho e força, e por partilharem todos os momentos da minha vida!

# Acknowledgments

There are so many people who were involved in the creation of this work. Some were intrinsically involved in the technical details, while others provided support and enriched my life in other ways. If I fail to mention your name, please understand that I am grateful that you helped me through this process when I needed it.

I begin by thanking my advisor, Professor Henrique Leonel Gomes, for his friendship, enthusiasm, energy, motivation, and undying spirit. He has been a great mentor, developing in me the technical skills I am presenting in this work, as well the ability to think critically and creatively. His teachings are priceless! This work would not have been possible without his tremendous support, guidance, and for the timeless opportunity he provided me to work on a challenging and innovative project, and for which I am deeply grateful.

I also thank my associated advisor, Dr. Rute Castelo Félix, for her friendship and enthusiasm. Her experience and insights were invaluable as I struggled to grasp the biological aspects of this work, for which I am deeply grateful.

Next, I would like to thank everyone who in some way participated directly or indirectly in this work, starting with my laboratory colleagues, Ana Mestre, Dr. Youssef Elamine, Dr. Sanaz Asgarifar, Dr. Leonardo Silva, Rosa Pires, Tiago Almeida, Fábio Cabrita, André Santos, Lino Gonçalves, Dr. Gabriel Gaàl, Dr. Tiago Carvalho, Rodrigo Santos, Joana Canudo, Dr. João Santos, and Dr. Paulo Rocha. I deeply thank you for your support, friendship, sharing, and all the good times and discussions. Know that it has been a privilege to work with each of you. In particular, I would like to express my gratitude to Ana Mestre, Dr. Youssef Elamine and Dr. Sanaz Asgarifar, we formed a good team for several years and we shared many good moments and bonds of friendship!

To all Professors and Doctors, namely, Maria C. R. Medeiros, Peter C. Hubbard, José Bragança, Deborah M. Power, Maria L. Cristiano, Fabio Biscarini, Jorge Morgado, Luís Alcácer, Quirina Ferreira, Ana Charas, Carmen S. R. Freire, Dago de Leeuw, Rui Guerra, Noélia Correia, Peter Stallinga, Ana M. Cavaco, Ana M. R. Costa, João Ventura, Paulo Aguiar, Patrícia A. Madureira, Clara Romero M.D., and Artur B. Lourenço M.D. Know that it has been a privilege to work with you, and that I am truly grateful for having accompanied me and helped to carry out this work through sharing and supporting your lab resources, in writing, and of course, for your friendship, and all the good times and discussions.

Special thanks to the coordinators of the Center for Electronics, Optoelectronics and Telecommunications (CEOT), Prof. Rui Guerra and Prof.ª Noélia Correia for financial support through

a research grant dedicated to the Sensors and Biology research group, for your friendship, and all the good times and discussions.

And finally, I want to thank all my family, your support was invaluable and decisive in completing this work. I am truly grateful to you for sharing every moment of my life.

First, to my dear wife Margarida, for her Donation and unconditional Love, for her commitment with which she has been presently with me on all the journeys of my life. Thank you for giving me the strength and confidence I needed to complete this work.

To Simba and Nala, our two cats and who are part of our life and family. The two were peerless companions every day I worked on this project.

To my Parents, Arminda, António, Odete and Amadeu, who are unconditionally present in my life, always giving me the confidence and support that I so needed to complete this work, giving me Love, Affection and Strength, and for sharing all the moments of my life!

To my brothers and nephews, for your support and fraternal friendship, giving me affection and strength, and for sharing every moment of my life!

# Declaration of Ethics

The research on the Glioblastomas was approved by the ethical committee of the Centro Hospitalar Universitário do Algarve, under the title "Efeito do microambiente na agressividade do gliobastoma − O papel da hipóxia (Refª UIF 122-2018)".

# Resumo

O desenvolvimento de instrumentos e métodos para estudos básicos de neurociência e biologia celular tem desempenhado um papel significativo no avanço de nossa compreensão sobre o processo biológico fundamental. A maior parte deste conhecimento foi recolhido através da utilização de métodos invasivos, como o método do patch clamp, para estudar a resposta elétrica das células neuronais. Avanços recentes na microeletrônica revolucionaram esses estudos, permitindo gravações não invasivas de elétrodos extracelulares usando elétrodos extracelulares conhecidos como tecnologia Microelectrode array (MEAS). Este avanço despertou um interesse significativo na comunidade científica, uma vez que abre uma gama mais ampla de aplicações, incluindo estudos fundamentais em neurociências, triagem de medicamentos, monitoramento ambiental e deteção de toxinas.

A tecnologia Microelectrode array (MEA) evoluiu para uma tecnologia madura, e é amplamente considerada como o padrão ouro para estudos eletrofisiológicos. No entanto, os MEAs foram otimizados principalmente para medir células excitáveis. Célula excitável é um termo usado para se referir a células com mecanismos biológicos que lhes permitem gerar potenciais de ação (APs). Dois exemplos de células excitáveis são os neurónios e as células cardíacas. As células somáticas, como células cancerosas, fibroblastos, células secretoras e células epiteliais, são consideradas tipos de células não eletrogéneas. As células não eletrogéneas carecem de mecanismos biológicos para gerar uma resposta a um estímulo elétrico. No entanto, as células não excitáveis têm outros mecanismos de sinalização que lhes permitem gerar flutuações elétricas. Um exemplo bem conhecido são as ondas químicas que se propagam através do tecido celular.

O processo de comunicação através de ondas químicas requer sincronização entre uma população de células. As ondas de cálcio são exemplos deste mecanismo de sinalização. As ondas químicas podem ser detetadas e registadas utilizando técnicas de fluorescência ótica. No entanto, a deteção ótica tem algumas desvantagens principais. Os métodos óticos requerem a incubação usando moléculas de fluorescência com uma vida útil limitada a algumas horas. Além disso, a necessidade de microscópios equipados com lasers, bem como sistemas de deteção ótica rápida. Além disso, as células são submetidas a pulso de luz, que pode interferir com o comportamento celular normal. Portanto, há uma forte necessidade de uma técnica de base elétrica que detete oscilações de tensão geradas por ondas químicas em tempo real. Esta tese posiciona-se neste contexto e tem como objetivo fabricar e testar dispositivos para registar sinais extracelulares gerados por células não excitáveis.

O trabalho baseia-se na experiência anterior do grupo, que foi crucial no desenvolvimento da técnica para medir sinais ultra fracos com amplitudes tão pequenas quanto alguns micro-volts na frequência de milihertz.

É fundamental ressaltar que o trabalho desenvolvido nesta tese baseia-se na experiência anterior do grupo, cuja contribuição foi fundamental para o desenvolvimento da técnica de medição de sinais ultrafracos com amplitudes de apenas alguns micro-volts. O grupo já demonstrou dispositivos baseados em eletrofisiológicos com um limite de deteção incomparável de 20 nanovolts. Há ainda alguns desafios a enfrentar. Um objetivo crítico é minimizar o ruído intrínseco dos dispositivos usando materiais inovadores, como polímeros condutores e substratos de celulose bacteriana nano fibrosa. Esta melhoria trará o limite de deteção do dispositivo para baixas tensões e permitir o acesso a sinais fracos, bem como para aumentar a relação sinal-ruído (SNR). Outro objetivo importante é estabelecer uma relação clara entre a geometria do elétrodo e as propriedades dos sinais nativos gerados pela população de células.

**Palavras-chave**: Bioeletrónica; Eletrónica orgânica; Transdutores; Polímeros condutores; Eletrofisiologia; Sinais extracelulares; Células não exitáveis.

# Abstract

The development of instruments and methods for basic neuroscience and cell biology studies has played a significant role in advancing our understanding about fundamental biological process. Most of this knowledge has been gathered through using invasive methods such as the patch clamp method, to study the electrical response of neuronal cells. Recent advancements in microelectronics have revolutionized these studies by enabling non-invasive extracellular electrode recordings using extracellular electrodes know as Microelectrode array (MEAS) technology. This breakthrough has sparked significant interest in the scientific community, as it opens a wider range of applications, including, fundamental studies in neurosciences, drug screening, environmental monitoring, and toxin detection.

Microelectrode array (MEA) technology has evolved into a mature technology, and it is widely considered as the gold standard for electrophysiological studies. Nevertheless, MEAs have been primarily optimized to measure excitable cells. Excitable cell is a term used to refer to cells with biological mechanisms that enable them to generate action potentials (APs). Two examples of excitable cells are neurons and cardiac cells. Somatic cells, such as cancer cells, fibroblasts, secretory cells, and epithelial cells, are considered non-electrogenic cell types. Non-electrogenic cells lack the biological mechanisms to generate a response to an electrical stimulus. However, non-excitable cells have other signaling mechanisms that allow them to generate electrical fluctuations. A well-known example are chemical waves which propagate across the cell tissue.

Communication process trough chemical waves requires synchronization among a population of cells. Calcium waves are examples of this signaling mechanism. Chemical waves can be detected and recorded using optical fluorescence techniques. However, the optical detection has a few major handicaps. Optical methods require the incubation using fluorescence molecules with a lifetime limited to a few hours. Furthermore, the require microscopes equipped with lasers as well as fast optical detection systems. Additionally, cells are subjected to light pulse, that may interfere with normal cell behavior. Therefore, there is a strong need for an electrical-based technique that detects voltage oscillations generated by chemical waves in real time. This thesis is positioned in this context and aims to fabricate and test devices to record extracellular signals generated by non-excitable cells.

The work builds on the group's previous experience, which was crucial in developing the technique for measuring ultra-weak signals with amplitudes as small as a few micro-volts in the millihertz frequency.

It is essential to emphasize that the work developed in this thesis is based on the group's previous experience, whose contribution was fundamental for the development of the technique for measuring ultra-weak signals with amplitudes of just a few micro-volts. The group has already demonstrated electrophysiological based devices with an unrivalled detection limit of 20 nanovolts. However, there are still some challenges to be addressed. A critical objective is to minimize the intrinsic noise of the devices using innovative materials, such as conductive polymers and nano−fibrous bacterial cellulose substrates. This improvement will bring the detection limit of the device to low voltages and allow access to faint signals as well as to increase the signal-to-noise ratio (SNR). Other important goal is to establish a clear relation between the electrode geometry and the properties of the native signals generated by the population of cells.

**Keywords:** Bioelectronics; Organic electronics; Conductive polymers; Ultra-low-noise electrophysiology; Extracellular signals; non-electrogenic cells.

# Index

# Index of Figures

# Index of Tables

# Index of Appendix Figures

# Index of Appendix Tables

# Abbreviations

| | |
|---|---|
| AC | Alternate Current |
| ADC | Analog-to-Digital Converter |
| AP | Action Potential |
| APDT | Auto Process Data Toolbox |
| ASIC | Acid-Sensing Ion Channel |
| ATCC | American Type Culture Collection |
| ATP | Adenosine Triphosphate |
| BC | Bacterial Cellulose |
| BNC | Bayonet Neill–Concelman |
| CAD | Computer-Aided Design |
| CNS | Central Nervous System |
| CP | Conjugated Polymers or Conductive Polymers |
| CPE | Constant-Phase Element |
| CR | Compilation Routine |
| DA | Data Address |
| DAT | Data Acquisition Toolbox |
| DC | Direct Current |
| DCT | Data Collection Toolbox |
| DFT | Density Functional Theory |
| DL | Double Layer |
| DMEM | Dulbecco’s Modified Eagle Medium |
| DMPR | Data Management and Processing Routine |
| DPT | Data Processing Toolbox |
| DSA | Digital Signal Analyzer |
| DUT | Device Under Test |
| EB | Embryoid Body |
| EDL | Electrical Double Layer |
| EDT | Experiment Data Table |
| EG | Ethylene Glycol |
| ESD | Energy of Power Spectral Density |
| F12–K | Kaighn's Modification of Ham's F–12 Medium |

| | |
|---|---|
| FBS | Fetal Bovine Serum |
| FFT | Fast-Fourier Transform |
| FHS | Fetal Horse Serum |
| FOT | Figure Options Toolbox |
| GHK | Goldman-Hodgkin-Katz |
| GMEM | Glasgow Modified Essential Medium |
| GUI | Graphical User Interface |
| HAA | Histogram Analysis Algorithm |
| HS | Hestrin and Schramm |
| IBI | Inter-Beat Interval |
| IC | Integrated Circuit |
| IDF | Inter-Digitated Fingers |
| LFP | Local Field Potential |
| LNA | Low-Noise Amplifier |
| MEAs | Micro-Electrode Arrays |
| mESC | Mouse Embryonic Stem Cells |
| MISFET | Metal ion sensitive field effect transistor |
| MS222 | Ethyl-3-aminobenzoate methane sulfonate salt |
| NADS | Numeric Array Data Structure |
| NDPT | Noise Data Processing Toolbox |
| NF | Noise Figure |
| OS | Operating System |
| OSR | Operation Status Register |
| PBS | Phosphate buffer solution |
| PEDOT:PSS | Poly(3,4-ethylenedioxythiophene) : polystyrene sulfonate |
| PET | Polyethylene terephthalate |
| PLGA | Poly(lactic-co-glycolic acid) |
| PMMA | Poly(methyl methacrylate) acid |
| PS | Power Spectrum |
| PSD | Power Spectral Density |
| RMS | Root Mean Square |
| RL | Recording Loop |
| RTPSD | Root of Power Spectral Density |

| | |
|---|---|
| SCP | Silver Conductive Paint |
| SDPT | Statistical Data Processing Toolbox |
| SEM | Scanning Electron Microscope |
| SiO2 | Silicon dioxide |
| SNR | Signal-to-Noise Ratio |
| SSIF | Smoothing Spline Interpolating Function |
| ST | Stimulation Toolbox |
| UHR | Ultra-High-Resolution |

# Chapter 1

# Introduction

This chapter introduces the motivation and objectives of the thesis, followed by an outline of its organization. It then emphasizes the major scientific contributions of this work and concludes with a list of the publications included as part of this thesis.

## 1.1 – Motivation and goals

In 1780, Luigi Galvani introduced the first concepts of bioelectricity through his electrical experiments on frog muscle tissues [1]. The pioneering work of Galvani inspired the scientific community to explore methodologies capable of electrically interacting with living cells and tissues. The meritorious work of Hodgkin and Huxley in 1952 on neurophysiology [2], contributed significantly to defining the ionic basis of nervous conduction and excitation, which later led to the designation of electrogenic cells, a term assigned to all living cells capable of generating an action potential (AP) [3]. For decades, the the electrophysiological scientific community had their activity focused on recording of APs, leading to the pursuit and development of different recording techniques, such as the voltage and/or current clamp [4–7], patch-clamp [8–10], sharp electrodes [11–13], microwires [14–16], and microelectrode arrays (MEAs) [17–20].

Patch-clamp based recording techniques played a crucial rule in the studies of the cells membrane transport function [21–23], making it possible to understand that each individual living cell act as a signal generator whenever an ionic conduction occur through a specific channel or pump in the cell membrane.

Considerable progress has been made in the development of microelectrode arrays (MEAs), which have enabled the monitoring of single cells and communication between electrogenic cells, particularly neurons organized in a neural network [26–31] and other electrogenic cells [28,30,36–38][32–35]. In the case of neurons, it is essential to identify the specific neuron that is generating an action potential, making spatial resolution a critical feature of the MEAs. To achieve spatial resolution, MEAs utilize very small area electrodes. However, in voltage detection mode, the intrinsic thermal noise of an electrode increases as the electrode size decreases. As a result, the thermal noise level of a MEA

electrode typically exceeds 10 μV, making it challenging to detect signals generated by non-electrogenic cells. These are cells incapable of generating an action potential [24]. Although non-electrogenic cells cannot fire action potentials, they have mechanisms for transporting ions across the cell membrane [25].

Calcium waves are a well-known example of ionic fluctuations that non-electrogenic cells generate to communicate with neighbor cells [39–42] and to carry information along a tissue. Optical techniques using calcium fluorescent dyes [43] are currently at the forefront of monitoring calcium waves [44–48]. However, electronic technologies offer higher experimental flexibility [49]. Electrical techniques are not selective. This means that they cannot identify the specific ionic species responsible for the ionic fluctuations, but they have the advantage of being entirely non-invasive and capable of monitoring bioelectrical fluctuations over extended periods, ranging from several hours to several weeks, in real-time. Therefore, extracellular electrodes and electrical techniques are highly valuable for tracking changes in cellular activity over time and for studying the dynamics of cell-cell communication.

The primary objective of this thesis is to design and develop electrophysiological sensing electrodes, along with their associated measurement techniques, capable of detecting the subtle signals generated by non-electrogenic cells in the millihertz frequency range. By addressing the challenge of detecting week signals, this research aims to provide insights into how non-electrogenic cells organize and communicate with each other to carry several biological functions, such a wound repair, tissue formation, cell migration, etc.

## 1.2 − Thesis organization

The thesis is divided into seven chapters, each of which addresses a specific aspect of the research topic. After this introductory chapter, which provides an overview of the thesis and its motivation, the following chapters are organized as follows:

Chapter 2 provides an overview of the electrodes developed for sensing living cells. Three types of devices will be considered: (i) the electrodes based on inorganic materials such as gold; (ii) electrodes based on conducting polymers; and (iii) the conducting polymer electrodes deposited on cellulose substrates. The focus will be on the device characteristics that impact the signal detection limit, such as the impedance, the noise limits, as well as the physical properties related to the electrode geometry. Cellular function is also briefly described, emphasizing on the aspects related to the generation of extracellular signals. The cell-electrode interface is explained to provide an understanding of how the extracellular signals are detected by an electrode.

Chapter 3 is focused on the instrumentation for recording extracellular signals, including the description of the microelectrodes and amplifier. Chapter 3 also includes a description of measurement techniques associated with the characterization of bioelectronic devices, including small-signal impedance, noise power spectral density (PSD), quasi-static, and transient current response to voltage pulses.

Chapter 4 focus on the methods and protocols used to handle and perform experiments with cell cultures.

Chapter 5 discuss the detection of bioelectrical signal generated by electrogenic cells using conducting polymer electrodes and the displacement current method. Zebrafish hearts are used to demonstrate the ability of PEDOT:PSS electrodes to detect bioelectrical signals.

Chapter 6 explores the use of ultra-low noise PEDOT: PSS electrodes deposited on bacterial cellulose membranes for the recording of ultra-weak extracellular signals generated by non-electrogenic cells. Analysis of the noise PSD and impedance of PEDOT:PSS electrode are carried out to characterize the sensing layer.

In Chapter 7, the significant contributions of this research are summarized, highlighting the key findings and insights gained. Suggestions for future research in this area are provided.

This thesis is accompanied by three appendices, labeled A to C, which provide detailed information about the computer data acquisition and analysis tool. The development of this software tool was a crucial aspect of the work carried out, enabling the acquisition, collection, processing, and analysis of bioelectrical signals. These appendices are an essential resource for anyone seeking to replicate or build upon this research and provide valuable insights into the methodology and techniques employed.

## 1.3 – Contributions to the scientific field of bioelectronics

This thesis has made several significant contributions to the field of bioelectronic devices and signal detection. These contributions can be summarized as follows:

- Identification of optimized recording methods for detecting bioelectrical signals generated by living cells.
- Demonstration of the effectiveness of conducting polymers and the displacement current method in enhancing the recording of bioelectrical signals generated by living cells.
- Identification of innovative strategies for reducing electrode impedance and electrical noise by employing conductive polymers and bacterial cellulose (BC) membranes as substrates.
- Development of ultra-low-noise organic-based electrodes for accessing bioelectrical signals generated by populations of non-electrogenic cells.

- Electrical characterization of the PEDOT:PSS/BC electrodes noise and impedance, with a comparative study of similar electrodes using gold electrodes and glass and on polyethylene terephthalate (PET) substrates.
- Benchmarking of the electrodes using standard and well-known biological signal sources.
- Characterization of discrete signals generated by populations of non-electrogenic cells.
- Development of a comprehensive software toolkit, the rcSoftware, designed for acquiring, collecting, and processing signals in an electrophysiological system.
-

# 1.4 – Peer reviewed publications

The contributions of this thesis have led to the following publications:

- "**Bioelectrical signal detection using conducting polymer electrodes and the displacement current method**"; **Pedro M. C. Inácio**, Ana L. G. Mestre, Maria C. R. Medeiros *Member IEEE*, Sanaz Asgarifar, Youssef Elamine, Joana Canudo, João M. A. Santos, José Bragança, Jorge Morgado, Fabio Biscarini and Henrique L. Gomes, *IEEE Sensors Journal*, Vol. 17, Issue 13, July 2017. DOI: 10.1109/JSEN.2017.2703834
- **"Extracellular Electrophysiological Measurements of Cooperative Signals in Astrocytes Populations"**; Ana L. G. Mestre, **Pedro M. C. Inácio**, Youssef Elamine, Sanaz Asgarifar, Ana S. Lourenço, Maria L. S. Cristiano, Paulo Aguiar, Maria C. R. Medeiros, Inês M. Araújo, João Ventura and Henrique L. Gomes, *Frontiers Neural Circuits*, Vol. 11, October 2017. DOI: 10.3389/fncir.2017.00080
- **"Ultrasensitive gold microstructured electrodes enabling the detection of extra-cellular longlasting potentials in astrocytes populations"**; Ana L. G. Mestre, Mónica Cerquido, **Pedro M. C. Inácio**, Sanaz Asgarifar, Ana S. Lourenço, Maria L. S. Cristiano, Paulo Aguiar, Maria C. R. Medeiros, Inês M. Araújo, João Ventura and Henrique L. Gomes, *Nature Scientific Reports*, Vol. 7, Issue 1, October 2017. DOI: 10.1038/s41598-017-14697-y
- "**Ultrasensitive bioelectronic devices based on conducting polymers for electrophysiology studies**"; Sanaz Asgarifar, **Pedro M. C. Inácio**, Ana L. Mestre, Henrique L. Gomes, *Chemical Papers*, Vol. 72, nº 7, July 2018. DOI: 10.1016/j.bios.2019.111708
- "**Insight into the sensing mechanism of an impedance based electronic tongue for honey botanic origin discrimination**"; Youssef Elamine, **Pedro M.C. Inácio**, Badiâa Lyoussi, Ofélia Anjos, Leticia M. Estevinho, Maria da Graça Miguel, Henrique L. Gomes, *Sensors and Actuators B: Chemical*, Vol. 285, April 2019, Pages 24-33. DOI: 10.1016/j.snb.2019.01.023

- "**Extracellular electrophysiological based sensor to monitor cancer cells cooperative migration and cell-cell connections**"; Sanaz Asgarifar, Ana L.G. Mestre, Rute C. Félix, **Pedro M.C. Inácio**, Maria L.S. Cristiano, Maria C.R. Medeiros, Inês M. Araújo, Deborah M. Power, Henrique L. Gomes, *Biosensors and Bioelectronics*, Vol. 145, December 2019, 111708. DOI: 10.1016/j.bios.2019.111708
- "**Ultra-low noise PEDOT:PSS electrodes on bacterial cellulose: A sensor to access bioelectrical signals in non-electrogenic cells**"; **Pedro M.C. Inácio**, Maria C.R. Medeiros, Tiago Carvalho, Rute C. Félix, Ana Mestre, Peter C. Hubbard, Quirina Ferreira, Jorge Morgado, Ana Charas, Carmen S.R. Freire, Fabio Biscarini, Deborah M. Power, Henrique L. Gomes, *Organic Electronics*, Vol. 85, October 2020, 105882. DOI: 10.1016/j.orgel.2020.105882

# 1.5 – Communications

The contributions and publications of this thesis have led to the following oral and poster communications:

- Poster: "**Bacterial cellulose on bioelectronics for the study and treatment of neurodegenerative disorders**"; Tiago Carvalho, Armando J. D. Silvestre, **Pedro C. Inácio**, Ana G. Mestre, Henrique L. Gomes, Carmen S. R. Freire, *3rd International EPNOE Junior Scientists Meeting*, 14−15th May 2018, Maribor, Slovenia.
- Oral: "**Electrical methodology to evaluate materials and devices for electrophysiological transducers**", **Pedro C. Inácio**, Ana G. Mestre, Peter C. Hubbard, Maria do Carmo Medeiros, Henrique Leonel Gomes, *Materiais 2019*, Universidade Nova de Lisboa, 14−17th April 2019, Lisbon, Portugal.
- Oral: "**Eletrónica implantável para comunicar com células**"; **Pedro C. Inácio**, Ana G. Mestre, Rute C. Félix, Peter C. Hubbard, Maria C.R. Medeiros, Henrique L. Gomes, "*Doutoramentos da UAlg e Cultura Científica: Visão Prática"*, Biblioteca Municipal de Faro. Universidade do Algarve, 17 January 2019, Faro, Portugal.
- Oral: "**Bioelectronic interfaces design for biomedical applications**"; **Pedro C. Inácio**, Ana G. Mestre, Rute C. Félix, Maria C.R. Medeiros, Henrique L. Gomes, *Seminário e Webinar: Design e Prototipagem*, Universidade do Algarve, 17 May 2019, Faro, Portugal.
- Oral: "**Electrophysiological measurement of bioelectrical activity using extracellular electrodes**"; Ana G. Mestre, **Pedro C. Inácio**, Maria C.R. Medeiros, Henrique L. Gomes, *Neuroimmunephysiology course*, 23th May 2019, Copenhagen, Denmark.

# References


1. Berggren, M.; Richter-Dahlfors, A. Organic Bioelectronics. *Adv. Mater.* **2007**, *19*, 3201–3213, doi:10.1002/adma.200700419.
2. Hodgkin, A.L.; Huxley, A.F. A quantitative description of membrane current and its application to conduction and excitation in nerve. *Bull. Math. Biol.* **1990**, *52*, 25–71, doi:10.1007/BF02459568.
3. Fewtrell, C. Ca2+ Oscillations in Non-Excitable Cells. *Annu. Rev. Physiol.* **1993**, *55*, 427–454, doi:10.1146/annurev.physiol.55.1.427.
4. Fröhlich, F. Membrane Voltage. *Netw. Neurosci.* **2016**, 3–17, doi:10.1016/b978-0-12-801560-5.00001-x.
5. Sheets, M.F.; Ten Eick, R.E. *Whole-Cell Voltage Clamp of Cardiac Sodium Current*; ACADEMIC PRESS, INC., 1994; Vol. 19;.
6. Perkins, K.L. Cell-attached voltage-clamp and current-clamp recording and stimulation techniques in brain slices. *J. Neurosci. Methods* **2006**, *154*, 1–18, doi:10.1016/j.jneumeth.2006.02.010.
7. Polder, H.R.; Weskamp, M.; Linz, K.; Meyer, R. Voltage-clamp and patch-clamp techniques. *Pract. Methods Cardiovasc. Res.* **2005**, 272–323, doi:10.1007/3-540-26574-0_16.
8. Hamill, O.P.; Marty, A.; Neher, E.; Sakmann, B.; Sigworth, F.J. Improved patch-clamp techniques for high-resolution current recording from cells and cell-free membrane patches. *Pflügers Arch. - Eur. J. Physiol.* **1981**, *391*, 85–100, doi:10.1007/BF00656997.
9. Neher, E.; Sakmann, B. Single-channel currents recorded from membrane of denervated frog muscle fibres. *Nature* **1976**, *260*, 799–802, doi:10.1038/260799a0.
10. Sigworth, F. Single Na+ channel currents. *Nature* 1980, *287*, 447.
11. Staley, K.J.; Otis, T.S.; Mody, I. Membrane properties of dentate gyrus granule cells: Comparison of sharp microelectrode and whole-cell recordings. *J. Neurophysiol.* **1992**, *67*, 1346–1358, doi:10.1152/jn.1992.67.5.1346.
12. Li, W.C.; Soffe, S.R.; Roberts, A. A direct comparison of whole cell patch and sharp electrodes by simultaneous recording from single spinal neurons in frog tadpoles. *J. Neurophysiol.* **2004**, *92*, 380–386, doi:10.1152/jn.01238.2003.
13. Hoogerwerf, A.C.; Wise, K.D. A three-dimensional microelectrode array for chronic neural recording. *IEEE Trans. Biomed. Eng.* **1994**, *41*, 1136–1146, doi:10.1109/10.335862.
14. Palmer, C. A microwire technique for recording single neurons in unrestrained animals. *Brain*

*Res. Bull.* **1978**, *3*, 285–289, doi:10.1016/0361-9230(78)90129-6.

15. Kubie, J.L. A driveable bundle of microwires for collecting single-unit data from freely-moving rats. *Physiol. Behav.* **1984**, *32*, 115–118, doi:10.1016/0031-9384(84)90080-5.
16. Ferguson, J.E.; Boldt, C.; Puhl, J.G.; Stigen, T.W.; Jackson, J.C.; Crisp, K.M.; Mesce, K.A.; Netoff, T.I.; Redish, A.D. Nanowires precisely grown on the ends of microwire electrodes permit the recording of intracellular action potentials within deeper neural structures. *Nanomedicine* **2012**, *7*, 847–853, doi:10.2217/nnm.11.157.
17. THOMASJR, C.; SPRINGER, P.; LOEB, G.; BERWALDNETTER, Y.; OKUN, L. A miniature microelectrode array to monitor the bioelectric activity of cultured cells. *Exp. Cell Res.* **1972**, *74*, 61–66, doi:10.1016/0014-4827(72)90481-8.
18. Connolly, P.; Clark, P.; Curtis, A.S.G.; Dow, J.A.T.; Wilkinson, C.D.W. An Extracellular microelectrode Array for monitoring electrogenic cells in culture. *Biosens. Bioelectron.* **1990**, *5*, 223–234, doi:10.1016/0956-5663(90)80011-2.
19. Novak, J.L.; Wheeler, B.C. Recording from the Aplysia Abdominal Ganglion with a Planar Microelectrode Array. *IEEE Trans. Biomed. Eng.* **1986**, *BME-33*, 196–202, doi:10.1109/TBME.1986.325891.
20. Jobling, D.T.; Smith, J.G.; Wheal, H. V. Active microelectrode array to record from the mammalian central nervous systemin vitro. *Med. Biol. Eng. Comput.* **1981**, *19*, 553–560, doi:10.1007/BF02442768.
21. Donlon, J.A.; Rothstein, A. The cation permeability of erythrocytes in low ionic strength media of various tonicities. *J. Membr. Biol.* **1969**, *1*, 37–52, doi:10.1007/BF01869773.
22. Kaestner, L. Cation Channels in Erythrocytes - Historical and Future Perspective. *Open Biol. J.* **2011**, *4*, 27–34, doi:10.2174/1874196701104010027.
23. Kaestner, L.; Wang, X.; Hertz, L.; Bernhardt, I. Voltage-Activated Ion Channels in Non-excitable Cells—A Viewpoint Regarding Their Physiological Justification. *Front. Physiol.* **2018**, *9*, 1–5, doi:10.3389/fphys.2018.00450.
24. Radivojevic, M.; Franke, F.; Altermatt, M.; Müller, J.; Hierlemann, A.; Bakkum, D.J. Tracking individual action potentials throughout mammalian axonal arbors. *Elife* **2017**, *6*, 1–23, doi:10.7554/eLife.30198.
25. Dragas, J.; Viswam, V.; Shadmani, A.; Chen, Y.; Bounik, R.; Stettler, A.; Radivojevic, M.; Geissler, S.; Obien, M.E.J.; Müller, J.; et al. In Vitro Multi-Functional Microelectrode Array Featuring 59 760 Electrodes, 2048 Electrophysiology Channels, Stimulation, Impedance Measurement, and Neurotransmitter Detection Channels. *IEEE J. Solid-State Circuits* **2017**, *52*, 1576–1590, doi:10.1109/JSSC.2017.2686580.

26. Obien, M.E.J.; Deligkaris, K.; Bullmann, T.; Bakkum, D.J.; Frey, U. Revealing neuronal function through microelectrode array recordings. *Front. Neurosci.* **2015**, *8*, 423, doi:10.3389/fnins.2014.00423.
27. Bakkum, D.J.; Frey, U.; Radivojevic, M.; Russell, T.L.; Müller, J.; Fiscella, M.; Takahashi, H.; Hierlemann, A. Tracking axonal action potential propagation on a high-density microelectrode array across hundreds of sites. *Nat. Commun.* **2013**, *4*, doi:10.1038/ncomms3181.
28. Müller, J.; Ballini, M.; Livi, P.; Chen, Y.; Radivojevic, M.; Shadmani, A.; Viswam, V.; Jones, I.L.; Fiscella, M.; Diggelmann, R.; et al. High-resolution CMOS MEA platform to study neurons at subcellular, cellular, and network levels. *Lab Chip* **2015**, *15*, 2767–2780, doi:10.1039/c5lc00133a.
29. Halbach, M.D.; Egert, U.; Hescheler, J.; Banach, K. Estimation of action potential changes from field potential recordings in multicellular mouse cardiac myocyte cultures. *Cell. Physiol. Biochem.* **2003**, *13*, 271–284, doi:10.1159/000074542.
30. Emmenegger, V.; Obien, M.E.J.; Franke, F.; Hierlemann, A. Technologies to study action potential propagation with a focus on HD-MEAs. *Front. Cell. Neurosci.* **2019**, *13*, 1–11, doi:10.3389/fncel.2019.00159.
31. Gandolfo, M.; Maccione, A.; Tedesco, M.; Martinoia, S.; Berdondini, L. Tracking burst patterns in hippocampal cultures with high-density CMOS-MEAs. *J. Neural Eng.* **2010**, *7*, 056001, doi:10.1088/1741-2560/7/5/056001.
32. Eversmann, B.; Jenkner, M.; Hofmann, F.; Paulus, C.; Brederlow, R.; Holzapfl, B.; Fromherz, P.; Merz, M.; Brenner, M.; Schreiter, M.; et al. A 128 × 128 CMOS Biosensor Array for Extracellular Recording of Neural Activity. *IEEE J. Solid-State Circuits* **2003**, *38*, 2306–2317, doi:10.1109/JSSC.2003.819174.
33. Ryynänen, T.; Pekkanen-Mattila, M.; Shah, D.; Kreutzer, J.; Kallio, P.; Lekkala, J.; Aalto-Setälä, K. Microelectrode array for noninvasive analysis of cardiomyocytes at the single-cell level. *Jpn. J. Appl. Phys.* **2018**, *57*, doi:10.7567/JJAP.57.117001.
34. Tertoolen, L.G.J.; Braam, S.R.; van Meer, B.J.; Passier, R.; Mummery, C.L. Interpretation of field potentials measured on a multi electrode array in pharmacological toxicity screening on primary and human pluripotent stem cell-derived cardiomyocytes. *Biochem. Biophys. Res. Commun.* **2018**, *497*, 1135–1141, doi:10.1016/j.bbrc.2017.01.151.
35. Zhu, H.; Scharnhorst, K.S.; Stieg, A.Z.; Gimzewski, J.K.; Minami, I.; Nakatsuji, N.; Nakano, H.; Nakano, A. Two dimensional electrophysiological characterization of human pluripotent stem cell-derived cardiomyocyte system. *Sci. Rep.* **2017**, *7*, 1–9, doi:10.1038/srep43210.
36. Sala, L.; Ward-Van Oostwaard, D.; Tertoolen, L.G.J.; Mummery, C.L.; Bellin, M.

Electrophysiological analysis of human pluripotent stem cell-derived cardiomyocytes (hPSC-CMs) using multi-electrode arrays (MEAs). *J. Vis. Exp.* **2017**, *2017*, 1–15, doi:10.3791/55587.

37. Antonenko, Y.N.; Rokitskaya, T.I.; Huczyński, A. Electrogenic and nonelectrogenic ion fluxes across lipid and mitochondrial membranes mediated by monensin and monensin ethyl ester. *Biochim. Biophys. Acta - Biomembr.* **2015**, *1848*, 995–1004, doi:10.1016/j.bbamem.2015.01.005.
38. Scorciapino, M.A.; Picci, G.; Quesada, R.; Lippolis, V.; Caltagirone, C. A Simulation Model for the Non-Electrogenic Uniport Carrier-Assisted Transport of Ions across Lipid Membranes. *Membranes (Basel).* **2022**, *12*, 292, doi:10.3390/membranes12030292.
39. Charles, A. Intercellular calcium waves in glia. *Glia* **1998**, *24*, 39–49, doi:10.1002/(SICI)1098-1136(199809)24:1<39::AID-GLIA5>3.0.CO;2-W.
40. Charles, A.C.; Merrill, J.E.; Dirksen, E.R.; Sandersont, M.J. Intercellular signaling in glial cells: Calcium waves and oscillations in response to mechanical stimulation and glutamate. *Neuron* **1991**, *6*, 983–992, doi:10.1016/0896-6273(91)90238-U.
41. Jaffe, L.F. Calcium waves. *Philos. Trans. R. Soc. B Biol. Sci.* **2008**, *363*, 1311–1317, doi:10.1098/rstb.2007.2249.
42. JAFFE, L. The discovery of calcium waves. *Semin. Cell Dev. Biol.* **2006**, *17*, 229–229, doi:10.1016/j.semcdb.2006.02.003.
43. van Meer, B.J.; Krotenberg, A.; Sala, L.; Davis, R.P.; Eschenhagen, T.; Denning, C.; Tertoolen, L.G.J.; Mummery, C.L. Simultaneous measurement of excitation-contraction coupling parameters identifies mechanisms underlying contractile responses of hiPSC-derived cardiomyocytes. *Nat. Commun.* **2019**, *10*, 1–9, doi:10.1038/s41467-019-12354-8.
44. Yang, Y.; Liu, X.W.; Wang, H.; Yu, H.; Guan, Y.; Wang, S.; Tao, N. Imaging Action Potential in Single Mammalian Neurons by Tracking the Accompanying Sub-Nanometer Mechanical Motion. *ACS Nano* **2018**, *12*, 4186–4193, doi:10.1021/acsnano.8b00867.
45. Herron, T.J.; Lee, P.; Jalife, J. Optical imaging of voltage and calcium in cardiac cells & tissues. *Circ. Res.* **2012**, *110*, 609–623, doi:10.1161/CIRCRESAHA.111.247494.
46. Kuga, N.; Sasaki, T.; Takahara, Y.; Matsuki, N.; Ikegaya, Y. Large-Scale Calcium Waves Traveling through Astrocytic Networks In Vivo. *J. Neurosci.* **2011**, *31*, 2607–2614, doi:10.1523/JNEUROSCI.5319-10.2011.
47. Verkhratsky, A.; Orkand, R.K.; Kettenmann, H. Glial calcium: Homeostasis and signaling function. *Physiol. Rev.* **1998**, *78*, 99–141, doi:10.1152/physrev.1998.78.1.99.
48. Cornell-Bell, A.; Finkbeiner, S.; Cooper, M.; Smith, S. Glutamate induces calcium waves in cultured astrocytes: long-range glial signaling. *Science (80-. ).* **1990**, *247*, 470–473,

doi:10.1126/science.1967852.

49. Spira, M.E.; Hai, A. Multi-electrode array technologies for neuroscience and cardiology. *Nat. Nanotechnol.* **2013**, *8*, 83–94, doi:10.1038/nnano.2012.265.

# Chapter 2

# Fundaments of bioelectronics

This chapter provides an overview of the fundaments behind the use of bioelectronic devices for recording ultra-weak extracellular signals. It begins by summarizing the current understanding of the technology, providing a survey of the characteristics and applications of bioelectronic devices. As a basic understanding of biology science related to living cells is required to comprehend the origin of the extracellular signals, some essential biological concepts are briefly introduced. However, a comprehensive and detailed discussion of biological processes related to cellular functions is beyond the scope of this thesis. Therefore, only the biological aspects related to the origin of extracellular signals are discussed. The chapter concludes with the discussion of the fundaments that support the interface of bioelectronic devices, including physical layers up to the mechanism for transducing of extracellular signals into an equivalent digitized form.

## 2.1 – Introduction on bioelectronics

The field of bioelectronics emerged from the landmark experiments conducted by Luigi Galvani in the 18th century, which established the electrical coupling of inorganic solids and excitable living tissues [1]. Galvani marked the first milestone for the emergence of the discipline today called “bioelectronics”, which involves the convergence of the disciplines of biology and electronics, but also encompassing the disciplines of materials and chemistry, which, in short, aim to investigate the paradigm of the interface between living cells and electronic devices.

Bioelectronics is a leading-edge technology currently being used for innovative pre-clinical research and development in a wide range of fields. Bioelectronic devices can monitor and regulate the interior environment of biological objects in real-time, making them ideal for therapeutic and implantable biomedical applications, including drug delivery, electrophysiological recording and regulation of intracellular activities [2,3]. The following sections provide an in-depth discussion of the biological, electronic, and materials science foundations that underlie bioelectronics research. The characteristics and applications of bioelectronic devices are also presented, with a focus on current

technological advances in recording techniques. Additionally, the role of electrical and mechanical properties of electrode fabrication materials, depending on their inorganic or organic composition, is discussed. This theoretical-based study has been developed and refined by several authors. The objective of this section is to present the key ideas and results in a uniform and organized way.

# 2.2 – Biology background

Biology science relates to all living things, and “living things” are all the diverse organisms descended from a single-celled ancestor that evolved almost 4 billion years ago [4]. This definition is based on a vast knowledge of centuries of research, as is the case of the term "cells", which was first attributed by Hooke in 1665, while studying the microstructures of cork under an optical instrument capable of magnifying objects in just 30X [5]. Since then, successive discoveries and technological innovations have made it possible to study cells microscopically and understand their origins, structures, and functions, that in the scope of this thesis, emphasis is given to the importance of certain brain cells, called glial cells, to understand their role in the brain neuronal network, focusing particularly on extracellular signaling functions.

## 2.2.1 – Cells origins, structures, and functions

Cells origins are divided into two types of organisms − prokaryotic and eukaryotic cells, being estimated by the scientists that eukaryotes evolved from prokaryotes around 2.7 billion years ago. Prokaryotes and eukaryotes vary in several important ways - these differences include structural variation − whether a nucleus is present or absent, and whether the cell has membrane-bound organelles, and molecular variation, including whether the DNA is in a circular or linear form. The differences are summarized in the Table 2.1 below [6].

**Table 2.1 –** Key differences between prokaryotic and eukaryotic cells.

| | **Prokaryote** | **Eukaryote** |
|---|---|---|
| **Nucleus** | Absent | Present |
| **Membrane-bound organelles** | Absent | Present |
| **Cell structure** | Unicellular | Mostly multicellular |
| **Cell size** | Smaller (0.1 – 5 μm) | Larger (10 – 100 μm) |
| **Complexity** | Simpler | More complex |
| **DNA form** | Circular | Linear |
| **Examples** | Bacteria, archaea | Animals, plants, fungi, protists |

This work only uses eukaryotic cells, including glial, neuronal, and muscle cells. For this reason, only the relevant cell functions related to the origin of extracellular signals generated by those eukaryotic cells are discussed.

A simplified structure of a eukaryotic cell is shown in Figure 2.1, showing the peripheral region of the cell called the cytoplasmic membrane, which, in addition to the nucleus, encompasses the cytoplasm, and other membrane-bound organelles which serve to compartmentalize cellular functions, such as energy metabolism, digestion of macromolecules, and transport of proteins.

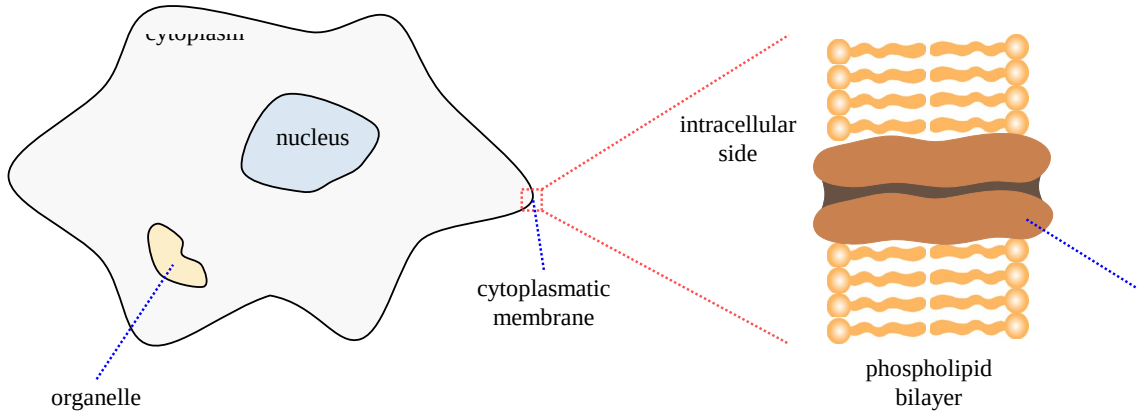


**Figure 2.1 –** Illustration of the basic structure of a eukaryotic cell and of the cytoplasmic membrane.

Besides enclosing the cell, the cell membrane supports the cell contents, acts as a selective barrier that determines what moves into and out of the cell, and plays a role in the communication between cells [7]. For this reason, the cell membrane, which in Figure 2.1 is called cytoplasmatic membrane, is particularly relevant to this work, as the cell membrane and its associated transport mechanisms allows cells to generate either electrical or ionic potential gradients, i.e., the so-called extracellular signals. Therefore, the source of extracellular signals always relies on the structure and functions of the cell membrane.

The cytoplasmatic membrane is composed of a phospholipid bilayer as depicted in Figure 2.1, with the hydrophilic “heads” (sphere-like shape) of the lipids facing the cell’s aqueous interior on one side of the membrane and the extracellular environment on the other. Note that, the membrane is not a rigid, or a static structure, but rather, it is an oily fluid, in which the proteins and lipids are in constant motion, as the cell membrane has selective permeability properties, where only small non-polar gases like the oxygen and carbon dioxide, and small uncharged molecules like water can diffuse freely across the lipid bilayer. Charged molecules such as ions cannot diffuse through the lipid bilayer regardless of the size. This membrane properties allows the membrane to move and change the shape of the cell [4].

Proteins and other molecules are embedded in lipids and, although the cytoplasmic membrane is essentially composed of lipids, cellular functions related to the origin of extracellular signals are

determined by proteins. Proteins can either be intrinsic or extrinsic, depending on whether the protein penetrates the phospholipid bilayer or is bounded to one of the inner or outer side of the lipid bilayer, respectively. For instance, extrinsic proteins protruding from cell membrane are responsible for binding and adhering to adjacent cells, while transport proteins are formed by one or more intrinsic protein arranged in a way that allow the formation of a tunnel (pore) through the cell membrane (as shown in Figure 2.1), whereby only small molecules and ions can move in or out. There are three types of transport proteins – channel protein, carrier protein, and ATP-powered pumps. Channel proteins only move ions across the cell membrane, while carrier proteins and ATP-powered pumps move ions or molecules from one side of the cell membrane to the other, whereas ATP-powered pumps require the use of energy derived from the breakdown of adenosine triphosphate (ATP). The regulation of the opening or gating functions of transport proteins is responsible for the generation of extracellular signals, but its complexity goes beyond the scope of this work, and only aspects related to the source of extracellular signals are discussed on the sections that follow.

### 2.2.2– Principles of extracellular signals of excitable and non-excitable cells

In biological terms, all cells due to their selectively permeable membrane properties and complex transport mechanisms, have capabilities to maintain very different ionic concentrations inside and outside of the cell membrane, and to perform ionic transactions. As ions are electrically charged particles, the flow or exchange of ions between the two separate media results in a potential difference ($\Delta U$). Under these circumstances, cell membranes may become: (i) balanced state, $\Delta U = 0$; (ii) overcharged, $\Delta U > 0$; (iii) undercharged, $\Delta U < 0$; and in any case, an equivalent membrane voltage ($V_M$) proportional to $\Delta U$, $V_m \propto \Delta U$, can be recorded electrically. $V_M$ is defined as the difference in electric potential between inside the cell, $\varphi_{intra}$, and outside the cell, $\varphi_{extra}$, given by,

$$V_M = \varphi_{intra} - \varphi_{extra} \tag{2.1}$$

For the purposes of understanding the origin of extracellular signals, in most cases, $\varphi_{extra}$ is considered constant, since the volume of the extracellular medium is assumed to be unequivocally greater than that of the intracellular medium. According to equation (2.1), whenever a cell is no impinged with any input, the balanced state is reached according to the chemical and electrical forces exerted by the ions until there are no net flow of ions. Under these circumstances, $V_M$ is constant, and is called the resting potential ($V_{rest}$), as it provides a neutral condition that allows the cell to rest after expending energy on its biological functions. However, whenever a cell is impinged with any input, i.e., when $\varphi_{intra} \neq \varphi_{extra}$; its response mechanism defines whether the cell is excitable or not (non-excitable).

Commonly, the term excitable refers to cells that are electrically excitable, such as muscle and neuronal cells, because this type of cells has voltage gate channels, a type of ion channel that provide cells the ability to sense and regulate their membrane potential in response to an external electrical stimulus. In addition to electrical sensitivity, cells can also sense changes in their membrane potential through mechanical, optical, thermal, and chemical stimuli; but regardless of the input to which a cell response, the common response of a cell is in form of ionic gradients, and as ions are electrical charged particles, it can be recorded electrically. Thus, despite non-excitable cells not having voltage gate channels, meaning they cannot sense changes in the membrane potential due to an electrical input, its biological functions will certainly require ionic transactions within the cell membrane, which by itself is already a signal source that implies changes in the membrane potential.

### 2.2.3– Resting potential

The resting potential is the basis of all extracellular signals, since extracellular signals are confined to a period of activity ($T$), during which $V_m$ oscillate, where the initial ($\varphi_i$) and final ($\varphi_f$) potential of the cell membrane oscillation tends to be the same, that is, considering that, $V_M \cong \varphi_i(0) \cong \varphi_f(T)$; on the assumption that $\varphi_{extra}$ remains unchanged, regardless of the variability of $\varphi_{intra}$. The phenomena that give rise to the resting potential are best described from an electrochemical point of view, where whenever two solutions of different ionic concentrations come into physical contact at a given instant, and in absence of an electrical force, ions flow from points from high concentration to low concentration, causing the system moving toward an equilibrium. In case of cell membrane, the membrane voltage ($V_M$) for which there is no net flow of ions is called the equilibrium potential ($V_{eq}$), i.e., the balanced state established by $\Delta U = V_M - V_{eq} = 0$. The equilibrium potential is also referred to as the reversal potential since the current flow changes its direction when comparing values of $V_M$ above and below $V_{eq}$. Nernst [8] was the first to establish a relation derived from statistical mechanics between the charge and concentration gradients of the ions to which a given ion channel is permeable as (Sterratt, 2011, pp. 37) [9],

$$V_{eq} = \frac{RT}{z_S F} \ln\left(\frac{[C_S]_{extra}}{[C_S]_{intra}}\right) \tag{2.2}$$

where $[C_S]_{extra}$ and $[C_S]_{intra}$ are the concentrations of an ionic species S in the extracellular and intracellular media, respectively; and $z_S$ is valence of the ion S. The remaining variables are constants. $R$ is the ideal gas constant, 8.314 J/(mol·K), $T$ is the absolute temperature, and $F$ is the Faraday's constant, $9.6485 \times 10^{-4}$ C/mol [10]. Nernst equation is useful to determining the $V_{eq}$ for a single ion, as it comprises the basis of extracellular signals. On the other hand, an alternative derivation known as

the *Nernst–Planck equation* offers a greater insight into the electrochemical process behind the source of extracellular signals, as it allows to express the electro-diffusion of ions across the ion channels.

In what follows, first it is assumed that $[C_S](x)$ is the concentration of an ion S measured in molecules per cubic centimeter, molecules/cm$^3$; and $V(x)$ the potential at the point $x$ across a cell membrane with a higher internal concentration of a positively charged ion S and lower external concentration of the ion S measured in volts, V. Due to the large concentration gradient, ion S will diffuse out of the cell, for instance, through an ionic channel. Fick's law (1855) provided an empirical description relating the diffusive flux ($J_{S,diff}$), arising from the diffusion of ion S down the concentration gradient as,

$$J_{S,diff} = -D_S \frac{\partial [C_S]}{\partial x} \tag{2.3}$$

where $D_S$ is the diffusion constant of ion S measured in square centimeters per second, cm$^2$/s. The other physical force that is responsible for the passive movement of ions is the electrical drift ($J_{S,drift}$) that is described by the microscopic version of the Ohm's law,

$$J_{S,drift} = -\frac{D_S F}{RT} z_S [C_S] \frac{\partial V}{\partial x} \tag{2.4}$$

where the electric field ($E \equiv -\partial V / \partial x$) is the gradient of the membrane potential $V(x)$. The sum of the diffusion and drift fluxes from equations (2.3) and (2.4) is the total flux across the membrane of an ion S ($J_S$) that describes the electro-diffusion of ion S as,

$$J_S = J_{S,diff} + J_{S,drift} = -D_S \left( \frac{\partial [C_S]}{\partial x} + \frac{z_S F}{RT} [C_S] \frac{\partial V}{\partial x} \right) \tag{2.5}$$

Equation (2.5), was developed by Nernst (1888) and Planck (1890) and is called the *Nernst–Planck equation*, but for the purposes of extracellular signals it is interesting to express Equation (2.5) as the flow of charge carried by the molecules, rather than the flow of the molecules themselves, i.e., considering that the current density ($I_S$) due to a particular ion S is proportional to the molar flux ($J_S$) of that ion and the charge it carries as,

$$I_S = F z_S J_S \tag{2.6}$$

where $I_S$ has units of amperes per square centimeters, A/cm$^2$. Furthermore, it is convenient to use the Nernst-Einstein relation which connects mobility ($\mu_S$) with the diffusion coefficient ($D_S$) as,

$$D_S = \frac{kT}{q} \mu_S \tag{2.7}$$

where $\mu_S$ has dimensions of square centimeters per volt second, cm$^2$/(V.s); $q$ is charge with units in coulombs, C; and $k$ is the Boltzmann's constant ($1.380658 \times 10^{-23}$ J/K). Also, since Equation (2.5) is expressed in terms of individual molecules, it is convenient to convert into its molar equivalent, by

dividing by Avogadro's number ($N_A$) ($6.022\times10^{-23}$ mol), as well to introduce $RT/F$, instead of $kT/q$ [11]. Thus, Equation (2.5) can be written as,

$$I_S = -\left(u_S z_S RT\frac{\partial[C_S]}{\partial x} + u_S {z_S}^2 F[C_S]\frac{\partial V}{\partial x}\right) \tag{2.8}$$

where the quantity $u$ consists of the molar mobility to a particular ion S given by $\mu_S/N_A$. Since at equilibrium, the diffusion and electrical forces are balanced, Equation (2.8) must be zero ($I_S = 0$) to fulfill the equilibrium condition. Note that, the solution of Equation (2.8) when $I_S = 0$ is the Nernst equation (2.2).

As the complex arrangement of the entire cell membrane structure depends on its permeability to each ion as well as the concentrations of nearby ions, the Nernst equation is far from the actual cell membrane potential. In these circumstances, the simplifying rules of equilibrium cannot be applied, and the derivation must make assumptions about the structure of the channel [12]. In order to take into account various ionic species, it is useful to introduce what is commonly called the *Goldman–Hodgkin–Katz voltage equation* (GHK), that provides a better approach to the true membrane potential when multiple ions are involved [13]. Essentially, GHK voltage equation assume (1) the electric field across the lipid membrane is constant, (2) the Nernst–Planck equation holds within the membrane, and (3) the ions all move independently. Given several ionic species involved in the ionic currents and concentration gradients, the total current ($I$) is the sum of the contributions of the currents to each ionic species, as consequence of the assumption 3. A particular example commonly used to describe the electrical signals of neuronal cells, considers a membrane permeable to three different ionic species, namely, sodium ($Na^+$), potassium ($K^+$), and chloride ($Cl^-$), with corresponding currents $I_{Na}$, $I_K$, and $I_{Cl}$. The total current ($I$) is empirically given by, (Ermentrout, 2010, pp. 21) [11],

$$I = I_{Na} + I_K + I_{Cl} = Fz_{Na}J_{Na} + Fz_K J_K + Fz_{Cl}J_{Cl} \tag{2.9}$$

where the equilibrium condition, that is given when $I = 0$; occurs when the membrane potential ($V_M$) is given by,

$$V_{eq} = \frac{RT}{F}\ln\left(\frac{P_{Na}[Na]_{extra} + P_K[K]_{extra} + P_{Cl}[Cl]_{intra}}{P_{Na}[Na]_{intra} + P_K[K]_{intra} + P_{Cl}[Cl]_{extra}}\right) \tag{2.10}$$

where $R$, $T$, and $F$ are the same constant described above; $[C_{ion}]_{extra}$ and $[C_{ion}]_{intra}$ are the extracellular and intracellular media concentrations and $P_j$'s are the permeability of the three ionic species, respectively. Equation (2.10) is the GHK equation, which is a generalization of the Nernst equation, but describing a steady state interdiffusion of three ionic species away from equilibrium, providing insight into the true influence of the cell membrane permeability on the equilibrium potential.

## 2.2.4– Equivalent circuit for the cell membrane: Electrical analogue

Previously, the electrical properties of cells were determined by the ionic species that move across the cell membrane according to the permeability of ion channels and concentration gradients. However, all the discussion has been done in a steady-state environment. For instance, the GHK equation (2.10) does not response to how changes in permeabilities have effect on electrical signals, because there may be energy barriers or blocking sites within the channel, and the ions flowing through the open channel (pore) may not obey the *Nernst–Planck equation* [11]. In these circumstances, the simplifying rules of equilibrium cannot be applied, and the derivation must make assumptions about the structure of the channel [12], thus requiring a complex analysis. A very useful way to analyze the membrane potential is in terms of electrical circuits, i.e., through an equivalent circuit model.

Although the cell membrane contains numerous conducting channels, it is best to first consider a cell membrane that is permeable to only one ionic species S, as schematically represented on the left side of Figure 2.2. Hence, using an intuitive perspective, the electrical equivalent circuit model to describe the behavior of the membrane potential ($V_M$), as well as the movement of ionic species between the inner and outer sides of the lipid bilayer that are mediated through an ion channel is given by: (1) a resistor, representing the conductive pathway from the ion channel permeable to a ion species S; (2) a battery source, representing the ionic gradients; and (3) a capacitor, representing the ability of the membrane to store charges, as shown on the right side of Figure 2.2. Besides, a switch is also included in the equivalent circuit to consider the capacitor charge or discharge condition.

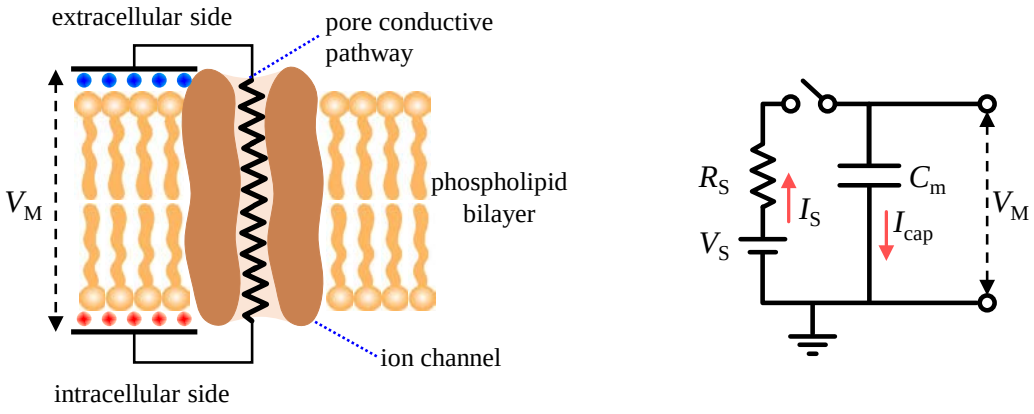


**Figure 2.2 –** The left schematic illustrates the cell membrane, consisting of an insulating lipid bilayer and an ion channel that allows the flow of ionic gradients. On the right, the equivalent electrical circuit of the membrane is depicted.

From an electrical perspective, the equivalent electrical circuit shown in Figure 2.2 is a passive RC circuit. The term passive refers to the fact that the circuit components, such as the resistor and

capacitor, do not generate an electrical signal on their own and remain unchanged regardless of the external stimulus. The circuit can only respond to an applied electrical signal.

Likewise, in biological terms a cell is considered to be passive if their electrical properties do not change during signaling even when exposed to an external stimulus. Under these circumstances, a cell is considered non-excitable.

## 2.2.5– Graded potentials

The terms “non-excitable” and “excitable” cells are used to distinguish the extracellular signalling capabilities of different types of cells. But regardless of cell type, all cells can generate ionic gradients, which are an implicit mechanism required by cells to perform their biological functions based on ionic transactions between both sides of the lipid bilayer. Since ions are electrical charged particles, ionic gradients generate signals in cells due to changes in membrane potentials. Thus, whenever an ionic gradient occurs, it can lead to a hyperpolarization or depolarization of the cell membrane, where a hyperpolarization occurs due to an increase in the number of electrical charges in the intracellular medium, causing an increase of $V_M$; while depolarization occurs due to the loss of intracellular polarization, causing a decrease of $V_M$. These changes on $V_M$ are referred as graded potentials.

Graded potentials are best described through an electrical analysis of the circuit model shown in Figure 2.2, so that, starting by considering the current through the pore conductive pathway permeable to a specific ion S ($\hat{I}_S$) which is represented by the resistance ($R_S$) due to its pore conductance path of ions S, and in series with a voltage source ($V_S$) that drives ions S according to the concentration gradients (chemical force). The strength of $V_S$ is the equilibrium potential ($V_{eq} \equiv V_S$) obtained with the Nernst equation, where the driving force ($\Delta E$) is $\Delta E = V_M - V_S$. Since $\hat{I}_S$ flows through a pure resistive path ($R_S$), then, Ohm’s law satisfies the criteria, so that $\hat{I}_S$ is given by,

$$\hat{I}_S = \frac{V_M - V_S}{R_S} \equiv g_S(V_M - V_S) \tag{2.11}$$

where the subscript S is the ionic species of interest. The resistance (symbolized as $R_S$) has units of ohm ($\Omega$), and is defined as $R_S \equiv 1/g$, where $g$ is the conductance with units of siemens (S). Here, $R_S$ is assumed as constant for this specific pore. As the cell membrane contains numerous ($N_S$) ionic channels permeable to an ionic species S, the equivalent electrical circuit must consider the overall membrane conductance per unit of area, same as the specific membrane conductance ($g_M$) measured in siemens per square centimeter ($S.cm^{-2}$), and given by, $g_M = N_S \times g_S$. Alternatively, $g_M$ may be converted into the specific membrane resistance ($R_M$) as, $R_M \equiv 1/g_M$, that is measured in ohms per square centimeter ($\Omega.cm^{-2}$). As the equilibrium potential given by the Nernst potential relies only on

the concentration gradient of an ionic species S, and not on the number of ionic channels permeable to the ionic species S, it follows that Equation (2.11) describing the pore conductive pathway ($\hat{I}_S$) can be rewritten as,

$$I_S = \frac{V_M - V_S}{R_M} \equiv g_M(V_M - V_S) \tag{2.12}$$

where $I_S$ is the pore conductive pathway per unit area. Since ions do not diffuse instantaneously through the pore-conducting pathway, in electrical terms, it means the cell membrane behaves as a capacitor in parallel with the pore-conducting pathway, as schematically shown in Figure 2.2. From a physical perspective, the lipid bilayer that constitutes the cell membrane acts as an insulating layer with dielectric properties, usually with a narrow thickness of 2 to 5 nm. Thus, whenever ceases an excess of positive charge on one side and an excess of negative charge in the other side of the cell membrane, cause the cell membrane to polarize accordingly to the number of charges ($q$) accumulated. Still, during a depolarization, charges are released in form of a current. The capacitance (symbolized as $C_m$) has units of farad (F), and is defined as,

$$C_m = \frac{q}{V_M} \tag{2.13}$$

where $C_m$ is the membrane capacitance and is assumed as constant for a specific nearby region of a pore conductive pathway. The total membrane capacitance ($C_M$), also referred as the specific membrane capacitance, relies on the entire dielectric surface area of the cell membrane, and is measured in farads per square centimeter ($F.cm^{-2}$). For extracellular signals purposes, it is important to comprehend that the current passing through the capacitance simply removes charge from one side of the membrane and accumulate in the other in a fully reversible manner and without evolving heat [12]. In electrical terms, it means that the extracellular signals are proportional to the how much charge ($q$) needs to be transferred from one side to other of the membrane to set up a potential difference, i.e., that the rate of change of the potential under a capacitive current flowing through the ionic channel is obtained by taking the time derivative of Equation (2.13) as,

$$I_{cap} = C_M \frac{dV_M}{dt} \tag{2.14}$$

where $I_{cap}$ is the capacitance per unit area.

In case of a close-circuit loop, i.e., the switch in the equivalent circuit shown in Figure 2.2 is closed, then accordingly to Kirchhoff's current law, the total current into the cell must sum to zero, thus leading to a first order, linear, ordinary equation,

$$I_m \equiv I_{cap} + I_S = C_M \frac{dV_M}{dt} + \frac{V_M - V_S}{R_M} = 0 \tag{2.15}$$

or, by rearranging Equation (2.15) terms,

$$\frac{dV_M}{dt} = -\frac{1}{\tau}(V_M - V_S) \tag{2.16}$$

where $I_m$ is the total membrane current due to membrane electrical properties; and $\tau$ is the membrane time constant given by the product of the specific membrane resistance and capacitance ($\tau = R_M C_M$), respectively. For the sake of simplicity, it is assumed that at rest $V_M = 0$, so that $V_M$ measures the deviation of the membrane potential from rest ($V_{rest}$) to equilibrium ($V_{eq}$), as well that the circuit switch is modeled by a voltage step. Then, the solution of Equation (2.16) in response to a voltage step is given by,

$$V_M(t) = u(t)V_S\left[1 - e^{-(t/\tau)}\right], \text{ for } 0 < t < T \tag{2.17}$$

where $T$ is the oscillation period; $u(t)$ is a unitary voltage step, which is zero for any $t < 0$ and $t > T$, and one for $0 < t < T$; and $V_S$ is the steady-state voltage level ($V_{ss}$), which typically is given by the Nernst equation (2.2), $V_{ss} \equiv V_S$. Note that the longer is the time course of the ionic gradient, $V_M$ approaches asymptotically to $V_S$ ($V_M \rightarrow V_S$), meaning the total current flowing through the ionic channel becomes more and more ohmic, so that in the limits $V_M \equiv R_M I_S$. Furthermore, as the oscillation period ($T$) is controlled by the cell, it is considered that for $t > T$, the cell returns to its resting condition. Under these circumstances, since the membrane capacitance is charged, the membrane potential ($V_M$) can only revert to its resting condition if $V_S$ changes polarization, so that $I_S - I_{cap} = 0$. In this case, the solution of the linear, ordinary equation is a voltage that decay exponentially in time,

$$V_M(t) = V_S e^{-(t/\tau)}, \text{ for } t > T \tag{2.18}$$

where $V_M$ measures the membrane potential back to its rest condition according to the same membrane time constant ($\tau$). In the left side of Figure 2.3, the upper voltage axis panel illustrates a graded potential according to equations (2.17) and (2.18) in response to a voltage step, $u$(t), as depicted in the voltage panels on the left side of Figure 2.3.

Graded potentials also rely on the contribution of several pore-conducting pathways along the cell membrane that have a selective permeability to different ionic species, such as the GHK approach described earlier. The inclusion of more pore conductive paths in the electrical circuit model allows to estimate membrane potential ($V_M$) more accurately. Such considerations are beyond the scope of this thesis. However, the strength of an extracellular signal requires may rely for instance on the contribution of the ATP-pumps, which has a high impact on the signal strength, since they allow move ions against the concentration gradients from one side of the cell membrane to the other at a higher rate if compared with a single ion channel.

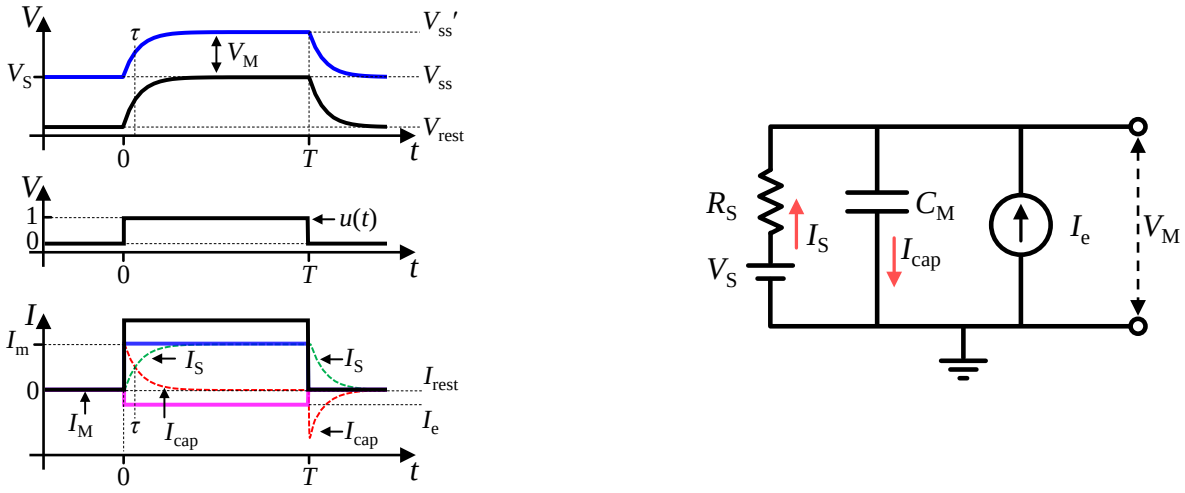


**Figure 2.3 –** Behaviour of the membrane potential ($V_M$) modeled by a parallel RC circuit in response to either a step of voltage or current. On the left side, the upper axis panel shows a solid black line representing $V_M$ as described by equations (2.17) and (2.18) in response to a voltage step, while a solid blue line representing $V_M$ as described by equations (2.23) and (2.24) in response to a step of current. The middle axis panel shows the voltage step, which is one for $0 < t < T$. The bottom axis panel shows the time course of the total membrane current ($I_M$) (thick black solid line), given by the sum of all currents in the close circuit loop, where the solid magenta line represents the current step ($I_e$), the solid blue line represents the current due to the membrane electrical properties ($I_m$) given by the sum of the ionic ($I_S$) (green dashed line) and capacitive ($I_{cap}$) (red dashed line) currents. On the right side, it is shown the equivalent electrical circuit considering a current injection ($I_e$) source.

In electrical terms, such behavior is accomplished by considering the equivalent circuit model shown in the Figure 2.2, requiring only to include in parallel a current injection source ($I_e$) capable of sourcing current either as input or output, such as the case of an ATP-pump. The right side of Figure 2.3 shows the equivalent circuit model described above, for which, according to the Kirchhoff's current law, the sum of all currents in the closed-circuit loop must be zero, so that, as before, leads to a first order, linear, ordinary equation,

$$I_M \equiv I_{cap} + I_S - I_e = C_M \frac{dV_M}{dt} + \frac{V_M - V_S}{R_M} - I_e = 0 \tag{2.19}$$

or, by rearranging Equation (2.19) terms,

$$\frac{dV_M}{dt} = -\frac{1}{\tau}(V_M - V_S) + \frac{1}{\tau} I_e R_M \tag{2.20}$$

where $I_M$ represents the total membrane current ($I_M$); and $I_e$ is the injected current subtracted from the other two current sources due to the membrane electrical properties, since it is assumed the convention that the current is positive when positive charges flow out of the cell membrane. Equations (2.20) and (2.16) are quite similar, differing only on a voltage offset level that is controlled by the $I_e$ sign convention and amplitude, or in other words, means whenever $I_e$ is different of zero, $I_e \neq 0$, a new steady state voltage level ($V_{ss}'$) is established. For the sake of simplicity, to solve the first order, linear, ordinary equation (2.20), $I_e$ is considered a current step. Taking in account that $I_e$ has been zero for some long enough period that the membrane potential is at rest, $V_M(0) \equiv V_S$, so that, at a given instant,

$I_e$ can be either stepped-up or down to a fixed value for $0 < t < T$, where $T$ is the current step period and is assumed long enough to ensure the time course of $V_M$ approaches asymptotically to $V_{ss}'$, $V_M(T) \rightarrow V_{ss}'$. Under these circumstances, the capacitive component is null, $dV_M/dt \rightarrow 0$, so that $V_{ss}'$ can be easily derived from Equation (2.20) as,

$$0 = -\frac{1}{\tau}(V_{ss} - V_S) + \frac{1}{\tau} I_e R_M \tag{2.21}$$

or, after re-arranging Equation (2.21),

$$V_{ss}' = V_S + I_e R_M \tag{2.22}$$

As before, since only the contribution of single ion channel permeable to an ion species S is being considered, $V_S$ is given by the Nernst equation (2.2), while the offset voltage level due to the inject current ($I_e$) is proportional to the charges moved through the ATP-pump. On the upper voltage panel in the left side of Figure 2.3, the solid blue line represents the membrane potential ($V_M$) time course in response to current step, considering the solution of equation (2.20) is given by,

$$V_M(t) = u(t) V_{ss}' \left[1 - e^{-(t/\tau)}\right] + V_S e^{-(t/\tau)}, \text{ for } 0 < t < T \tag{2.23}$$

taking into account all the considerations mentioned above, so that $T$ is the oscillation period; $V_{ss}'$ is the new steady-state voltage level in response to a current step given by equation (2.22); and $u(t)$ is the unitary voltage step, which is zero for any $t < 0$ and $t > T$, and one for $0 < t < T$. For guidance purposes, the panel in the left side of Figure 2.3 includes in the bottom a current axis, where each thick solid line represents the time course of a current, so that the black line represents $I_M$ as described in equation (2.19), the blue line represents $I_m$ as described by equation (2.15), and finally the magenta line represents the injected current step ($I_e$). As soon as the cell oscillation period ($T$) ends, i.e., after the injected current steps back to zero, $I_e = 0$, then for $t > T$, the cell returns to its previously equilibrium condition, which before, it was considered the current step was turned on after $V_M \rightarrow V_S$. Under these circumstances, the membrane potential ($V_M$) reverts to its equilibrium condition because the sign convention of $I_e$ changes, so that $I_M = I_S + I_{cap} + I_e = 0$, where the solution of this linear, ordinary equation is a voltage that decay exponentially in time, that measures the membrane potential back to its equilibrium condition according to the same membrane time constant ($\tau$),

$$V_M(t) = V_S + (V_{ss}' - V_S) e^{-(t/\tau)}, \text{ for } t > T \tag{2.24}$$

or, in case the cell intends to return to its resting condition, equation (2.24) resumes to,

$$V_M(t) = V_{ss}' e^{-(t/\tau)}, \text{ for } t > T \tag{2.25}$$

So far, all considerations regarding graded potentials were grounded on linear principles for a single ion channel permeable to an ion species S. While such considerations were of great use to comprehend the nature of changes in the membrane potential that give rises to extracellular signals, it does not provide information about how different results may be achieved when considering more

complex environments, such as the case proposed by GHK equation (2.10) which relates the interdiffusion of three ion channels permeable to different ion species, or if non-linear principles were considered. Such considerations are beyond the scope of this thesis. Another important aspect about graded potentials is that regardless of whether the graded potential is generated with or without a source of current injection, both the rise and fall times of membrane potentials are always controlled by the electrical properties of cell membrane, namely, by the membrane time constant ($\tau$) in a predicable way, since the electrical properties do not change over time. This property is determinant on the temporal scale of graded potentials (the extracellular signal), and it's the reason why different cells have signals of different temporal scales. Regarding the strength of graded potentials, changes in membrane potential due to concentration gradients are likely to be relatively weak compared to an electrical signal based on drift currents, as discussed later in Section 2.2.6.

### 2.2.6– Action Potential

Beyond graded potentials, excitable cells have voltage sensitivity channels, also known as voltage gate channels, which under a certain threshold voltage ($V_{th}$), i.e., when $V_M > V_{th}$, causes excitable cells to trigger an electrical response mechanism consisting of a signal of disproportionate strength to the perturbation, known as an action potential (AP). This means that APs are a consequence of changes in the electrical properties of membrane permeability, so that at a given potential, an ion channel opens (hence the name gate), causing a momentary short circuit through the pore conductive pathway between the internal and external media of the cell, which in electrical terms corresponds to a voltage spike as consequence of the immediate flow of electrical charges. For this reason, the equivalent circuit model depicted in Figure 2.2 includes a shaded region including a current injection source operating as a stimulus current ($I_{ext}$) in parallel with the pore conductive pathway and the cell membrane potential.

Beyond graded potentials, excitable cells have voltage sensitivity channels, also known as voltage gate ion channels (VGIC), which under a certain threshold voltage ($V_{th}$), i.e., when $V_M > V_{th}$, causes excitable cells to trigger an electrical response mechanism consisting of a signal of disproportionate strength to the perturbation, known as an action potential (AP). This means that APs are a consequence of changes in the electrical properties of membrane permeability, so that at a given potential where $V_M > V_{th}$, an ion channel opens (hence the name gate) so drastically that it leads to a spontaneous depolarization of the cell membrane due to an intrinsic drift of ions across the pore conductive pathway between the cytoplasmatic and external media of the cell membrane. In electrical terms, Cole, and

Curtis (1938) were the first to interpret their measurements of APs on squid giant axon, having considered that the membrane potential of an AP is modeled by graded potentials as described earlier in Section 2.2.5. However, they have considered a voltage-varying conductance to model the pore conductive pathway, so that whenever $V_M > V_{th}$, their electrical circuit model takes in account the electrical drift between the cytoplasmic and external media due to the drastic decrease of the ion channel conductance. This means that such cellular behavior can be modeled by the electrical equivalent circuits shown earlier in Figure 2.2 and Figure 2.3, requiring only to consider a voltage-varying conductance. In ideal conditions, the voltage-varying conductance can be interpreted as a switch in parallel with the non-variable conductance to bypass the conductance of the ion channels permeable to an ionic species whenever $V_M > V_{th}$.

Generation of APs are far more complex than just the contribution of a single ion channels permeable to an ionic species S. A detailed analysis on how excitable cells generate APs goes beyond the scope of this thesis, still the basic concepts are introduced below, as within the course of this thesis, the recording of APs will be made for the purposes of validation and characterization of the recording method.

Starting by considering the previous discussion of graded potentials, it is intuitively possible to perceive that since the cell membrane is strongly polarized and has dielectric properties, that is, there is a component $dV_M/dt$ in the system, then, whenever a disruptive current is introduced into the system, the faster is the disruption of ions, the stronger the extracellular signal, hence APs are also commonly referred to as “spikes”. Another important aspect of APs has respect to the additional number of ionic species that are simultaneously engaged in the generation of an AP, so that while one (or more) ion channels permeable to an ion species depolarize the membrane potential due to the flow of ions into the cytoplasmatic medium, other ion channels will flow ions out of the membrane in response to the input stimulus, so that cell can repolarize its membrane potential due to an excess of positive charges. These two aspects referred above: (i) the dielectric properties of the membrane, $dV_M/dt$, and (ii) the number of ion channels permeable to different ion species, define the strength and period of APs, and that is why APs generated by different cell types has different shapes, periods, and amplitudes.

Since it is assumed that the dielectric properties of the membrane are kept constant during the generation of APs to a particular cell type, the key difference between APs produced by different cell types is related to the ion species involved either in the depolarization and repolarization of the membrane potential.

In animal cells, there are two primary types of APs. One type is generated by voltage-gated sodium channels (VG-$Na^+$ channels), the other by voltage-gated calcium channels (VG-$Ca^{2+}$ channels). VG-$Na^+$ channels are responsible for AP initiation and propagation in excitable cells, including nerve,

muscle, and neuroendocrine cell types [12,14]. VG-$Na^+$ channels are also expressed at low levels in non-excitable cells, however their physiological role is unclear [15]. On the other hand, VG-$Ca^{2+}$ channels are responsible for mediation of $Ca^{2+}$ influx in response to membrane depolarization and regulation of intracellular processes, such as contraction, secretion, neurotransmission, and gene expression in many different cell types [16,17]. VG-$Ca^{2+}$ channels activity is essential to couple electrical signals in the cell surface to physiological events in cells [18]. Despite VG-$Na^+$ and VG-$Ca^{2+}$ channels being the two selective ion channels of foremost importance in the generation of APs, other ion channels are often related to the generation and propagation of APs, such as the contribution of potassium ($K^+$) [19–21], chloride ($Cl^-$) [22–24], and Magnesium ($Mg^{2+}$) [25,26] selective ion channels. On the course of this thesis, nerve and cardiac pacemaker cells will be used, and for this reason, the main the contribution of each selective ion channels on the AP shape, period, and strength are illustrated in panels (a) and (b) of Figure 2.4.

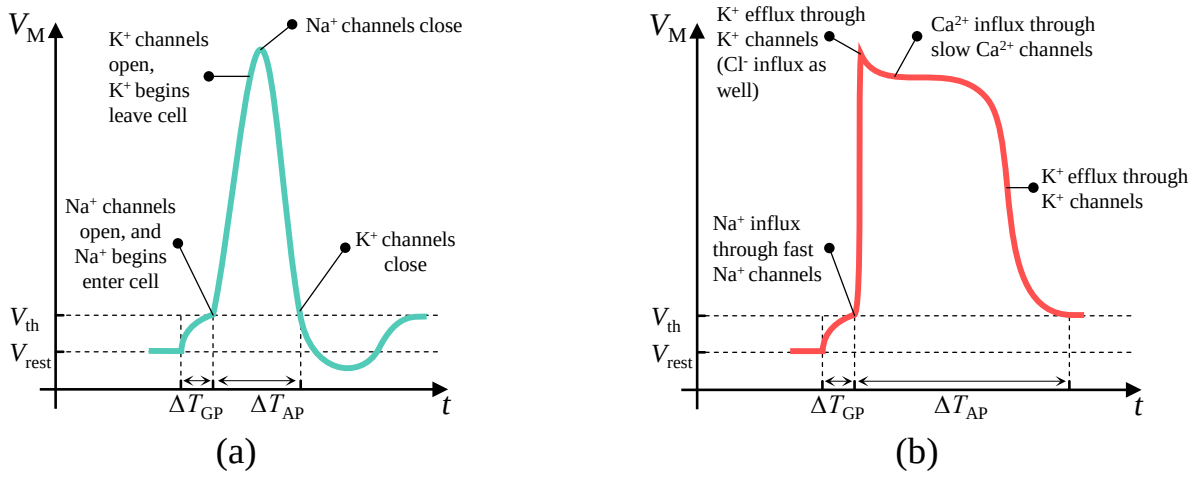


**Figure 2.4** – Illustration of the dependence of the shape, period and strength of action potentials (APs) due to the contribution of permeable ion channels to different ion species. Panel (a) shows an AP generated by nerve cells, while Panel (b) shows an AP generated by cardiomyocyte cells. On both panel (a) and (b) $\Delta T_{GP}$ and $\Delta T_{AP}$ represents the graded potential and action potential periods, respectively.

In electrical terms, the membrane potential ($V_M$) of the APs illustrated in panels (a) and (b) of Figure 2.4 can be intuitively defined according to the principles discussed earlier for graded potentials in Section 2.2.5, requiring only to consider the state of the VGICs. Therefore, whenever an VGIC is in its closed state, i.e., it behaves as a passive ion channel permeable to an ion species S to which its pore conducting pathway has a constant conductance ($g_S$) and polarized according to the direction of the concentration gradient ($V_S$), while whenever an VGIC is in its open state, the conductance of the pore conducting pathway is represented with the symbol $\hat{g}_S$, so that $g_S \gg \hat{g}_S$, and is also polarized according to the direction of the concentration gradient ($V_S$). Under these circumstances and assuming the cell is isopotential, then $V_M$ of the AP illustrated in panel (a) of Figure 2.4 satisfies,

$$C_{\mathrm{M}}\frac{dV_{\mathrm{M}}}{dt} = -\hat{g}_{\mathrm{Na}}(V_{\mathrm{M}} - V_{\mathrm{Na}}) - \hat{g}_{\mathrm{K}}(V_{\mathrm{M}} - V_{\mathrm{K}}) - I_{\mathrm{L}} \tag{2.26}$$

and the AP illustrated in panel (b) of Figure 2.4 satisfies,

$$C_{\mathrm{M}}\frac{dV_{\mathrm{M}}}{dt} = -\hat{g}_{\mathrm{Na}}(V_{\mathrm{M}} - V_{\mathrm{Na}}) - \hat{g}_{\mathrm{K}}(V_{\mathrm{M}} - V_{\mathrm{K}}) - \hat{g}_{\mathrm{Ca}}(V_{\mathrm{M}} - V_{\mathrm{Ca}}) - \hat{g}_{\mathrm{Cl}}(V_{\mathrm{M}} - V_{\mathrm{Cl}}) - I_{\mathrm{L}} \tag{2.27}$$

where $I_{\mathrm{L}}$ is called the leak current, which accounts for the passive flow of ions through non-gated channels. The solution of the first order, linear, ordinary equations (2.26) and (2.27) requires more considerations that are beyond the scope of this thesis, as it needs to account with mathematical models to fit the temporal changes on each pore conductive pathway conductance.

## 2.3– Detection of extracellular signals

Both electronic devices and living cells communicate with electrical signals, but the charge carriers they use are different. Electronic devices rely on electrons in a crystalline lattice, while cells use ions in a polar fluid. The mobility of electrons in silicon is about $10^3$ $cm^2/Vs$, whereas the mobility of ions in water is around $10^{-3}$ $cm^2/Vs$ [1]. The huge difference in charge carrier mobility between electronic devices and live cells requires the use of an intermediary device (transducer) that allows a physical connection between the two interfaces, so that a signal originating from one of the interfaces is transformed into an equivalent signal with the mobility properties of the other interface, and vice versa. This process of signal transformation is known (or called) by transduction.

In the context of this thesis, electrodes are used as transducer devices to monitor, record, and analyze extracellular signals. The term 'electrode' was coined by Faraday in December 1883 to define the 'surfaces or ports through which electricity enters or exits decomposing substances' [27]. This section aims to provide a fundamental understanding of the transduction mechanism and its impact on the recorded extracellular signals. To achieve this goal, the section begins with a survey of the technological advancements that led to the development of transducer devices. Next, the behavior of a transducer device in an ionic solution is described. Finally, the cell-electrode interface is discussed to develop a qualitative description of an extracellular signal. By the end of this section, readers should have a comprehensive understanding of the principles of signal transduction and its role in measuring extracellular signals.

### 2.3.1– Bioelectronics: an historical perspective

From an electrophysiological (biophysical) perspective, one of the most significant technological breakthroughs for recording of extracellular signals was the introduction of an experimental procedure, known as the voltage-clamp procedure. This technique was first introduced by Cole and Marmont (1949), and later refined by Hodgkin, Huxley, and Katz (1949, 1952). For over 50 years, the voltage-clamp was the gold standard biophysical technique for studying ion channels [12]. With the voltage-clamp, researchers were able to hold the membrane potential constant while recording the resulting ionic currents, enabling a more precise understanding of the properties and behaviour of ion channels.

The voltage clamp technique (or intracellular recording in voltage clamp mode) uses a two micro-electrode configuration. One electrode is used for recording the current flowing through the cell membrane while the other electrode is used to held (clamped) the membrane potential at a constant value by the experimenter [13]. While this technique has been valuable for studying ion channels, it does have some drawbacks. The main issue is that it requires two microelectrodes to be impaled into the cell, making the experimental procedure complicated, expensive, and invasive. This can also lead to cell death [28].

To better understand the new recording techniques developed to replace the voltage clamp, it is essential to start by contextualizing how successive technological advances in electronics have paved the way for the development of new methodologies for cell interfaces and recording. By examining the evolution of electronic technologies, we can appreciate the contributions that these advancements have made to the field of electrophysiology and understand how they have enabled the creation of new techniques for recording and analysing biological signals.

The emergence of micro and nano integrated circuits marked a milestone in the newborn discipline of bioelectronics, as the size of electronic circuits equaled or became even smaller than the size of living cells, these developments paved the way for the creation of innovative bioelectronic interfaces with a wide range of potential biomedical applications. This vision was prescient, and researchers were quick to embrace these technologies to push the boundaries of what was possible in electrophysiology. In particular the work published by Wise and Angel in 1970 [29], was particularly meritorious, as it provided a ground-breaking example of how to apply these new technologies in practical ways. The pioneering approach of using integrated circuits as extracellular microprobes for chronic in vivo recording of single neurons in the cat cortex, in addition to being ground-breaking, has also inspired further investigations into electrode materials, geometry, and fabrication techniques.

Two years later, in 1972, Thomas introduced the first planar multielectrode array (MEAs) for *in vitro* recording of cultured embryonic chick heart cells [30]. Thomas noted that changes in electrode

design or techniques to increase extracellular impedance during recording could eventually allow single cell activity to be monitored using MEAs.

Since there, significant advances have been made in bioelectronic devices, as documented in Jerome Pine's review of MEA development history [31]. Most studies have focused on reducing electrode size to achieve single cell measurements, with material science playing a crucial role in these efforts [32–35]. In the early days of bioelectronic device development, metals and metal alloys were the main electrically conductive materials explored for electrode development. Gold was the standard choice due to its inertness, low exchange-current density in biological fluids, and suitability for high-resolution electrodes [29,36,37].

In the field of materials science, the ground-breaking discovery by Shirakawa, MacDiarmid, and Heeger in 1977 marked a significant turning point in electrode material technology. Their Nobel-winning work involved the first synthesis of electrically conducting organic polymers using halogen derivatives of *polyacetylene* [38] . This breakthrough opened the door to a new era in electrode material development, laying the foundation for soft, conformable, and biocompatible organic-based electrodes. In this thesis, conducting polymer-based electrodes will be utilized to fabricate extracellular electrodes for electrophysiological sensing.

### 2.3.2– Transduction: Electrode-Electrolyte interface

Section 2.2 focused on understanding the origin of extracellular signals without considering the electrical properties of the external environment surrounding cells. It was assumed that cells were surrounded by an ion-rich solution or electrolyte media, providing the conditions for ionic exchanges. However, to comprehend the transduction mechanism for detecting extracellular signals, the electrolyte and the electrical properties of the electrodes become crucial. The electrolyte serves as a conductive medium for the transportation of charge through the movement of ions to the electrodes, while the function of the electrodes is to convert energy in the form of ionic carriers to electronic carriers (electrons).

The extracellular signals as described by Equation (2.8), result from the ionic exchanges of a cell, which cause changes in the volumetric space (electrolyte medium) around the cells. These changes affect the entire equilibrium of the system including the electrode potential due to the diffusion and electrical forces of an ionic species S. Therefore, the transduction mechanism is closely related to the electrochemical balance of the electrode-electrolyte interface. However, the electrode potential has further implications that depend on the electrode material properties, the electrolyte composition, and the resulting electrochemical reactions. Extensive quantitative models describing the behavior at the

electrode-electrolyte interface have been reviewed extensively elsewhere [39–45]. The discussion in this section aims to provide a sufficient model to describe the electrodes behavior regarding extracellular signals.

### 2.3.2.1– Interfacial Capacitance: Helmholtz, Gouy-Chapman, and Stern

Electrochemical theory explains that when two phases of different electrochemical properties are brought into contact, a redistribution of charge and potential occurs at the interface until, at equilibrium, the electrochemical potentials of the charge carriers in both phases are equal. This redistribution of charge and potential results in an electrified interface and determines the electrochemical properties of the electrolyte-solid system [46].

In recording extracellular signals, electrified interfaces refer of an electrode and an electrolyte solution. Under zero-bias conditions, this contact leads the establishment of a space charge layer, between the two-phase materials as illustrated in Figure 2.5 (a). If the electrode has no applied bias voltage, there is no potential difference across the electrode/electrolyte interface, even though a space charge layer is formed at the interface due to chemical reactions, rather than electrochemical processes.

When considering a given electrode potential (V), the space charge layer formed at the electrode/electrolyte interface leads to the formation of an *ion cloud* near the interface. The thermal and electrical forces acting on the ions are balanced to form a time-averaged ionic distribution. The concentration of ions that accumulate in the electrolyte to counter the surface charge of the electrode varies from a maximum value at their closest approach to the electrode to their bulk concentration, which is relatively far away from the influence of the electrode [40]. The accumulation of positive (or negative) charge at the interface of the electrode and electrolyte solution is partially neutralized by the gathering of counterions in the solution through the action of Coulomb's force, resulting in a structured space charge layer that is commonly referred to as the electrical double-layer (EDL), because it is in this region that intense electric fields occur due to electrochemical reactions. The EDL consists of two layers. The first, called the Stern layer (also known as the Helmholtz layer), results from the

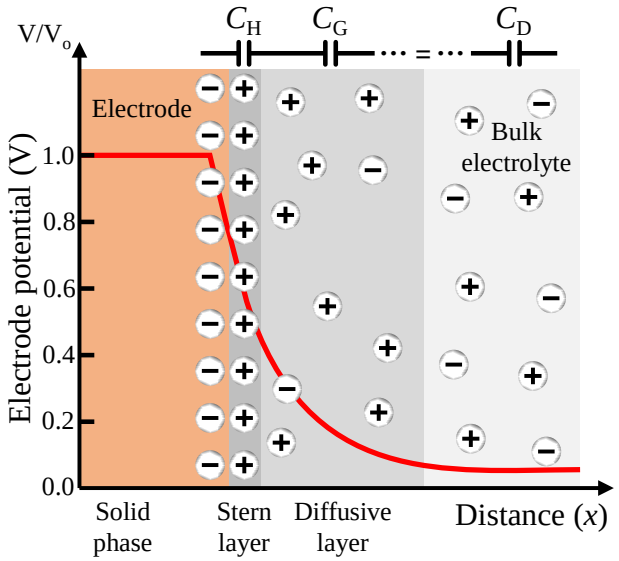


**Figure 2.5** – Simplified model of the equilibrium electrical double layer (EDL) at the charged electrode surface.

accumulation of counterions on the surface of the electrode, while the second layer, called the Gouy-Chapman layer, results from the diffusion layer extending outward from the Stern surface [47].

This ability of the electrolyte to store a quantity of charge ($Q$), for a given potential, is a static capacitance ($C$), as previously described in equation (2.13), which, in turn, is proportional to the interfacial capacitance ($C_I$) or as commonly referred to as electrical double layer capacitance ($C_D$), i.e., $C_I \equiv C_D$. However, each layer of the EDL makes a different contribution. The simplest model to describe the contribution of the Stern layer is to assume a two-dimensional space and that the charge in the electrolyte side is located in the *outer Helmholtz plane* (OHP), that is the diffusive layer depicted in Figure 2.5 (a). Under these assumptions, it is allowed to use the parallel-plates capacitor equation to define the Stern layer capacitance $C_H$, as,

$$C_H = \frac{\varepsilon_o \varepsilon_r}{d_{OHP}} \tag{2.28}$$

where $\varepsilon_0$ is the dielectric permittivity of free space ($8.85419\times10^{-12}$ F/m), $\varepsilon_r$ is the relative dielectric permittivity of the medium between the two plates (electrodes), $d_{OHP}$ is the distance from the electrode, and $A$ is the exposed area of the electrode in contact with the electrolyte which was proposedly omitted from (2.28) in the assumption that $C_H$ is the capacitance per unit area ($F/m^2$) [40].

Although a spatial charge in the electrolyte is not two-dimensional, and for this reason the simple model proposed by Helmholtz suffered from an inadequacy; it neglected the dependence of capacity on potential which had been observed experimentally, such as predicted by equation (2.13). In this regard, in 1910 and 1913, Gouy and Chapman suggested a modification on the Helmholtz model by considering the diffusive charge layer does not assume a layer of hydrated ions “stuck” at the OHP, nor a linear voltage drop across the “dielectric” (electrolyte) layer. The derivation of this model, discussed by Bard and Faulkner [49], will not be repeated here, only that, how for small applied voltages (<50 mV) it predicts a potential profile in the space charges region that is defined as a decaying exponential,

$$V(x) = V_o e^{-(x/L_D)} \tag{2.29}$$

where $x$ is the distance from the electrode, $V_o$ is the electrode potential for $x = 0$, and $L_D$ is the *Debye length*. The Debye length characterizes the spatial decay of potential and can be viewed as the characteristic thickness of the diffuse layer,

$$L_D = \sqrt{\frac{\varepsilon_o \varepsilon_r V_t}{2n^0 z^2 q}} \tag{2.30}$$

where $V_t$ is the thermal voltage ($kT/q$), $n^0$ is the bulk number concentration of ions in the electrolyte (ions/liter), $z$ is the valence of the ions, and $q$ is the charge on an electron ($1.60219\times10^{-19}$ C). Figure

2.5 includes a profile representation of the electrode potential according to equation (2.29) [40]. Thus, the differential capacitance per unit area (in F/m$^2$) proposed by Gouy and Chapman ($C_G$) can be calculated by,

$$C_G = \frac{\varepsilon_o \varepsilon_r}{L_D} \cosh\left(\frac{zV_o}{2V_t}\right) \tag{2.31}$$

where the first term ($\varepsilon_0\varepsilon_r/L_D$) is simply the capacitance per unit area of two plates separated by a distance $L_D$, and the effects of mobile charges are compensated for by the hyperbolic cosine. Unfortunately, the model proposed by Gouy-Chapman to estimate $C_I$ yields capacitance values that vary more sharply with applied voltage (typically overestimating capacitance values) than do experimental measurements, and does not show the finite plateau of capacitance with increasing applied voltage that occurs in real systems [49].

For these reasons, later in 1924, Stern proposed a new model to describe the behavior of the EDL that is given by the charges accumulated in the OHP ($C_H$) in series with the Gouy-Chapman model of the diffusive layer ($C_G$), yielding an expression for the EDL capacitance ($C_D$),

$$\frac{1}{C_D} = \frac{1}{C_H} + \frac{1}{C_G} \tag{2.32}$$

where $C_D$ is the total charge accumulated on the EDL (in F/m$^2$), and $C_H$ and $C_G$ are defined according to equations (2.28) and (2.31), respectively, to account for the linear potential drop across $C_H$ and with an approximately exponential potential drop beyond the OHP ($C_G$), as illustrated in Figure 2.5 [40,41]. It is interesting to note that the thickness of the EDL reflects on the electric double layer capacitor ($C_D$) since, the deeper the EDL, the higher capacitance behavior is observed. So as the case of the surface electrode area ($A$), which even though equation (2.32) do not provide evidence about the dependence of $A$ because it was assumed that $C_D$ represents the total accumulated charge density.

### 2.3.2.2– The overpotential and charge transfer resistance

The discussion above as shown that the magnitude of the electrode potential is related to the electrode surface charge and the thickness of the EDL. On the other hand, the EDL must account for the DC current path across the electrode-electrolyte interface, which behaves as a nonlinear resistive element in parallel with the interfacial capacitance described above. In this regard, the electrode surface charge reflects on the electric double layer resistor ($R_{DL}$), where the movement of charge into or out of an electrode displaces the electrode potential from its equilibrium ($V_o$) to a new value ($V$). This displacement ($V - V_o$) is referred to as the overpotential ($\eta$), which according to the model suggested by Vetter in 1967 [50], it is given by the sum of four independent overpotentials,

$$\eta = V - V_o = \eta_t + \eta_d + \eta_r + \eta_c \tag{2.33}$$

where $\eta_t$ is due to the charge transfer through the EDL; $\eta_d$ is due to the diffusion of reactants to and from the electrode; $\eta_r$ is due to chemical reactions at the electrode; and $\eta_c$ is due to exchange of metal atoms with the corresponding ions in the electrolyte solution (crystallization). Having in focus the recording of extracellular signals, the overpotential component of upmost importance to the present discussion is $\eta_t$ since it must occur for any steady-state current to flow, as well is considerably larger than the others at conditions "near" equilibrium. Still, in conditions of higher current densities, such as the case of when the applied potential is pushed further from equilibrium, the contribution of $\eta_d$ becomes more significant and a limiting factor due to the limited rates of reactants. It is interesting to note that for biological applications, there is no evidence that the overpotentials due to chemical reactions ($\eta_r$) and crystallization ($\eta_c$) are significant [41].

As mentioned above in section 2.3.2.1, the process by which equilibrium is obtained when an electrode is placed in an electrolyte under zero-bias conditions rapidly engages in chemical reactions. In this state of equilibrium, the equal but opposite oxidation and reduction currents balanced each other, and the resulting net current of the interface is zero. The absolute value of this current for a given surface per area is referred to as the exchange current density ($J_o$) given in units of amperes per square centimeter (A/cm$^2$). $J_o$ is dependent on the material properties of the electrode, the electrolyte composition, and the resulting oxidation-reduction reactions. The latter is what makes determination of $J_o$ difficult; as the electrochemical reaction that dominates this exchange current is not known. For these reasons, $J_o$ is often determined experimentally by measuring the charge transfer resistance ($R_t$) around the equilibrium potential of the electrode in the electrolyte of interest [40].

Given that it is possible to measure the exchange current density for the system of interest when passing additional current (externally applied) through an electrode, the effects on the electrode overpotential (and hence its $I$–$V$ characteristics) provides information that can be used to determine the current that will flow as a result of an applied potential and, in turn, allows to estimate the charge transfer resistance ($R_t$). A detailed discussion to determine $R_t$ to the resulting applied current ($J$) is detailed in the work by Kovacs [40], where it can be found that using small-signal analysis in the linear regime of the resulting $I$–$V$ characteristics for specific conditions ($\beta$ = 0.5, T = 37 °C, $z$ = 1) and overpotentials less than 50 mV peak, it is possible to approximate $R_t$ in ohms per square centimeter ($\Omega$/cm$^2$) as,

$$R_t = \frac{V_t}{J_o z} \tag{2.34}$$

where $\beta$ is the *symmetry factor* that reflects the energy barrier differences for the oxidation and reduction reactions and T is the absolute temperature in kelvin (K). It is interesting to note that here, the resulting current ($J$) can be calculated directly from Ohm's law as,

$$J = \frac{\eta_t}{R_t} = \frac{J_o z \eta_t}{V_t} \tag{2.35}$$

At this point the model of an electrode placed in an electrolyte is a voltage dependent capacitor ($C_I \equiv C_D$) determined from (2.32), in parallel with a charge transfer resistance ($R_t$) determined from (2.34) taking into account the specific conditions mentioned above. The relative impedances of these two elements determines the basic and the essential characteristics of the electrode, neglecting diffusion limits and the "bulk" solution resistance, that are discussed in the section that follows.

### 2.3.2.3– Impedance due to diffusion (Warburg impedance)

As mentioned before, in situations of specific conditions, the charge transfer overpotential ($\eta_t$) dominates the resistive part of the electrode impedance without considering diffusion and the "bulk" solution resistance. However, the situation changes when the current density ($J_S$) (AC or DC) is so large that reactants are not able to diffuse from the bulk to the interface fast enough and, in turn, the current becomes limited by the diffusion overpotential ($\eta_d$). To account for the diffusion current, an additional impedance element ($Z_W$) must be placed in series with the charge transfer resistance ($R_t$), since physical diffusion and charge transfer must occur as a serial process. For electrodes operating near DC potentials at high current densities, Cobbold developed a theoretical model of $Z_W$ that allows estimating the steady-state diffusion resistance for near DC conditions [40]. Nonetheless, more complex effects of diffusion must be considered under AC fields.

In 1899, Warburg [40] proposed a model to describe the impedance ($Z_W$) due to diffusion in response to a sinusoidal forcing function acting on the ions at the metal-electrolyte interface varies with frequency as,

$$|Z_W| = \frac{k}{\sqrt{f}} \tag{2.36}$$

where $k$ is a constant determined by the electrochemistry and mobility of the ions involved in the charge transfer reaction and $f$ is the excitation frequency. However, the Warburg model only accounts to semi-finite linear diffusion, and in turn, it has been reported limitations due to restrictive diffusion of inserted species through the electrode [51]. The derivation of this model, discussed elsewhere [40–42,49] will not be repeated, only that $Z_W$ can be represented by either a series or parallel combination of a resistance ($R_W$) and capacitance ($C_W$) (both non-linear), and if placed in series with the charge

transfer resistance ($R_t$), it effectively models the behavior of a metal electrode in solution under AC conditions [41].

For a parallel combination ($Z_W = R_W \parallel C_W$), provided that the diffusion is dominated by a single ion species S and the electrode is operated near equilibrium, $Z_W$ is determined by the following equations of $R_W$ and $C_W$ [40],

$$Z_W = \left[\frac{1}{R_W} + \frac{1}{j2\pi C_W}\right]^{-1} \tag{2.37}$$

which yields,

$$R_W = \frac{10^3 V_t}{z^2 q n^3 \sqrt{\pi f D}} \tag{2.38}$$

and

$$C_W = \frac{1}{2\pi R_W} \tag{2.39}$$

where $f$ is the frequency in Hertz (Hz), $D$ is the diffusion coefficient in square centimeters per second ($cm^2/s$) of the ion species S in question, $R_w$ is in ohms square centimeters ($\Omega \bullet cm^2$) and $C_w$ is in Coulomb per square centimeter ($C/cm^2$).

One interesting particularity of the Warburg diffusion impedance to note is that through the substitution of (2.39) into (2.37), it can be observed that $Z_w$ has a constant magnitude of,

$$|Z_W| = \sqrt{2} R_W \tag{2.40}$$

with a constant phase of exactly $-45°$ and independent of frequency.

The consideration of the Warburg diffusion element in the circuit analysis is mostly relevant for fitting the measured data with a theoretical model to extract parameters, having in account that when electrochemical reactions proceed at a slow rate (lower frequencies), the resulting $R_t$ will be large and will dominate the resistive part of the measurement and the overall impedance will vary as $1/f$. Oppositely, in instances where the charge transfer reactions proceed rapidly (higher frequencies), the diffusion limiting components (Warburg elements) will dominate the resistive path, resulting in an overall impedance variation of $1/f^2$. However, as pointed out by Bockris, Reddy, and Gamboa-Aldeco [42], in real situations examined in electrochemistry-based interfaces, the Warburg impedance is relatively small, where the resistance is in milliohm per square centimeters ($m\Omega/cm^2$), which is why it is often disregarded from the circuit analysis of an electrode-electrolyte interface.

### 2.3.2.4– Spreading resistance

So far, the whole circuit elements of the electrode-electrolyte interface described above neglected the “bulk” solution resistance, that is, a resistance element encountered by a current spreading out from an electrode into a conductive solution (electrolyte) towards a distant counter electrode. This element is referred to as the spreading resistance ($R_C$) and is determined by the geometric surface area of the electrode. Thus, the equations relating to this parameter are not normalized for surface area as those elements previously presented have been. A model for determining $R_C$ is discussed in detail by Kovacs [40], where it can be found that for general cases, $R_C$ is determined by integrating the series resistance of shells of solution outward from the electrode as,

$$R_C = \frac{\rho L}{A} \tag{2.41}$$

where $\rho$ is the resistivity of the electrolyte solution in Ohm centimeters (Ω.cm), $L$ is the distance between two electrodes in centimeters (cm) and $A$ is the cross-sectional area in square centimeters ($cm^2$) of the solution through which the current flows. As there are numerous electrodes of different shapes and configurations, the estimation of the $R_C$ element must be estimated accordingly to the electrodes morphology. Typically, configurations of two planar electrodes in parallel with only one side exposed to the electrolyte solution are used to record extracellular signals. However, the electrodes shape may vary. For rectangular shaped electrodes, the $R_C$ element is controlled by the electrodes depth ($W$) and width ($D$) as,

$$R_C = \frac{\rho \ln\left(\frac{4L}{W}\right)}{\pi L} \tag{2.42}$$

and, for circular shaped electrodes, the $R_C$ element is controlled by the electrodes radius ($r$) as,

$$R_C = \frac{\rho}{4r} \tag{2.43}$$

From equations (2.41) to (2.43), it can be seen that oppositely to the other circuit elements of the electrode-electrolyte interface discussed above, $R_C$ varies as the square root of the electrodes surface area (for symmetrical shapes). This observation is of paramount importance, as will be discussed later, the electrodes surface area is a determinant factor for the design of electrodes for the detection of ultra-weak extracellular signals to reduce the electrodes noise, even in situations where the electrode geometry is by far larger than the physical size of the biological subject.

### 2.3.2.5 – Summary of electrode-electrolyte interface

The complete circuit model of the electrode-electrolyte interface discussed so far appears as shown in Figure 2.6. This model is known as Randles and Somerton electrode-electrolyte circuit model [51], and as the authors entitled their work, it was developed for the purposes of model the "kinetics of rapid electrode reactions", and it is sufficient to relate the detection of extracellular signals with metal electrodes.

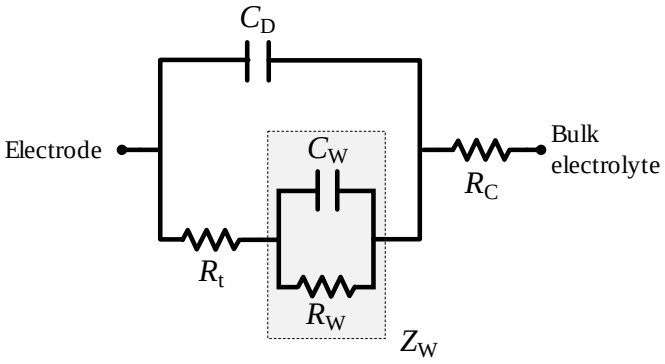


**Figure 2.6** – Equivalent circuit model of the electrode-electrolyte interface.

The Randles and Somerton model accounts for the interfacial capacitance of the EDL ($C_D$) in parallel with the interfacial charge transfer resistance of the EDL ($R_t$) and to the diffusion related Warburg element, here shown as the parallel RC circuit combination between $R_W$ and $C_W$. As mentioned before, the Warburg element is a particular case for which the phase angle is a constant −45° and independent of frequency because it accounts with the simplest diffusion situation that is, it only accounts for the linear distance from the electrode. For these reasons, a constant phase element ($Z_{CPE}$) may be considered instead to account for the frequency dependency of the diffusion. The electrode model also accounts to the spreading resistance ($R_C$) that represents the effect of current spreading from the localized electrode to a distant counter electrode.

Later, it is shown how these circuit elements that constitutes the basis of an electrode-electrolyte interface can be used for the implementation of a cell-electrode interface. Furthermore, it is important to note that in real measurements, there are parasitic elements that results from the implementation of electrodes, and, in turn, theses parasitic elements ease the leakage of currents. A model of the electrode-electrolyte interface to account to these parasitic elements is discussed in detail by Kovacs [40], and later was supplemented by Borkholder [41], and this discussion will not be repeated here, only that there are two main parasitic elements that can be found on most electrode-electrolyte interfaces. One is the parasitic capacitance resulting from the leakage current to the ground, commonly known as the stray capacitance ($C_S$), and the other the parasitic capacitance resulting from adjacent electrodes, commonly known as the fringing capacitance ($C_c$). Typically, $C_s$ appears in the equivalent circuit model of the electrode-electrolyte interface between the electrode's nodes and ground, while $C_c$ appears as a capacitance between two adjacent (parallel) electrodes, that is, a parallel capacitive element to the interfacial capacitance ($C_D$). For most applications, parasitic elements due to fringing

effects can be neglected, as long as the inter-electrodes distance ($L$) is considerably far apart. On the other hand, stray capacitances due to the leakage current to the ground must be considered, specially, in cases where a conductive/semi-conductive substrate and/or a passivation layer are used on the electrode's structure and may be neglected since the thickness of the dielectric layers and/or of passivation is thick enough.

### 2.3.3– Electrode noise and signal conditioning

As with most systems, it is rare for ideal conditions to exist, and as a result, unwanted disturbances can be observed in the output of the system. These disturbances are commonly referred to as *noise* and its effects are obscureness or interference with a desired output [52]. Since the focus of this thesis is on the recording of extracellular signals, the discussion aims to provide the statistical and probability concepts which are fundamental to modelling electronic noise, as well as the basic strategies employed to handle noisy signals, also known as signal conditioning methods.

There is a very broad range of noise sources that can be present in electrical systems, which is why it is convenient to distinguish and aggregating them into two major classes: intrinsic and extrinsic noise sources. The first refers to intrinsic physical effects on the circuit elements that compose the system; here, the electrodes and the recording instrumentation. The second class encompasses all coupled noise sources that arise from interactions between the electronic circuit and the surrounding environment. Examples of extrinsic noise sources are atmospheric-based noise (electrical storms, galactic radiation), glitches induced by fast switching digital circuits, coupling from nearby electrical circuits, etc. In this section, focus only are given to the first class of noise sources [53], as the study of extrinsic noise sources are beyond the scope of this thesis.

#### 2.3.3.1– Electrical Noise

In the previous sections, extracellular signals and the electrode-electrolyte interface were treated as deterministic quantities; that is, they were characterized according to known (precise) average rates with no random deviations. However, noise is a totally random signal. It consists of frequency components that are random in amplitude and phase. On the other hand, the noise randomness behaves as an ergodic random process, that is, the noise properties are the same for different samples and, in turn, it is possible to obtain temporal averages of the sampling functions over time, $v_n(t)$.

For the purposes of analysis electronic noise sources, it is interesting to note that resistors elements suffer from heating effects, that is, the voltage drop across the resistor elements dissipates electrical power, P = I×V, into heat energy, which according to Ohm's law the dissipated power across the

resistor, $P = V^2/R$, follows a quadratic dependence on the voltage drop across the resistor elements. On the other hand, capacitive and inductive elements are considered noiseless elements, since the noise generated by those elements are in most situations neglectable if compared with the noise generated by resistive elements. It is common practice in electrical engineering to measure the root mean square (RMS) values of sampling functions over time, $v_{rms}(t)$, and according to,

$$v_{rms} = \sqrt{\frac{1}{T_p}\int_0^T v_n(t)dt} \tag{2.44}$$

where $T_p$ is the measurement period of $v_n(t)$. Although the long-term $v_{rms}(t)$ values of a signal can be measured, the exact amplitude at any instant of time cannot be predicted. If the instantaneous amplitude of noise could be predicted, noise would not be a problem [52]. Even so, it is possible to predict the randomness of the noise, usually because much of intrinsic noise sources follows a Gaussian and normal distribution of the instantaneous amplitude with time. These aspects have been reviewed in detail in the literature [52–54] and will not be repeated here. For this work, all the electronic noise sources that are discussed below are considered as Gaussian and as ergodic random processes. Moreover, if multiple noise sources are presented in the electrical system, each noise source is considered independent and uncorrelated, meaning that the cumulative noise contribution can be expressed in mean square units as the sum of the individual mean square components of each component. In RMS terms, the total noise ($v_{T,rms}$) is represented by:

$$v_{T,rms} = \sqrt{\sum_{n=1}^{N} {v_{n,rms}}^2} \tag{2.45}$$

### 2.3.3.2 – Thermal noise (Johnson or Nyquist noise)

Johnson noise that is also referred to as thermal noise, consists of thermal induced random fluctuations in the charge carriers of any material with a finite resistivity. Although the average motion of the charge carriers is zero, the instantaneous random motion of such free carriers generates instantaneous charge gradients which, in turn, produce wide-band random voltage fluctuations. These fluctuations are characterized by an ergodic Gaussian random process, that can be modelled either by an equivalent voltage noise source, $v_n$, in series with a noise-free resistor or an equivalent current noise source in parallel with a noise-free resistor as shown in the insets of Figure 2.7 (a) and (b), respectively. For these reasons, the intrinsic noise of any circuit element has been empirically shown to be thermal [55], following the standard Johnson noise equation for the RMS voltage noise of a resistor:

$$v_{\text{rms}} = \sqrt{\int_{f_1}^{f_2} 4kTR(f)\,\mathrm{d}f} = \sqrt{4kTR\Delta f} \quad (2.46)$$

or its equivalent RMS current noise ($i_{\text{rms}}$) as,

$$i_{\text{rms}} = \sqrt{\int_{f_1}^{f_2} \frac{4kT}{R(f)}\,\mathrm{d}f} = \sqrt{\frac{4kT}{R}\Delta f} \quad (2.47)$$

where $k$ is Boltzmann's constant, T is the absolute temperature in Kelvin (K), $\Delta f$ is the bandwidth of interest ($f_2 - f_1$) in Hertz (Hz), and $R$ is the resistance or the real part of the conductor's impedance in Ohms (Ω). The most relevant feature of thermal noise is its independence with frequency, whereby the power spectral density (PSD) of a thermal noise source is constant from DC to near infrared (up to $10^{12}$ Hz), which is why is considered a source of white noise [53]. For the same reason, Figure 2.7 plots RMS noise versus resistance, since the latter depends on spectral bandwidth ($\Delta f$), not the actual frequency, and therefore, the units quoted in Figure 2.7 are obtained as the voltage (V/√Hz) or current (A/√Hz) with respect to the square root of the bandwidth. It is noteworthy that for spectral analysis of the electrode noise, equations (2.46) and (2.47) can conveniently be expressed in their power spectral density functions by:

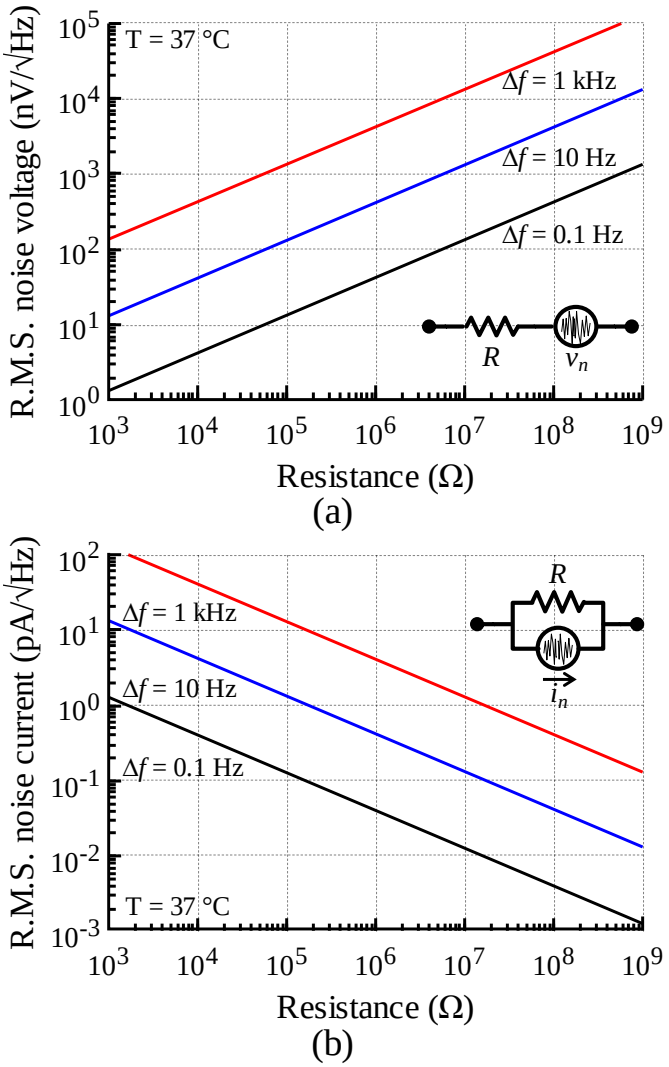


**Figure 2.7** – Theoretical noise plotted versus the real part of the total electrode impedance for $T$ = 37 °C. (**a**) R.M.S. noise voltage ($v_{\text{rms}}$) according to (2.48). (**b**) R.M.S. noise current ($i_{\text{rms}}$) according to(2.49). The plotted $v_{\text{rms}}$ and $i_{\text{rms}}$ on panels (a) and (b) consider three different bandwidths of 0.1, 10, and 1000 Hz.

$$S_{\text{V}} \equiv \frac{\langle v_{\text{n}} \rangle^2}{\Delta f} = 4kTR\,,(\text{V}^2/\text{Hz}) \quad (2.48)$$

and,

$$S_{\text{I}} \equiv \frac{\langle i_{\text{n}} \rangle^2}{\Delta f} = \frac{4kT}{R}\,,(\text{A}^2/\text{Hz}) \quad (2.49)$$

where $S_{\text{V}}$ and $S_{\text{I}}$ represents the voltage and current noise PSD functions, respectively; and the terms $\langle v_{\text{n}} \rangle^2$ and $\langle i_{\text{n}} \rangle^2$ refers to the square average of the voltage and current noise source, respectively.

As the thermodynamics equilibrium of a physical system are inevitable in most scenarios, thermal noise is considered the fundamental noise level of any electrical system, that is, other sources of noise in an electrical system, such as those that will be discussed below, are considered as excess noise, and should be treated as independent according to the equation (2.45).

### 2.3.3.3 – Shot noise

Electrical systems like the electrode-electrolyte interface described before, are composed of several circuit elements of different electrical properties and, in turn, whenever charge carriers (electric current) flow through such electrical system continuously, is common to observe voltage and current random fluctuations in the electrical system terminals. These fluctuations are the sum of pulses of current resulting from discrete events, that is, because in electrical systems, each carrier transport one electric charge ($q$), and some circuit elements behaves as potential barriers to the passage of charges, on the arrival of a charge to the potential barrier led to a "collision" that causes an impulse current. Hence, the name "*shot*" noise arises from the granule effect of the sum of pulse currents, which causes random fluctuations in the electrical system terminals. A detailed discussion of the shot noise has been carried out by Demir and Vincentelli [54] for electrical systems in general, as well as by Hassibi [56], who performed a comprehensive study of noise processes in electrode-electrolyte interfaces, including the analysis of the shot noise. For this reason, the shot noise discussion will not be repeated here, only that it can be found in the analysis of Demir and Vincentelli [54] and Hassibi [56] that shot noise, regardless of the electrical system in focus, is a function of direct (DC) current flow ($I_{DC}$). This is because in electrode-electrolyte interfaces, the charge transfer due to redox processes, occurs almost instantaneously. Under these circumstances, the current spectral density of the shot noise ($S_{I,sh}$) can be expressed as:

$$S_{I,sh} \equiv \frac{\langle i_{sh} \rangle^2}{\Delta f} = 2zqI_{DC}\,, (A^2/Hz) \qquad (2.50)$$

and its RMS value ($i_{sh}$),

$$i_{sh} = \sqrt{2zqI_{DC}\Delta f} \qquad (2.51)$$

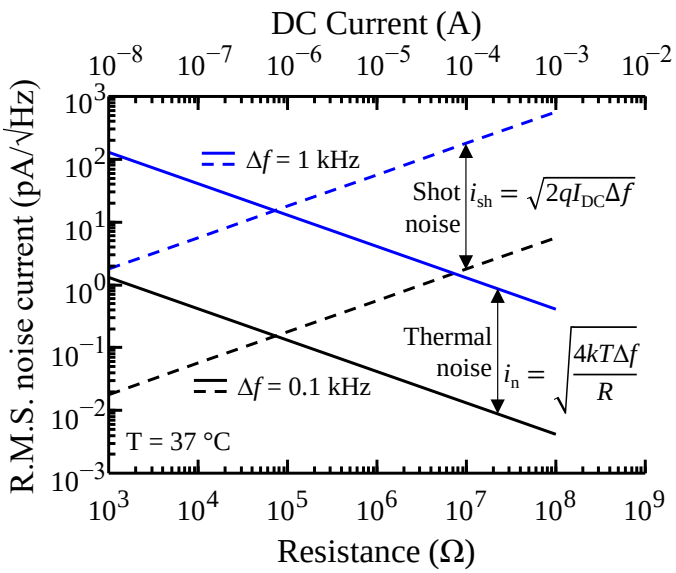


**Figure 2.8** – Plot of the theoretical R.M.S. noise current of thermal noise and shot noise represented by solid and dashed lines, respectively, for T = 37 °C. The thermal noise ($i_n$) and shot noise ($i_{sh}$) are plotted according to equations (2.49) and (2.53) for bandwidths of 0.1 and 1000 Hz, respectively.

where $q$ is the electric charge constant in Coulombs, $I_{DC}$ is the direct current in amperes (A), $\Delta f$ is the bandwidth of interest in Hertz (Hz), and $z$ is the valence number of the ion species. In equation (2.50), the term $\langle i_{sh} \rangle^2$ refers to the mean square of the current noise source, that is, to the average of the sum of all discrete current pulses over time. It is noteworthy that for spectral analysis of the electrode noise, either equation (2.50) or (2.51) are only valid in low frequency regions, and, in turn, as shown in equation (2.50), the shot noise current is proportional to the square root of the noise power per Hertz of bandwidth, meaning that shot noise is frequency independent, and is a white noise containing constant noise power per Hertz of bandwidth. This observation becomes clearer if observed graphically. To this end, a comparison of the theoretical R.M.S. current noise between thermal noise and shot noise is shown in Figure 2.8, the thermal noise current being plotted as a function of the real part of the impedance according to equation (2.49), and the shot noise being plotted as a function of the direct current ($I_{DC}$) flowing through the whole electric system according to equation (2.51).

### 2.3.3.4 – 1/*f* noise (flicker noise)

In many interdisciplinary discussions spanning areas such as acoustics, physics, biology, economics, construction, and probably others, the spectral density of a population of data that has been documented exhibits an unpredictable increase without limits as the frequency decreases [57–62]. The particularity of this well-documented phenomena is that, in datasets from distinct systems or even in datasets collected with equal systems, the rate of increment of the spectral density as the frequency decreases follows a $1/f^{\alpha}$ characteristic with the exponent α to be generally reported unitary ($\alpha = 1$), however it has been also reported to take values from 0.5 to 2 ($0.5 \leq \alpha \leq 2$). For this reason, this phenomenon has been referred to as $1/f$ noise.

Here the discussion will, for obvious reasons, focus on the increase in noise levels commonly seen in electrical systems as the frequency decreases. It is noteworthy that in literature $1/f$ noise is also referred to as "*flicker* effect" (or flicker noise), because it was first observed in vacuum tubes, the term *flicker* effect being probably due to the flickering observed in the plate current. Other terms are also used to refer to $1/f$ noise, such as semiconductor noise, low-frequency noise, pink noise, current noise and contact noise. The reason for finding numerous references in the literature to describe the same phenomenon is mainly due to so far, no unified theoretical explanation for $1/f$ noise has been proposed and its physical origins remains unsolved [52,57].

Still, from the results of experimental work (measurements), some empirical and theoretical models have been proposed in the literature [52,59,63]. Surprisingly, Hooge's empirical model after several revisions and experiments by many, continues to be valid and adapted to describe the

spectral density of 1/*f* noise, but with a caveat, the model accounts for the passage of a direct time-invariant current ($I_{DC}$) through the electrical system, however, the model was not refuted in situations where no current was applied. The result, considering homogeneous samples, proposed by Hooge's to determine the voltage and current spectral density of the 1/*f* noise ($S_{1/f}$) are given by:

$$\frac{S_{1/f}}{\langle v_{n,1/f}\rangle^2} = \frac{S_{1/f}}{\langle i_{n,1/f}\rangle^2} = \frac{K}{f^{\alpha}} \tag{2.52}$$

where $K$ is a constant unique to a particular electrical system proportional to rate between the Hooge's parameter ($a_H$) and the number of charge carriers ($N_C$); $f$ is the frequency; and the exponent $\alpha$ is a constant, typically in the range of 0.5 to 2, depending on the properties of the electrical systems. In equation (2.52), both terms $\langle v_{n,1/f}\rangle^2$ and $\langle i_{n,1/f}\rangle^2$ refers to the mean square of the voltage and current noise sources, respectively. Although the estimation of 1/*f* noise spectral density is based on an empirical model, since 1/*f* noise spectral density is inversely proportional to frequency, it is possible to determine the noise content in a frequency band by integration over the range of frequencies in which our interest lies, regarding that the 1/*f* noise is a stochastic process modelled by a zero mean ergodic Gaussian. The result is the total noise power ($P_n$) considered for a frequency band ($\Delta f$) given by:

$$P_n = \int_{f_L}^{f_U} \frac{K}{f}\,df = K\ln\left(\frac{f_U}{f_L}\right) \tag{2.53}$$

where both $P_n$ and $K$ have units in watts (W), and $f_U$ and $f_L$ are the upper and lower frequency limits of the frequency band ($\Delta f$) being considered. It is interesting to note that the noise power over any decade in frequency, so that, $f_U = 10 f_L$, simplifies equation (2.53) to:

$$P_n = 2.3K \tag{2.54}$$

Equation (2.54) shows that 1/*f* noise results in an equal noise power per decade of frequency and, since the 1/*f* noise is uncorrelated, that means the total noise power increases as the square root of the number of frequency decades. An important fact concerning 1/*f* noise is that measuring accuracy cannot be improved by increasing the length of the measuring time. On contrary, when measuring white noise (e.g. thermal or shot noise), the accuracy increases as the square root of the measuring time.

### 2.3.3.5 – Signal conditioning

In addition to electrical interface noise considerations, recording instrumentation also settles another layer of physical limitations, i.e. it includes more sources of noise, since the recording system is composed of a network of circuit elements, making it difficult to analyze the individual contribution of each component from a noise standpoint. Therefore, for the purposes of recording extracellular

signals, a noise model is helpful to simply noise analysis. Take for example the common recording circuit shown in Figure 2.9 used for the recording of extracellular signals. In this circuit, all electrical system is schematically representing the noisy components, considering a voltage source ($v_S$) to account with time-varying signals generated by living cells transduced by an electrode, here represented by the electrode impedance element ($Z_e$), that is connected to a first stage amplifier circuit. In this example, the amplifier circuit accounts only for an input impedance element ($Z_i$), which establishes a voltage divider circuit between the amplifier input and common ground, causing a signal attenuation given by:

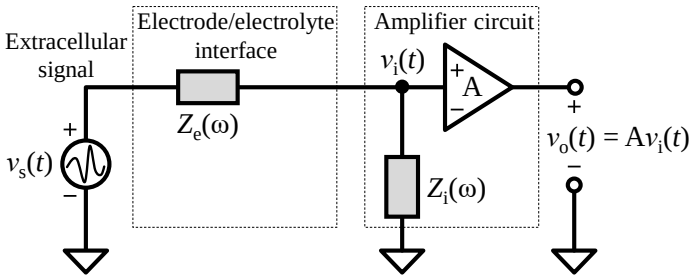


**Figure 2.9** – Common recording circuit used for the recording of extracellular signals. The time-varying extracellular signal ($v_S$) is attenuated by the voltage divider created by the electrode impedance ($Z_e$) and the amplifer circuit input impedance ($Z_i$). Thus, the lower the electrode impedance ($Z_e$), the lower the signal loss.

$$v_i = v_S \frac{Z_i(\omega)}{Z_i(\omega) + Z_e(\omega)} \tag{2.55}$$

However, beyond the noise sources, other circuitry may contribute for signal attenuation, such as the AC coupling, bias resistors to ground and parasitic elements. In general cases, the amplifier circuit is a commercial instrument and, in turn, the unique parameter that can be managed to enhance with the highest impact on the signal conditioning is the electrode impedance element ($Z_e$). Under these circumstances, since most of the voltage will drop across the largest impedance, it is desirable to limit that of the electrode as much as possible. For measurement of ultra-weak extracellular signals, it is desirable for the electrode impedance to be significantly lower than that of the cellular membrane if changes in the membrane impedance are to be observed. In any case, the common strategy is to reduce the electrode impedance, which can be accomplished by either increasing the geometric size of the electrode or by increasing the surface area through control of electrode roughness. This is the focus of the next section 2.3.4. Motchenbacher [52], as well as Moura and Darwazeh [53], carried out a detailed discussion on how to optimize the amplifier circuit input impedance element ($Z_i$), and it should not be repeated here, as it is outside the scope of this thesis. Even so, it is worth mentioning that amplifier circuits have an intrinsic characteristic called gain (A), which, as the name of the circuit implies, the purpose of the amplifier circuit is to increase the amplitude of the input signal ($v_i$) by a factor proportional to its gain, resulting in an output signal ($v_o$) given by:

$$v_o = Av_i \tag{2.56}$$

The most important considerations, with regard to the gain of the amplifier circuit, is that both the signal and the noise amplitudes are amplified (increased) by the same amount. For this reason, the

performance of the amplifier circuit must be analyzed according to the following parameters: noise factor (F), noise figure (NF) and signal-to-noise ratio (SNR). The SNR is a measure of signal attenuation expressed as the ratio between the signal ($v_s$) and noise ($v_n$) amplitudes (i.e. SNR = $v_s$ / $v_n$). The noise factor (F) is a figure-of-merit for a device or a circuitry with respect to noise and is used to measure the degradation of the SNR as the signal passes through device or circuitry. According to IEEE standards [64], "the noise factor of a two-port device is the ratio of the available output noise power per unit bandwidth to the portion of that noise caused by the actual source connected to the input terminals of the device, measured at the standard temperature of 290 K". This definition can be expressed in an equivalent form as:

$$F = \frac{SNR_{in}}{SNR_{out}} \equiv \frac{S_{s,in} \Big/ S_{n,in}}{S_{s,out} \Big/ S_{n,out}} \tag{2.57}$$

where $SNR_{in}$ and $SNR_{out}$ represents the signal-to-noise ratio at the input and output of the device or circuitry, respectively. Equation (2.57) also expresses the noise factor (F) as a ratio between the input and output powers of the signals ($S_{s,in}$ and $S_{s,out}$) and noise ($S_{n,in}$ and $S_{n,out}$) amplitudes, which is a useful representation to express the noise figure (NF) if the power ratios are in decibels (dB) units. The noise figure (NF) is a measure of the signal-to-noise degradation commonly attributed to evaluate the amplifier circuitry given by: NF = 10log(F).

### 2.3.3.6 – Signal detection limit

Having described the sources of intrinsic noise at the electrode-electrolyte interfaces (thermal, shot and 1/*f* noise), as well as the signal conditioning considerations, it is now possible to discuss the impact of electrode noise on the detection limits of ultra-weak extracellular signals. In this regard, it must be first considered the intrinsic noise of a cell membrane. Bier [65] as performed a detailed discussion on noise evaluation in a cell membrane, and therefore, this discussion will not be repeated here, only that, cells generate both equilibrium ($S_{eq}$) and nonequilibrium ($S_{noneq}$) noise, and that, as stated by Bier in his final remarks, "nonequilibrium noise may not just be noise, but actually a signal". For this reason, Bier considers that it would be wrong to take all cell membrane noise ($S_M = S_{eq} + S_{noneq}$) in the dominator of a signal-to-noise ratio. Still, during the following discussion of the limits of detecting extracellular signals with electrodes, for the sake of simplicity, the cell membrane will be assumed to be noiseless; and only the characteristics of the extracellular signals to be measured will be considered. For obvious reasons, it would be difficult and complex to synthetize the characteristics of extracellular signals to the full range of living cells. Therefore, rough estimates for the expected amplitude ($V_S$),

length ($T_S$) and periodicity ($f_S$) of extracellular signals driven by ionic or electrical forces will be considered, these characteristics being sufficient to discuss the electrodes detection limits. Table 2.2 summarizes the typical range of action potentials (APs) generated by neurons and discrete signals generated by astrocyte and glioma cells measured by different authors.

Starting with fast time-varying signals, as is the case with APs, either because the periodicity is very fast or because the signal length is short, according to Nyquist sampling theory, the analog signal needs to be recorded with a resolution sampling rate of at least 2.3-times faster than the normally expected signal frequency, which in turn requires a bandwidth ($\Delta f$) of at least 1 kHz for acquiring APs. Under these circumstances, and considering the circuit model of the electrode-electrolyte interface shown in Figure 2.6, the extracellular signal will flow mostly through the noiseless capacitive path of the high capacitance of the EDL ($C_D$), which is considered short-circuited for high frequencies in most practical situations, and, in turn, the dominant electrode noise is thermal and proportional to the spreading resistance of the electrolyte ($R_C$).

**Table 2.2 – Estimated characteristics of extracellular signals triggered by ionic or electrical forces.**

| | **Extracellular signals driven by electrical forces (e.g. APs)** | ***Ref.*** |
|---|---|---|
| **Amplitude ($V_S$)** | Strong ($V_S$ < 5 mV) | |
| **Length ($T_S$)** | Short ($T_S$ < 300 ms) | [73–80] |
| **Periodicity ($f_S$)** | Fast ($f_S$ < 350 Hz) | |

| | **Extracellular signals driven by ionic forces** | ***Ref.*** |
|---|---|---|
| **Amplitude ($V_S$)** | Weak ($V_S$ < 5 μV) | |
| **Length ($T_S$)** | Long ($T_S$ < 120 s) | [81–87] |
| **Periodicity ($f_S$)** | Slow ($f_S$ < 1 Hz) | |

On the other hand, measurements of slow and weak time-varying signals with periodicity range up to one signal per second ($f_S$ < 1 Hz), require the use of narrow bandwidths ($\Delta f$) that include the DC component of the signal, usually bandwidths up to 25 Hz are used. Under these circumstances, the electrochemical reactions at the electrode-electrolyte interface proceed at slow rate, and, in turn, extracellular signals flow through the EDL resistance ($R$t) and capacitance ($C_D$). As $R_t >> R_C$, $R_t$ dominates the resistive path, and the electrode model becomes a parallel RC, so that, the overall impedance is roughly proportional to $1/f$ (as would be expected for a parallel RC circuit), so is the noise. Note that in situations where the charge transfer reactions are rapid, the diffusion-limiting components, such as the Warburg impedance element ($Z_W$), dominate the resistive pathway, resulting in an overall impedance change of $1/f^2$ [41,66]. However, for the purpose of recording extracellular signals, the influence of the $Z_W$ is small and therefore it is often neglected [67–70].

Although the recording of fast or slow time-varying signals depends on different electrode circuit elements, either $C_D$, $R_t$, or $R_C$ depends on the electrode surface. For this reason, the usual strategy for

reducing electrode impedance is to increase the electrode surface area, and the focus of the discussion in the next section.

### 2.3.4 – Electrode impedance and conductive polymers

As mentioned above, it is often desirable to lower the electrode impedance for signal-to-noise (SNR) considerations, which for the purpose of developing electrodes for live cell measurements, these considerations can be summarized into two general conditions: (i) electrodes designed for measurements of single cell characteristics; and (ii) electrodes designed for measurements of populations of cells characteristics. When single cell characteristics are to be analyzed, increasing the geometric size of the electrode beyond that of the cell is undesirable. On the other hand, when it is intended to analyze the characteristics of the cell population, the case study in this thesis, although the geometric size of the electrode is not such a preponderant limiting factor as in the previous case, the size-dependent electrode impedance is an open issue that limits the detection sensitivity of microelectronic sensors due to the excessive noise [69,74,86], restricting microelectrodes to the detection of extracellular signals with a few microvolts of amplitude, i.e. signals generated by excitable cells. In this regard, it is worth mentioning Neto [74] discussion about if the impedance of the electrodes matters. In the final remarks of Neto work, for the purpose of recording *in vivo* local field potentials (LFPs) on rat brains, she concludes that as long as the electrode impedance magnitude stays well below the input impedance of the amplifier, the electrode impedance isn't an issue, but focus should rather be given to bio-compatible materials. In this thesis, it will be addressed the Neto perspective for the development of new technological advances in the recording of ultra-weak extracellular signals, but with one caveat, simultaneously encompassing the use of bio-compatible materials both for the manufacture of the electrode and the substrate, so that significantly reduction of the electrode impedance is achieved.

Typically, strategies for reducing electrode impedance are accomplished by increasing the electrode surface area or engineering the electrode roughness by "growth" or deposition of particles to form nano/microstructures. But, due to the wide variety of existing strategies to decrease electrode impedance, it would be impossible to provide a complete overview of all electrode's structures, particular properties, and electrode circuit models. For this reason, the discussion that follows will be limited to a proposed extension of the electrode circuit model considering the contribution of electrodes made of organic polymeric materials, specifically made of poly(3,4-ethylenedioxythiophene) polystyrene sulfonate (PEDOT:PSS), which is a known intrinsically conductive polymer (CP) used in the development of transducer devices for biomedical applications,

as well as in several industrial applications (e.g. solar panels and organic light emitting diodes (OLEDs)).

### 2.3.4.1 – Poly(3,4-ethylenedioxythiophene) polystyrene sulfonate (PEDOT:PSS)

The poly(3,4-ethylene dioxythiophene) (PEDOT) is a π – conjugated polymer with high electrical conductivity that was invented at Bayer AG research laboratories by Jonas, Heywang and Werner Schmidtberg, and became public knowledge on April 22, 1988, through the patent application (DE 38 13 589 A) as the Bayer PEDOT invention. Despite the tremendous breakthrough attained with the Bayer PEDOT invention, the Bayer PEDOT was considered an insoluble polymer, which made its processibility difficult. To address this issue, a new soluble complex formulation of PEDOT, the so-called PEDOT:PSS, was developed in the following years in collaboration between Jonas and Werner Krafft at Bayer AG and Agfa-Gevaert research laboratories in Germany, whose collaboration quickly resulted in a clever and innovative combination of the Bayer PEDOT invention with Agfa's well-known film antistatic agent, the poly(styrene sulfonic acid) (PSS). The combination of PEDOT with PSS as a counterion was later recognized as a truly innovative aspect, as the PEDOT:PSS complex was found to be processable from the resulting very stable micro dispersion in water, thus ensuring its processability on an industrial scale to fabricate PEDOT:PSS films using different deposition techniques [87]. Elschner, Kirchmeyer, Lövenick, Merker, and Reuter [87] carried out a detailed discussion on the principles and applications of PEDOT:PSS films, and for this reason only the properties of the PEDOT:PSS films that are sufficient to describe the influence on the robustness and impedance of the electrode will be discussed, these properties being extremely important in the development of electrodes for biomedical applications.

Compared to inorganic materials, such as metal oxide films, which can be deposited on a variety of substrates, flexibility, stiffness, strength, and interfacial shear strength (adhesion) are the mechanical properties that give robustness to PEDOT:PSS-based electrodes, since PEDOT:PSS films do not crack upon bending [88], as well as the Young's modulus of different PEDOT:PSS forms have been reported to be between 0.8 to 2.4 GPa [89]. Although, either the internal cracking or delamination of PEDOT:PSS coatings deposited on metallic electrodes has been observed in neural electrodes [90–93]; delamination due to electrolysis of water and subsequent bubble formation [94], and these are degradation aspects related to the change of molecular configuration of PEDOT chains under various aging conditions [95,96], *in situ* thermal and ultraviolet-visible (UV-vis) exposure [97], and high current densities [94,98]. The immediate consequence of the degradation of the mechanical properties, is the loss of conductivity. For this reason, a common strategy that can be used to both reduce electrode

impedance and simultaneously improve long-term mechanical properties is accomplished by increasing the electrode's thickness, since the structure, and the morphology of the PEDOT:PSS films are influenced by the thickness and this in turn determines many properties connected ultimately with the carrier transport in PEDOT:PSS [99]. However, it is noteworthy that despite the excellent transparency in the visible spectrum of thin PEDOT:PSS films (with nanometric thicknesses) [100–103], the use of thick PEDOT:PSS films degrades their optical properties, which for biomedical applications, in most situations is not critical. On the other hand, from the point of view of industrial scale, thick PEDOT:PSS films are beneficial to reduce production costs, as they allow the use of inkjet or screen-printing deposition techniques [104]; and from an electrical perspective, they allow increase the volumetric capacitance ($C_V$) [105,106]. The consideration of the volumetric capacitance in the electrode impedance model will be discussed later.

Another strategy (which can also be used simultaneously with increasing the thickness of the electrode) is accomplished with the use of either primary or secondary doping agents. Primary doping refers for the addition of small nonstoichiometric quantities of a material to conductive polymers that lead to a strong increase in conductivity of these polymers, while secondary doping refers to an additive that further increases the conductivity of an already doped polymer by up to several orders of magnitude [107]. Many studies have already reported different uses of primary and secondary doping, but such a discussion is beyond the scope of this work. Even so, refer to table 9.3 in the work of Elschner, Kirchmeyer, Lövenick, Merker, and Reuter [87] for an extensive summary on the additives and their effect on the conductivity of PEDOT:PSS films; and that, the highest conductivity ever achieved for PEDOT:PSS films was 6323.9 ± 364.5 S/cm [108].

Finally, a very important aspect to highlight are the low pH values of both the PEDOT:PSS aqueous solutions and the doping agents used for manufacturing and improving the electrical and mechanical properties of the electrodes, since the electrodes must present none or residual cytotoxicity levels for living cell [109–112], and this in turn is related ultimately to the chemical stability of the oxidized PEDOT:PSS films. In this regard, commercially available PEDOT (e.g. Baytron® P or Clevios™), which are aqueous dispersions of PEDOT provided with an excess of the polymeric dopant PSS (typically at a 2.5:1 to 6:1 weight ratio versus PEDOT) [113] exhibit strong acidic property with a pH value of less than 3, this acidity condition being reported beneficial for the aqueous dispersion and conductivity of PEDOT:PSS, since the acid acts as catalyst for the reaction [87]. Nonetheless, the presence of $SO_3H$ groups in PSS and in turn in the electrodes made of PEDOT:PSS can release $H^+$ in the solution [114], this being the aspect of major concern for cytotoxicity of living cells, especially when the electrodes are exposed to post-treatments with secondary doping based on acidic solutions.

### 2.3.4.2 – Volumetric capacitance

When considering the increase in the surface area of the electrode via pores or structures, as is the case with PEDOT:PSS electrodes, the circuit model presented for the electrode-electrolyte interface must consider the larger volumetric geometry. In this regard, Proctor, Rivnay and Malliaras [105] performed a detailed discussion on the volumetric capacitance in conducting polymers, having proposed that the volumetric capacitance ($C_V$) in Farads per cubic centimeters (F/cm$^3$) is inversely proportional to the average distance ($\alpha$) between sites on the porous electrodes. The result is,

$$C_V \equiv \frac{C_D{}'}{\alpha} \equiv \frac{L}{\alpha}\frac{\varepsilon_o\varepsilon_r}{t}A \tag{2.58}$$

where $L$ is the length of the conductive polymer film necessary for modelling the whole film as $N$ number of double layer capacitors ($C_D$) in parallel ($N = L/\alpha$); $C_D{}'$ represents the capacitance per unit area in Farads per square centimeters (F/cm$^2$), expressed as: $C_D{}' = C_D/A = \varepsilon_0\varepsilon_r/t$. Here, $C_D$ represents the classical electrode double layer capacitance for a metal electrode under the influence of an applied potential, where $t$ is the distance between the center of the ions and the metal plate. Later, Sahalianov and Singh [115] introduced the phenomenological parameter corresponding to the intrinsic volumetric capacitance of conductive polymers, having proposed the use of density functional theory (DFT) to calculate the volumetric capacitance of conductive polymer films in nano-scaled and molecular systems. This discussion will not be repeated here, only that the whole capacitance from CP is best described considering a quantum capacitance model rather than a classical capacitance model, having their results shown that “the capacitance of conducting polymers originates from the charges stored in atomistic Stern layers formed by counterions and doped polymeric chains. This classifies the conducting polymers as double-layer supercapacitors rather than pseudo-capacitors relying on charge transfer between polymer and redox-active solutes in electrolyte”. Such perspective on how the CP store or transfer charge is discussed in detail by Berggren and Malliaras [116].

For the purposes of recording extracellular signals, the greatest benefit from the high capacitance and mixed electronic/ionic conductivity obtained with the use of PEDOT:PSS electrodes has been shown to be the low interfacial resistance [117–121], which in turn, settles the detection limits of the thermal noise, and consequently, a high recording quality due to a substantial increase of the signal-to-noise ratio, this aspect being the focus in study of Chapter 7.

## 2.3.5 – Cell-electrode interface

Bioelectrical signals, like those described before in section 2.2, would be signals measured by an electrode inserted directly into the cell membrane (e.g. patch-clamp technique), and these signals are

referred to as intracellular or transmembrane signals. The recording of signals with extracellular electrodes, on the other hand, are called extracellular signals, since there is no invasion (penetration) of the cell body and the signal detection inherently depends both on the geometry and volumetry of the electrode and on the coupling properties of the cell membrane to the electrodes, that is, the contact (adhesion) of the cell membrane to the sensing electrode. In this regard, in practical situations, there are no ideal contact conditions, and in turn, there are small regions of close adhesion where the cell membrane is separated from the electrode by 1 to 15 nm, and other regions where the membrane is more loosely coupled exhibiting a separation of up to 100 nm [41]. As the entire cell body is bath by an electrolyte, these regions between the cell membrane and the electrode are filled with electrolyte, and exhibits a resistance referred to as the seal resistance ($R_{seal}$), which can be approximated using (2.41), that is, by the spreading resistance ($R_C$), as it considers the conduction path through the electrolyte. Furthermore, although an extracellular signal arises from the entire cell body, it can be assumed that all basal membrane currents flowing from the bottom gaps between the cell membrane and the electrode flow through $R_{seal}$, thus establishing a voltage drop between the electrode and the electrolyte that can be measured with an electrode. It is worth mentioning that, the closer the coupling between the cell and the electrode, the greater is $R_{seal}$, this aspect being the reason why $R_{seal}$ is one of the most important physical parameters that define the electrical coupling between cells and electrodes [122].

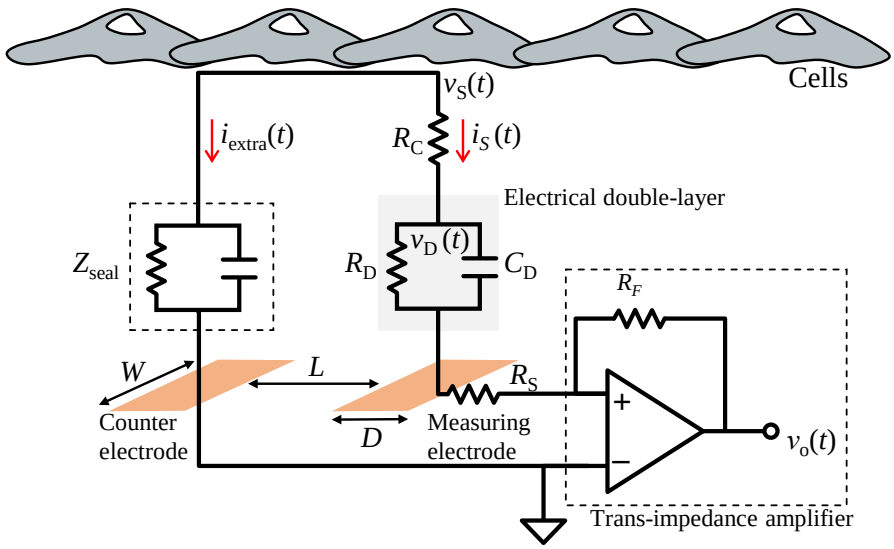


**Figure 2.10** – Illustration of the electrical coupling of extracellular signals detected with microelectrodes. $i_{extra}(t)$ represents the all current generated by the cells that flows through the electrolyte sealing impedance ($Z_{seal}$), while $v_s(t)$ represents the extracellular signal potential created and that can be measured relative to a distant reference electrode (here the counter electrode and ground). Here, the measuring circuit is closed using a trans-impedance amplifier. The dimensions of electrode depth ($D$), width ($W$) and gap ($L$) are merely representative of a rectangular shaped electrode and are conveniently shown to highlight the dependence of the electrode-electrolyte interface according to the area of the electrode, although the electrode volumetry is purposely omitted for the sake of simplicity.

Another important aspect and difficult one is the problem of describing the extracellular current emanating from a randomly oriented sheet of cells covering an electrode ($i_{extra}$). For the sake of simplicity, this aspect can be synthetized assuming $i_{extra}(t)$ is a time varying signal composed by a cooperative action between cells that is given by the sum of all the currents emanating from all the cells that cover the sensing electrode, resulting in a potential drop in the sensor electrode ($v_S(t)$) equivalent to the extracellular signal potential (e.g. the graded or action potentials previously described in sections 2.2.5 and 2.2.6, respectively). In this situation, an equivalent circuit model can be derived for a system comprised by two parallel electrodes, of which one electrode act as measuring (also commonly referred to as the sensing or recording electrode) and the other as a distant counter and ground electrode, to describe the electrode/electrolyte interface considering the presence of living cells covering the device surface as shown in Figure 2.10. In Figure 2.10, $v_S$ is modelled by the spreading resistance ($R_C$) in series with the electrical double-layer (EDL), here represented as the parallel between the capacitance ($C_D$) and the resistance ($R_D$) of the EDL, while the counter electrode considers the flow of $i_{extra}(t)$ generated by the cells through the overall seal impedance ($Z_{seal}$) that is composed by the electrolyte impedance in series with the counter electrode EDL. It is worth mentioning that although the previously described equivalent circuit model of the electrode-electrolyte interface that is shown in Figure 2.6 considers the "Warburg" diffusion element, for the purposes of recording extracellular signals, the contribution of this impedance element is small, as it purposes is useful for simulation of the low-frequency dispersion on the impedance. For this reason, "Warburg" diffusion element is negligible and not included in the equivalent circuit model shown in Figure 2.10.

Other circuit components to consider is the resistive path ($R_S$) due to the use of PEDOT:PSS electrodes and the amplifier input impedance ($Z_i$). Usually, $R_S$ is negligible since $R_S \ll R_C$, but if PEDOT:PSS electrodes are used, is important to ensure that $R_S \ll R_C$, and that $R_C \ll Z_{seal}$, so that the extracellular signal is coupled to the measuring electrodes. As for $Z_i$, it is important to ensure that the whole electrode impedance ($Z_e$) that is composed by the series between the $R_C$ and the EDL (i.e. $C_D \parallel R_D$) is much smaller than $Z_i$, $Z_e \ll Z_i$, so that the signal attenuation is minimum.

Finally, the extracellular signals potential, $v_S(t)$, generated by cells, are amplified by means of a voltage amplifier, yet, a trans-impedance amplifier can be used to amplify the current fluctuations, $i_s(t)$. This current appears as a displacement current across the EDL capacitance ($C_D$). In Figure 2.10, the output voltage, $v_o(t)$, is given by,

$$v_o(t) = -R_F i_S(t) \tag{2.59}$$

where $R_F$ is the feedback resistance and $i_S(t)$ the current flowing through the measuring electrode. Details of the model to detect the displacement current can be found in the study by Medeiros [123]

and for this reason, this discussion it will not be repeated. Later, in chapter 5 the displacement current detection method will be discussed considering the use of PEDOT:PSS electrodes.

Assuming $v_s(t)$, is a rising ramp with a slope ($m$) that is given by $m = dv_S / dt$, the detected current can be approximated as,

$$i_S(t) \cong \frac{mt}{R_D + R_C} + mC_D\left(1 - e^{-t/\tau}\right) \tag{2.60}$$

$i_S(t)$ is the sum of two independent terms, a component proportional to $v_S(t) = mt$, and a transient term with a peak amplitude proportional to the product $mC_D$ that decays with a time constant ($\tau$) that is approximately given by $\tau \cong R_C C_D$. According to (2.60), $C_D$ act as a multiplier factor for the current. Basically, a rapidly varying voltage signal produces a large transient displacement current across the capacitor, and thence, the measured current signal shape is proportional to the derivative of the original signal $v_S(t)$. Furthermore, as the size (amplitude) and shape of extracellular signals are highly variable, even for a single cell type, changes in extracellular signal morphology due to electrode-electrolyte interface parameters must also be considered.

## 2.4 – Conclusions

This chapter provides a comprehensive review of the fundamental theory behind cellular activity and the detection of extracellular signals using electrodes. It begins by discussing the basics of electrode-electrolyte interfaces and provides a model for analysing the effects of various factors, including electrode material, geometry, and frequency bandwidth. Additionally, the chapter explores the different types of electrical noise sources that can affect signal recording and the various signal conditioning methods that can be used to mitigate their effects. Overall, this chapter provides a solid foundation for the subsequent chapters.

# References


1. Fromherz, P. Neuroelectronic Interfacing: Semiconductor Chips with Ion Channels, Nerve Cells, and Brain. *Nanoelectron. Inf. Technol.* **2003**, 781–810.
2. Fang, J.; Huang, S.; Liu, F.; He, G.; Li, X.; Huang, X.; Chen, H.; Xie, X. Semi-Implantable Bioelectronics. *Nano-Micro Lett.* **2022**, *14*, 125, doi:10.1007/s40820-022-00818-4.
3. Pavlov, V.A.; Tracey, K.J. Bioelectronic medicine: updates, challenges and paths forward. *Bioelectron. Med.* **2019**, *5*, 1, doi:10.1186/s42234-019-0018-y.
4. Sadava, D.E.; Hillis, D.M.; Heller, H.C.; Hacker, S.D. *Life: the science of biology*; Funston, J.,

Pritchard-Martinez, C., Eds.; 9th ed.; Sinauer Associates, Inc.: Sunderland, 2009; Vol. 2; ISBN 978-1319010164.

5. Freeman, S.; Quillin, K.; Allison, L.; Black, M.; Podgorski, G.; Taylor, E.; Carmichael, J. *Biological Science*; Wilbur, B., Ed.; 6th ed.; Pearson Education, Inc.: New York, 2007; ISBN 9781292165073.
6. Gleichmann, N. *Technological Networks, Cell Science*. Sudbury, UK July 8, 2021, pp. 1–7.
7. VanPutte, C.L.; Regan, J.L.; Russo, A.F. *Seeley's Essentials of Anatomy & Physiology*; 10th ed.; McGraw-Hill Education: New York, 2019; ISBN 978-1-260-09286-8.
8. Nernst, W. Zur Kinetik der in Lösung befindlichen Körper. *Zeitschrift für Phys. Chemie* **1888**, *2U*, 613–637, doi:10.1515/zpch-1888-0274.
9. Sterratt, D.; Graham, B.; Gillies, A.; Wilshaw, D. The basis of electrical activity in the neuron. In *Principles of Computational Modelling in Neuroscience*; Cambridge University Press, 2011; pp. 13–46.
10. Fröhlich, F. Membrane Voltage. *Netw. Neurosci.* **2016**, 3–17, doi:10.1016/b978-0-12-801560-5.00001-x.
11. Ermentrout, G.B.; Terman, D.H. *Mathematical Foundations of Neuroscience*; Interdisciplinary Applied Mathematics; Springer New York: New York, NY, 2010; Vol. 35; ISBN 978-0-387-87707-5.
12. Hille, B. *Ion Channels of Excitable Membranes, third edition (Sunderland: sinauer associates)*; 3rd ed.; Sinauer Associates, Inc, 2001; ISBN 0878933212.
13. Hammond, C. *CELLULAR AND MOLECULAR NEUROPHYSIOLOGY FOURTH EDITION*; Hammond, C., Ed.; 4th ed.; Academic Press, Elsevier: London, UK, 2014; ISBN 978-0-12-397032-9.
14. Hodgkin, A.L.; Huxley, A.F. A quantitative description of membrane current and its application to conduction and excitation in nerve. *Bull. Math. Biol.* **1990**, *52*, 25–71, doi:10.1007/BF02459568.
15. Black, J.A.; Waxman, S.G. Noncanonical roles of voltage-gated sodium channels. *Neuron* **2013**, *80*, 280–91, doi:10.1016/j.neuron.2013.09.012.
16. Catterall, W.A. Voltage-Gated Calcium Channels. *Cold Spring Harb. Perspect. Biol.* **2011**, *3*, a003947–a003947, doi:10.1101/cshperspect.a003947.
17. Zamponi, G.W.; Striessnig, J.; Koschak, A.; Dolphin, A.C. The Physiology, Pathology, and Pharmacology of Voltage-Gated Calcium Channels and Their Future Therapeutic Potential. *Pharmacol. Rev.* **2015**, *67*, 821–870, doi:10.1124/pr.114.009654.
18. Yu, F.H.; Catterall, W.A. The VGL-Chanome: A Protein Superfamily Specialized for Electrical

Signaling and Ionic Homeostasis. *Sci. STKE* **2004**, *2004*, doi:10.1126/stke.2532004re15.

19. Gonzalez Sabater, V.; Rigby, M.; Burrone, J. Voltage-Gated Potassium Channels Ensure Action Potential Shape Fidelity in Distal Axons. *J. Neurosci.* **2021**, *41*, 5372–5385, doi:10.1523/JNEUROSCI.2765-20.2021.
20. Kim, D.M.; Nimigean, C.M. Voltage-Gated Potassium Channels: A Structural Examination of Selectivity and Gating. *Cold Spring Harb. Perspect. Biol.* **2016**, *8*, a029231, doi:10.1101/cshperspect.a029231.
21. Aria, M.M. Bioelectricity and excitable membranes. In *Electrophysiology Measurements for Studying Neural Interfaces*; Elsevier, 2020; pp. 1–23.
22. Martinez, A.H.; Mohiuddin, S.S. *Biochemistry, Chloride Channels*; StatPearls Publishing, 2022;
23. Sørensen, A.T.; Ledri, M.; Melis, M.; Nikitidou Ledri, L.; Andersson, M.; Kokaia, M. Altered Chloride Homeostasis Decreases the Action Potential Threshold and Increases Hyperexcitability in Hippocampal Neurons. *eneuro* **2017**, *4*, ENEURO.0172-17.2017, doi:10.1523/ENEURO.0172-17.2017.
24. Rahmati, N.; Hoebeek, F.E.; Peter, S.; De Zeeuw, C.I. Chloride Homeostasis in Neurons With Special Emphasis on the Olivocerebellar System: Differential Roles for Transporters and Channels. *Front. Cell. Neurosci.* **2018**, *12*, 101, doi:10.3389/fncel.2018.00101.
25. Barjas Qaswal, A. Magnesium Ions Depolarize the Neuronal Membrane via Quantum Tunneling through the Closed Channels. *Quantum Reports* **2020**, *2*, 57–63, doi:10.3390/quantum2010005.
26. Payandeh, J.; Pfoh, R.; Pai, E.F. The structure and regulation of magnesium selective ion channels. *Biochim. Biophys. Acta - Biomembr.* **2013**, *1828*, 2778–2792, doi:10.1016/J.BBAMEM.2013.08.002.
27. Ross, S. Faraday consults the scholars: the origins of the terms of electrochemistry. *Notes Rec. R. Soc. Lond.* **1961**, *16*, 187–220, doi:10.1098/rsnr.1961.0038.
28. Hernández-Ochoa, E.O.; Schneider, M.F. Voltage clamp methods for the study of membrane currents and SR Ca2+ release in adult skeletal muscle fibres. *Prog. Biophys. Mol. Biol.* **2012**, *108*, 98–118, doi:10.1016/j.pbiomolbio.2012.01.001.
29. Wise, K.D.; Angell, J.B.; Starr, A. An Integrated-Circuit Approach to Extracellular Microelectrodes. *IEEE Trans. Biomed. Eng.* **1970**, *BME-17*, 238–247, doi:10.1109/TBME.1970.4502738.
30. THOMASJR, C.; SPRINGER, P.; LOEB, G.; BERWALDNETTER, Y.; OKUN, L. A miniature microelectrode array to monitor the bioelectric activity of cultured cells. *Exp. Cell Res.* **1972**,

*74*, 61–66, doi:10.1016/0014-4827(72)90481-8.

31. Pine, J. A History of MEA Development. In *Advances in Network Electrophysiology*; Springer US, 2006; pp. 3–23.
32. Wise, K.D.; Angell, J.B. A Low-Capacitance Multielectrode Probe for Use in Extracellular Neurophysiology. *IEEE Trans. Biomed. Eng.* **1975**, *BME-22*, 212–219, doi:10.1109/TBME.1975.324562.
33. Gross, G.W.; Rieske, E.; Kreutzberg, G.W.; Meyer, A. A new fixed-array multi-microelectrode system designed for long-term monitoring of extracellular single unit neuronal activity in vitro. *Neurosci. Lett.* **1977**, *6*, 101–105, doi:10.1016/0304-3940(77)90003-9.
34. Gross, G.W. Simultaneous Single Unit Recording in vitro with a Photoetched Laser Deinsulated Gold Multimicroelectrode Surface. *IEEE Trans. Biomed. Eng.* **1979**, *BME-26*, 273–279, doi:10.1109/TBME.1979.326402.
35. Pine, J. Recording action potentials from cultured neurons with extracellular microcircuit electrodes. *J. Neurosci. Methods* **1980**, *2*, 19–31, doi:10.1016/0165-0270(80)90042-4.
36. Humpston, G. The essential role of gold in the fabrication of microwave electronics systems. *Gold Bull.* **1999**, *32*, 75–79, doi:10.1007/BF03216613.
37. Goodman, P. Current and future uses of gold in electronics. *Gold Bull.* **2002**, *35*, 21–26, doi:10.1007/BF03214833.
38. Shirakawa, H.; Louis, E.J.; MacDiarmid, A.G.; Chiang, C.K.; Heeger, A.J. Synthesis of electrically conducting organic polymers: halogen derivatives of polyacetylene, (CH) x. *J. Chem. Soc. Chem. Commun.* **1977**, 578–580, doi:10.1039/c39770000578.
39. Randles, J.E.B. Kinetics of rapid electrode reactions. *Discuss. Faraday Soc.* **1947**, *1*, 11, doi:10.1039/df9470100011.
40. Kovacs, G.T.. *Enabling technologies for cultured neural networks*; Stenger, D.A., McKenna, T.M., Eds.; Academic Press, 1994; ISBN 0126659702.
41. Borkholder, D.A. Cell Based Biosensors Using Microelectrodes, Stanford University: Palo Alto, 1998.
42. Bockris, J.O.; Reddy, A.K.N.; Gamboa-Aldeco, M. *Modern Electrochemistry 2A*; 2nd ed.; Kluwer Academic Publishers: Boston, 2002; Vol. 2A; ISBN 0-306-46166-8.
43. Wang, J.; Wu, C.; Hu, N.; Zhou, J.; Du, L.; Wang, P. Microfabricated Electrochemical Cell-Based Biosensors for Analysis of Living Cells In Vitro. *Biosensors* **2012**, *2*, 127–170, doi:10.3390/bios2020127.
44. Groß, A.; Sakong, S. Modelling the electric double layer at electrode/electrolyte interfaces. *Curr. Opin. Electrochem.* **2019**, *14*, 1–6, doi:10.1016/j.coelec.2018.09.005.

45. Dourado, A.H.B. Electric Double Layer: The Good, the Bad, and the Beauty. *Electrochem 2022, Vol. 3, Pages 789-808* **2022**, *3*, 789–808, doi:10.3390/ELECTROCHEM3040052.
46. Siu, W.M.; Cobbold, R.S.C. Basic properties of the electrolyte—$SiO_2$—Si system: Physical and theoretical aspects. *IEEE Trans. Electron Devices* **1979**, *26*, 1805–1815, doi:10.1109/T-ED.1979.19690.
47. Ahmed, M.M.M.; Imae, T. Graphene-Based Nanolayers Toward Energy Storage Device. In *Nanolayer Research*; Elsevier, 2017; pp. 353–389.
48. Bard, A.J.; Faulkner, L.R. *Electrochemical Methods: Fundamentals and Applications*; Wiley, 2001; ISBN 978-0-471-04372-0.
49. Vetter, K.J. *Electrochemical Kinetics:Theoretical Aspects*; Academic Press: New York, 1967; ISBN 9780127202518.
50. Bisquert, J.; Garcia-Belmonte, G.; Bueno, P.; Longo, E.; Bulhões, L.O.. Impedance of constant phase element (CPE)-blocked diffusion in film electrodes. *J. Electroanal. Chem.* **1998**, *452*, 229–234, doi:10.1016/S0022-0728(98)00115-6.
51. Randles, J.E.B. Kinetics of rapid electrode reactions. *Discuss. Faraday Soc.* **1952**, *1*, 11, doi:10.1039/df9470100011.
52. Motchenbacher, C.D.; Connelly, J.A. (Joseph A. *Low-noise electronic system design*; Wiley: New York, 1993; ISBN 978-0-471-57742-3.
53. Moura, L.; Darwazeh, I. Introduction to Linear Circuit Analysis and Modelling: From DC to RF. *Igarss 2014* **2005**, 1–5, doi:10.1007/s13398-014-0173-7.2.
54. Demir, A.; Sangiovanni-Vincentelli, A. *Analysis and Simulation of Noise in Nonlinear Electronic Circuits and Systems*; 1st ed.; Springer US: Boston, MA, 1998; Vol. 425; ISBN 978-1-4613-7777-1.
55. Gesteland, R.; Howland, B.; Lettvin, J.; Pitts, W. Comments on Microelectrodes. *Proc. IRE* **1959**, *47*, 1856–1862, doi:10.1109/JRPROC.1959.287156.
56. Hassibi, A.; Navid, R.; Dutton, R.W.; Lee, T.H. Comprehensive study of noise processes in electrode electrolyte interfaces. *J. Appl. Phys.* **2004**, *96*, 1074–1082, doi:10.1063/1.1755429.
57. Keshner, M.S. 1/f noise. *Proc. IEEE* **1982**, *70*, 212–218, doi:10.1109/PROC.1982.12282.
58. Lindner, B. Effects of noise in excitable systems. *Phys. Rep.* **2004**, *392*, 321–424, doi:10.1016/j.physrep.2003.10.015.
59. Milotti, E. 1/f noise: a pedagogical review. **2002**.
60. Gilden, D.L.; Thornton, T.; Mallon, M.W. 1/*f* Noise in Human Cognition. *Science (80-. ).* **1995**, *267*, 1837–1839, doi:10.1126/science.7892611.
61. Verveen, A.A.; Derksen, H.E. Fluctuation Phenomena in Nerve Membrane. *Proc. IEEE* **1968**,

*56*, 906–916, doi:10.1109/PROC.1968.6443.

62. Carpinteri, A.; Lacidogna, G.; Accornero, F. Fluctuations of 1/f Noise in Damaging Structures Analyzed by Acoustic Emission. *Appl. Sci.* **2018**, *8*, 1685, doi:10.3390/app8091685.
63. Stephany, J.F. Origin of 1/ *f* noise. *J. Appl. Phys.* **1975**, *46*, 665–667, doi:10.1063/1.321682.
64. Kreer, J.G. IRE Standards on Methods of Measuring Noise in Linear Twoports, 1959. *Proc. IRE* **1960**, *48*, 60–68, doi:10.1109/JRPROC.1960.287380.
65. Bier, M. How to evaluate the electric noise in a cell membrane? *Acta Phys. Pol. B* **2006**, *37*, 1409–1424.
66. Rocha, P.R.F.; Schlett, P.; Kintzel, U.; Mailänder, V.; Vandamme, L.K.J.; Zeck, G.; Gomes, H.L.; Biscarini, F.; de Leeuw, D.M. Electrochemical noise and impedance of Au electrode/electrolyte interfaces enabling extracellular detection of glioma cell populations. *Sci. Rep.* **2016**, *6*, 34843, doi:10.1038/srep34843.
67. Rotenberg, Z.A.; Dribinskii, A. V.; Lukovtsev, V.P.; Khozyainova, N.S. Electrochemical impedance of microelectrodes. *Russ. J. Electrochem.* **2000**, *36*, 879–882, doi:10.1007/BF02757062.
68. Neto, J.P.; Baião, P.; Lopes, G.; Frazão, J.; Nogueira, J.; Fortunato, E.; Barquinha, P.; Kampff, A.R. Does impedance matter when recording spikes with polytrodes? *Front. Neurosci.* **2018**, *12*, 1–9, doi:10.3389/fnins.2018.00715.
69. Elschner, A.; Kirchmeyer, S.; Lovenich, W.; Merker, U.; Reuter, K. *PEDOT*; 1st ed.; CRC Press: Boca Raton, 2010; ISBN 9780429137389.
70. Paetzold, R.; Heuser, K.; Henseler, D.; Roeger, S.; Wittmann, G.; Winnacker, A. Performance of flexible polymeric light-emitting diodes under bending conditions. *Appl. Phys. Lett.* **2003**, *82*, 3342–3344, doi:10.1063/1.1574400.
71. Qu, J.; Ouyang, L.; Kuo, C.; Martin, D.C. Stiffness, strength and adhesion characterization of electrochemically deposited conjugated polymer films. *Acta Biomater.* **2016**, *31*, 114–121, doi:10.1016/j.actbio.2015.11.018.
72. Cui, X.T.; Zhou, D.D. Poly (3,4-Ethylenedioxythiophene) for Chronic Neural Stimulation. *IEEE Trans. Neural Syst. Rehabil. Eng.* **2007**, *15*, 502–508, doi:10.1109/TNSRE.2007.909811.
73. Green, R.A.; Matteucci, P.B.; Hassarati, R.T.; Giraud, B.; Dodds, C.W.D.; Chen, S.; Byrnes-Preston, P.J.; Suaning, G.J.; Poole-Warren, L.A.; Lovell, N.H. Performance of conducting polymer electrodes for stimulating neuroprosthetics. *J. Neural Eng.* **2013**, *10*, 016009, doi:10.1088/1741-2560/10/1/016009.
74. Zhou, D.; Greenbaum, E. *Implantable Neural Prostheses 2*; Zhou, D., Greenbaum, E., Eds.; Biological and Medical Physics, Biomedical Engineering; 1st ed.; Springer New York: New

York, NY, 2009; Vol. 2; ISBN 978-0-387-98119-2.

75. Kung, T.A.; Langhals, N.B.; Martin, D.C.; Johnson, P.J.; Cederna, P.S.; Urbanchek, M.G. Regenerative Peripheral Nerve Interface Viability and Signal Transduction with an Implanted Electrode. *Plast. Reconstr. Surg.* **2014**, *133*, 1380–1394, doi:10.1097/PRS.0000000000000168.
76. de Brito, B.C.; Smits, E.C.P.; van Hal, P.A.; Geuns, T.C.T.; de Boer, B.; Lasance, C.J.M.; Gomes, H.L.; de Leeuw, D.M. Ultralow Power Microfuses for Write-Once Read-Many Organic Memory Elements. *Adv. Mater.* **2008**, *20*, 3750–3753, doi:10.1002/adma.200800960.
77. Shi, Y.; Zhou, Y.; Che, Z.; Shang, J.; Wang, Q.; Liu, F.; Zhou, Y. Degradation phenomena and degradation mechanisms for highly conductive PEDOT:PSS films. *Mater. Lett.* **2022**, *308*, 131106, doi:10.1016/j.matlet.2021.131106.
78. Schultheiss, A.; Gueye, M.; Carella, A.; Benayad, A.; Pouget, S.; Faure-Vincent, J.; Demadrille, R.; Revaux, A.; Simonato, J.-P. Insight into the Degradation Mechanisms of Highly Conductive Poly(3,4-ethylenedioxythiophene) Thin Films. *ACS Appl. Polym. Mater.* **2020**, *2*, 2686–2695, doi:10.1021/acsapm.0c00301.
79. Oechsle, A.L.; Heger, J.E.; Li, N.; Yin, S.; Bernstorff, S.; Müller-Buschbaum, P. *In Situ* Observation of Morphological and Oxidation Level Degradation Processes within Ionic Liquid Post-treated PEDOT:PSS Thin Films upon Operation at High Temperatures. *ACS Appl. Mater. Interfaces* **2022**, *14*, 30802–30811, doi:10.1021/acsami.2c05745.
80. Crispin, X.; Marciniak, S.; Osikowicz, W.; Zotti, G.; van der Gon, A.W.D.; Louwet, F.; Fahlman, M.; Groenendaal, L.; De Schryver, F.; Salaneck, W.R. Conductivity, morphology, interfacial chemistry, and stability of poly(3,4-ethylene dioxythiophene)-poly(styrene sulfonate): A photoelectron spectroscopy study. *J. Polym. Sci. Part B Polym. Phys.* **2003**, *41*, 2561–2583, doi:10.1002/polb.10659.
81. Sakkopoulos, V.S.; Dalas, E.; Paliatsas, N.; Emmanouil, K.; Malkaj, P.; Choulis, S.A.; Angelopoulos, A.; Fildisis, T. Correlation between Thickness, Conductivity and Thermal Degradation Mechanisms of PEDOT:PSS Films.; 2010; pp. 178–181.
82. Song, J.; Ma, G.; Qin, F.; Hu, L.; Luo, B.; Liu, T.; Yin, X.; Su, Z.; Zeng, Z.; Jiang, Y.; et al. High-Conductivity, Flexible and Transparent PEDOT:PSS Electrodes for High Performance Semi-Transparent Supercapacitors. *Polymers (Basel).* **2020**, *12*, 450, doi:10.3390/polym12020450.
83. Vosgueritchian, M.; Lipomi, D.J.; Bao, Z. Highly Conductive and Transparent PEDOT:PSS Films with a Fluorosurfactant for Stretchable and Flexible Transparent Electrodes. *Adv. Funct. Mater.* **2012**, *22*, 421–428, doi:10.1002/adfm.201101775.
84. Friedel, B.; Keivanidis, P.E.; Brenner, T.J.K.; Abrusci, A.; McNeill, C.R.; Friend, R.H.;

Greenham, N.C. Effects of Layer Thickness and Annealing of PEDOT:PSS Layers in Organic Photodetectors. *Macromolecules* **2009**, *42*, 6741–6747, doi:10.1021/ma901182u.

85. Gunaydin, O.; Demir, A.; Demir, G.E.; Yücedağ, İ.; Çoşut, B. The Preparation of Transparent Organic Field Effect Transistor Using a Novel EDOT Functional Styrene Copolymer Insulator With a PEDOT:PSS Gate Electrode. *Macromol. Res.* **2018**, *26*, 164–172, doi:10.1007/s13233-018-6023-2.
86. Elschner, A.; Lövenich, W. Solution-deposited PEDOT for transparent conductive applications. *MRS Bull. 2011 3610* **2011**, *36*, 794–798, doi:10.1557/MRS.2011.232.
87. Proctor, C.M.; Rivnay, J.; Malliaras, G.G. Understanding volumetric capacitance in conducting polymers. *J. Polym. Sci. Part B Polym. Phys.* **2016**, *54*, 1433–1436, doi:10.1002/polb.24038.
88. Volkov, A. V.; Wijeratne, K.; Mitraka, E.; Ail, U.; Zhao, D.; Tybrandt, K.; Andreasen, J.W.; Berggren, M.; Crispin, X.; Zozoulenko, I. V. Understanding the Capacitance of PEDOT:PSS. *Adv. Funct. Mater.* **2017**, *27*, 1700329, doi:10.1002/adfm.201700329.
89. MacDiarmid, A.G.; Epstein, A.J. The concept of secondary doping as applied to polyaniline. *Synth. Met.* **1994**, *65*, 103–116, doi:10.1016/0379-6779(94)90171-6.
90. Shi, Y.; Zhou, Y.; Shen, R.; Liu, F.; Zhou, Y. Solution-based synthesis of PEDOT:PSS films with electrical conductivity over 6300 S/cm. *J. Ind. Eng. Chem.* **2021**, *101*, 414–422, doi:10.1016/j.jiec.2021.05.036.
91. Sultana, N.; Chang, H.C.; Jefferson, S.; Daniels, D.E. Application of conductive poly(3,4-ethylenedioxythiophene):poly(styrenesulfonate) (PEDOT:PSS) polymers in potential biomedical engineering. *J. Pharm. Investig.* **2020**, *50*, 437–444, doi:10.1007/s40005-020-00485-w.
92. Cameron, J.; Skabara, P.J. The damaging effects of the acidity in PEDOT:PSS on semiconductor device performance and solutions based on non-acidic alternatives. *Mater. Horizons* **2020**, *7*, 1759–1772, doi:10.1039/C9MH01978B.
93. Rahimzadeh, Z.; Naghib, S.M.; Zare, Y.; Rhee, K.Y. An overview on the synthesis and recent applications of conducting poly(3,4-ethylenedioxythiophene) (PEDOT) in industry and biomedicine. *J. Mater. Sci.* **2020**, *55*, 7575–7611, doi:10.1007/s10853-020-04561-2.
94. Ahmad Ruzaidi, D.A.; Mahat, M.M.; Shafiee, S.A.; Mohamed Sofian, Z.; Mohmad Sabere, A.S.; Ramli, R.; Osman, H.; Hamzah, H.H.; Zainal Ariffin, Z.; Sadasivuni, K.K. Advocating Electrically Conductive Scaffolds with Low Immunogenicity for Biomedical Applications: A Review. *Polymers (Basel).* **2021**, *13*, 3395, doi:10.3390/polym13193395.
95. Baek, S.; Green, R.A.; Poole-Warren, L.A. Effects of dopants on the biomechanical properties of conducting polymer films on platinum electrodes. *J. Biomed. Mater. Res. A* **2014**, *102*, 2743–

54, doi:10.1002/jbm.a.34945.

96. Chen, S.; Song, L.; Tao, Z.; Shao, X.; Huang, Y.; Cui, Q.; Guo, X. Neutral-pH PEDOT:PSS as over-coating layer for stable silver nanowire flexible transparent conductive films. *Org. Electron.* **2014**, *15*, 3654–3659, doi:10.1016/j.orgel.2014.09.047.
97. Sahalianov, I.; Singh, S.K.; Tybrandt, K.; Berggren, M.; Zozoulenko, I. The intrinsic volumetric capacitance of conducting polymers: pseudo-capacitors or double-layer supercapacitors? *RSC Adv.* **2019**, *9*, 42498–42508, doi:10.1039/C9RA10250G.
98. Berggren, M.; Malliaras, G.G. How conducting polymer electrodes operate. *Science (80-. ).* **2019**, *364*, 233–234, doi:10.1126/science.aaw9295.
99. Koutsouras, D.A.; Lingstedt, L. V.; Lieberth, K.; Reinholz, J.; Mailänder, V.; Blom, P.W.M.; Gkoupidenis, P. Probing the Impedance of a Biological Tissue with PEDOT:PSS-Coated Metal Electrodes: Effect of Electrode Size on Sensing Efficiency. *Adv. Healthc. Mater.* **2019**, *8*, doi:10.1002/adhm.201901215.
100. Ganji, M.; Elthakeb, A.T.; Tanaka, A.; Gilja, V.; Halgren, E.; Dayeh, S.A. Scaling Effects on the Electrochemical Performance of poly(3,4-ethylenedioxythiophene (PEDOT), Au, and Pt for Electrocorticography Recording. *Adv. Funct. Mater.* **2017**, *1703018*, 1–12, doi:10.1002/adfm.201703018.
101. Dijk, G.; Rutz, A.L.; Malliaras, G.G. Stability of PEDOT:PSS-Coated Gold Electrodes in Cell Culture Conditions. *Adv. Mater. Technol.* **2020**, *5*, 1900662, doi:10.1002/admt.201900662.
102. Pranti, A.S.; Schander, A.; Bödecker, A.; Lang, W. PEDOT: PSS coating on gold microelectrodes with excellent stability and high charge injection capacity for chronic neural interfaces. *Sensors Actuators, B Chem.* **2018**, *275*, 382–393, doi:10.1016/j.snb.2018.08.007.
103. Wang, A.; Jung, D.; Lee, D.; Wang, H. Impedance Characterization and Modeling of Subcellular to Micro-sized Electrodes with Varying Materials and PEDOT:PSS Coating for Bioelectrical Interfaces. *ACS Appl. Electron. Mater.* **2021**, doi:10.1021/acsaelm.1c00687.
104. Fendyur, A.; Mazurski, N.; Shappir, J.; Spira, M.E. Formation of Essential Ultrastructural Interface between Cultured Hippocampal Cells and Gold Mushroom-Shaped MEA-Toward ?IN-CELL? Recordings from Vertebrate Neurons. *Front. Neuroeng.* **2011**, *4*, 1–14, doi:10.3389/fneng.2011.00014.
105. Medeiros, M.C.R.; Mestre, A.; Inácio, P.; Asgarif, S.; Araújo, I.M.; Hubbard, P.C.; Velez, Z.; Cancela, M.L.; Rocha, P.R.F.; de Leeuw, D.M.; et al. An electrical method to measure low-frequency collective and synchronized cell activity using extracellular electrodes. *Sens. Bio-Sensing Res.* **2016**, *10*, 1–8, doi:10.1016/j.sbsr.2016.06.002.
106. Komendantov, A.O.; Venkadesh, S.; Rees, C.L.; Wheeler, D.W.; Hamilton, D.J.; Ascoli, G.A.

Quantitative firing pattern phenotyping of hippocampal neuron types. *Sci. Rep.* **2019**, *9*, 17915, doi:10.1038/s41598-019-52611-w.

107. Dipalo, M.; Amin, H.; Lovato, L.; Moia, F.; Caprettini, V.; Messina, G.C.; Tantussi, F.; Berdondini, L.; De Angelis, F. Intracellular and Extracellular Recording of Spontaneous Action Potentials in Mammalian Neurons and Cardiac Cells with 3D Plasmonic Nanoelectrodes. *Nano Lett.* **2017**, *17*, 3932–3939, doi:10.1021/acs.nanolett.7b01523.
108. Xu, D.; Fang, J.; Zhang, M.; Wang, H.; Zhang, T.; Hang, T.; Xie, X.; Hu, N. Synchronized intracellular and extracellular recording of action potentials by three-dimensional nanoroded electroporation. *Biosens. Bioelectron.* **2021**, *192*, 113501, doi:10.1016/j.bios.2021.113501.
109. Klauke, N.; Smith, G.L.; Cooper, J. Extracellular recordings of field potentials from single cardiomyocytes. *Biophys. J.* **2006**, *91*, 2543–2551, doi:10.1529/biophysj.106.085183.
110. Hai, A.; Shappir, J.; Spira, M.E. Long-Term, Multisite, Parallel, In-Cell Recording and Stimulation by an Array of Extracellular Microelectrodes. *J. Neurophysiol.* **2010**, *104*, 559–568, doi:10.1152/jn.00265.2010.
111. Fendyur, A.; Spira, M.E. Toward on-chip, in-cell recordings from cultured cardiomyocytes by arrays of gold mushroom-shaped microelectrodes. *Front. Neuroeng.* **2012**, *5*, 1–10, doi:10.3389/fneng.2012.00021.
112. Racz, R.R.; Kollo, M.; Racz, G.; Bulz, C.; Ackels, T.; Warner, T.; Wray, W.; Kiskin, N.; Chen, C.; Ye, Z.; et al. jULIEs: nanostructured polytrodes for low traumatic extracellular recordings and stimulation in the mammalian brain. *J. Neural Eng.* **2022**, *19*, 016041, doi:10.1088/1741-2552/ac514f.
113. Mestre, A.L.G.; Cerquido, M.; Inácio, P.M.C.; Asgarifar, S.; Lourenço, A.S.; Cristiano, M.L.S.; Aguiar, P.; Medeiros, M.C.R.; Araújo, I.M.; Ventura, J.; et al. Ultrasensitive gold micro-structured electrodes enabling the detection of extra-cellular long-lasting potentials in astrocytes populations. *Sci. Rep.* **2017**, *7*, 1–11, doi:10.1038/s41598-017-14697-y.
114. Inácio, P.M.C.; Mestre, A.L.G.; Medeiros, M.C.R.; Asgarifar, S. Electrophysiological signals detection using ink-jet printed polymer and the displacement current method. 5.
115. Rocha, P.R.F.; Schlett, P.; Schneider, L.; Drö, M.; Mailä, V.; Gomes, H.L.; Blom, P.W.M.; De Leeuw, D.M. Low frequency electric current noise in glioma cell populations. *J. Mater. Chem. B* **2015**, *3*, 5035–5039, doi:10.1039/c5tb00144g.
116. Cabello, M.; Ge, H.; Aracil, C.; Moschou, D.; Estrela, P.; Quero, J.M.; Pascu, S.I.; Rocha, P.R.F. Extracellular electrophysiology in the prostate cancer cell model PC-3. *Sensors (Switzerland)* **2019**, *19*, 1–11, doi:10.3390/s19010139.
117. Rocha, P.R.F.; Medeiros, M.C.R.; Kintzel, U.; Vogt, J.; Araújo, I.M.; Mestre, A.L.G.;

Mailänder, V.; Schlett, P.; Dröge, M.; Schneider, L.; et al. Extracellular electrical recording of pH-triggered bursts in C6 glioma cell populations. *Sci. Adv.* **2016**, *2*, e1600516, doi:10.1126/sciadv.1600516.

118. Kuga, N.; Sasaki, T.; Takahara, Y.; Matsuki, N.; Ikegaya, Y. Large-Scale Calcium Waves Traveling through Astrocytic Networks In Vivo. *J. Neurosci.* **2011**, *31*, 2607–2614, doi:10.1523/JNEUROSCI.5319-10.2011.
119. Asgarifar, S.; Mestre, A.L.G.; Félix, R.C.; Inácio, P.M.C.; Cristiano, M.L.S.; Medeiros, M.C.R.; Araújo, I.M.; Power, D.M.; Gomes, H.L. Extracellular electrophysiological based sensor to monitor cancer cells cooperative migration and cell-cell connections. *Biosens. Bioelectron.* **2019**, *145*, 111708, doi:10.1016/j.bios.2019.111708.

# Chapter 3

# Instruments and methods for recording extracellular signals

This chapter discusses the recording of cellular signals using electrophysiological sensing electrodes, including metal and conducting polymer electrodes. The first part of the chapter covers the design and fabrication process of the electrodes used in this work, including the prototyping and assembly protocols for the sample holders. In the second part, we explore the process of extracting insights from recorded extracellular bioelectrical activity using computer-based processing techniques. To facilitate data acquisition, collection, and processing, we developed a custom software called *rcSoftware*. While this chapter provides a brief introduction and overview of the software, a detailed description is provided in Appendix A to avoid making this chapter too lengthy and complex to follow.

## 3.1 – Sensing electrode

The designing and fabrication of sensing device for monitoring the *in-vitro* extracellular bioelectrical activity of living cells requires meeting specific criteria, such a low-impedance electrodes and a layer that facilitates the adherence of cells to the electrodes. To achieve these objectives, researchers optimize the shape and dimensions of the electrodes. This optimization is achieved by combining the morphology of the substrate l with the fabrication techniques that allow the deposition of metallic materials or conductive polymers, either on plain or three-dimensional surfaces. For transducer devices based on plain substrates, polymers and glass are are common materials. Three-dimensional surfaces, however, offer greater opportunities for integrating synthesized or natural surfaces built in nano and microstructures. Typically, the growth of nanopillars [1–3] and mushroom-like [4–7] structures on top of plain substrates or the use of nanofibrils networks of poly(lactic-co-glycolic acid) (PLGA) [8–11] and of bacterial cellulose (BC) membranes [12–14] are examples of the synthetized surfaces engineered to augment the surface roughness, as discussed earlier in Chapter 2. This study explores a novel method to enhance the surface roughness by using dry bacterial cellulose (BC) membranes as substrate. The BC was developed at Aveiro University, Aveiro, Portugal, by Dr.

Carmen Freire and fabricated at the Centre for Research in Ceramics and Composite Materials (CICECO), Aveiro, Portugal, by Dr. Tiago Carvalho.

Throughout the research period of this thesis, four types of electrodes were used. The first and second type of electrodes, hereafter referred to as IT devices, were developed in Instituto Superior Técnico (IST), Lisboa, Portugal, by Prof. Jorge Morgado and fabricated in the Instituto de Telecomunicações (IT) research facilities in collaboration with Prof. Luis Alcácer. The IT devices played a crucial role to achieve the objectives of this thesis, as they were specifically designed to incorporate electrodes of different materials either deposited on glass and BC membranes. The first type of electrode utilized gold, while the second type utilized conductive polymer.

The third and fourth types of electrodes were based on standard technology, were employed to facilitate comparisons between the results obtained with IT devices. The third type is the commercial 8 Well PET Arrays purchased to Applied Biophysics, New York, USA, consisting of patterned gold electrodes on a polyethylene terephthalate (PET) substrate. The fourth type of electrodes are the PHILIPS devices that were developed in the Philips Research Laboratories in Eindhoven, Netherlands, in collaboration with Dr. Dago de Leeuw, consisting of patterned gold electrodes on thermal oxidized silicon wafers.

## 3.2 – Bacterial cellulose (BC)

In this thesis, transducer devices were developed using BC membranes synthetized by the *Gluconacetobacter sacchari* bacteria. The basic steps for the fabrication of BC membranes require isolate the *G. sacchari* bacteria from Kombucha tea and perform their incubation in Petri dishes filled with Hestrin and Schramm (HS) based media containing glucose, sucrose, fructose, mannitol, or glycerol as carbon sources, for a 5-day period and at 30 °C. Then, a 2-day pre-inoculum period was needed to growth enough bacteria colonies at 30 °C, in static conditions and in HS media. After this period, a 250 mL Erlenmeyer flask was used to growth the BC by withdraw 5 mL of the *G. Sacchari* suspended in the culture media and mix with 45 mL of production medium. The flask was kept at 30 °C, in a static incubator, for 96 hours. After the incubation period, wet BC membrane was withdrawn from the flask to be first wash, submitted to a whitening procedure, and then dried at 105 °C. Figure 3.1 (a,b) shows photographs of the wet and dry BC membrane immediately after completing the washing and drying protocol steps. A detailed discussion of the fabrication and characterization of the BC membranes properties used in this thesis may be found in the work by Trovatti [15]. Scanning electron microscope (SEM) images of a BC membrane morphological structure and cross-section view are shown in Figure 3.1 (c,d), respectively. The SEM images were taken using an Analytical Ultra-

High-Resolution (UHR) Schottky Emission Scanning Electron Microscope SU-70 instrument operating at 4 kV. Figure 3.1 (c) provide detail view of the randomly entangled nanofibrous networks, as well as some trapped bacteria.

Sections 3.3 and 3.4 are described how the dry BC membranes were used to combine its native properties of smoothness, roughness, and water containment with the deposition of conductive conjugated polymers (CP) dissolved in aqueous solutions, as well as bare gold. This approach enabled the engineering of nanostructured electrodes that promote cell adhesion, reduce electrode impedance, and serve as the foundational material for the entire device structure.

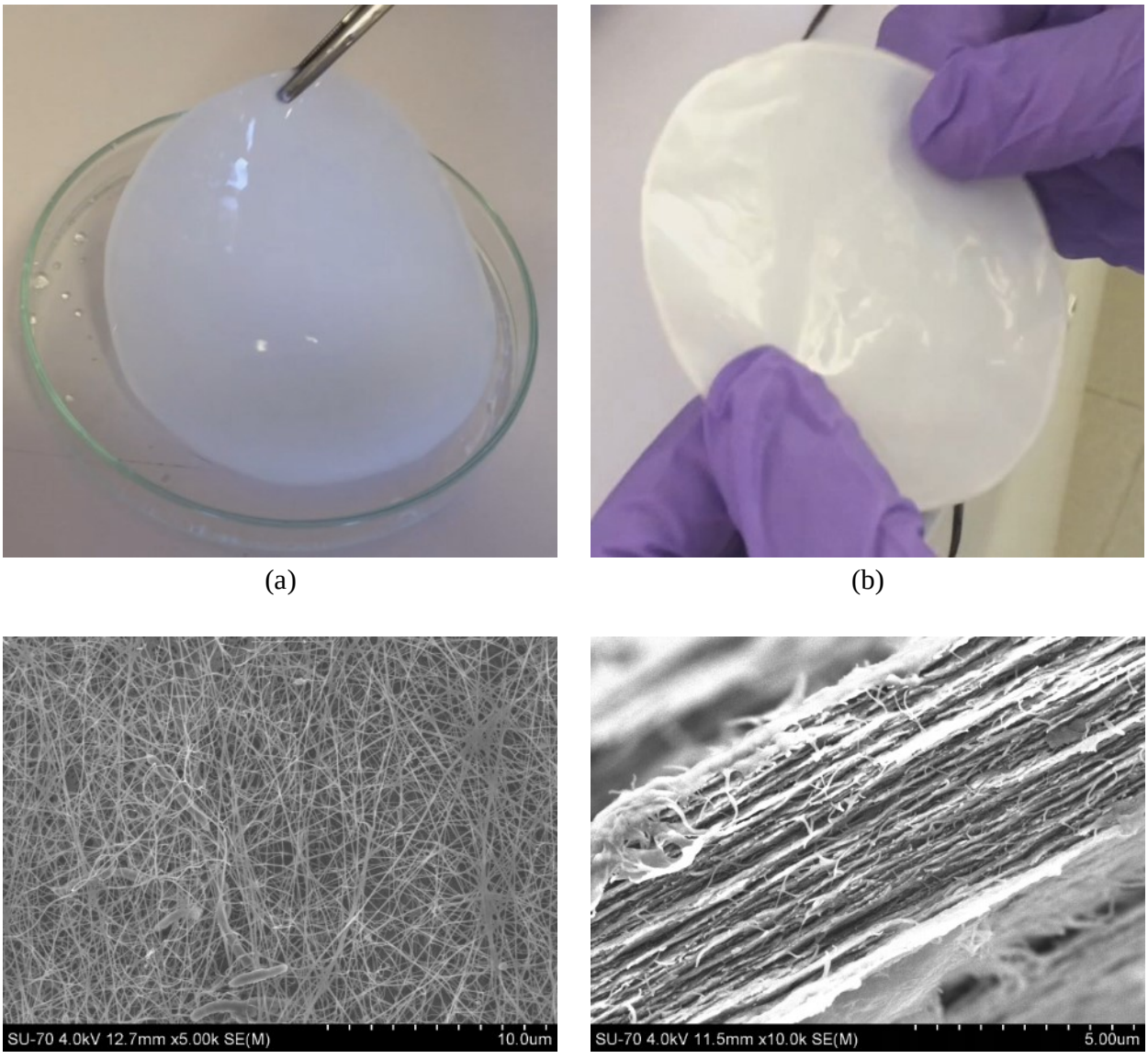


**Figure 3.1 –** Photographs of the nanofibrous bacterial cellulose (BC) membranes. (**a,b**) Wet and dry BC membranes after completion of the whitening and drying manufacturing steps by Trovatti [15], respectively. (**c**) Morphological structure of the random-distributted nanofibers including entangled bacteria inside the BC mesh. (**d**) Cross-section view of the BC membrane. All photographs have copyright to Dr.[a] Carmem Freire, CICECO, Aveiro, Portugal.

## 3.3 – IT devices made with gold electrodes

The IT devices based on gold electrodes were custom-designed to support the research work carried out in this thesis. Gold electrodes were deposited in several types of substrates including, glass microscope slices glass substrates (1 mm thick clear soda-lime and twin frosted), and dry BC membranes. To improve the gold adhesion to the glass substrate a thin layer of chromium (Cr), 2 nm thick was used. Chromium was not used when gold was deposited on BC. Gold was deposited by thermal evaporation using an Edwards coating system E306A. The electrode design was defined by a shadow mask. Two type of shadow masks were used consisting of laser cut pieces One type of shadow mask was made of 30 µm thick polyimide film with a high temperature resistant single-side adhesive layer (aka Kapton® film), and the other type of 80 µm thick stainless-steel sheet.

In this thesis, two main electrode designs were utilized: the parallel rectangular finger-shaped electrodes and the circular electrodes as illustrated in Figure 3.2 (a,b), respectively. The dimensions of parallel rectangular fingers-shaped electrodes vary according to the electrodes width ($L$), length ($W$), and inter-electrode distance ($D$). Similarly, for the case of circular electrodes, the diameter ($\phi$) and inter-electrode distance ($D$) were varied including, the gold track width ($L$) and length ($W$). It is important to note that the dimensions and shape of the vessel sealant layer used to support the cell medium will control the lengths of the finger-shaped electrodes or gold tracks, as it will be discussed in Section 3.7.

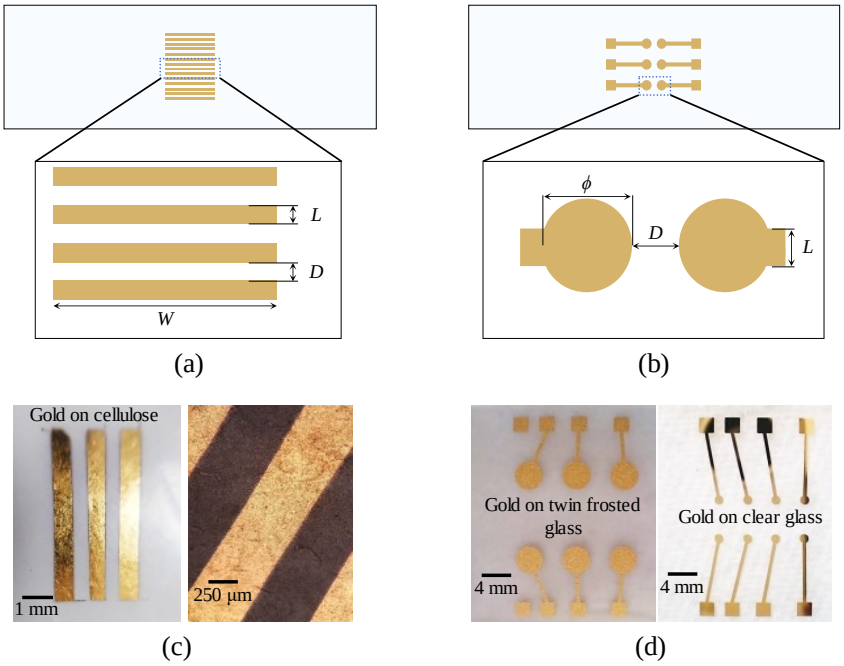


**Figure 3.2 –** Typical electrodes design of the IT devices made with gold electrodes. (**a,b**) Illustration of the typical electrodes design used, namely, parallel finger and circular shape design, respectively. (**c**) Photograph and micrograph of gold parallel finger electrodes on BC. (**d**) Photographs of parallel circular electrodes with different diameters. On the left, gold electrodes were deposited on twin frosted glass, while on right plain and clear glass was used.

Figure 3.2 (c,d) shows photographs of IT devices made with gold electrodes on BC and on glass substrates, respectively. The gold electrodes shown in the left position of Figure 3.2 (c) are 10 mm long, 0.5 mm wide and have a gap distance of 0.5 mm. On the right, Figure 3.2 (c) includes a micrograph highlighting the surface roughness of the gold electrodes deposited in BC. Figure 3.2 (d) depicts two IT devices with circular electrodes of different sizes. In the IT device on the left, twin frosted glass was used for deposition of gold electrodes with 3.5 mm of diameter and gap distances of 2.5 mm and 7.5 mm between the side-by-side and counter parallel electrodes, respectively. The circular gold electrodes are connected to a 2 mm x 2 mm square pad through a 0.5 mm wide gold track. The length of the gold tracks varies within 3.8 mm to 4.25 mm. In the IT device shown on the right, plain and transparent glass was used for deposition of gold electrodes with 1 mm of diameter and gap distances of 2.5 mm and 4 mm between the side-by-side and counter parallel electrodes, respectively. The circular gold electrodes are connected to a 2 mm x 2 mm square pad through a 0.5 mm wide gold track. The length of the gold tracks varies within 7.8 mm to 8 mm.

## 3.4 – IT devices made with PEDOT:PSS electrodes

Some IT devices were made with poly(3,4-ethylenedioxythiophene) : polystyrene sulfonate (PEDOT:PSS) electrodes, a well-known conductive polymer [16–19]. The PEDOT:PSS electrodes were deposited through on several type of substrates including, glass microscope slices and bacterial cellulose membranes using inkjet print technique. The inkjet printing was carried on with a Fujifilm Dimatrix Material Printer, DMP-2831. The printer comes with empty proprietary cartridges (Fujifilm DMC-11610), which were filled with AGFA Orgacon™ transparent conductive inkjet ink solution (IJ-1005) [20,21]. A detail description of the printing protocol may be found in the jetting instructions for Orgacon™ IJ-1005 document [22]. The electrode patterns are customizable through use of graphical software tools to convert vectorial graphics into printing sequences for the deposition of microdroplets of the PEDOT:PSS solution. However, the minimum electrode dimensions are limited to the DMP-2831 printer resolution, which is 2.4 pL drop volume resulting in about 30 μm dot size [23]. Repeating the same printing sequence, is a standard procedure to adjust the thickness of the PEDOT:PSS electrodes. Different thickness of PEDOT:PSS electrodes were fabricated, having been used 8, 10 and 15 repetitions of the same printing sequence. All samples were annealed on a hot plate at 60 ºC for 8 hours. After annealing, the samples were subjected to chemical post-treatments, through immersion of the samples into stock solutions. The stock solutions used were the dichloroacetic acid (DCA), dimethyl sulfoxide (DMSO), methyl ammonium iodide (MAI), ethylene glycol (EG), and hexafluoroacetone (HFA). After immersion, the samples were dried in a vacuum oven at 60ºC for 12

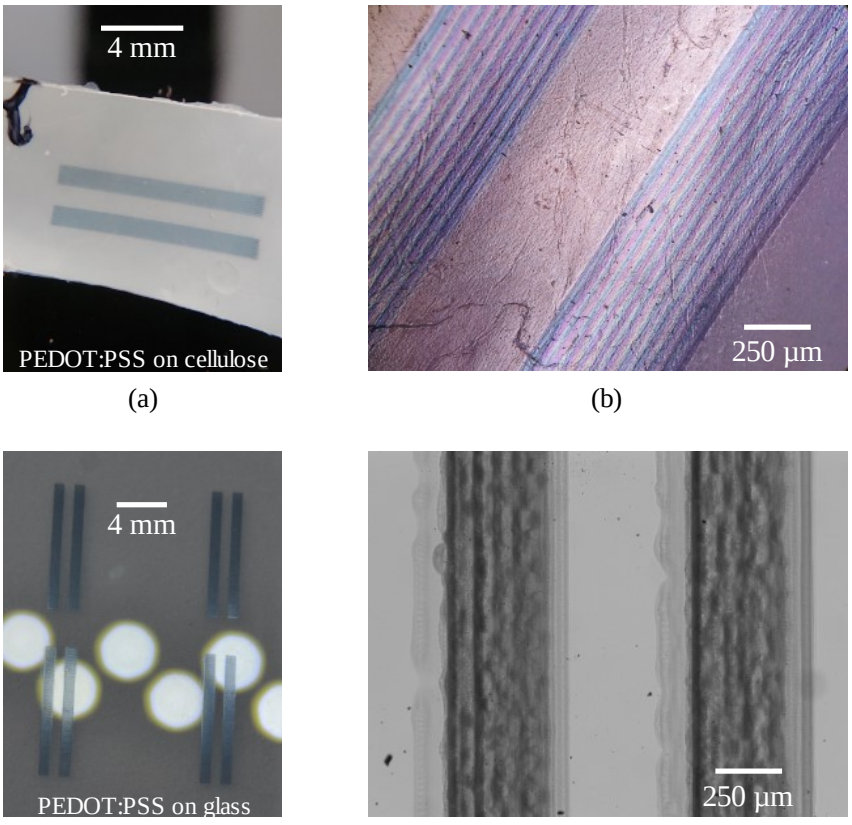


**Figure 3.3 –** Typical electrodes design of the IT devices made of inkjet print PEDOT:PSS electrodes. (**a,c**) Photographs and (**b,d**) micrographs of the PEDOT:PSS electrodes on BC membranes and clear glass, respectively.

hours. As for the electrodes design, the same shape and dimensions previously detailed at section 3.3 for IT devices made with gold electrodes were used, namely, the parallel rectangular finger-shaped electrodes shown in Figure 3.2 (a). Figure 3.3 shows the photographs and micrographs of the typical IT devices made of inkjet print PEDOT:PSS electrodes on BC membranes and on glass.

The electrode samples printed on glass with less than 10 printing sequences were found to be more susceptible to detachment or delamination when exposed to brief and low-intensity deionized water jets. This was observed even in electrodes that had undergone chemical post-treatments.

## 3.5 – Commercial 8 Well PET Arrays (IBIDI devices)

Three commercial configurations were purchased to Applied Biophysics, namely, the 8W1E PET [24], 8W20idf PET [25] and 8WCP PET. Because the 8WCP PET configuration is old, unfortunately it can no longer be consulted in the manufacturer website, reason why no reference is provided. All samples contain 8 well PET arrays and have the same pattern of gold electrodes per well on a polyethylene terephthalate (PET) substrate. Also, all gold tracks between the electrodes and larger contact pads are insulated with a thin layer of cured photoresist polymer.

The 8W1E PET device consist of a single circular electrode with a diameter of 250 μm located in the center, resulting in a total electrode area ($A_e$) of 0.049 mm$^2$. The 8W20idf PET device consists of an interdigitated finger (IDF) arrangement. The IDF configuration has eleven fingers, each measuring 4.5 mm in length ($W$) and 0.08 mm in width ($D$), spaced ($L$) by 0.4 mm, resulting in a total electrode area ($A_e$) of 3.98 mm$^2$. The 8WCP PET device consists of a parallel arrangement of eight interdigitated fingers. With a total electrode area ($A_e$) of 30 mm$^2$, the electrodes' fingers are spaced ($L$) by 0.25 mm, each measuring 7.5 mm in length ($W$) and 0.5 mm in width ($D$).

**Table 3.1** – Summary of the IBIDI devices configurations used in this thesis.

| **Reference** | **Shape** | **Dimensions** | | | |
|---|---|---|---|---|---|
| | | Diameter ($\phi$) | Spacing ($L$) | | Area ($A_e$) |
| 8W1E PET | Circular | 0.250 mm | 3 mm | | 0.049 mm$^2$ |
| | | Length ($W$) | Width ($D$) | Spacing ($L$) | Area ($A_e$) |
| 8W20idf PET | Interdigitated | 4.5 mm | 0.08 mm | 0.4 mm | 3.98 mm$^2$ |
| 8WCP PET | Parallel | 7.5 mm | 0.5 mm | 0.25 mm | 30 mm$^2$ |

Figure 3.4 (a−c) depicts three commercially available IBIDI device configurations scaled to their original dimensions. The yellow and orange regions in Figure 3.4 always represent the open gold and the cured photoresist polymer layers, respectively. The electrode layout of each IBIDI device is depicted in Figure 3.4 (d−f). Table 3.1 summarizes the three IBIDI devices layout specifications. Figure 3.4 (g−h) depicts a photograph of the 8WCP PET device as well as a computer-aided design (CAD) of the sample holder structure created by Pedro Inácio to allow for a simple physical connection to any IBIDI device to the recording instrumentation. The sample holder consists of two laser-cut pieces made of transparent PMMA. The 95 mm long and 50 mm wide PMMA piece is used as bottom support of the IBIDI device as well of the top PMMA piece that holds nine gold-plated spring-loaded probes horizontally aligned and spaced 3.2 mm apart. The mechanical connection between the lower and upper PMMA pieces is performed with two stainless steel springs, screws, and nuts. The two screws are used as vertical guidance axis ensuring the spring-loaded probes kept the same horizontal position. The two springs are used to obtain a mechanical force that keeps the two pieces of PMMA apart. To connect the IBIDI device with the vertical spring-loaded probes, a third vertical and centrally located screw is used to adjust the vertical position of the upper PMMA piece. Thus, the connection protocol of the IBIDI devices requires the user to position the IBIDI device over the lower PMMA piece and twist the centrally located screw head.

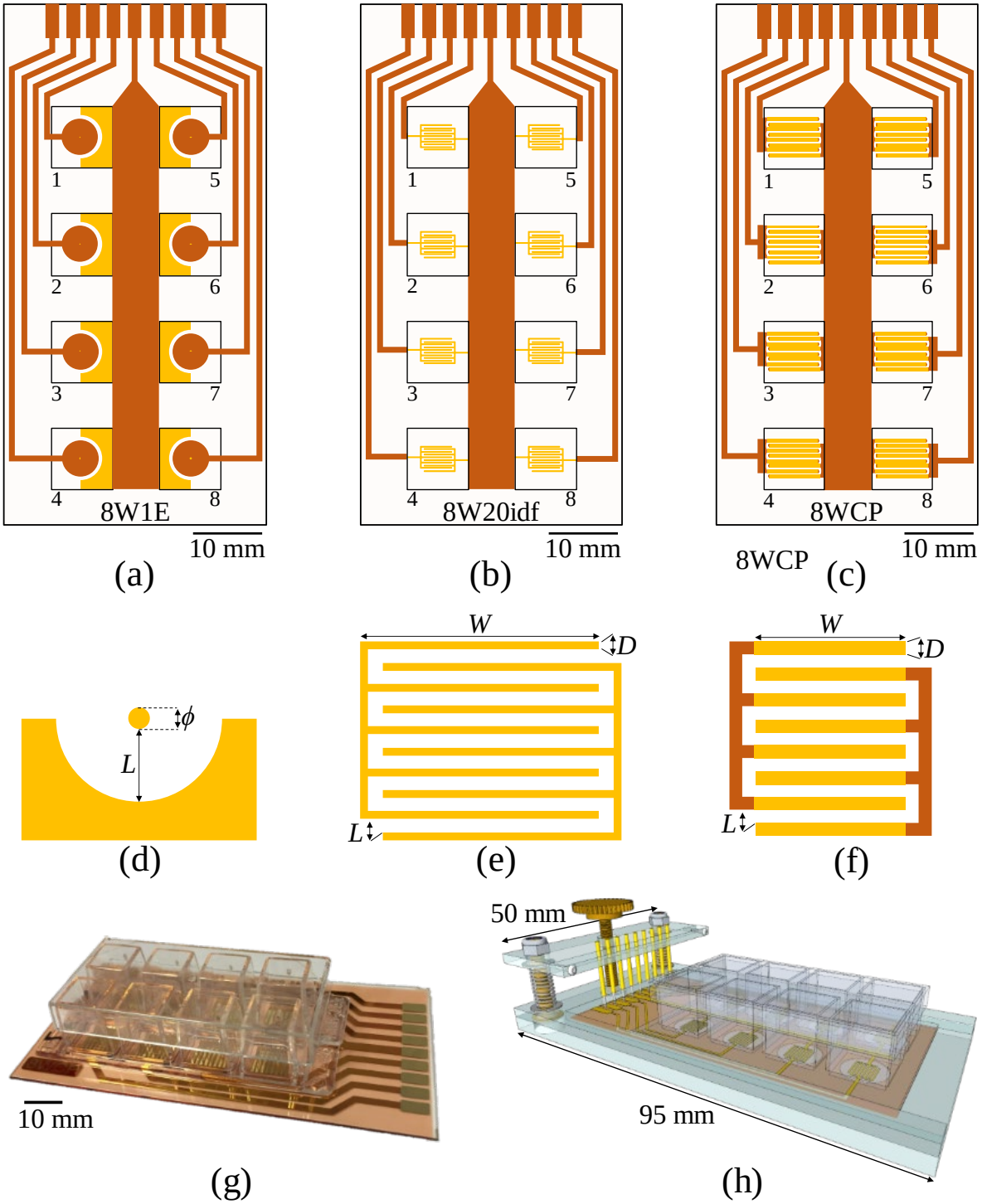


**Figure 3.4 –** (**a**–**c**) Illustration of the commercial 8 Well PET arrays manufactured by Applied Biophysics. (**d**–**f**) Detail view of the electrodes shape and dimensions. (**e**) Photograph of a 8WCP PET array sample. (**h**) CAD design of a prototype mechanical support structure for connecting IBIDI devices to recording equipment..

## 3.6 – PHILIPS devices

The PHILIPS devices used in this work were manufactured using thermally oxidized silicon wafers as substrates. The sensing electrodes are gold interdigitated fingers fabricated by thermal evaporation. To improve the gold adhesion to the Sio2 surface, a thin layer of Cr was used. The rectangular fingers

measure 1 mm in length ($L$), 5 µm in width ($D$), and have an inter-electrode distance ($L$) of 10 µm. The length of each interdigitated set is 10 mm. Each MEAs achieves an $A_e$ = 3.035 mm$^2$. However, the effectiveness of $A_e$ is controlled by the vessel internal width, which in this work has an area of $A_e \approx$ 0.286 mm$^2$ .The vessel dimensions are 3.5 mm wide and 15 mm long. Figure 3.5 (a) illustrates the PHILIPS device proportionally dimensioned to the original size as well, a detail view of the electrode shapes and dimensions. Figure 3.5 (b) shows a micrograph of one set of MEAs covered with C6 glioma cells. Figure 3.5 (c,d) depicts the CAD model and photograph, respectively, of the prototyped sample holder structure developed by Pedro Inácio to provide facile physical connection to the recording instrumentation of the four sets of MEAs. The mechanical support was designed to be assembled in a sandwich-like structure consisting of two laser-cut 40 mm square pieces made of transparent PMMA. A GCC LaserPro Spirit LS [26] equipped with a 40W $CO_2$ laser was used to cut the PMMA. One PMMA piece is the bottom sandwich layer, intended to support the PHILIPS device and four vertically aligned stainless-steel screws. The other PMMA piece is used to vertically hold eight spring-loaded gold-coated probes, precisely spaced according to the gold pads designed in all PHILIPS devices as well, it also includes support a 0.525 mL container that is 3.5 mm wide, and 15 mm long, centrally located between the contact probes. A 1.5 mm thick O-ring made of silicone rubber with internal diameter of 10 mm was used as sealant. Note that the O-ring is inserted between the contact probes

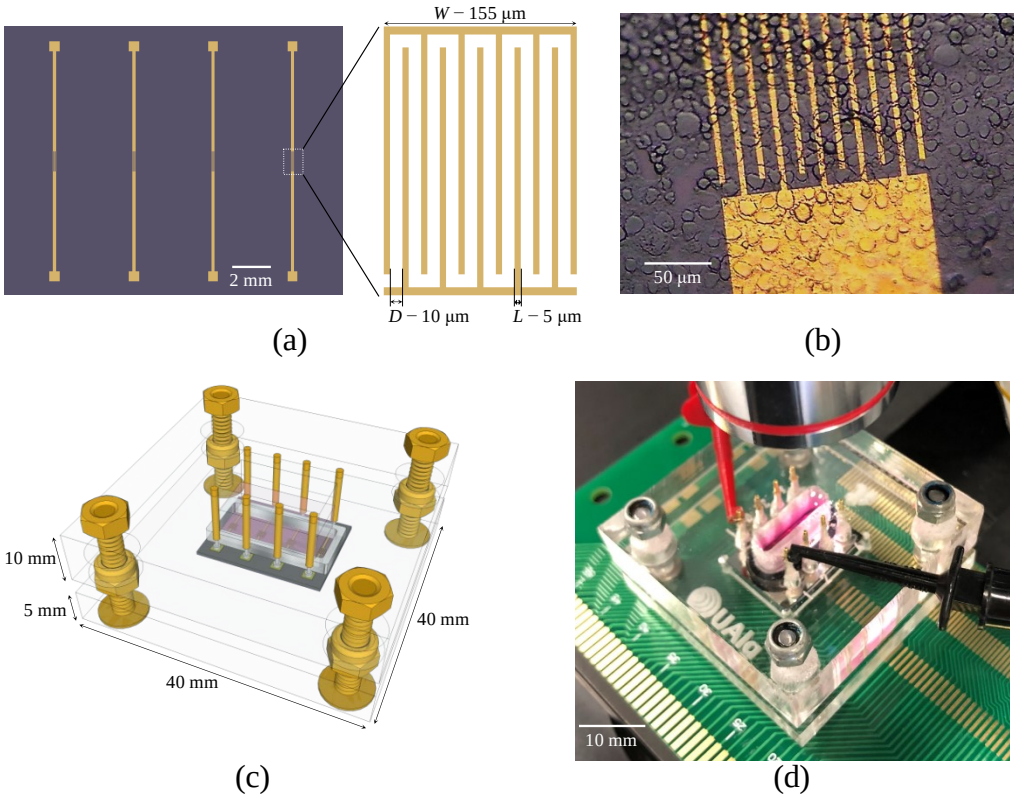


**Figure 3.5** – (**a**) Illustration of the Philips device as well a detail view of the MEAs shape and dimensions. (**b**) Micrograph of one set of MEAs covered with C6 glioma cells. (**c,d**) CAD design and photograph of the prototyped mechanical support structure to connect PHILIPS devices.

pillars, forcing the O-ring to deform into a long oval shape, and become approximately linear in the regions of the MEAs. This observation is important because, as referred above it delimits the MEAs length and consequently the $A_e$ value. Therefore, the assembly protocol is relatively simple and fast, only requiring the user to centrally position the PHILIPS device on the lower PMMA piece and then compress the upper PMMA piece using four stainless-steel nuts to ensure a tight seal but without compressing too much, considering the fragility of the silicon substrate.

Because PHILIPS devices use thermal oxidized silicon wafers as substrate, the upper layer where the gold electrodes are deposited is insulating while the bottom silicon layer is conductive. This design allows PHILIPS devices to operate as a capacitor like structure (metal-insulator-semiconductor field effect transistors (MISFET)). In order to operate the device as a capacitor, the sample holder structure includes five drilled holes at the bottom of the PMMA piece to provide electrical access to the silicon substrates.

## 3.7 – IT devices sample holder

A sample holder was developed to assemble in a sandwich-like structure all IT devices, consisting of two laser-cut pieces made of 3 mm thick transparent poly(methyl methacrylate) acid (PMMA). A GCC LaserPro Spirit LS [26] equipped with a 40W $CO_2$ laser was used to cut the PMMA. One of the PMMA pieces (piece A) was used as supporting layer, and the other PMMA piece (piece B) to compress the sealing layer, a 35 mm in diameter petri dish [27] and the IT device using six pairs of stainless-steel screws and nuts. The vectorial design and assemblage guide of the two PMMA pieces are illustrated in Figure 3.6 (a,b), respectively. Note that piece B has a 36 mm diameter circular opening located in the center. This opening may be convenient to allow inspection of the sample under inverted microscopes. Therefore, a 1 mm thick standard microscope slice with 75 mm in length by 25 mm in width was used to support the IT device. Piece B has four rectangular laser cut openings which are needed to glue the four extra pieces of PMMA labelled as piece C in Figure 3.6 (a,b), respectively. Piece C is used to insert large gold-plated pin, proving connection of the IT device electrodes to the recording instrumentation. The connection between each electrode and a gold-plated pin is carried on with 25 μm thick gold wires (Heraeus, Hanau, Deutschland) [28,29] and silver conductive paint (SCP) (Electrolube, UK) [30]. The sealing layer is usually performed with O-rings, making a hole in the Petri dish equal to the inner diameter of the O-ring used. Alternatively, the sealing layer may also consist of a laser cut part made from 100 μm up to 1 mm thick silicone rubber sheet. Figure 3.6 (c,d) shows the CAD model and photograph of the IT devices mechanical support fully assembled, respectively.

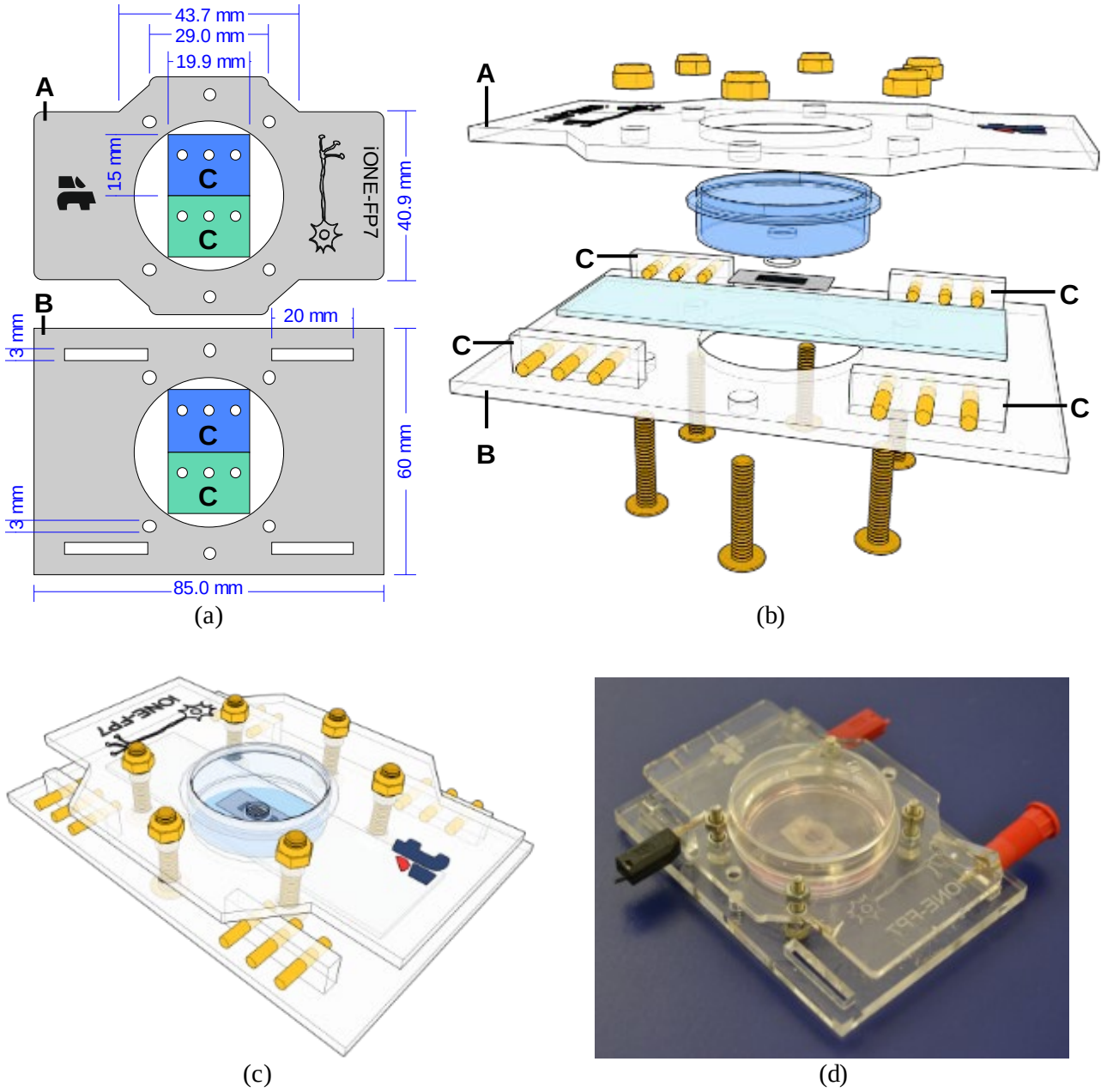


**Figure 3.6 –** Sample holder developed for IT devices. (**a**) Vectorial design used to laser-cut the transparent poly(methyl methacrylate) acid (PMMA) sheet into pieces A, B and C. (**b**) CAD model of the assemblage process of the IT device using the PMMA pieces A, B and C. (**c,d**) CAD model and photograph of the IT device assembled in the mechanical support, respectively.

## 3.8 – Cleaning and Storage

All devices used in this work were kept stored in sealed boxes before use to avoid contamination. Often, the devices were reused to the purpose of repeating the same experiment. In these cases, the devices were kept assembled in the mechanical supports, and the chambers were cleaned using the following three steps: (i) the device chamber is kept filled for 5 minutes with a 5% chlorine bleach solution mixed on milli-Q water to kill any contaminants; (ii) the solution in the chamber is replaced

by 1X phosphate buffer solution (PBS) for another 5 minutes while simultaneously is exposed to UV radiation from the laminar flow cabinet; (iii) the PBS solution in the chamber is replaced by milli-Q water and kept for another 5 minutes to dissolve the residues of salts left from the PBS solution.

No device was ever reused after being disassembled from the mechanical support. Regarding the mechanical supports, the reusable pieces made of PMMA were cleaned with a jet of a 5% chlorine bleach solution mixed on milli-Q water to kill any contaminants. After about 5 minutes, all pieces were washed with a distilled water jet bath. Next, a jet bath with a 70% ethylic alcohol solution were performed and left in room temperature to dry. The O-rings are often reusable and cleaned with the same cleaning procedure described above to clean the mechanical supports PMMA pieces. Petri dishes were always discarded after each experiment.

## 3.9 – Device electrical characterization

This thesis employed four distinct types of devices in its experimental work, each with distinctive differences. The devices vary in their materials for the sensing electrodes and substrates, as well as differences in the shapes and sizes of the electrodes. All devices have material compositions that support cell attachment and growth. To further promote cell attachment, poly-L-lysine amino acid coatings were applied to either the electrodes or the substrates for IBIDI and PHILIPS devices, as well as IT devices with electrodes deposited on glass. A detailed description of the procedures for the poly-L-lysine amino acid coatings can be found in Chapter 4.

Experiments were conducted to assess the longevity of cell populations that were seeded on BC membranes with and without electrodes. Although no analytical cytotoxicity analyses were performed on the cell media, pH measurements of the media and impedance measurements of the gold and PEDOT:PSS electrodes were conducted. Additionally, periodic visual inspections were carried out under a microscope. During the two-week experimental period, no signs of premature cell death were observed, considering that the cell media was changed daily.

Regarding the electrodes of the devices used, the most notable differences are due to the electrode's geometry and material. The use of larger sized electrodes implies the electrode probes a larger number of cells.

As discussed in Chapter 2, the electrode-electrolyte interface is modeled by the EDL that is formed at the interface between the electrode and the electrolyte solution. The EDL layer is modeled by an equivalent RC circuit that explains both the steady stated and DC response as well as the AC response to electrical signals. Recently, Medeiros et al. [31] used this simplified equivalent circuit to describe the electrical coupling of cell signals to the electrode.

When recording low frequency signals, the thermal noise of the electrode-electrolyte interface must be minimized to improve the signal-to-noise ratio (SNR). At low frequencies, the double-layer resistance ($R_{DL}$) is the dominant resistive path and the main source of thermal noise.

To determine the values for the $R_{DL}$ and $C_{DL}$ components of an equivalent circuit, it is crucial to extract them accurately. The experimental impedance curves as a function of frequency are often fitted to an equivalent circuit model to obtain the $R_{DL}$ and $C_{DL}$ values. However, sometimes the impedance curves deviate significantly from the expected circuit behavior, making it difficult to extract reliable values from the fitting. In such cases, a quasi-static capacitance-voltage method is used instead.

In this method, a slow voltage ramp is applied to the electrode/electrolyte system, and the corresponding current hysteresis loop is monitored as a function of the ramp speed (dv/dt). Since the current hysteresis loop is caused by the displacement current ($i_C = C_{DL}$ x $(dv/dt)$), $C_{DL}$ can be extracted by measuring the displacement current. However, hysteresis loops are often not purely capacitive, and they appear tilted around the xx-axis due to a DC component. This component must also be extracted and used to correct the actual displacement current values.

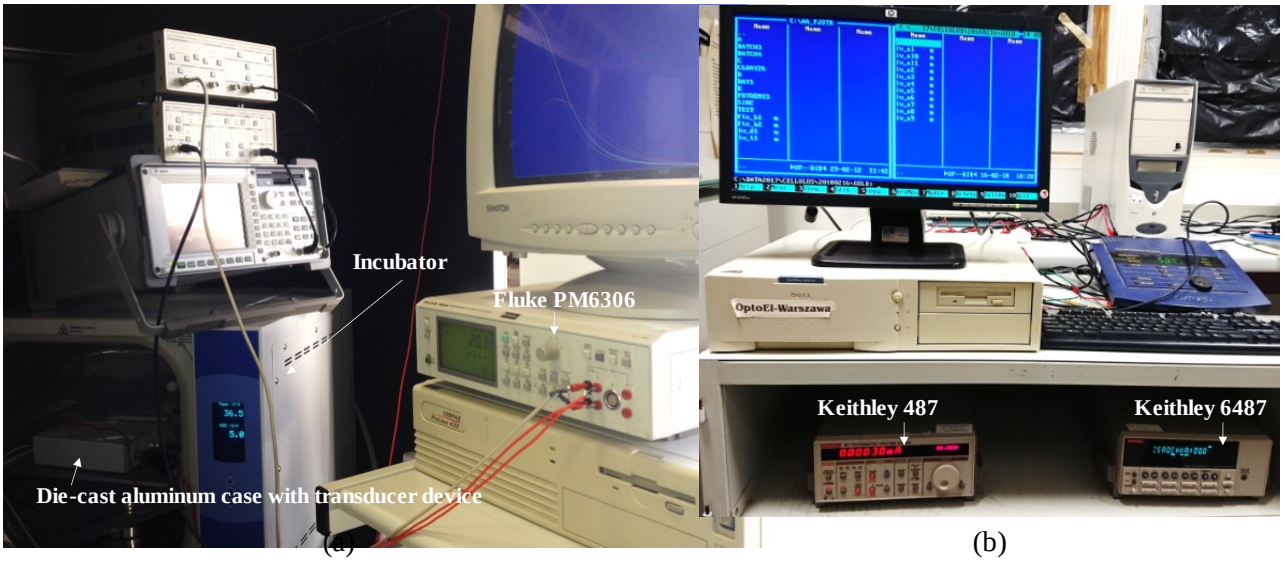


**Figure 3.7 –** Photographs of the experimental set-up. (a) Impedance and (b) current recording systems.

The experimental procedures to carry out the quasi- static impedance measurements are described in Chapter 4. Figure 3.7 shows two photographs of the electrical instrumentation used to carry out the impedance measurements. Figure 3.7 (a) shows the RLC meter Fluke PM6306 that measures the impedance as function of the frequency. Figure 3.7 (b) shows a picommeter/voltage source Keithley 487 that generates a well-defined voltage ramp and measures the corresponding displacement current across $C_{DL}$.

Finally, since the electrode geometry varies depending on the transducer device used, the recorded signals, the noise, and impedance measurements were normalized. The normalization used consists of dividing the recorded data by the electrode area. In all experiments, the electrode area is noted.

## 3.10 – Ultra-low noise recording system requirements

For the purposes of this thesis, the recording system was tune for the detection of ultra-weak extracellular signals sourced from non-electrogenic cells. Typically, ultra-weak extracellular signals have amplitudes no greater than tens of microvolts or picoamps [31–34], as well as consists of slow varying signals scaled in seconds. Furthermore, as the signal detection method consists of using large area electrodes, the amplitude of ultra-weak signals and the intrinsic noise generated by the cell population are expected to be proportional to the number of cells per electrode [35], and to the pink noise [36]. Therefore, to level the signals at the ADC input, the amplifier gain was adjusted according to the expected signal and noise amplitude, but also considering the signal frequency, period and source that can either be voltage or current. Thence, either a voltage or current amplifier circuit is needed for the recording of cell signals. In case of voltage amplifier circuit, because voltage signals are often biased with a DC electrochemical offset potential (DC component), the transducer device must be DC coupled to the amplifier input to ensure the detection of ultra-weak signals in their natural form, but at the cost of holding the entire input signal power across all frequencies, that is, the higher is the DC component of the signal, the lower is the signal resolution at the ADC input. A work-around is to use AC coupling that allows remove the DC component with minimal signal distortion down to a few tens of microhertz, e.g., for a 30 mHz corner frequency due to AC coupling, the detection limit of ultra-weak extracellular signals is settled to about 33 seconds, a reasonable detection limit. As for the current amplifier circuit, as the ADC input is sampled in voltage, a trans-impedance amplifier circuit is needed to convert the input current signal into an equivalent voltage signal while simultaneously allows amplify the ultra-weak extracellular signals. Occasionally, the use of a customizable low-pass filter (LPF) or high-pass filter (HPF) may be needed to extend the amplifier gain/sensitivity to higher values either on voltage or current sensing modes. Note that using AC coupling for sensing voltage signals is equivalent to using an HPF, but with a fixed corner frequency. Likewise, in current sensing mode, the transimpedance amplifier circuit has an implicit LPF by limiting the bandwidth as a function of its sensitivity to input signals.

Finally, the system design must include a shield to isolate the recording system and transducer device from the electromagnetic interferences (EMI), such as those caused by radio waves, and from

local vibrations, such as human walking and talking, while at the same time meets with a compatible environment for living cells.

## 3.11 – Ultra-low noise recording system

In this thesis, the voltage and current amplifier circuits consists of two commercial low-noise amplifiers (LNAs), the Low Noise Voltage Preamplifier − SR560 [37] and the Low Noise Current Preamplifier − SR570 [38]. Both instruments are manufactured by Stanford Research Systems, Sunnyvale, California, USA. Both LNAs have a customizable front-end that allows to adjust either the gain or sensitivity, depending on when the SR560 or SR570 LNA is used, respectively, as well to tune a LPF and a HPF either individually or simultaneously. On both LNAs, the low-noise gain mode was used to allocate the amplifier gain toward the amplifier input to quickly lift ultra-weak signals above the amplifier circuit noise floor. In particular, the voltage LNA (SR560) was always configured in common mode, that is connecting the transducer device to input port A and record the signals according to the reference potential of the amplifier. As for the coupling, either the DC or AC coupling were used, which allowed adjusting the amplifier gain ($A_v$) up to 5000X to match the ± 5 V input range of the ADC connected to the 50 Ω amplifier output. Whenever DC coupling was used, the front potentiometer of the SR560 was adjusted to shift the DC component of the signal close to the amplifier's reference level, preventing the overload condition. As for the current LNA (SR570), the amplifier sensitivity ($A_i$) was always adjusted to match the ± 5 V input range of the ADC connected to the 50 Ω amplifier output, but without exceed a sensitivity of 100 nV/A when recording ultra-weak extracellular signals to restrict the bandwidth of the amplifier at 200 Hz.

The 50 Ω outputs of the LNA were connected to an Agilent 35670A Fast-Fourier Transform (FFT) Digital Signal Analyzer (DSA) using a 0.5 m long low-noise coaxial cable. The DSA, which is currently owned by Keysight Technologies in Santa Rosa, USA [39], was always configured in single-channel mode, limiting measurements to the DSA's channel 1 input. Channel 1 includes an LNA circuit at the input that enables gain and coupling mode adjustments between DC or AC before connecting the device under test (DUT) to a 16-bit amplitude resolution ADC unit. Throughout this thesis, the LNA gain and coupling at the input of channel 1 were configured to 1 and DC, respectively. Using this recording system, the noise spectral analysis of the DUT was carried out, as well as the recording of ultra-weak extracellular signals.

To conduct ultra-low noise measurements, the transducer device was placed inside a die-cast aluminum case that holds an isolated Bayonet Neill–Concelman (BNC) connector to plug the transducer device to the LNA via a 1 meter long low noise coaxial cable. The die-cast aluminium case was placed inside an incubator at a controlled atmospheric temperature and percentage of carbon

dioxide ($CO_2$) to create a favourable environment for living cells. To protect the recording system from electromagnetic interference (EMI), the entire recording system was placed inside a 1 meter cube-shaped Faraday cage made of 5 mm thick iron and positioned on top of an anti-vibrational mounts at each corner. Figure 3.8 (a) shows a schematic diagram the ultra-low noise recording system as described above. Figure 3.8 (b) displays a photograph of the transducer device placed inside the die-cast aluminum case that is connected to the recording system.

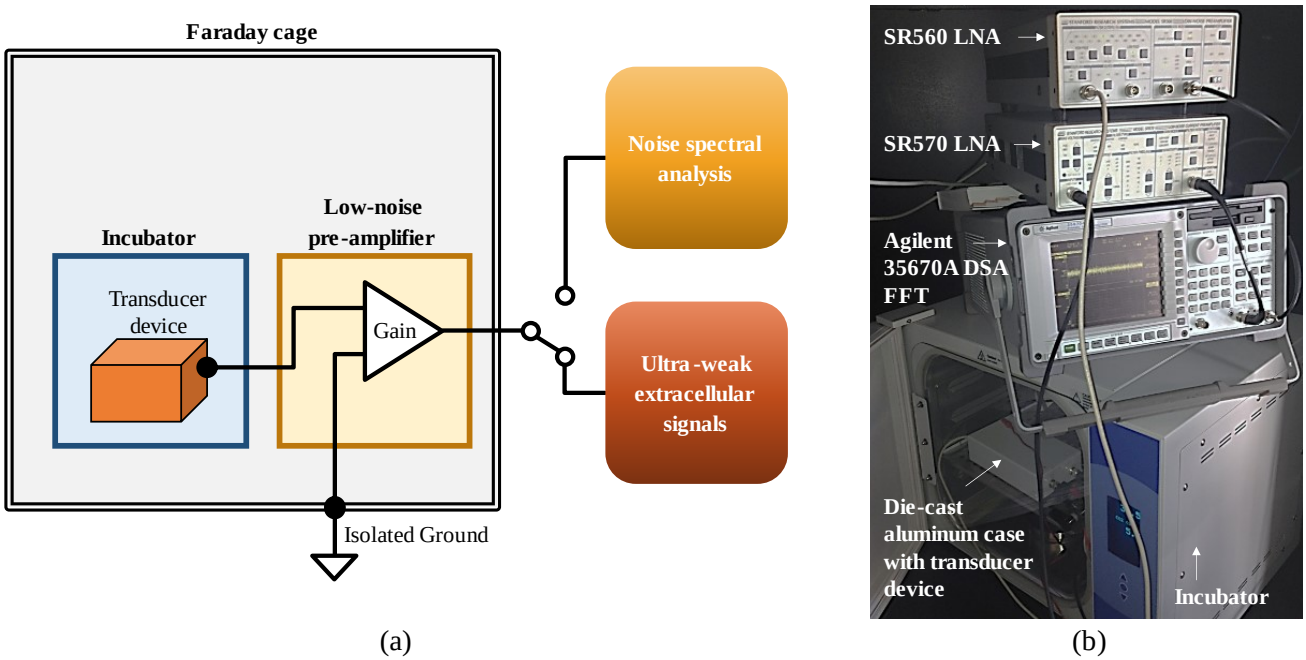


(a) (b)

**Figure 3.8 –** Set-up of the ultra-low noise recording system. (a) Schematic representation and (b) photograph of the entire system inside the Faraday cage.

## 3.12 – *rcSoftware*: A MATLAB-based application for control of an electrophysiological system – signal acquisition, storage, and processing

*rcSoftware* is a comprehensive toolkit designed for signal acquisition, collection, and processing in an ultra-low electrophysiological system setup. While it was specifically developed for this system, the data collection and processing tools can be adapted for use with different recording instrumentation. The program was developed using MATLAB, with the core module designed for control of the instrumentation while providing real-time access to signal processing tools. The *rcSoftware* has functions for performing time series and statistical analyses. Time series analysis offers the possibility to calculate average periodograms using a conventional arithmetic method or the Bartlett method. Statistical analysis is provided in two forms, the time-weighted average method, and the histogram method, each of which can be used to analyze signal morphological parameters

(amplitude, area, length, inter-signal length, frequency, noise level, and SNR). Minimal background knowledge is required to operate and process data using high-level tools, making it an accessible option for researchers interested in the field of electrophysiology. Since the release of the first version, the *rcSoftware* has been used in a variety of published work by our research group, and its user base has grown considerably.

### 3.12.1 − Introduction

Performing real-time electrophysiological experiments usually requires an expensive set-up. In many cases, the apparatus consists of a combination of different instrumentation that requires an autonomous management system. In such scenarios, there are two common options available. The first is to use the software provided by the manufacturer, which often requires a license fee. The second option is to use an open-source toolkit that is already available for the specific setup [40–44]. However, it can be challenging to find commercially available software that is tailored to the specific needs of a particular instrumentation setup. This can be especially difficult for academic research and development groups who may have limited resources.

The *rcSoftware* was designed specifically for control, data management, and signal processing. However, it is worth considering the possibility that Keysight Technologies instruments [45] (the manufacturer of the (DSA instrument could offer comparable solutions through a partnership width Eggplant software [46] or through the Keysight VEE Pro software [47]. As mentioned in reference [8], it should be noted that both solutions require software development and licensing fees, which are typically several thousand dollars or more.

While the 35670A Data Link software [48] can be download for free at the Keysight Technologies website and does not require a license, it should be noted that it is only useful for experienced users with extensive training. To use the software, users must become familiar with the equipment and be able to repeatedly perform the same measurements and store data protocols in the equipment's internal memory buffers. The software is also limited in that it requires full-time human supervision and can only be used to transfer data to a local PC. Additionally, it does not provide access to visualize or process raw data.

Similar to many customized in-house solutions [49–51], the *rcSoftware* was developed as part of this work. Given the time required to develop an entire application using a low-level programming language, as well as the graphical user interface (GUI), the solution for developing the *rcSoftware* was to use high-level programming platforms, also known as application programming interfaces (APIs). APIs are common in the development of research and development of software tools. Examples of

such platforms are the LabVIEW [52–55], Python [56–59] and MATLAB [60–65]. These platforms are preferable to facilitate the programming time efficiency and avoid large scripts.

After evaluating the pros and cons of various high-level platforms, the MATLAB was chosen for the development of *rcSoftware* for the following reasons: (i) familiarity and expertise with the language; (ii) ease of deployment to any operating system (OS) without requiring the target platform to install the MATLAB, yet at a cost of a MATLAB (through a commercial license to use the deploy tool); (iii) Robust support for creating a user-friendly graphical user interface (GUI); (iv) use of the proprietary binary file format (.mat file extension) for loading and saving large datasets of recorded data,; (v) an extensive library of functions that are required for data and signal processing.

Given these advantages described above, the *rcSoftware* was developed with a simple and intuitive GUI providing all necessary tool for autonomous control of the Keysight 35670A (DSA) and for real-time data collection and processing.

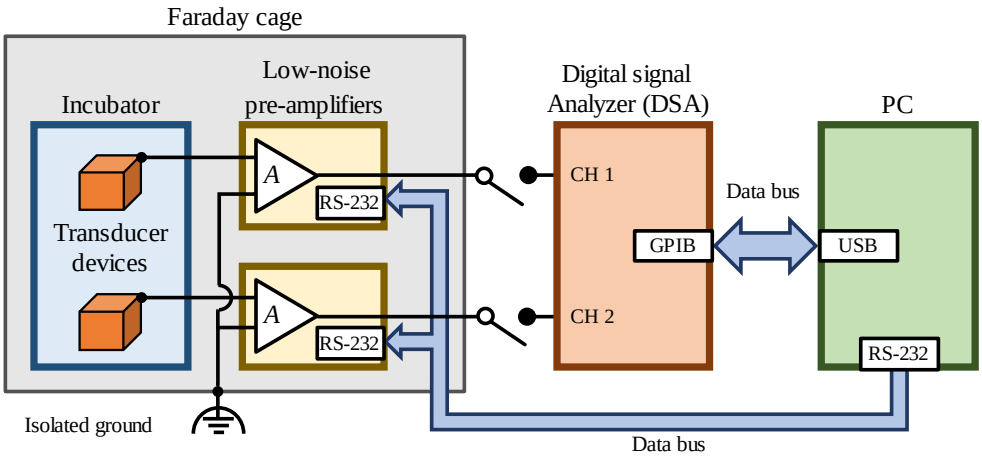


(a)

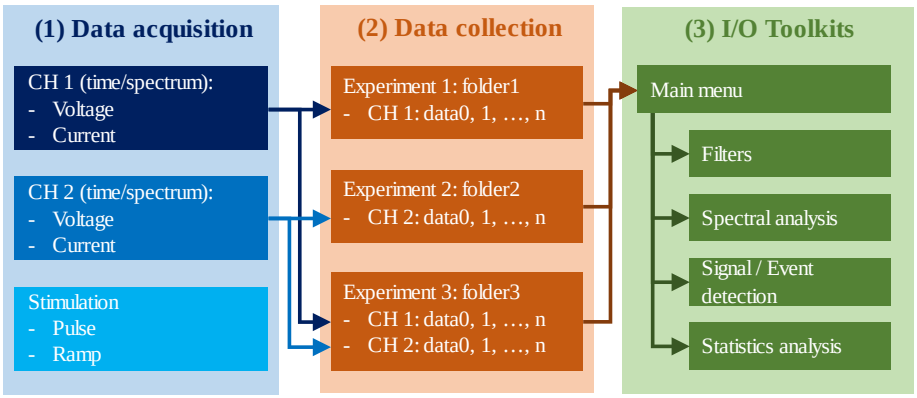


(b)

**Figure 3.9 –** (**a**) Schematic diagram of the ultra-low noise electrophysiological recording system. (**b**) Workflow of the rcSoftware: (1) The data acquisition module allows the user to select the type of data recording, either by manual or autonomous control of the instrumentation; (2) The data acquisition module allows the user to select the data location; (3) The I/O toolkit module allows the user to process the stored data in real time and provides access to various processing tools.

The main purpose of *rcSoftware* is to include autonomous control and processing tools, thereby avoiding permanent human super-vision, highly qualified technical expertise, and programing skills. This results in a significant improvement in the time-efficiency to conduct experiments and leading to quicker publication of data. The following sections contain descriptions of the system specifications and an overview of the acquisition, collection, and processing toolboxes. Detailed descriptions of the *rcsoftware* can be found in Appendix A−C.

### 3.12.2 − System specifications

The ultra-low-noise electrophysiological setup consists of a low-noise preamplifier (LNA) connected to a digital signal analyzer (DSA). The Stanford SR560 voltage LNA (Stanford Research Systems, Sunnyvale, USA) [37] is used for voltage measurements, while a Stanford SR570 current LNA (Stanford Research Systems, Sunnyvale, USA) [38] is used for current measurements. The Agilent 35670A FFT DSA (currently owned by Keysight Technologies, Santa Rosa, USA) [39] with 2-channel is used. A Keysight 82357B USB/GPIB Interface High-Speed USB 2.0 (Keysight Technologies, Santa Rosa, USA) [66] was used to provide the physical interface between the DSA and a local PC. As for the LNA, a generic USB/RS-232 adapter is used for the physical interface. Note that the RS -232 interface of the LNAs allows listen-only communication, so the *rcSoftware* is not able to provide fully autonomous control of the instruments.

The *rcSoftware* requires a local PC, running MATLAB version 2014b [67] or later, and a version of a Virtual Instrument Software Architecture (VISA) installed on the local PC to allow MATLAB to access the physical layers of the GPIB interface. Installing Keysight IO libraries suite software with version 17.0 or later automatically installs and sets up all required drivers, VISA and the USB/GPIB interface. The Keysight IO libraries suite can be viewed and downloaded from the Keysight website [68]. For debugging device communication, it is recommended to install the Keysight Command Expert utility. The generic USB/RS-232 adapter on Windows® computers running Windows 8.0 or later and the generic OS drivers are sufficient. On Macintosh or Linux OS distributions, the user must make sure to find a working driver if OS cannot assign a generic driver. Figure 3.9 (a) shows a schematic diagram of low-noise electrophysiological instrumentation.

### 3.12.3 − *rcSoftware* overview

The *rcSoftware* operates based on the workflow diagram shown in Figure 3.9 (b), numbered (1) through (3) and summarized below. First, module (1) represents the data acquisition phase and is executed by the data acquisition toolbox (DAT) shown in Figure 3.10 (a). DAT performs live

experiments to record electrophysiological signals, which also includes a beta version of an electrical pulse stimulation toolbox (ST). The second module (2) refers to the data acquisition options required to assemble the raw data into organized structural arrays. While DAT is running, data from live experiments are immediately available and can be used with the data processing toolbox (DPT) shown in Figure 3.10 (c). For offline work, the data collection toolbox (DCT) shown in Figure 3.10 (b) was developed to facilitate the processing scripts required to organize raw data files into numeric array data


(a)

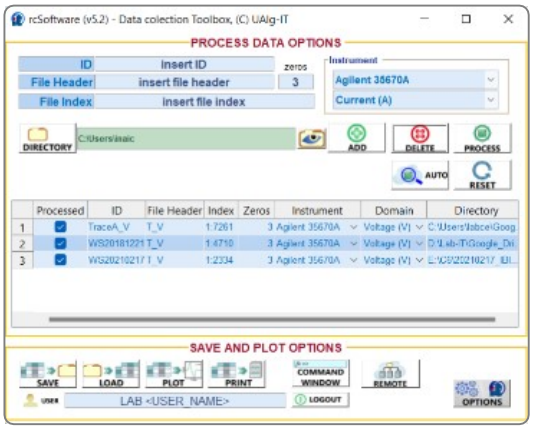


(b)

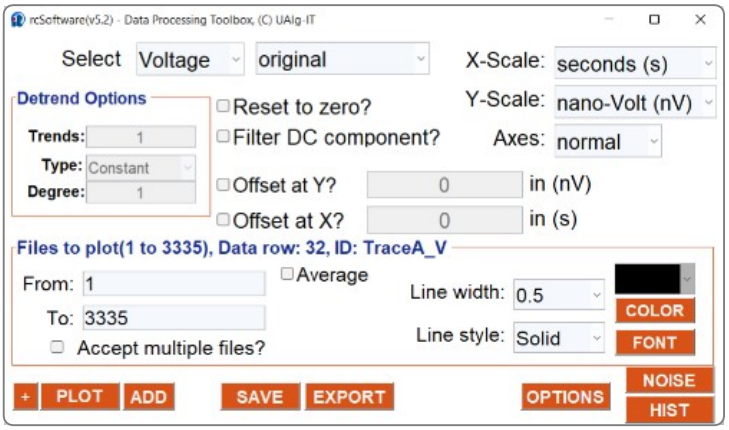


(c)

**Figure 3.10 –** Layouts of the graphical user interface (GUI) of the *rcSoftware* toolkits. (**a**) Data acquisition toolkit (DAT). (**b**) Data collection toolkit (DCT). (**c**) Data processing toolkit (DPT).

structures (NADS). Third, module (3) consists of the Data Processing Toolbox (DPT) shown in Figure 3.10 (c), which contains a set of tools for: (i) preprocessing the data with filters, (iii) visualizing the recorded data, and (iii) performing time series and statistical analysis.

## 3.13 – Summary

In this section, the four types of transducer devices used for electrophysiological measurements are described. One of the transducers was constructed using solely organic materials, with BC serving as the scaffold material and standard inkjet print technique utilized to deposit patterned PEDOT:PSS electrodes. Gold electrodes were also deposited on BC with the same patterns as those used on the PEDOT:PSS electrodes, which were used to provide a comparison with the PEDOT:PSS electrodes. In order to broaden the scope of electrode characterization, different electrodes based on both gold and PEDOT:PSS electrodes were patterned on glass, PET, and BC. To aid readers in understanding the differences between the electrode designs, a summary of all electrode parameters, including electrode aspect ratio, materials, and substrate, is provided Table 3.2.

Two methods were employed to extract the values of the circuit $R_{DC}$ and $R_{DL}$ that describe the electrical double-layer. The first method involved fitting the impedance versus frequency curve, while the second method involved measuring the displacement current at different speeds upon applying voltage ramps.

The ultra-low noise system used to amplify, filter, and record ultra-weak extracellular signals and analyze the noise spectrum of transducer devices was detailed. The chapter concludes with a description of the software developed to control and process the data measured by the ultra-low noise system.

**Table 3.2 –** Description of electrode shapes, design, and dimensions, as well of the substrate materials.

| Representation | Shape | Design | Dimensions | Area ($A_e$) | Substrate |
|---|---|---|---|---|---|
| 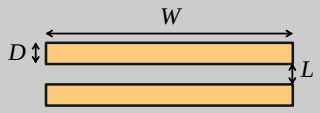 | Planar finger shape | Parallel electrodes | – Length ($W$)<br>– Depth ($L$)<br>– Gap ($D$) | $2 \times L \times W$ | – Glass<br>– Bacterial cellulose<br>– PET |
| 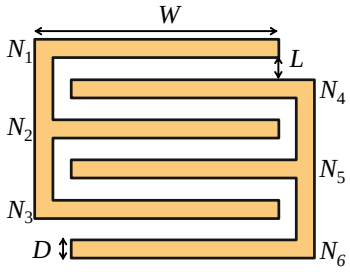 | Planar finger shape | Inter-digitated electrodes | – Length ($W$)<br>– Depth ($L$)<br>– Gap ($D$)<br>– Finger number ($N_n$) | $L \times W \times \Sigma N_n$ | – Silicon wafer<br>– PET |
| 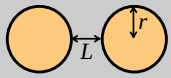 | Planar circular shape | Parallel electrodes | – Diameter ($Ø = 2r$)<br>– Gap ($D$) | $\pi \times r^2$ | – Glass<br>– PET |

# References


1. Gudur, A.; Ji, H.-F. Bio-Applications of Nanopillars. *Front. Nanosci. Nanotechnol.* **2016**, *2*, 1–10, doi:10.15761/fnn.1000140.
2. Xie, C.; Lin, Z.; Hanson, L.; Cui, Y.; Cui, B. Intracellular recording of action potentials by nanopillar electroporation. *Nat. Nanotechnol.* **2012**, *7*, 185–190, doi:10.1038/nnano.2012.8.
3. Xie, C.; Hanson, L.; Xie, W.; Lin, Z.; Cui, B.; Cui, Y. Noninvasive neuron pinning with nanopillar arrays. *Nano Lett.* **2010**, *10*, 4020–4024, doi:10.1021/nl101950x.
4. Rabieh, N.; Ojovan, S.M.; Shmoel, N.; Erez, H.; Maydan, E.; Spira, M.E. On-chip, multisite extracellular and intracellular recordings from primary cultured skeletal myotubes. *Sci. Rep.* **2016**, *6*, 36498, doi:10.1038/srep36498.
5. Hai, A.; Shappir, J.; Spira, M.E. Long-Term, Multisite, Parallel, In-Cell Recording and Stimulation by an Array of Extracellular Microelectrodes. *J. Neurophysiol.* **2010**, *104*, 559–568, doi:10.1152/jn.00265.2010.
6. Mestre, A.L.G.A.L.G.; Cerquido, M.; Inácio, P.M.C.P.M.C.; Asgarifar, S.; Lourenço, A.S.A.S.; Cristiano, M.L.S.M.L.S.; Aguiar, P.; Medeiros, M.C.R.M.C.R.; Araújo, I.M.I.M.; Ventura, J.; et al. Ultrasensitive gold micro-structured electrodes enabling the detection of extra-cellular

long-lasting potentials in astrocytes populations. *Sci. Rep.* **2017**, *7*, 1–11, doi:10.1038/s41598-017-14697-y.

7. Ojovan, S.M.; Rabieh, N.; Shmoel, N.; Erez, H.; Maydan, E.; Cohen, A.; Spira, M.E. A feasibility study of multi-site,intracellular recordings from mammalian neurons by extracellular gold mushroom-shaped microelectrodes. *Sci. Rep.* **2015**, *5*, 14100, doi:10.1038/srep14100.
8. Lee, J.Y.; Bashur, C.A.; Goldstein, A.S.; Schmidt, C.E. Polypyrrole-coated electrospun PLGA nanofibers for neural tissue applications. *Biomaterials* **2009**, *30*, 4325–4335, doi:10.1016/j.biomaterials.2009.04.042.
9. Liang, D.; Hsiao, B.S.; Chu, B. Functional electrospun nanofibrous scaffolds for biomedical applications. *Adv. Drug Deliv. Rev.* **2007**, *59*, 1392–1412, doi:10.1016/j.addr.2007.04.021.
10. Erbas Kiziltas, E.; Kiziltas, A.; Rhodes, K.; Emanetoglu, N.W.; Blumentritt, M.; Gardner, D.J. Electrically conductive nano graphite-filled bacterial cellulose composites. *Carbohydr. Polym.* **2016**, *136*, 1144–1151, doi:10.1016/j.carbpol.2015.10.004.
11. Miao, Y.-E.; Liu, T. Electrospun Nanofiber Electrodes. In *Electrospinning: Nanofabrication and Applications*; Elsevier, 2019; pp. 641–669.
12. Valtakari, D.; Liu, J.; Kumar, V.; Xu, C.; Toivakka, M.; Saarinen, J.J. Conductivity of PEDOT : PSS on Spin-Coated and Drop Cast Nanofibrillar Cellulose Thin Films. *Nanoscale Res. Lett.* **2015**, doi:10.1186/s11671-015-1093-y.
13. Khan, S.; Ul-Islam, M.; Khattak, W.A.; Ullah, M.W.; Park, J.K. Bacterial cellulose-poly(3,4-ethylenedioxythiophene)-poly(styrenesulfonate) composites for optoelectronic applications. *Carbohydr. Polym.* **2015**, *127*, 86–93, doi:10.1016/j.carbpol.2015.03.055.
14. Khan, S.; Ul-Islam, M.; Ullah, M.W.; Israr, M.; Jang, J.H.; Park, J.K. Nano-gold assisted highly conducting and biocompatible bacterial cellulose-PEDOT:PSS films for biology-device interface applications. *Int. J. Biol. Macromol.* **2018**, *107*, 865–873, doi:10.1016/j.ijbiomac.2017.09.064.
15. Trovatti, E.; Serafim, L.S.; Freire, C.S.R.; Silvestre, A.J.D.; Neto, C.P. Gluconacetobacter sacchari: An efficient bacterial cellulose cell-factory. *Carbohydr. Polym.* **2011**, *86*, 1417–1420, doi:10.1016/j.carbpol.2011.06.046.
16. Shirakawa, H.; Louis, E.J.; MacDiarmid, A.G.; Chiang, C.K.; Heeger, A.J. Synthesis of electrically conducting organic polymers: halogen derivatives of polyacetylene, (CH) x. *J. Chem. Soc. Chem. Commun.* **1977**, 578–580, doi:10.1039/c39770000578.
17. Tourillon, G.; Garnier, F. New electrochemically generated organic conducting polymers. *J. Electroanal. Chem. Interfacial Electrochem.* **1982**, *135*, 173–178, doi:10.1016/0022-0728(82)90015-8.

18. Heywang, G.; Jonas, F. Poly(alkylenedioxythiophene)s—new, very stable conducting polymers. *Adv. Mater.* **1992**, *4*, 116–118, doi:10.1002/adma.19920040213.
19. Corradi, R.; Armes, S.P. Chemical synthesis of poly(3,4-ethylenedioxythiophene). *Synth. Met.* **1997**, *84*, 453–454, doi:10.1016/S0379-6779(97)80828-4.
20. AGFA-Gevaert NV Printed Conductors - Specialty Products Available online: https://www.agfa.com/specialty-products/solutions/conductive-materials/printed-conductors/ (accessed on May 5, 2022).
21. AGFA-Gevaert NV *ORGACON TM Transparent Conductive Inkjet Ink: IJ-1005*;
22. AGFA-Gevaert NV *Jetting instructions for ORGACON TM IJ-1005*;
23. FUJIFILM Dimatix, I. *Dimatix® Materials Printer DMP-2850: System Description*; Santa Clara, 2021;
24. 8W1E (8 Well PET) – Applied BioPhysics Inc. Available online: https://applied-biophysics-inc.myshopify.com/products/8w1e-pet-8-well-array (accessed on Apr 22, 2022).
25. 8W20idf PET (8 Well PET) – Applied BioPhysics Inc. Available online: https://applied-biophysics-inc.myshopify.com/collections/8-well-pet-arrays/products/8wcp-pc-8w20idf-8-well-array (accessed on Apr 22, 2022).
26. Gencontech Laser Marking Spirit LS Laser Engraver | GCC provides Laser Engravers, Vinyl Cutters, and UV Printers Available online: https://www.gccworld.com/product/laser-engraver-supremacy/spirit-ls (accessed on May 7, 2022).
27. Sarstedt AG & Co. KG Tissue culture dish, (ØxH): 35 x 10 mm, surface: Standard Available online: https://www.sarstedt.com/en/products/laboratory/cell-tissue-culture/cultivation/product/83.3900/ (accessed on May 7, 2022).
28. Heraeus Electronics AW-99 Gold Bonding Wire for the Most Demanding Looping and Finest Pad Pitch.
29. Heraeus Electronics Heraeus Electronics - Gold Bonding Wires Available online: https://www.heraeus.com/en/het/products_and_solutions_het/bonding_wires/gold_bw/gold_bw_page.html (accessed on May 7, 2022).
30. Electrolube Silver conductive paint (SCP) Available online: https://electrolube.com/product/scpsilver-conductive-paint/ (accessed on May 7, 2022).
31. Medeiros, M.C.R.; Mestre, A.; Inácio, P.; Asgarif, S.; Araújo, I.M.; Hubbard, P.C.; Velez, Z.; Cancela, M.L.; Rocha, P.R.F.; de Leeuw, D.M.; et al. An electrical method to measure low-frequency collective and synchronized cell activity using extracellular electrodes. *Sens. Bio-Sensing Res.* **2016**, *10*, doi:10.1016/j.sbsr.2016.06.002.
32. Rocha, P.R.F.; Medeiros, M.C.R.; Kintzel, U.; Vogt, J.; Araújo, I.M.; Mestre, A.L.G.;

Mailänder, V.; Schlett, P.; Dröge, M.; Schneider, L.; et al. Extracellular electrical recording of pH-triggered bursts in C6 glioma cell populations. *Sci. Adv.* **2016**, *2*, e1600516, doi:10.1126/sciadv.1600516.

33. Rocha, P.R.F.; Schlett, P.; Schneider, L.; Drö, M.; Mailä, V.; Gomes, H.L.; Blom, P.W.M.; De Leeuw, D.M. Low frequency electric current noise in glioma cell populations. *J. Mater. Chem. B* **2015**, *3*, 5035–5039, doi:10.1039/c5tb00144g.
34. Rocha, P.R.F.; Silva, A.D.; Godinho, L.; Dane, W.; Estrela, P.; Vandamme, L.K.J.; Pereira-Leal, J.B.; de Leeuw, D.M.; Leite, R.B. Collective electrical oscillations of a diatom population induced by dark stress. *Sci. Rep.* **2018**, *8*, 5484, doi:10.1038/s41598-018-23928-9.
35. Asgarifar, S.; Mestre, A.L.G.; Félix, R.C.; Inácio, P.M.C.; Cristiano, M.L.S.; Medeiros, M.C.R.; Araújo, I.M.; Power, D.M.; Gomes, H.L. Biosensors and Bioelectronics Extracellular electrophysiological based sensor to monitor cancer cells cooperative migration and cell-cell connections. *Biosens. Bioelectron.* **2019**, *145*, 111708, doi:10.1016/j.bios.2019.111708.
36. Szendro, P.; Vincze, G.; Szasz, A. BIO-RESPONSE TO WHITE NOISE EXCITATION. *Electro- and Magnetobiology* **2001**, *20*, 215–229, doi:10.1081/JBC-100104145.
37. Stanford Research Systems (SRS). Low Noise Voltage Preamplifier - SR560 Available online: https://www.thinksrs.com/products/sr560.htm (accessed on Jan 20, 2022).
38. Stanford Research Systems (SRS). Low Noise Current Preamplifier - SR570 Available online: https://www.thinksrs.com/products/sr570.htm (accessed on Jan 20, 2022).
39. Keysight Technologies. 35670A FFT Dynamic Signal Analyzer, DC-102.4 kHz | Keysight Available online: https://www.keysight.com/zz/en/product/35670A/fft-dynamic-signal-analyzer-dc1024-khz.html (accessed on Jan 20, 2022).
40. Rothman, J.S.; Silver, R.A. Neuromatic: An integrated open-source software toolkit for acquisition, analysis and simulation of electrophysiological data. *Front. Neuroinform.* **2018**, *12*, 14, doi:10.3389/FNINF.2018.00014/BIBTEX.
41. Imfeld, K.; Neukom, S.; Maccione, A.; Bornat, Y.; Martinoia, S.; Farine, P.A.; Koudelka-Hep, M.; Berdondini, L. Large-scale, high-resolution data acquisition system for extracellular recording of electrophysiological activity. *IEEE Trans. Biomed. Eng.* **2008**, *55*, 2064–2073, doi:10.1109/TBME.2008.919139.
42. Putzeys, J.; Raducanu, B.C.; Carton, A.; De Ceulaer, J.; Karsh, B.; Siegle, J.H.; Van Helleputte, N.; Harris, T.D.; Dutta, B.; Musa, S.; et al. Neuropixels Data-Acquisition System: A Scalable Platform for Parallel Recording of 10 000+ Electrophysiological Signals. *IEEE Trans. Biomed. Circuits Syst.* **2019**, *13*, 1635–1644, doi:10.1109/TBCAS.2019.2943077.
43. Mannatunga, K.S.; Ali, S.H.M.; Crespo, M.L.; Cicuttin, A.; Samarawikrama, J.G. High

Performance 128-Channel Acquisition System for Electrophysiological Signals. *IEEE Access* **2020**, *8*, 122366–122383, doi:10.1109/ACCESS.2020.3007082.

44. Suter, B.A.; O'Connor, T.; Iyer, V.; Petreanu, L.T.; Hooks, B.M.; Kiritani, T.; Svoboda, K.; Shepherd, G.M.G. Ephus: Multipurpose data acquisition software for neuroscience experiments. *Front. Neural Circuits* **2010**, *4*, 100, doi:10.3389/FNCIR.2010.00100/BIBTEX.
45. Keysight Technologies. Electronic design, test automation & measurement equipment | Keysight. Available online: https://www.keysight.com/zz/en/home.html (accessed on Mar 16, 2022).
46. Eggplant software. Eggplant Homepage. Available online: https://www.eggplantsoftware.com/ (accessed on Mar 16, 2022).
47. Keysight Technologies. Keysight VEE Pro 9.32. Available online: https://www.meilhaus.de/en/vee-pro.htm (accessed on Mar 19, 2022).
48. Keysight Technologies. 35670A DataLink | Keysight. Available online: https://www.keysight.com/zz/en/lib/software-detail/computer-software/35670a-datalink-1425653.html (accessed on Mar 16, 2022).
49. Grant, G.B.; Werblin, F.S. Low-cost data acquisition and analysis programs for electrophysiology. *J. Neurosci. Methods* **1994**, *55*, 89–98, doi:10.1016/0165-0270(94)90044-2.
50. Pratt, M. The Pros and Cons of Developing Your Own Software Versus Outsourcing. Available online: https://www.business.org/software/apps/the-pros-and-cons-of-developing-your-own-software-versus-outsourcing/ (accessed on Jan 19, 2022).
51. Ustinov, N. Building An In-House Solution Vs. Buying Software: Pros And Cons To Consider Available online: https://www.forbes.com/sites/forbestechcouncil/2021/07/29/building-an-in-house-solution-vs-buying-software-pros-and-cons-to-consider/ (accessed on Jan 19, 2022).
52. Wang, S.; Han, H.; Gao, K.; Wang, Z.; Zhang, C.; Yang, M.; Wu, Z.; Wu, Z. A user-friendly LabVIEW software platform for grating based X-ray phase-contrast imaging. *J. Xray. Sci. Technol.* **2015**, *23*, 189–199, doi:10.3233/XST-150480.
53. Morse, D.H.; Antolak, A.J.; Bench, G.S.; Roberts, M.L. A flexible LabVIEW$^{TM}$-based data acquisition and analysis system for scanning microscopy. *Nucl. Instruments Methods Phys. Res. Sect. B Beam Interact. with Mater. Atoms* **1999**, *158*, 146–152, doi:10.1016/S0168-583X(99)00507-8.
54. Kirkman, I.W.; Buksh, P.A. Data acquisition and control using National Instruments' "LabVIEW" software. *Rev. Sci. Instrum.* **1992**, *63*, 869–872, doi:10.1063/1.1142631.
55. Muyskens, M.A.; Glass, S. V.; Wietsma, T.W.; Gray, T.M. Data Acquisition in the Chemistry Laboratory Using LabVIEW Software. *J. Chem. Educ.* **1996**, *73*, 1112,

doi:10.1021/ed073p1112.

56. Akam, T.; Walton, M.E. pyPhotometry: Open source Python based hardware and software for fiber photometry data acquisition. *Sci. Rep.* **2019**, *9*, 3521, doi:10.1038/s41598-019-39724-y.
57. Weber, S.J. PyMoDAQ: An open-source Python-based software for modular data acquisition. *Rev. Sci. Instrum.* **2021**, *92*, doi:10.1063/5.0032116.
58. Koerner, L.J.; Caswell, T.A.; Allan, D.B.; Campbell, S.I. A Python Instrument Control and Data Acquisition Suite for Reproducible Research. *IEEE Trans. Instrum. Meas.* **2020**, *69*, 1698–1707, doi:10.1109/TIM.2019.2914711.
59. Neto, A.; Fernandes, H.; Duarte, A.; Carvalho, B.B.; Sousa, J.; Valcárcel, D.F.; Hron, M.; Varandas, C.A.F. FireSignal-Data acquisition and control system software. *Fusion Eng. Des.* **2007**, *82*, 1359–1364, doi:10.1016/j.fusengdes.2007.02.016.
60. Nickell, S.; Förster, F.; Linaroudis, A.; Del Net, W.; Beck, F.; Hegerl, R.; Baumeister, W.; Plitzko, J.M. TOM software toolbox: Acquisition and analysis for electron tomography. *J. Struct. Biol.* **2005**, *149*, 227–234, doi:10.1016/j.jsb.2004.10.006.
61. Egert, U.; Knott, T.; Schwarz, C.; Nawrot, M.; Brandt, A.; Rotter, S.; Diesmann, M. MEA-Tools: An open source toolbox for the analysis of multi-electrode data with MATLAB. *J. Neurosci. Methods* **2002**, *117*, 33–42, doi:10.1016/S0165-0270(02)00045-6.
62. Sieczkowski, K.; Sondej, T. A method for real-time data acquisition using Matlab software. *Proc. 23rd Int. Conf. Mix. Des. Integr. Circuits Syst. Mix. 2016* **2016**, 437–442, doi:10.1109/MIXDES.2016.7529782.
63. Uppuluri, A. V.; Jost, R.J. MATLAB-based ERS SAR data acquisition and processing software for classroom use. *IEEE Natl. Radar Conf. - Proc.* **2004**, 524–528, doi:10.1109/nrc.2004.1316480.
64. Schultz, R.C.; Ives, R.W. Biometric data acquisition using MATLAB GUIs. *Proc. - Front. Educ. Conf. FIE* **2005**, *2005*, 1–5, doi:10.1109/fie.2005.1612189.
65. Asaad, W.F.; Eskandar, E.N. A flexible software tool for temporally-precise behavioral control in Matlab. *J. Neurosci. Methods* **2008**, *174*, 245–258, doi:10.1016/j.jneumeth.2008.07.014.
66. Keysight Technologies. 82357B USB/GPIB Interface High-Speed USB 2.0 | Keysight Available online: https://www.keysight.com/zz/en/product/82357B/usb-gpib-interface-high-speed-usb-2-0.html (accessed on Mar 16, 2022).
67. The MathWorks Inc. Matlab - system requirements - release 2014b, (2014) Available online: https://www.mathworks.com/content/dam/mathworks/mathworks-dot-com/support/sysreq/files/SystemRequirements-Release2014b_Windows.pdf (accessed on Jan 18, 2022).

68. Keysight Technologies. IO Libraries Suite Available online: https://www.keysight.com/zz/en/lib/software-detail/computer-software/io-libraries-suite-downloads-2175637.html (accessed on Jan 18, 2022).

# Chapter 4

# Biological cell cultures and Methods

Chapter 2 describes the biological cell cultures, the methods used for device characterization, and the methods for analysis of recorded extracellular signals. The first part of this chapter describes all the biological materials used, including information about the cells and the protocols for cell culture and handling. In the second part, this chapter is focused on describing the experimental procedures used for electrical characterization of the sensing electrodes, including, small-signal impedance, electrical noise, and electrophysiological measurements. The chapter concludes with a description of the methods used to analyze and process the weak signals.

## 4.1 – Biological cells and organs selected

One of the key aspects of this thesis is focused on the development and optimization of sensing electrodes that can be used for electrophysiological sensing in the millihertz frequency range. Our primary objective is to enhance the impedance, geometry, and area of the electrodes to obtain the highest possible Signal-to-Noise Ratio (SNR). Additionally, we aim to use these electrodes to measure bioelectrical activity that is generated by non-electrogenic cell populations. This presents a significant challenge as there is very limited information available regarding the nature of these signals. However, it is known that non-electrogenic cells can generate ionic fluctuations, which can be detected using extracellular electrodes. Typically, these ionic oscillations are measured using optical fluorescence probes. While it is possible to speculate that the duration of an ionic oscillation measured using an optical probe may be similar to the corresponding electrical oscillation detected using an extracellular electrode, this is merely a hypothesis. The shape of a bioelectrical signal generated by a population of non-electrogenic cells and recorded using extracellular electrodes remains largely unknown.

To optimize the newly developed electrodes for measuring non-electrogenic cells, it is crucial to first characterize them using standard and well-known biological signal sources. In this regard, we have selected Zebrafish hearts as an ideal biological signal source for evaluation and benchmarking of our newly developed electrodes. Zebrafish hearts are easy to handle, generate reliable and well-defined action potentials (cardiac signals) and are small enough (3mm long) to be positioned in a small

electrode. Therefore, they provide an excellent floating biological signal source for evaluating the performance of our electrodes.

Having optimize and validate the sensing electrodes using the zebrafish hearts we are now ready to explore the electrodes in more challenging recordings. One particularly interesting recording involves measuring the cardiac beatings of embryoid bodies (EBs). EBs are collections of pluripotent cells that, through physiological stimuli, can be stimulated to differentiate into cardiac muscle cells, that is, into cardiomyocyte cells. It is noteworthy that EBs are composed of cardiomyocytes. The main difference between EBs and a zebrafish heart is the number of cells that contribute to the generation of the AP. In simpler terms, EBs are small cell clusters with just a few hundred cells that can organize to produce a cardiac beating, just like an ultra-small heart.

However, since only a small portion of the EB is beating, the corresponding AP signal is often weak and difficult to detect. As a result, EBs are an appropriate biological entity to demonstrate the detection limits of our electrodes and recording system. In addition, we can control the frequency of the beating by using drugs such as adrenaline to increase the rate or verapamil to lower it. This adds an additional degree of freedom in the validation process of our sensing electrodes.

To evaluate our system in the high frequency domain we also use neurons as testing cells. Neurons generate action potentials that are just a few milliseconds long and are commonly referred to as spikes. For this purpose we choose mouse neuroblasts (Neuro-2A cells), which is a commercial immortalized cell line. However electrophysiological results are not presented here because the emphasis of this thesis is in recording low frequency bioelectrical signals.

Furthermore, we opted to measure populations of rat fibroblasts (C6 cells) in our study. C6 cells are glial cells that are isolated from the brain of a rat with glioma. Glial cells have the unique ability to establish cell-cell junctions and synchronize their physiological functions using endogenous $Ca^{2+}$ elevations or oscillatory currents (i.e., ion gradients) that can be measured using extracellular electrodes. C6 cell cultures are both robust and easy to handle and are commonly used in *in vitro* studies as reported in the literature. It is important to mention here that immortal cell cultures, also known as clonal cells or cell lines, are cells that can proliferate indefinitely either by an artificial process or spontaneously, as in the case of cancer cells. An immortal cell line is best suited for *in vitro* routine studies because of the low variability between newborn cells in repeated cultures. Primary cultures are cells harvested directly from explants of a living organism that have been exposed extensively to a specific nutritional condition to allow them to thrive and develop a senescent phenotype. The major disadvantage of primary cultures is their batch-to-batch variability and shorter lifespan compared to immortalized cell cultures.

To fully evaluate the capabilities of our electrodes, we also employed them to measure ex-vivo tissues. Unlike 2D cell cultures, tissues are 3D structures consisting of several types of cells, including neurons and other cell types, organized in a complex and realistic biological entity. Therefore, the use of tissue samples is crucial to validate if the signals measured in 2D cell cultures are representative of the ones measured in a more complex biological system. A high-grade human glioblastoma multiform (hGBM) tumor samples from biopsies was chosen because it was readily available from the Centro Hospitalar Universitário do Algarve. Electrophysiological measurements carried out in the tumor samples is briefly discussed in the last chapter in the context of suggestion for further work. The electrophysiological activity of tumor samples is believed to induce seizures in [1], [2].

### 4.1.1 – C6 cells, CCL-107™

Rat fibroblast cells (C6 cells) were purchased from the America Type Culture Collection (ATCC) Organization, Manassas, Virginia, USA [12]. The C6 cells were derived from a glial cell strain cloned from a rat glial tumor. C6 glioma cells usually have an irregular, flattened shape. They are usually characterized by a typical bipolar fibroblast-like morphology [15]. C6 cells were grown in culture plates containing Kaighn's Modification of Ham's F–12 medium (F–12K medium) supplemented with 15% fetal horse serum (FHS), 2.5% fetal bovine serum, and 1% penicillin and streptomycin and maintained in a humidified atmosphere at 5% CO2 and 37 °C. During the 96-hour growth period, the medium was changed once every 48 hours. Then the cells were harvested and transferred to the sensing device using the suspension method. Cells were removed from the culture plates using a cell scraper and diluted in 400 (L of culture medium to obtain a cell suspension containing between 50k and 300k cells. The cell suspension was used to seed the cells on the surface of the transducer. It usually takes 2 hours for C6 cells to settle on the surface. Figure 4.1 (b) shows a microscopic image of a C6 cell culture.

Ana Mestre, Rita Monteiro, and Dr. Rute Félix were the only individuals responsible to care, handle and prepare cell cultures for experiments.

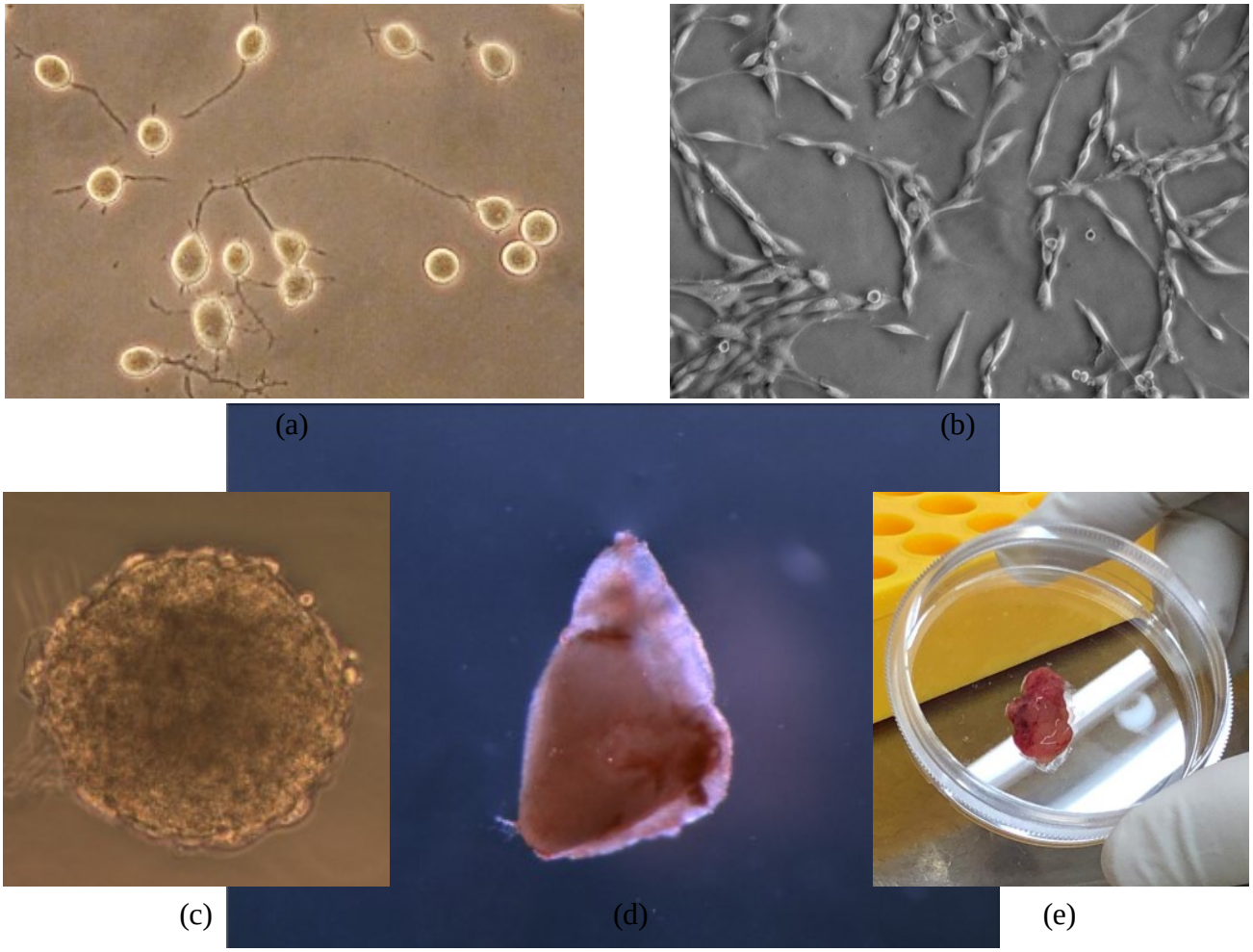


**Figure 4.1 –** Photographs of the biological material used in this work. (**a**) Neuro-2a cells. (**b**) C6 cells. (**c**) Embryoid body (EB) of cardiomyocyte cells. (**d**) Zebrafish heart in supension on Krebs medium. (**e**) Human glioblastoma multiforme (hGBM) tumor tissue.

### 4.1.2 – Neuro-2a cells, CCL-131™

Mouse neuroblast cells (Neuro-2a cells) were purchased from the America Type Culture Collection (ATCC) Organization, Manassas, Virginia, USA [5]. Neuro-2a cells are mouse neuroblasts with neuronal and amoeboid stem cell morphology isolated from a spontaneous tumor of a strain A albino mouse. Neuro-2a cells were grown in culture plates containing Dulbecco's Modified Eagle Medium (DMEM) with 10% fetal bovine serum (FBS) and 1% penicillin and streptomycin and maintained in a humidified atmosphere at 5% CO2 and 37°C. The same protocol previously described for C6 cells was used to grow, harvest, and suspend Neuro-2a cells. Figure 4.1 (a) shows a microscopic image of a Neuro-2a cell culture.

Ana Mestre was the only individual responsible to care, handle and prepare cell cultures for experiments.

### 4.1.3 – Embryoid Bodies (EBs)

Cardiomyocyte EBs consist of differentiated mouse embryonic stem cells (mESCs) [6]. mESCs were differentiated by the hanging drop method in mESC culture medium containing 20% FBS (differentiation medium). The differentiation protocol of mESC to cardiomyocyte cells was the same as described and detailed in the work of Fuegemann, C.J. [7]. Briefly, 100 cells were cultured for 48 hours in 20 µL hanging drops of differentiation medium to initiate the formation of EBs. Subsequently, the EBs were grown in suspension in differentiation medium in a bacterial Petri dish for 3 days before being transferred to the sensor devices. Each EB has an average diameter that varies between 300 and 400 µm [8]. Transfer of the EBs from the Petri dish cultures to the sensor electrodes was performed using a hand scraper to detach the EBs and a micropipette to transfer and position the EBs onto the transducer electrode. Figure 4.1 (c) shows a micrograph of an EB with cardiomyocyte cells attached to the Petri dish.

EBs were kindly provided by Prof. Dr. José Bragança, Algarve Biomedical Center Research Institute - ABC-RI, Portugal, Portugal. Dr João Santos and Dr Leonardo Silva were the only individuals responsible for the culture and handling of the differentiation of mESCs into cardiomyocyte cells, and I express my gratitude for their tireless cooperation.

### 4.1.4 – Zebrafish Hearts

Wild-type zebrafish (Danio rerio) of the strain AB that were three to six months old (3−4 cm standard length, 2.0−3.0 g) and sexually mature were used for this work. Fish were maintained at 26−28 °C with a 14/10 light:dark photoperiod and fed dried brine shrimp (Artemia salina) twice daily at 11:00 and 18:00 [28]. Zebrafish were anesthetized and sacrificed by immersion in water with an overdose of 300 mg/L ethyl 3-aminobenzoate methanesulfonate salt (MS222). The hearts of zebrafish were surgically removed and placed in Krebs solution (400 µL) at 24 ºC. Under these conditions, the hearts continued to beat for up to 24 hours. The heart of an adult zebrafish is about 1 mm in size and beats about twice per second. The care of the fish and the experiments complied with national legislation for the use of laboratory animals under a Group 1 license issued by the General Veterinary Directorate of the Portuguese Ministry of Agriculture, Rural Development and Fisheries. Zebrafish hearts were handled with a micropipette and positioned on the sensor electrodes. Figure 4.1 (d) shows a microscopic image of a zebrafish heart culture.

The zebrafish hearts were kindly provided by Dr. Peter Hubbart, Centro de Ciências do Mar (CCMAR), Universidade do Algarve, Faro, Portugal. He was the only responsible person licensed

under the Group 1 license to care for, handle, and perform surgical procedures on the animals. All zebrafish hearts were surgically removed to perform *ex-vivo* studies.

### 4.1.5 – Human Glioblastoma Multiforme (hGBM) tumor tissues

Tissue samples of hGBM tumor were obtained from biopsies of high-grade hGBM (HGG). Tissues were maintained in DMEM medium containing 10% FBS and 1% penicillin and streptomycin. The tissues were cut with a surgical scalpel into small structures that fit into the surface of the transducer devices. Figure 4.1 (e) shows a photograph of a tissue sample from the hGBM tumor.

All samples of hGBM tumor tissue were obtained from biopsies of high-grade hGBM (HGG) and were kindly provided by a team of neurosurgeons Dr. Clara Romero and Dr. Artur B. Lourenço from nearby Faro Hospital, Portugal. They were the only individuals responsible for surgery and handling tumor tissues. In the University of the Algarve research facilities, either Ana Mestre or Rita Monteiro were the only individuals responsible to care, prepare and handle the tumor tissues for experiments, always under supervision of Dr. Patrícia A. Madureira. The declaration of ethics follows attached to this thesis at page x.

### 4.1.6 – Sterilization and coating procedures

The entire system, which includes the transducer unit mounted on the mechanical structure, was always irradiated with ultraviolet (UV) radiation ($\lambda = 265$ nm) in a laminar flow hood for 15 minutes for sterilization before biological material was applied. Because the mechanism of cell-electrode coupling is of paramount importance to improve signal detection, coatings of poly-L-lysine solution (0.01%) from Sigma-Aldrich, St. Louis, Missouri, EEA, were prepared to promote cell adhesion to the transducer surface after UV irradiation. On silica-based substrates, UV irradiation was useful to decrease the contact angle of water, making the surface hydrophilic [29,30] and consequently more receptive to the chemical bonds of the poly-L-lysine coating and cells. The poly-L-lysine coatings consist of covering the entire surface of the transducer with the poly-L-lysine solution for 5 minutes. Then the poly-L-lysine solution is removed, washed twice with sterile water, and kept in a laminar flow hood for 2 hours.

Ana Mestre was the only individual responsible to perform sterilization and coating procedures.

# 4.2 – Electrical procedures

All electrical measurements were always made with the device assembled in the mechanical support and placed inside a die-cast aluminum housing with insulated BNC connectors to connect the electrodes to the instrumentation (see Figure 3.7 (a) and Figure 3.8 (b)). Figure 4.2 shows a schematic diagram of the connections between the transducer and the recorder.

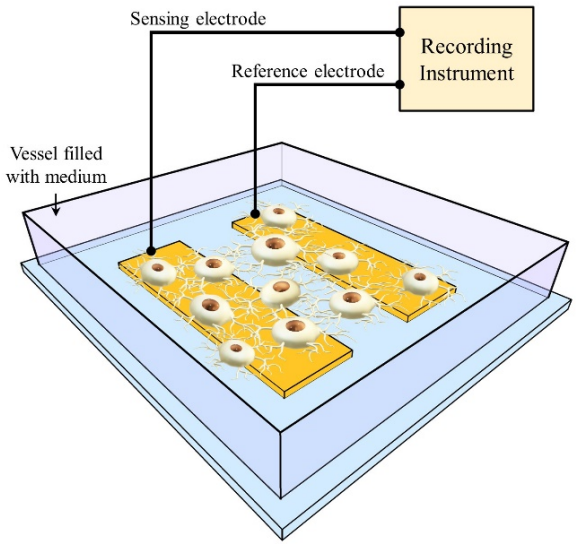


**Figure 4.2 –** Schematic diagram of the electrodes connected to the recording instrumentation.

## 4.2.1 – Impedance measurements

Impedance measurements were made using a Fluke PM6306 LCR meter from Fluke Corporation, Everett, Washington, USA. A self-developed software called RCL, which runs only on Microsoft computers DOS, was used to remotely control, and perform all measurements in this work. There are only a few general settings that were the same when setting up the Fluke regardless of the type of experiment, such as the test signal, test circuit, and measurement mode. The test signal used was a voltage field with an amplitude of 50 mV AC and a bias component of 0 V DC. The test circuit used was a parallel resistor-capacitor admittance circuit ($R_P \parallel C_P$). Continuous mode was used as the measurement mode, with the average function disabled. For impedance spectral analysis, a set of 50 predetermined test frequencies with a logarithmic distribution from 50 Hz to 1 MHz was always used. As with the transient impedance analysis, the test frequency was selected manually depending on the requirements of the experiment.

### 4.2.2 – Cyclic voltammetry measurements

Current measurements of transient response on voltage ramps with different step rates (d*v*/d*t*) were performed using a Keithley 487 Source Meter from Keithley Instruments Inc. in Cleveland, Ohio, USA. In-house developed software called FET, which runs only on Microsoft DOS computers, was used to remotely control and perform all measurements in this work. The FET was a critical part of the cyclic voltammetry measurements because the Keithley voltage source had to be remotely controlled to increase the ramp amplitude at a fixed rate. Although the Keithley 487 can provide a voltage as low as 0.2 mV, the routines from FET limit the minimum voltage step value to 0.5 mV. In general, the cyclic voltammetry measurements were made with voltage ramps of 100 mV at a rate of change of voltage with respect to time (d*v*/d*t*) of 0.5 mV. Only in cases where the equilibrium current at 100 mV was not reached, the amplitude of the voltage ramp was increased by 100 mV until an equilibrium current was reached.

### 4.2.3 – Spectral noise measurements

Spectral noise measurements were made using the setup described in Chapter 3 and recorded using the *rcSoftware* data acquisition toolbox (DAT) described in Appendix A. All noise spectra reported in this thesis were performed using the procedure described here. First, the DUT was positioned in a die-cast aluminum housing and connected to the insulated BNC connectors. Then, the DUT was connected to the voltage or current LNA connected to DSA input channel 1 via a 1-m-long low-noise coaxial cable. Before and after performing noise spectrum measurements, an impedance spectrum was always obtained to determine the resistive and capacitive frequency dependence of the transducer interface, which is necessary to understand the noise spectrum measurements as well as to adjust the LNA gain. Regardless of the LNA used, all settings related to the LNAs and the DSA were remotely controlled via DAT, except for the setting of the DC offset potentiometer at the front end of the SR560 LNA, which must be manually adjusted. For the measurement of spectral noise of voltage or current, the gain or sensitivity of the amplifier was selected according to the impedance of the transducer via DAT. Both the SR560 and the SR570 LNA were set for low-noise operation. As for the DSA, except for the spectral sweep, the same basic configurations were always used for the spectral noise measurements via DAT. As with the basic DSA settings, DAT was set to always record the time and frequency dependence of DSA input channel 1. Trace A always records the time dependence and Trace B records the frequency dependence in units of power spectrum density (PSD). The PSD was calculated using a rectangular window FFT with a fixed resolution of 4096 samples per window, which corresponds to

the frequency resolution of 1600 samples defined in DAT. DAT was configured to perform an autonomous spectral sweep in capture table mode. The capture table was populated with 15 entries to sweep the bandwidth of channel 1 in 15 bands, i.e., 6.25 Hz, 12.5 Hz, 25 Hz, 50 Hz, 100 Hz, 200 Hz, 400 Hz, 800 Hz, 1.6 kHz, 3.2 kHz, 6.4 kHz, 12.8 kHz, 25.6 kHz, 51.2 kHz, and 102.4 kHz. In addition, the Average option was enabled and set to 100 to have DSA return the calculated average noise spectral window. The final smooth spectra were obtained using a MATLAB script that summarizes the non-overlapping frequencies of each band. All frequency spans represent an average of at least 100 continuous recordings.

### 4.2.4 – Extracellular signal measurements

For the recording of the discrete extracellular signals, the same experimental setup and procedures were used as previously described for the measurement of spectral noise, including the basic configurations of the DAT. However, for recording discrete extracellular signals, it is necessary to set the DAT to perform measurements in specific time windows that are adjusted according to the type of extracellular signal. The typical time windows for recording signals such as APs and FPs generated by Neuro-2A cells, EBs from cardiomyocyte cells, and zebrafish hearts were 0.5 s, 1 s, 2 s, 4 s, 8 s, and 16 s, whereas time windows of 32 s, 64 s, 128 s, and 256 s were used for recording slowly varying ionic potential gradients scaled in seconds generated by C6 cells and hGBM tissue. Nevertheless, the range of DSA input channel 1 is of paramount importance for recording discrete extracellular signals. Normally, the DSA is set to handle the input range automatically when no human supervision is available during recording. The use of the automatic range mode is a safety measure to ensure that the optimal range is set according to the initial voltage level of input channel 1. However, when measuring slow time-varying signals, such as those generated by C6 cells and hGBM tumor samples, the signal amplitude increases over time, and in turn, the voltage level of input channel 1 is often exceeded in "Auto' mode, causing the unit ADC to overflow. For this reason, the range of input channel 1 must be set to a fixed range that doubles the amplitude of the signal. This process is not controlled by DAT, requiring human supervision.

## 4.3 – Analysis of extracellular signals

There are numerous published methods to analyze discrete signals generated by electrogenic cells (e.g. APs and FPs) because these signals are reproducible between different experimental trials, such as methods for analysis of changes in conduction velocity [12], spike train characteristics [13,14], beat frequency [15], signal shape [16], and functional classification of agents [15]. However, in non-

electrogenic cells, typical spontaneous activity is based on discrete extracellular signals that are not reproducible like the signals generated by electrogenic cells. The nature of spontaneous activity of non-electrogenic cells varies depending on cell type and external stimulus, such as changes in pH [36], $Ca^{2+}$ level [17–19], and inhibition of $K^{+}$, $Ca^{2+}$, and $Na^{+}$ channels [20]. Therefore, the principles of analysis of discrete extracellular signals generated by non-electrogenic cells must be approached in a manner that allows comparison of various parameters related to the signal shape from either a signal-to-signal or signal-to-sequence perspective.

The analysis methods described in this section were used to process the recorded data presented in later chapters. The analysis of the discrete extracellular signals was performed offline after completion of the experiments using the *rcSoftware* Data Processing Toolbox (DPT), the Noise Data Processing Toolbox (NDPT), and the Statistical Data Processing Toolbox (SDPT) described in Appendix A. Nevertheless, the use of MATLAB scripts and Microsoft Excel sheets were essential for performing statistical analyzes.

### 4.3.1 – Signal extraction

Voltage/current time traces recorded with *rcSoftware* DAT use interval recording windows. The window interval ($T$) can be changed, and the sampling resolution ($T_S$) is automatically determined by the DSA. Appendix C details how the DSA adjusts the sampling resolution based on the window interval. This information is useful for signal extraction because a discrete signal can be truncated between two or more windows (depending on the signal length and window period), and regardless of best efforts to minimize the delay between two consecutive windows, some information of the signal is permanently lost. Nevertheless, each time trace retains the timestamp of acquisition, so that all time traces can be arranged in a data matrix according to their original timestamp. This feature is important to extract some time-related information from the signal that must not be lost, such as the distance between two local maxima (peaks) or the signal length. Finally, the use of the recovered signal information may contribute to some statistical discrepancies.

The following sections describe in detail the signal information extracted from individual signals and signal sequences, and the statistical methods used to analyze them.

### 4.3.2 – Signal parameter extraction

Signal parameter extraction is divided into two classes: (i) signal-to-signal parameters and (ii) signal-to-sequence parameters. Signal-to-signal parameters characterize the information related to individual discrete signals, such as length ($T$), amplitude ($V$), area ($A$), and signal-to-noise ratio (SNR).

illustrates four individual signals that mimic the shape of typical discrete signals generated by non-electrogenic cells. It is worth noting that all signal parameters were analyzed using a baseline, as shown in Figure 4.3. Signals whose shape consists of a single upward or downward component, as shown in Figure 4.3 (a,b), are referred to as monophasic or single-phase signals; and signals whose shape consists of both upward and downward components, as shown in Figure 4.3 (c,d), are referred to as biphasic or two-phase signals.

The parameters extracted from the monophasic and biphasic signals were the amplitude of the upward (U) and/or downward (D) signal ($V_U$ or $V_D$), the length ($T_U$ or $T_D$), the area ($A_U$ or $A_D$), and the signal-to-noise ratio (SNR). The SNR was always determined as the ratio between the signal amplitude ($V_P$) and the baseline noise ($V_N$), i.e.., SNR = $V_P$ / $V_N$. For single-phase signals, $V_P$ is given by the $V_U$ or $V_D$ component; while for two-phase signals $V_P$ is given by the sum of the absolute value of $V_U$ and $V_D$ components, also known as the peak-to-peak amplitude value of the signal ($V_{PP}$), that is $V_P = V_{PP} = |V_U| + |V_D|$.

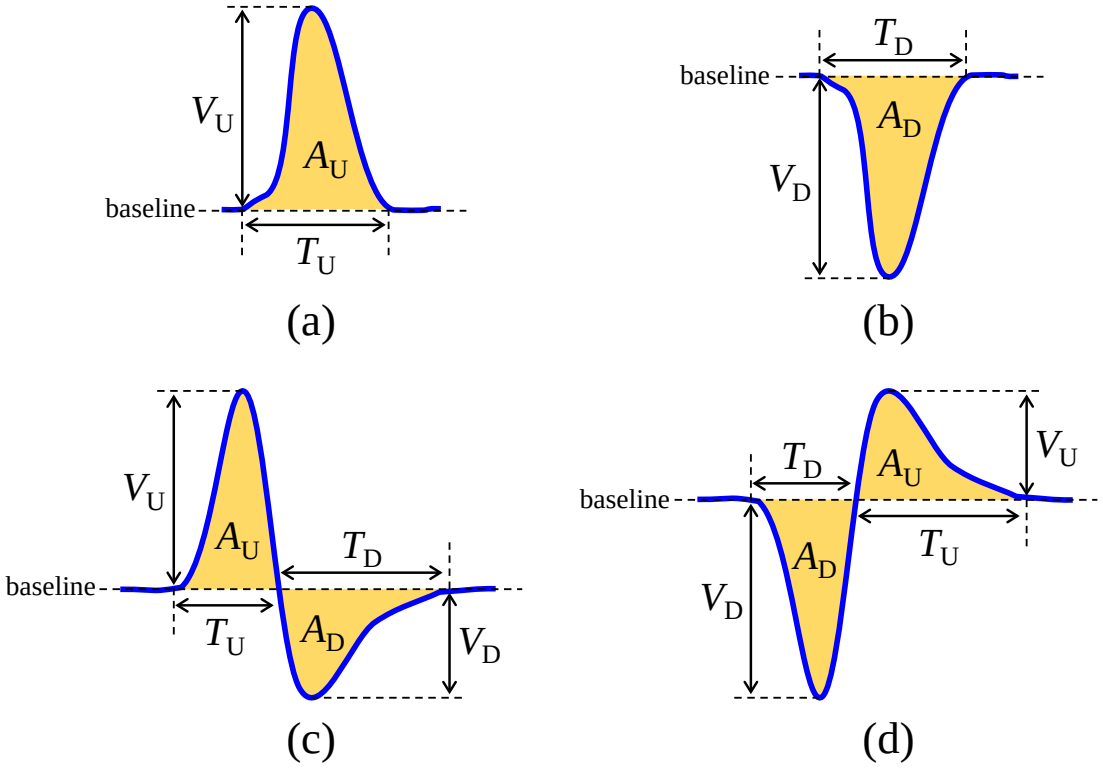


**Figure 4.3 –** Illustration of the signal shape of various discrete signals generated by nonelectrogenic cells and the parameters extracted from each signal as a function of baseline. (a,b) Single-phase signal characterized by rising and falling potential, respectively. (c,d) Two-phase signal characterized by an upward and a downward potential or vice versa. The yellow areas always represent the signal range of each upward (AU) and/or downward component (AD).

Signal-to-sequence parameters characterize the information related to sequences of discrete signals. In the measurement of discrete signals generated by cells, the parameters related to sequences of discrete signals are usually analyzed in terms of two consecutive local maxima (peaks) that share

the same polarization, such as the amplitude variation ($P$) and the inter-peak interval ($T_{IPI}$), later referred to as the inter-spike interval ($T_{ISI}$) or inter-beat interval ($T_{IBI}$). The amplitude variation ($P$) is a useful parameter for determining whether a signal sequence is amplitude modulated (AM) because it allows the discrete shape of the amplitude envelope to be extracted. The interval between peaks ($T_{ISI}$) refers to the frequency modulation of the signal (FM) and allows extracting information from the cell synchronization process. Figure 4.4 illustrates two examples of successive discrete signals as if they were recorded within a signal sequence.

The first example in Figure 4.4 (a), shows two successive single-phase signals consisting of an ascending potential. In this case, the peak-to-peak parameters are referred to as upward interval ($T_{UISI}$) and upward amplitude variation ($P_U$). The second example in Figure 4.4 (b) shows two consecutive biphasic signals consisting of a downward potential and an upward potential. In this case, the peak-to-peak parameters are referred to as the downward ($T_{DISI}$) or upward ($T_{UISI}$) inter-spike interval and the downward ($P_D$) or upward ($P_U$) amplitude variation. In any case, amplitude variation ($P$) is a useful parameter for determining whether a signal sequence is amplitude modulated (AM) because it allows the discrete shape of the amplitude envelope to be extracted. The interval between peaks ($T_{ISI}$) refers to the frequency modulation of the signal (FM) and allows extracting information from the cell synchronization process. Four types of signal sequences are commonly observed: (i) non-periodic sequences; (ii) quasi-periodic sequences; (iii) red-shift sequences (decrease in signal frequency); (iv) blue-shift sequences (increase in signal frequency).

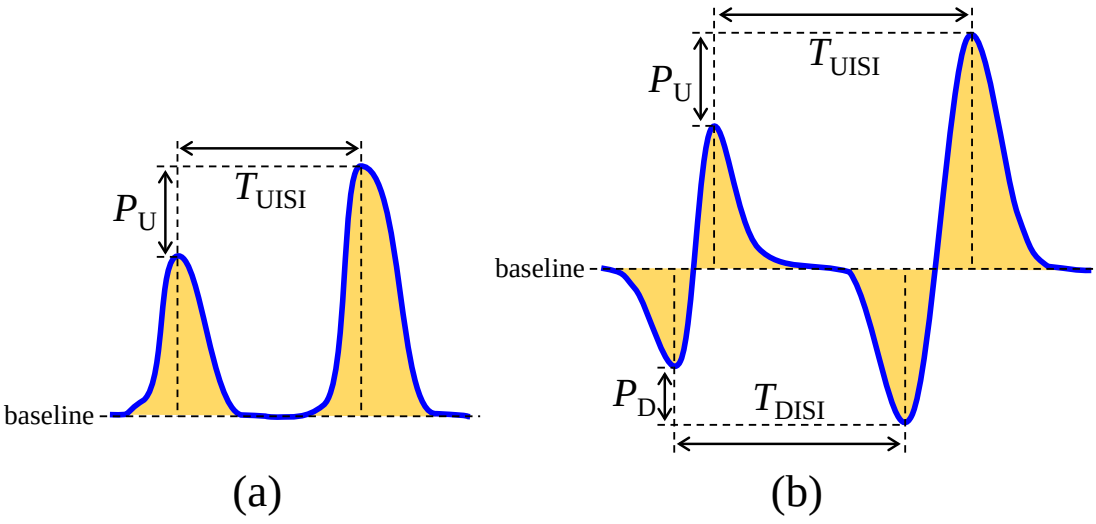


**Figure 4.4 –** Illustration of two examples of successive discrete signals as if they were recorded within a signal generated by non-electrogenic cells. (**a**) Sequence of monophasic signals characterized by an upward potential. (**b**) Sequence of biphasic signals characterized by a downward followed by an upward potential. The yellow areas always represent the signal range of each upward (AU) and/or downward component (AD).

The typical experimental procedure used in this work to extract the signal information was performed manually signal by signal, but using tools provided by the *rcSoftware* DPT such as. the use

of the Euclidean ruler (Tool 2), which allows to measure the maximum horizontal and vertical distances between two or three data samples; and the signal area (Tool 16), which allows to measure either the total or the biased component of the signal length (*T*), amplitude (*V*) and area (*A*). To estimate the SNR, the *rcSoftware* NDPT was used to determine the statistical noise amplitude, and the calculus of SNR were carried out manually using MATLAB code, despite the *rcSoftware* NDPT allows estimates the SNR and signal amplitude.

### 4.3.3 – Statistical analysis

After extracting the signal parameters, further processing is required to summarize the experimental results. In this work, statistical analysis of the parameters was typically performed using the high-level tools of the *rcSoftware* SDPT, even if the signal parameters were extracted manually. The main feature of the SDPT high-level routines is the ability to process each parameter and organize it into bins along a time axis and perform the time-weighted average and histogram analysis. The time-weighted analyzes also allow tracking the maximum and minimum parameter value for each bin, as well as the standard deviation. The statistical methods provided by the SDPT *rcSoftware* are described in detail in Appendix A, which also includes Figure A.8, which plots some signal parameters extracted with SDPT along a time axis.

## 4.4 – Summary

In this chapter, we provide a detailed account of the biological materials used and the experimental procedures employed to handle and perform live experiments with the newly developed electrodes. Zebrafish hearts and embryonic bodies of cardiomyocyte cells were selected as the standard signal sources. We also use immortal C6 cell culture lines as they are robust and reliable cultures that have been extensively researched and documented. Additionally, primary cultures of astrocytes were chosen to demonstrate the application of our electrodes and measurement methods in neurosciences.

To inspect whether measurement if 2D cell cultures could provide useful information to interpret data recorded in a real 3D biological tissue, we selected high-grade glioblastoma tumor tissues. Table 4.1 summarizes all the electrogenic and non-electrogenic biological structures used in the study.
Furthermore, the chapter outlines the protocols utilized to characterize the sensing electrodes, record data, and analyze the results.

**Table 4.1 –** Summary of all biological material used in this thesis. The non-electrogenic biological structures are listed on the right side, while the electrogenic biological structures are listed on the left side.

| Electrogenic | | |
|---|---|---|
| **Structure** | **Type** | **Name** |
| Cell | Neuronal | Neuro2A |
| Tissue | Cardiac | EB of cardiomyocyte |
| Organ | Cardiac | Zebrafish heart |

| Non-electrogenic | | |
|---|---|---|
| **Structure** | **Type** | **Name** |
| Cell | Glial | Astrocytes |
| Cell | Glial | C6 |
| Tissue | Multiple | Human Glioblastoma |

# References


1. Molenaar, R.J. Ion Channels in Glioblastoma. *ISRN Neurol.* **2011**, *2011*, 1–7, doi:10.5402/2011/590249.
2. Gallego, O. Nonsurgical Treatment of Recurrent Glioblastoma. *Curr. Oncol.* **2015**, *22*, 273–281, doi:10.3747/co.22.2436.
3. America Type Culture Collection (ATCC) Organization C6 cells (CCL-107) Available online: https://www.atcc.org/products/ccl-107 (accessed on May 21, 2022).
4. Wypych, D.; Bara, J. Cross-Talk in Nucleotide Signaling in Glioma C6 Cells. 31–59, doi:10.1007/978-94-007-4719-7.
5. America Type Culture Collection (ATCC) Organization Neuro-2a cells (CCL-131) Available online: https://www.atcc.org/products/ccl-131 (accessed on May 21, 2022).
6. Kranc, K.R.; Oliveira, D. V.; Armesilla-Diaz, A.; Pacheco-Leyva, I.; Catarina Matias, A.; Luisa Escapa, A.; Subramani, C.; Wheadon, H.; Trindade, M.; Nichols, J.; et al. Acute loss of Cited2 impairs nanog expression and decreases self-renewal of mouse embryonic stem cells. *Stem Cells* **2015**, *33*, 699–712, doi:10.1002/stem.1889.
7. Fuegemann, C.J.; Samraj, A.K.; Walsh, S.; Fleischmann, B.K.; Jovinge, S.; Breitbach, M. Differentiation of Mouse Embryonic Stem Cells into Cardiomyocytes via the Hanging-Drop and Mass Culture Methods. *Curr. Protoc. Stem Cell Biol.* **2010**, 1–13, doi:10.1002/9780470151808.sc01f11s15.
8. Inacio, P.M.C.; Mestre, A.L.G.; De Medeiros, M.D.C.R.; Asgarifar, S.; Elamine, Y.; Canudo, J.; Santos, J.M.A.; Braganca, J.; Morgado, J.; Biscarini, F.; et al. Bioelectrical Signal Detection Using Conducting Polymer Electrodes and the Displacement Current Method. *IEEE Sens. J.* **2017**, *17*, 3961–3966, doi:10.1109/JSEN.2017.2703834.

9. Li, J.; Hubbard, P.C.; Canário, A.V.M. Male zebrafish ( Danio rerio ) odorants attract females and induce spawning. *Aquac. Fish.* **2018**, *3*, 139–144, doi:10.1016/j.aaf.2018.06.004.
10. Wang, R.; Hashimoto, K.; Fujishima, A.; Chikuni, M.; Kojima, E.; Kitamura, A.; Shimohigoshi, M.; Watanabe, T. Light-induced amphiphilic surfaces. *Nature* **1997**, *388*, 431–432, doi:10.1038/41233.
11. Machida, M.; Norimoto, K.; Watanabe, T.; Hashimoto, K.; Fujishima, A. The effect of SiO 2 addition in super-hydrophilic property of TiO 2 photocatalyst. *J. Mater. Sci.* **1999**, *34*, 2569–2574, doi:10.1023/A:1004644514653.
12. Israel, D.A.; Edell, D.J.; Mark, R.G. Time delays in propagation of cardiac action potential. *Am. J. Physiol. Circ. Physiol.* **1990**, *258*, H1906–H1917, doi:10.1152/ajpheart.1990.258.6.H1906.
13. Keefer, E.W.; Gramowski, A.; Stenger, D.A.; Pancrazio, J.J.; Gross, G.W. Characterization of acute neurotoxic effects of trimethylolpropane phosphate via neuronal network biosensors. *Biosens. Bioelectron.* **2001**, *16*, 513–525, doi:10.1016/S0956-5663(01)00165-8.
14. Xia, Y.; Gopal, K. V.; Gross, G.W. Differential acute effects of fluoxetine on frontal and auditory cortex networks in vitro. *Brain Res.* **2003**, *973*, 151–160, doi:10.1016/S0006-8993(03)02367-9.
15. Aravanis, A.M.; DeBusschere, B.D.; Chruscinski, A.J.; Gilchrist, K.H.; Kobilka, B.K.; Kovacs, G.T.. A genetically engineered cell-based biosensor for functional classification of agents. *Biosens. Bioelectron.* **2001**, *16*, 571–577, doi:10.1016/S0956-5663(01)00171-3.
16. Borkholder, D.A.; D, B.; Kovacs, G.T.A. An Approach to the Classification of Unknown Biological Agents with Cell Based Sensors. In Proceedings of the 1998 Solid-State, Actuators, and Microsystems Workshop Technical Digest; Transducer Research Foundation, Inc.: San Diego, CA USA, 1998; pp. 178–182.
17. Mestre, A.L.G.A.L.G.; Cerquido, M.; Inácio, P.M.C.P.M.C.; Asgarifar, S.; Lourenço, A.S.A.S.; Cristiano, M.L.S.M.L.S.; Aguiar, P.; Medeiros, M.C.R.M.C.R.; Araújo, I.M.I.M.; Ventura, J.; et al. Ultrasensitive gold micro-structured electrodes enabling the detection of extra-cellular long-lasting potentials in astrocytes populations. *Sci. Rep.* **2017**, *7*, 1–11, doi:10.1038/s41598-017-14697-y.
18. Mestre, A.L.G.; Inácio, P.M.C.; Elamine, Y.; Asgarifar, S.; Lourenço, A.S.; Cristiano, M.L.S.; Aguiar, P.; Medeiros, M.C.R.; Araújo, I.M.; Ventura, J.; et al. Extracellular Electrophysiological Measurements of Cooperative Signals in Astrocytes Populations. *Front. Neural Circuits* **2017**, *11*, 1–9, doi:10.3389/fncir.2017.00080.
19. Cabello, M.; Ge, H.; Aracil, C.; Moschou, D.; Estrela, P.; Quero, J.M.; Pascu, S.I.; Rocha, P.R.F. Extracellular electrophysiology in the prostate cancer cell model PC-3. *Sensors (Switzerland)*

**2019**, *19*, 1–11, doi:10.3390/s19010139.

20. Rocha, P.R.F.; Schlett, P.; Schneider, L.; Drö, M.; Mailä, V.; Gomes, H.L.; Blom, P.W.M.; De Leeuw, D.M. Low frequency electric current noise in glioma cell populations. *J. Mater. Chem. B* **2015**, *3*, 5035–5039, doi:10.1039/c5tb00144g.

# Chapter 5

 *IEEE Sensors Journal*, Vol. 17, Issue 13, July 2017. DOI: 10.1109/JSEN.2017.2703834

# Bioelectrical signal detection using conducting polymer electrodes and the displacement current method

Conducting polymer electrodes based on poly(3,4-ethylenedioxythiophene):polystyrene sulfonate was used to record electrophysiological signals from autonomous cardiac contractile cells present in embryoid bodies. Signal detection was carried-out by measuring the displacement current across the polymer/electrolyte double-layer capacitance and compared with voltage detection. While for relatively low capacitance electrodes the voltage amplification provides higher signal quality, for high capacitive electrodes the displacement current method exhibits a higher signal-to-noise ratio. It is proposed that the displacement current method combined with high capacitive polymer-based electrodes is adequate to measure clusters of cells and whole organs. Our approach has a great potential in fundamental studies of drug discovery and safety pharmacology.

## 5.1− Introduction

The reliable and long-term stable monitoring of extracellular signals from cultured electrogenic cells and small organs is essential to conduct scientific research in several areas, including the study of neuronal network processes, effects of pharmacological drugs and mechanisms underlying pathological conditions.

Microelectrode arrays (MEAs) are considered to be the state-of-art platform for the development of cell-based sensors[1]–[3]. These are substrate-integrated extracellular electrode matrices kept in contact with cells. Efforts are currently in progress to improve MEA technology. These efforts have been directed at (i) decreasing the device dimensions and (ii) improving the electrical coupling between the cell and the sensing device. Smaller devices are better for parallel activity mapping, hence the application of nanofabrication technologies in this field. The second goal being pursued is the lowering of electrode impedance. One successful strategy is to use conducting polymers. It has been shown that polymers offer low impedance that facilitates signal transduction from the cell to the

recording electrode [4]–[10]. The low interfacial impedance has been attributed to the large area of the swelled polymer matrix in an aqueous environment [7],[11].

Conducting polymers are particularly attractive as sensing electrodes to monitor embryoid bodies (EB) and small organs. EBs are three dimensional organoid structures comprised of hundreds or even thousands of cells of the three germ layers derived from embryonic stem cells. Cardiomyocytes derived from EBs formation [12]–[15] and embryonic chicken hearts [16] are well studied examples. To record cooperative signals produced by these organs or organoids, small area electrodes are not crucial. Small area electrodes provide spatial resolution required to address single cells or specific phenomena, such as the travelling speed of extracellular calcium waves [15]. Electrode active areas in the scale of few mm2 minimize the impedance and enhance signal quality. Furthermore, large area electrodes are facile to fabricate by ink-jet printing into flexible and conformable substrates and can be made disposable.

When immersed in an electrolyte solution, polymer-based electrodes exhibit a low impedance because of the low resistance of the polymer/cell culture medium interface, that minimizes the thermal noise [17], and the large interfacial capacitance. In this report, we exploit this high interfacial capacitance in a detection method that measures the displacement current across the interface. This method is highly sensitive to rapid variations in the electrical potential caused by extracellular ionic fluctuations. We also demonstrate that when the effective capacitance is high, extracellular recordings in current amplification mode have higher quality than measurements using voltage amplification.

Since the displacement current method benefits from large area electrodes, it is proposed that this strategy is appropriate to develop sensing electrodes aiming at studying *in vitro* cell aggregates and whole organs. Small organs/organoids are considered interesting research tools in fundamental studies for drug discovery, and cytotoxic pharmacological assays [18][19]. A number of organ models have already been generated and continue to be optimized, including models of the liver, lung, kidney, gut, bone, breast, eye and brain [20]–[22]. In the present work, first we briefly describe the ink-jet printed polymer electrodes, the EBs, and schematize the circuit describing the electrical coupling between the cells and the extracellular electrode. Next, the equation of the displacement current is introduced. Finally, experimental results comparing the displacement current method to voltage measurements are presented and discussed.

# 5.2− Experimental

Poly(3,4-ethylenedioxythiophene):polystyrene sulfonate, also known as PEDOT:PSS was provided by AFGA Orgacon$^{TM}$. Electrodes were inkjet printed on glass substrates. Printing was performed in air using a Fujifilm Dimatix Material Printer (DMP) 2831, with a DMC-11610 cartridge.

Samples were annealed on a hot plate at 60°C for 8h. After annealing, they were immersed in ethylene glycol, to increase their conductivity, and then dried in a vacuum oven at 60°C for 12h.

As test cells, we used spontaneously beating cardiomyocytes differentiated from mouse embryonic stem cells (mESC) as described elsewhere [23]. mESC were differentiated using the hanging-drop method in mESC culture medium, containing 20% FBS (differentiation medium). Briefly, 100 cells were cultured in 20 μL hanging drops of differentiation medium for 48 hours to initiate EBs formation. Next, EBs were grown in suspension for 3 days in a bacterial petri dish in differentiation medium before being transferred to the sensing devices. Each EB has an average diameter that varies between 300 and 400 μm.

The sensing electrodes with cells were maintained in GMEM culture medium at 37ºC in an incubator with a humidified atmosphere with 5% of CO2. The culture chamber is formed by a standard petri dish 50 mm diameter attached to the sensing device through an O-ring with 3 mm diameter.

The recording system has voltage and current amplifiers. In voltage detection mode, we used gains of 2000 and 5000 and in current detection we used a sensitivity of 20 nA/V. The preamplifiers were connected to a signal analyzer (Agilent 35670A) that performs real time analysis of an experiment.

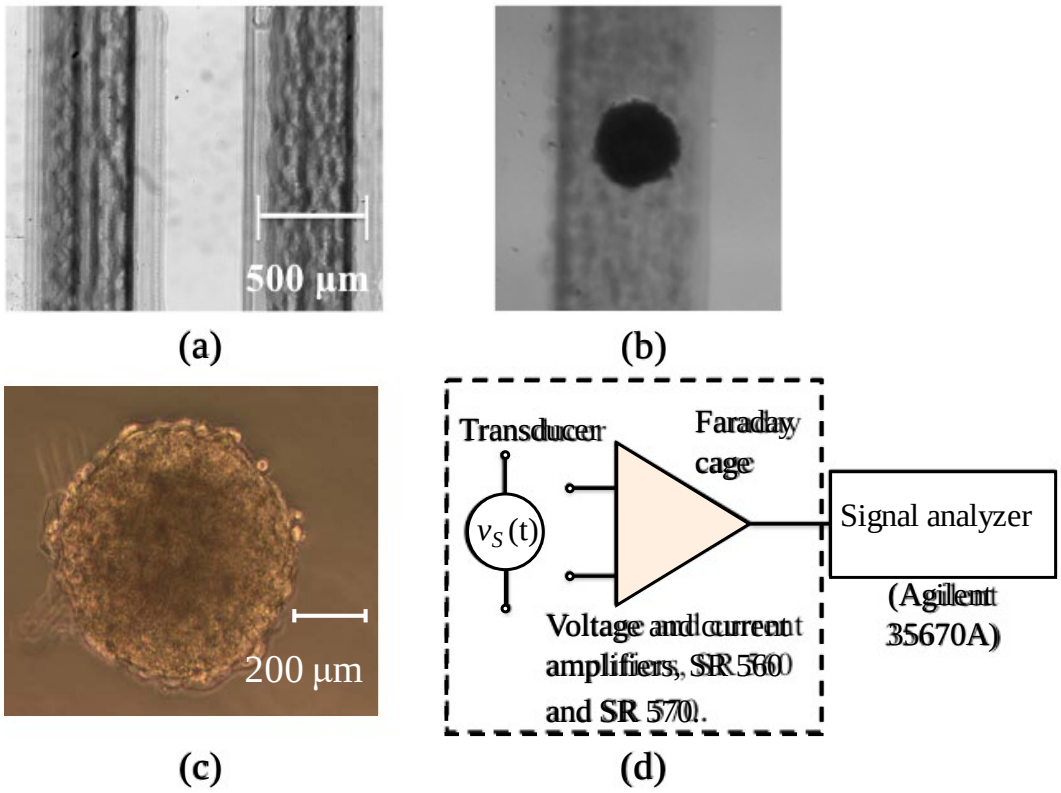


**Figure 5.1 –** Cells and electrodes used. (**a**) Photograph of two parallel polymer electrodes ink-jet printed on top of a glass substrate. (**b**) Photograph of an EB on top of a PEDOT:PSS electrode. (**c**) Photograph of fresh isolated EB and (**d**) schematic diagram of the measurement set-up. © 2017 IEEE.

Further analyses were carried out offline, using tools written for MATLAB. Small signal impedance measurements were carried out using an impedance analyzer, Fluke PM6306.

Figure 5.1 shows two parallel PEDOT:PSS electrodes printed on glass substrates. On top of the electrode is a typical EB with multiple foci of contractile activity.

## 5.3– Equivalent circuit model

The sensor comprises two parallel electrodes of depth *D* and length *W*, separated by a gap distance *L* as shown in Figure 5.2. One of the electrodes acts as measuring electrode and the other as a counter-electrode. The electrodes are connected to a trans-impedance amplifier or alternatively to a voltage amplifier. The impedance of these electrodes has an important role in the system response, since it determines the electrical coupling of the extracellular signal to the sensing electrode. The interface between cells and microelectrodes *in vitro* has been described using an electrical equivalent circuit.

The equivalent circuit shown in Figure 5.2 embodies the electrical coupling between the cell and the electrode. This circuit is a simplified version of the standard model used in literature [1], [2], [22],

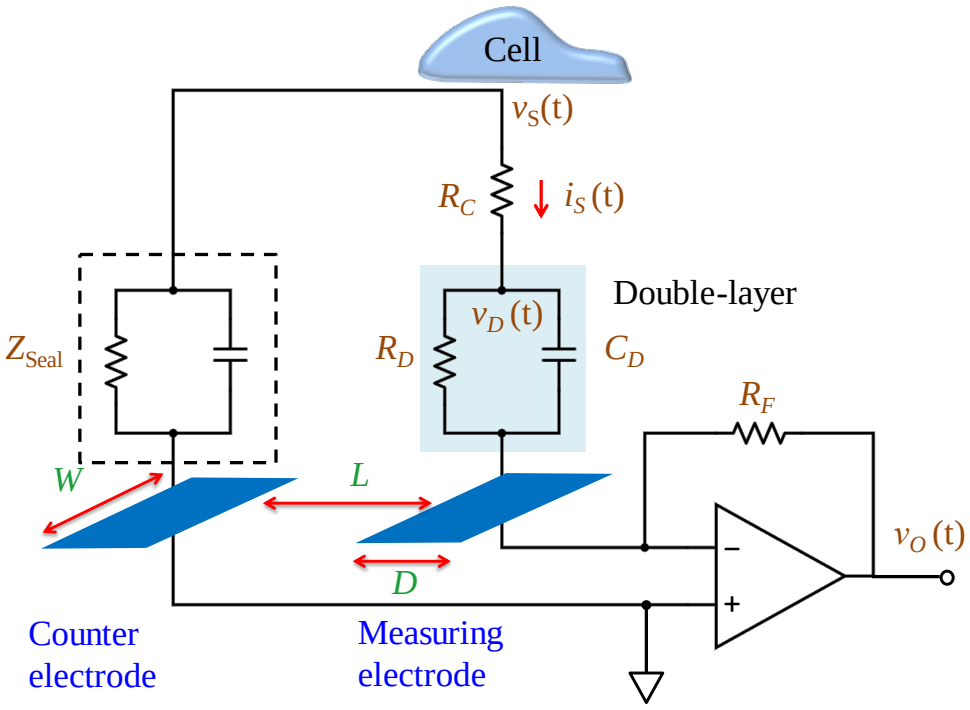


**Figure 5.2 –** Schematic diagram representing the electrical coupling between the EB and the measuring circuit. A trans-impedance amplifier is used. The amplified signal is $i_S(t)$. $W$ = 3900 µm, $L$ = 500 µm, and $D$ = 500 µm. © 2017 IEEE.

[23]. Basically, this equivalent model takes into account the electrical double-layer established at a metal/electrolyte interface. The parallel circuit network is formed by the double-layer resistance, $R_D$, and the Helmholtz-Gouy-Chapmann double-layer capacitance, $C_D$, in series with the spreading resistance, $R_C$, that accounts for the signal loss into the surrounding electrolyte. A similar circuit describes the counter electrode. The electrical path from the sensing to the counter electrode has very high impedance, $Z_{seal}$, due to the large distance. This equivalent circuit is a reduction of a more complex model, that includes a constant-phase-angle impedance to take into account the impedance dispersion at low frequencies. For the sake of simplicity this element is not included in Figure 5.2.

The cells generate a*t* voltage, $v_S(t)$. In MEAs these voltage fluctuations are amplified by means of a voltage amplifier. Here, we amplify the corresponding current fluctuations, $i_S(t)$. This current appears as a displacement current across the double layer capacitance ($C_D$) and is amplified by a transimpedance amplifier. The output voltage , $v_o(t)$, is given by,

$$v_o(t) = -R_F i_s(t) \tag{5.1}$$

where $R_F$ is the feedback resistance and $i_S(t)$ the current flowing through the measuring electrode impedance. This detection method is referred to as the displacement current method. Details of the model can be found in a study by Medeiros et al. [26]. The detected current, assuming that $v_S(t)$, is a rising ramp with slope $\frac{dv_S(t)}{dt}$, can approximated as,

$$i_S(t) \cong \frac{v_S(t)}{R_D + R_C} + \frac{dv_S(t)}{dt} C_D\left(1 - e^{-t/\tau}\right) \tag{5.2}$$

$i_S(t)$ signal is a transient with a peak amplitude proportional to the product $\frac{dv_S}{dt} C_D$ that decays with a time constant $\tau = C_D\ (R_D \parallel R_C)$. Here $R_C$ is the spreading resistance that accounts for the signal loss into the surrounding electrolyte and $R_D$ is the double-layer resistance as represented in Figure 5.2. From Equation (5.2) we can see that, $C_D$ acts as a multiplying factor for the current. Basically, a rapidly varying voltage signal produces a large transient displacement current across the capacitor. Under these conditions, the measured current signal shape is also proportional to the derivative of the original signal $v_S(t)$.

# 5.4− Results

In a typical experiment a freshly isolated EB is placed on top of a PEDOT:PSS electrode. After a short period of equilibration with electrophysiology medium, the EB beat spontaneously at a typical frequency of 1 Hz. Measurements remain stable for up to two days of continuous recording. The cell

culture medium is replaced every 4 hours. PEDOT:PSS electrodes were stable over the course of the experiment.

The contractile activity of each EB was measured either as a current signal, using a Stanford low-noise current amplifier (SR 570), or, alternatively, in voltage mode using a voltage amplifier (SR 560) connected to a dynamic signal analyzer. The signals were recorded in the same EB/electrode system separated by a time interval required to change the amplifier. A detail view of the signals in current and in voltage is shown in the insets of Figure 5.3. Both signals are bipolar. The spikes in current reach amplitude of 120 pA in an average noise of 16 pA. Voltage signals reach values of 0.6 μV in a noise level of 0.1 μV (peak-to-peak). Figure 5.3 (a) and (b) show the power spectral density (PSD) for voltage and for current respectively. Both PSDs result from averaging16 traces of length = 64 s. The line at 1.2 Hz (followed by the harmonics) shows the beating frequency of the EB. The PSD of the noise of the bare electrodes (without EB) is compared with the signal PSD for bare electrodes. For both voltage and current noise, PSD increases at lower frequencies, however the voltage PSD has an approximate frequency dependence of −20 dB/dec for low frequencies, whereas the current noise PSD frequency dependence in only approximately −5 dB/dec. Therefore, low frequency signals benefit from being measured in current mode, as demonstrated in Figure 5.3 where at 1.2 Hz the voltage signal power to noise is $SNR_V$ = 14 dB, whereas for the current signal the $SNR_I$ = 18.1 dB.

It is important to point out that the sensitivity and signal quality described above was possible to achieved because of the very low impedance electrodes used. Small-signal impedance measurements show that the electrodes have at the frequency of 100 Hz a capacitance of 199 nF and a resistance of only 2.5 kΩ.

Electrical readings were carried out using a total number of 10 EBs. The bar graph in Figure 5.4 (a) shows the average SNR obtained for current ($SNR_I$) and voltage amplification ($SNR_V$).

The fact that at low frequencies the noise in current is lower than in voltage is in agreement with theoretical predictions. An ideal lossless capacitor does not produce thermal noise. The thermal noise generated by the electrode is generated only by the resistive part of the double-layer ($R_P$). The PSD of the noise in current, $S_I(\omega)$ and the PSD of the voltage noise, $S_V(\omega)$, generated by the double-layer are given by,

$$S_I(t) = \frac{4kT}{R_P(\omega)}\left[\frac{\mathrm{A}^2}{\mathrm{Hz}}\right] \text{ and } S_V(t) = 4kTR_P(\omega)\left[\frac{\mathrm{V}^2}{\mathrm{Hz}}\right] \tag{5.3}$$

where $R_P(\omega)$ is the real part of the electrode admittance at particular frequency, $k$ the Boltzmann constant and $T$ the absolute temperature. From Equation (5.3) it is clear that the higher the resistance $R_P$, smaller is the current thermal noise and higher the voltage thermal noise. It is also known that $R_P$ increases for low frequencies [27]. In summary, the low noise behavior at low frequencies in current

measurement mode, contrasts with traditional voltage measurements where noise dominates at low frequencies. Experimentally, the noise at low frequencies does not decrease, but flattens out (see Figure 5.3 (b)). This behavior is possibly caused by additional contribution to the noise from the trans-impedance amplifier.

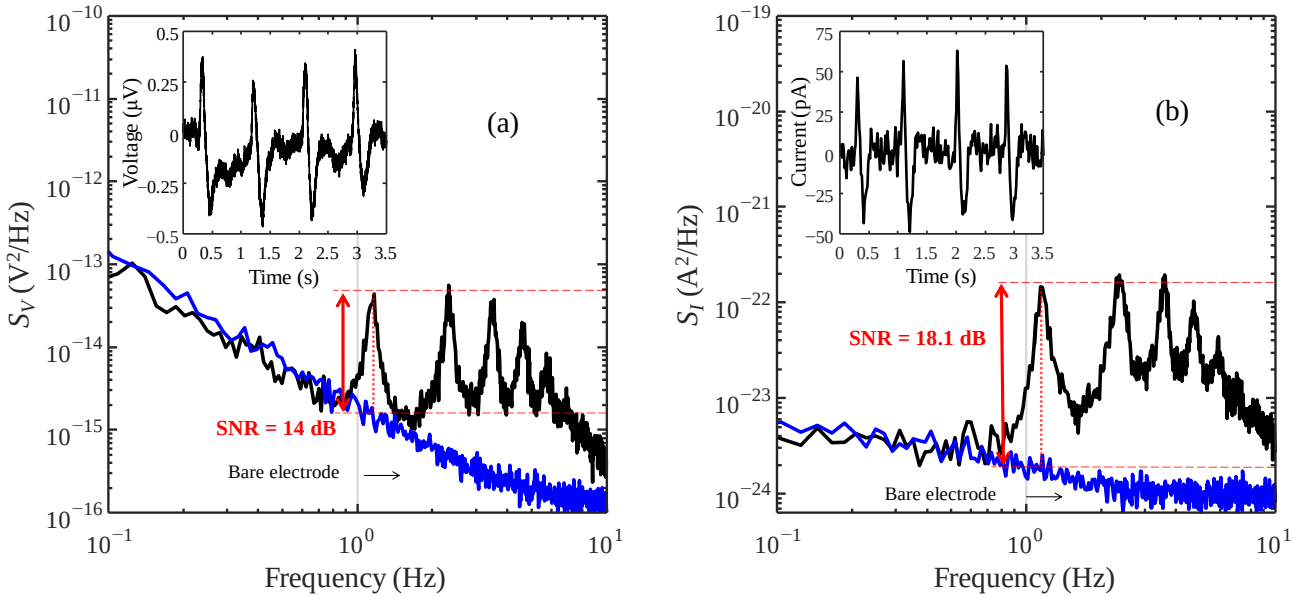


**Figure 5.3 –** Comparison between voltage and current signals measured using the same EB/electrode system. (**a**) Power spectral density (PSD) of voltage signals, (**b**) PSD of current signals. Insets show a short time interval trace in voltage (a) and in current (b). The bottom line (bare electrode) is the noise PSD of the electrode without cells. © 2017 IEEE.

In order to understand the role of the capacitance on the SNR, recordings were carried out in four different electrodes with different interfacial capacitances. Ten EBs were individually measured at each electrode. The bar graph in Figure 5.4 (a) shows the average SNR obtained for both current and voltage amplification as function of the electrode capacitance. For low capacitance electrodes the voltage detection method provides a better signal-to-noise (SNR) ratio. However, as the electrode capacitance increases, this behavior is inverted, and current detection method gives increasing higher SNRs comparatively with voltage detection. This means that the electrode capacitance is so large that the current spikes generated by the displacement current can compensate for the additional thermal noise. In current amplification the noise is inverse proportional to the resistance (see Equation (5.3)). Furthermore, the displacement current method also performs the derivative of the noise fluctuations. In spite of that, the signal quality improves. The reason is that the low frequency voltage noise (for $f <$ 1 Hz) is not entirely due to the thermal noise. As shown in Figure 5.3 for low frequencies, the voltage noise of the bare electrode ($S_V$) increases following a $1/f^2$ dependence. The origin of this excess noise is not clear yet but is typical of polarized faradaic interfaces [28]. At low frequencies the excess noise degrades the SNR in voltage amplification. In contrast, in current amplification the low-frequency

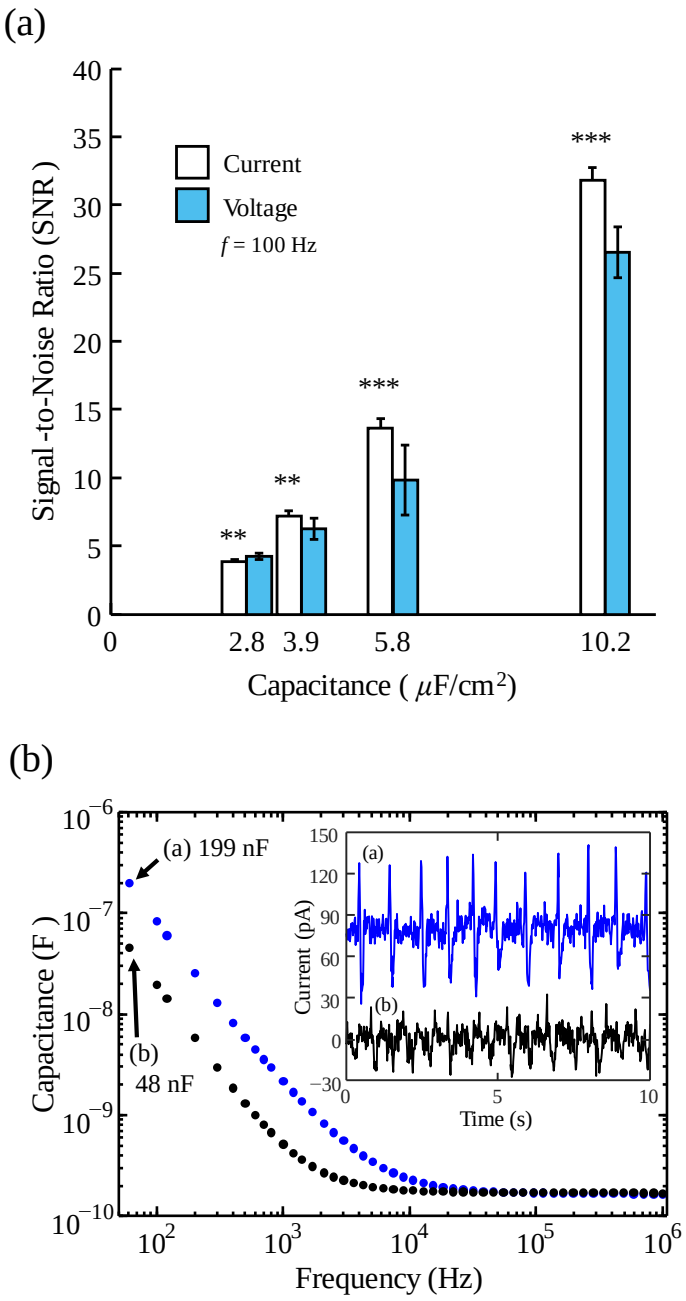


**Figure 5.4 –** (a) Comparison between the means of SNRI and SNRV for four independent electrodes. The capacitances were measured at a frequency of 100 Hz. The statistical analysis was performed using Student t-test. (**) indicates a *P* value < 0.01; and (***) indicates *P* value < 0.001. The values are the mean ± standard deviation of 10 observations. (b) Frequency dependence of the capacitance of two PEDOT:PSS electrodes with the same physical dimensions but different capacitances/roughness. The inset shows the corresponding time traces of signals. The upper time trace (a) is shifted vertically by 75 pA. © 2017 IEEE.

noise does not rise as much as in voltage mode. In current amplification, the electrode noise follows 1/*f* dependence, and it flattens out at low frequencies (*f* < 0.3 Hz). This low-frequency dependence of the noise in current, eventually benefits the measurements in current detection.

Next, we present how the electrode impedance parameters affect the signal amplitude. For that, were used two sets of electrodes with the same physical dimensions but with different polymer

roughness and consequently different values of capacitance. Variations on polymer roughness are introduced during the ink-jet printing process. For a particular printing run, roughness increases with the number of printed layers. However, when electrodes are deposited in different printing runs there is also variability caused by environmental factors (humidity, temperature) or even changes in the ink solution such as aging.

The capacitance versus frequency of the two electrode systems is shown in Figure 5.4 (b). The capacitance is strongly frequency dependent. This frequency dependence is typical of conducting electrodes immersed into electrolyte solutions. At low frequencies the capacitance reflects the interfacial double layer capacitance. As the frequency increases the measured capacitance becomes the series sum of electrolyte capacitance in series with the double-layer capacitance. The frequency response of PEDOT:PSS electrodes immersed in cell culture mediums has been described in a previous publication [17].

The signals recorded for the two electrode systems are shown in the inset of Figure 5.4 (b). As expected, the signal quality increases approximately in line with the increase on the electrode capacitance/roughness.

The displacement current method presented here can measure weak bioelectrical signals. It was shown that signals with amplitudes of only 0.6 μV peak-to-peak can be detected with a SNR higher than 30. This value compares favorably with the best SNRs of 10 reported for state-of-the-art MEAs [12],[15] and for nanowire-based transistors [16]. Notably, this high SNR is achieved even when the cells are not grown directly on the recording electrodes but simply placed on top of the electrodes. The main factor behind this ultra-high sensitivity is the use of large area electrodes with an associated high capacitance ($C > 4$ μF/cm$^2$ at 100 Hz) provided by the polymer/electrolyte interface.

As general empirical guideline, the displacement current method provides higher SNR than voltage measuring methods when the electrode/electrolyte interfacial capacitance (measured at 100 Hz) is above 4 μF/cm$^2$ and the measurement bandwidth is below 10 Hz. Furthermore, the method is also advantageous to record signals that vary on a relative short time scale, typically shorter than 1 second.

The advantage of the displacement current method was demonstrated here by measuring cardiac signals. However, this method is also particularly suitable to record other interesting biological signals. A well-known example is the recording of extracellular calcium waves. Extracellular calcium oscillations cause voltages gradients that propagate trough populations of cells at speeds between 10 and 30 microns per second and generate signals in a time scale of seconds [26],[29]. These signals are significant slower than action potentials produced by nervous cells which last for 2−3 milliseconds. The use of large capacitive electrodes does not impose bandwidth limitations, but the voltages gradients are fast enough to cause a displacement current across a capacitive electrode. Recently, we

have used the displacement current method to record ultra-week signals produced by glioma cells. These are tumor cells that generated burst of signals possibly involved in epileptic seizures [30].

## 5.5− Conclusions

Large area conducting polymer electrodes produced by inkjet printing provide good electrophysiological readings both in conventional voltage measurement as well as in measurements of the displacement current.

The comparison between the voltage and the current signals is shown to provide a clear insight in the role of the double layer capacitance in shaping the signal as well as in controlling the SNR. The noise generated by the electrodes at low frequencies increases substantially more in voltage mode than it does when measurements are carried out in current mode. This explains why the SNR is better in current mode, which is particularly suited for low-frequency measurements. Furthermore, because the displacement current is proportional to the voltage derivative, the method is appropriate for fast varying signals.

The facile and low-cost production of ink-jet printed polymer electrodes makes them attractive as disposable electrodes to conduct electrophysiological measurements in small organs.

# References

[1] M. E. Spira and A. Hai, “Multi-electrode array technologies for neuroscience and cardiology,” *Nat. Nanotechnol.*, vol. 8, no. 2, pp. 83–94, 2013.

[2] A. Hierlemann, U. Frey, S. Hafizovic, and F. Heer, “Growing Cells Atop Microelectronic Chips: Interfacing Electrogenic Cells In Vitro With CMOS-Based Microelectrode Arrays,” *Proc. IEEE*, vol. 99, no. 2, pp. 252–284, Feb. 2011.

[3] M. E. J. Obien, K. Deligkaris, T. Bullmann, D. J. Bakkum, and U. Frey, “Revealing neuronal function through microelectrode array recordings,” *Front. Neurosci.*, vol. 9, no. JAN, p. 423, 2015.

[4] M. Sessolo, D. Khodagholy, J. Rivnay, F. Maddalena, M. Gleyzes, E. Steidl, B. Buisson, and G. G. Malliaras, “Easy-to-fabricate conducting polymer microelectrode arrays,” *Adv. Mater.*, vol. 25, no. 15, pp. 2135–2139, 2013.

[5] K. Svennersten, K. C. Larsson, M. Berggren, and A. Richter-Dahlfors, “Organic bioelectronics in nanomedicine,” *Biochim. Biophys. Acta - Gen. Subj.*, vol. 1810, no. 3, pp. 276–285, 2011.

[6] S. Löffler, B. Libberton, and A. Richter-Dahlfors, “Organic Bioelectronic Tools for Biomedical

Applications," *Electronics*, vol. 4, no. 4, pp. 879–908, 2015.

[7] P. Leleux, J. M. Badier, J. Rivnay, C. Bénar, T. Hervé, P. Chauvel, and G. G. Malliaras, "Conducting Polymer Electrodes for Electroencephalography," *Adv. Healthc. Mater.*, vol. 3, no. 4, pp. 490–493, 2014.

[8] S. Tsukada, H. Nakashima, and K. Torimitsu, "Conductive Polymer Combined Silk Fiber Bundle for Bioelectrical Signal Recording," vol. 7, no. 4, 2012.

[9] X. Cui and D. C. Martin, "Electrochemical deposition and characterization of poly(3,4-ethylenedioxythiophene) on neural microelectrode arrays," *Sensors Actuators, B Chem.*, vol. 89, no. 1–2, pp. 92–102, 2003.

[10] A. Blau, A. Murr, S. Wolff, E. Sernagor, P. Medini, G. Iurilli, C. Ziegler, and F. Benfenati, "Flexible, all-polymer microelectrode arrays for the capture of cardiac and neuronal signals," *Biomaterials*, vol. 32, no. 7, pp. 1778–1786, 2011.

[11] J. Rivnay, P. Leleux, M. Ferro, M. Sessolo, A. Williamson, D. a. Koutsouras, D. Khodagholy, M. Ramuz, X. Strakosas, R. M. Owens, C. Benar, J.-M. Badier, C. Bernard, and G. G. Malliaras, "High-performance transistors for bioelectronics through tuning of channel thickness," *Sci. Adv.*, vol. 1, no. 4, pp. e1400251–e1400251, 2015.

[12] U. Egert and T. Meyer, "Heart on a Chip – Extracellular Multielectrode Recordings from Cardiac Myocytes in Vitro," pp. 432–453, 2003.

[13] K. Banach, M. D. Halbach, P. Hu, J. Hescheler, and U. Egert, "Development of electrical activity in cardiac myocyte aggregates derived from mouse embryonic stem cells," vol. 60153, pp. 2114–2123, 2003.

[14] A. Blazeski, R. Zhu, D. W. Hunter, S. H. Weinberg, K. R. Boheler, E. T. Zambidis, and L. Tung, "Electrophysiological and contractile function of cardiomyocytes derived from human embryonic stem cells," *Prog. Biophys. Mol. Biol.*, vol. 110, no. 2–3, pp. 178–195, 2012.

[15] U. Egert, K. Banach, and T. Meyer, "Analysis of Cardiac Myocyte Activity Dynamics with Micro-Electrode Arrays," pp. 274–290, 2003.

[16] B. P. Timko, T. Cohen-karni, G. Yu, Q. Qing, B. Tian, and C. M. Lieber, "Electrical Recording from Hearts with Flexible Nanowire Device Arrays 2009," 2009.

[17] M. C. R. Medeiros, A. L. G. Mestre, P. M. C. Inácio, J. M. L. Santos, and M. Inês, "Performance assessment of polymer based electrodes for in vitro electrophysiological sensing : the role of the electrode impedance," in *SPIE Organic Photonics+ Electronics*, 2016, pp. 994404-994404–8.

[18] A. Khademhosseini, "Organ Engineering : Design , Technology , and Integration Organ Engineering : Design , Technology , and," no. September, 2016.

[19] C. Y. Chan, P.-H. Huang, F. Guo, X. Ding, V. Kapur, J. D. Mai, P. K. Yuen, and T. J. Huang,

"Accelerating drug discovery via organson-chips.," *Lab Chip*, vol. 13, no. 24, pp. 4697–710, 2013.

[20] C. Willyard, "The boom in mini stomachs, brains, breasts, kidneys and more," *Nature*, vol. 523, no. 7562, pp. 520–522, 2015.

[21] M. J. Wilmer, C. P. Ng, H. L. Lanz, P. Vulto, L. Suter-Dick, and R. Masereeuw, "Kidney-on-a-Chip Technology for Drug-Induced Nephrotoxicity Screening," *Trends Biotechnol.*, vol. 34, no. 2, pp. 156–170, 2016.

[22] S. C. D. Models, "Organoids : 3D miniatures are booming," pp. 35–37, 2015.

[23] K. R. Kranc, D. V. Oliveira, A. Armesilla-Diaz, I. Pacheco-Leyva, A. Catarina Matias, A. Luisa Escapa, C. Subramani, H. Wheadon, M. Trindade, J. Nichols, K. Kaji, T. Enver, and J. Bragança, "Acute loss of Cited2 impairs nanog expression and decreases selfrenewal of mouse embryonic stem cells," *Stem Cells*, vol. 33, no. 3, pp. 699–712, 2015.

[24] M. E. J. Obien, K. Deligkaris, T. Bullmann, D. J. Bakkum, and U. Frey, "Revealing neuronal function through microelectrode array recordings," *Front. Neurosci.*, vol. 8, no. JAN, p. 423, Jan. 2015.

[25] B. Eversmann, M. Jenkner, F. Hofmann, C. Paulus, R. Brederlow, B. Holzapfl, P. Fromherz, M. Merz, M. Brenner, M. Schreiter, R. Gabl, K. Plehnert, M. Steinhauser, G. Eckstein, D. Schmitt-Landsiedel, and R. Thewes, "A 128 x 128 CMOS Biosensor Array for Extracellular\rRecording of Neural Activity," *Ieee J. Solid-State Circuits*, vol. 38, no. 12, pp. 2306–2317, 2003.

[26] M. C. R. Medeiros, A. Mestre, P. Inácio, S. Asgarif, I. M. Araújo, P. C. Hubbard, Z. Velez, M. L. Cancela, P. R. F. Rocha, D. M. de Leeuw, F. Biscarini, and H. L. Gomes, "An electrical method to measure low-frequency collective and synchronized cell activity using extracellular electrodes," *Sens. Bio-Sensing Res.*, vol. 10, pp. 1–8, 2016.

[27] K. J. Aoki, "Frequency-dependence of electric double layer capacitance without Faradaic reactions," *J. Electroanal. Chem.*, pp. 1–9, 2016.

[28] A. Hassibi, R. Navid, R. W. Dutton, T. H. Lee, A. Hassibi, R. Navid, R. W. Dutton, and T. H. Lee, "Comprehensive study of noise processes in electrode electrolyte interfaces Comprehensive study of noise processes in electrode electrolyte interfaces," 2004.

[29] A. Politi and R. Heinrich, "Intercellular Ca2 + wave propagation through gap-junctional Ca2 + diffusion : a theoretical study," vol. 80, no. 1, pp. 1996–1998, 2001.

[30] P. R. F. Rocha, M. C. R. Medeiros, U. Kintzel, J. Vogt, I. M. Araújo, A. L. G. Mestre, V. Mailänder, P. Schlett, M. Dröge, L. Schneider, F. Biscarini, D. M. De Leeuw, and H. L. Gomes, "Extracellular electrical recording of pH-triggered bursts in C6 glioma cell populations," pp. 1–9, 2016.

C. R. Medeiros *Member IEEE*, Sanaz Asgarifar, Youssef Elamine, Joana Canudo, João M. A. Santos, José Bragança, Jorge Morgado, Fabio Biscarini and Henrique L. Gomes, Bioelectrical Signal Detection Using Conducting Polymer Electrodes and the Displacement Current Method, *IEEE Sensors Journal*, Vol. 17, Issue 13, July 2017.

# Chapter 6

Published in Elsevier *Organic Electronics*, Vol. 85, October 2020. DOI: 10.1016/j.orgel.2020.105882

# Ultra-low noise PEDOT:PSS electrodes on bacterial cellulose: A sensor to access bioelectrical signals in non-electrogenic cells

This study is focused on the particular advantages of organic-based devices to measure cells that do not generate action potentials, also known as non-electrogenic cells. While there is a vast literature about the application of organic conductors to measure neurons, cardiomyocytes and brain tissues, electrical measurements of non-electrogenic cells are rare. This is because non-electrogenic cells generate weak signals with frequencies below 1 Hz. Designing low noise devices in a millihertz frequency range is extremely challenging due to the intrinsic thermal and 1/*f* type noise generated by the sensing electrode. Here, we demonstrate that the coating of cellulose nanofibers with conducting PEDOT:PSS ink allows the fabrication of a nanostructured surface that establishes a low electrical double-layer resistance with liquid solutions. The low interfacial resistance combined with the large effective sensing area of PEDOT:PSS electrodes minimizes the thermal noise and lowers the amplitude detection limit of the sensor. The electrode noise decreases with frequency from 548 nV r.m.s at 0.1 Hz to a minimum of 6 nV r.m.s for frequencies higher than 100 Hz. This low noise makes it possible to measure low frequency bioelectrical communication signals, typical of non-electrogenic cells, that have until now been difficult to explore using metallic-based microelectrode arrays. The performance of the PEDOT:PSS-based electrodes is demonstrated by recording signals generated by populations of glioma cells with a signal-to-noise ratio as high as 140.

## 6.1− Introduction

Organic conductors and semiconductors are widely accepted as ideal materials to develop the next generation of electrophysiological sensing devices [1−4]. Organic-based electronics possesses the desired mechanical compliance with soft matter and elicit signals with a better signal-to-noise ratio (SNR) than conventional metallic electrodes [5−10]. A number of studies in the literature have demonstrated the superior performance of organic semiconductors when incorporated into structures,

such as simple electrodes or transistors [11], to record bioelectrical signals from electrogenic cells, like neurons [6,12,13] and cardiomyocytes [14–16] and even for in vivo recordings [17,18].

The good electrical performance of organic-based devices is partly due to the low interfacial impedance, when in contact with liquids. Organic conducting polymers, and in particular, poly(3,4-ethylenedioxythiophene):polystyrene sulfonate (PEDOT:PSS), have an extremely high capacitance. Rivnay et al. [19] showed for the first time the intriguing feature that the capacitance in PEDOT:PSS films scales with their thickness and introduced the concept of volumetric capacitance [20].

The origin of the high capacitive behavior has been also addressed by Volkov et al. [21] who related the high capacitance with the polymer morphology. The authors based their arguments on the fact that as PEDOT:PSS consists on a two-phase structure, formed by hole-conducting PEDOT-rich grains and ion-conducting PSS-rich grains, the capacitance originates from electrical double layers formed along the interfaces between nano-scale PEDOT-rich and PSS-rich interconnected grains.

While the capacitance of PEDOT:PSS electrodes with electrolyte solutions has been well-documented, the corresponding parallel interfacial resistance, often also named charge transfer resistance or ionic resistance of the double layer, has not received so much attention, probably because scientists in this area have focused on recording action potentials. Action potentials generated by neurons or cardiac cells are fast varying signals occurring in milliseconds; their low impedance path is the interfacial capacitor. The corresponding parallel resistance is a high impedance path for alternate (ac) signals and essentially only contributes to sensor thermal noise. Nonetheless, it is desirable to have a relatively low resistance because it improves the signal-to-noise ratio.

When recording signals generated by non-electrogenic cells, the low frequency ($f$ < 1 Hz) noise is of utmost importance. For frequencies below 1 Hz, both the thermal noise and the $1/f$ noise, also known as pink noise [22], combine to increase the noise of the sensing electrode. This problem is aggravated by the low amplitude of the non-electrogenic cell signals, typically below 10 μV.

In biology, low frequency signals are particularly relevant because there is an enormous variety of cell-cell communication mechanisms that use extremely low frequency ($f$ < mHz) signals. For example, cancer cells use low frequency signals to proliferate, migrate and synchronize their activity [23,24]. Recently, the measurement of bioelectrical signals generated by non-electrogenic cells has started to attract attention. Using gold-based electrodes, we previously reported the recording of these low frequency signals in astrocyte populations and in glioma cells [25–28], and others have also reported the recording of signals in prostate cancer cells [29] using similar electrodes. Other approaches have used organic-based transistors to stimulate astrocytes [30] and silver nanowires to record astrocyte signals [31]. However, the detection of these low frequency cellular signals with a

good signal-to-noise ratio relies on the use of very large sensing areas ($cm^2$ range). This strategy has two severe handicaps: firstly, there is a total lack of spatial resolution and, secondly, the co-occurrence of many uncorrelated signals results in an overall signal that resembles noise.

In this study, we propose that organic-based devices, due to their low interfacial resistance with liquids, offer a disruptive technology to access an important class of low frequency bioelectrical communications in non-electrogenic cells. The low interfacial resistance of organic devices has two important roles that are presented and discussed. First, the low resistance minimizes the thermal noise and, second, provides a low impedance path for slow varying or long-lasting signals. This steady-state component of the signal contributes to increase the recorded signal strength, therefore increasing the SNR.

With the perspective of taking full advantage of the electronic properties of the organic thin films, we deposited PEDOT:PSS on bacterial cellulose (BC) substrates. BC is a biomaterial produced by some non-pathogenic bacteria in the form of wet membranes [32]. In comparison with plant cellulose, BC has several advantages such as high purity, superior water uptake capacity and mechanical robustness. In the context of PEDOT:PSS-based electrophysiological devices, BC offers a number of crucial advantages. Particularly relevant is the good adhesion of PEDOT:PSS to the BC substrates. PEDOT:PSS does not delaminate from BC substrates, as often occurs in flat substrates, such as glass. In addition, BC has a peculiar 3D porous structure composed of nano- and micro-fibrils [32] whose micro-roughness provides an enhanced active area to contact with cells. Further, such microarchitecture and porosity can be adjusted by controlling the bacteria fermentation process [33]. The high affinity for water results in hydrogel-like properties, which are ideal to host cells. In addition, BC is approved by United States Food and Drug Administration (FDA) to be used in biomedical devices [34] and it has been explored in tissue engineering [35], wound healing [36,37], and drug delivery [38–43] among others. However, to the best of our knowledge, the use of BC membranes has never been addressed for electrophysiological-based devices.

The basic concepts of the interfacial electrical double-layer and the role of each impedance component (capacitance and resistance) on the recorded signal shape and thermal noise is presented. Then, the low frequency impedance of PEDOT:PSS deposited either on glass or on bacterial cellulose (BC) is compared with a gold electrode. The thermal noise of the different sensing surfaces is compared to establish the detection limit of each type of electrode. The well-characterized beating of a zebrafish heart is used to benchmark the relative performance of each of the sensing surfaces being analyzed. The optimized sensor using PEDOT:PSS on bacterial cellulose is then applied to record oscillations in glioma cells. Finally, the advantages of using PEDOT:PSS-based electrodes in low frequency electrophysiology studies are discussed.

# 6.2− Materials and methods

## 6.2.1– Fabrication of nanofibrous bacterial cellulose

Bacterial cellulose membranes were produced by the *Gluconacetobacter sacchari* strain, in Hestrin and Schramm (HS) medium, using glucose as the carbon source [44]. In more detail, flasks with the *G. sacchari* bacteria were kept in static conditions, at 30 °C, for 96 h. After that period, the membranes were removed and treated three times with 0.5 M of sodium hydroxide, at 90 °C, for 30 min. Afterwards, the membranes were purified by washing with distilled water. In order to obtain thin membranes, wet membranes were dried at 40 °C.

## 6.2.2– Electrodes

A standard ink-jet printer (DMP-2831, Fujifilm Dimatix Material Printer) was used to print the sensing devices. Poly(3,4-ethylenedioxythiophene):polystyrene sulfonate, also known as PEDOT: PSS, was purchased from AGFA Orgacon™. The PEDOT:PSS ink was loaded into a proprietary cartridge model (DMC-11610, Fujifilm). Each printed electrode was the result of eight consecutive prints, resulting in 8 layers of PEDOT:PSS, which corresponds to a thickness of approximately 500 nm. The samples were annealed on a hot plate at 60 °C for 8 h. After annealing, the films were immersed into ethylene glycol (EG) and then dried in a vacuum oven at 60 °C for 12 h. Gold electrodes were deposited by thermal evaporation through a shadow mask. The electrodes are approximately 200 nm thick. The electrode design consisted of parallel fingers with equal dimensions, with a depth (*D*) of 0.5 mm, length (*W*) of 10 mm, and separated by a gap distance (*L*) of 0.5 mm, forming a total printed electrode area of 5 $mm^2$. Only 2 $mm^2$ was used for sensing. A photograph of the fabricated electrodes made of gold and PEDOT:PSS on bacterial cellulose and of PEDOT:PSS on a glass slide is shown in Figure 6.1 (b).

## 6.2.3– Electrical and atomic force microscopy characterization

The entire electrical system was maintained within a large iron Faraday cage to minimize external interference. The small-signal impedance measurements were carried out using an RCL meter (Fluke PM 6306), within a frequency range of 50 Hz–1 MHz, by applying an ac voltage of 50 mV. Electrical noise measurements were performed using low noise voltage and current pre-amplifiers (SR 560, and the SR 570 Stanford Research Systems) configured for single-ended input. The preamplifiers were connected to a dynamic signal analyzer (DSA) (35670A, Agilent). The DSA recorded the output signal

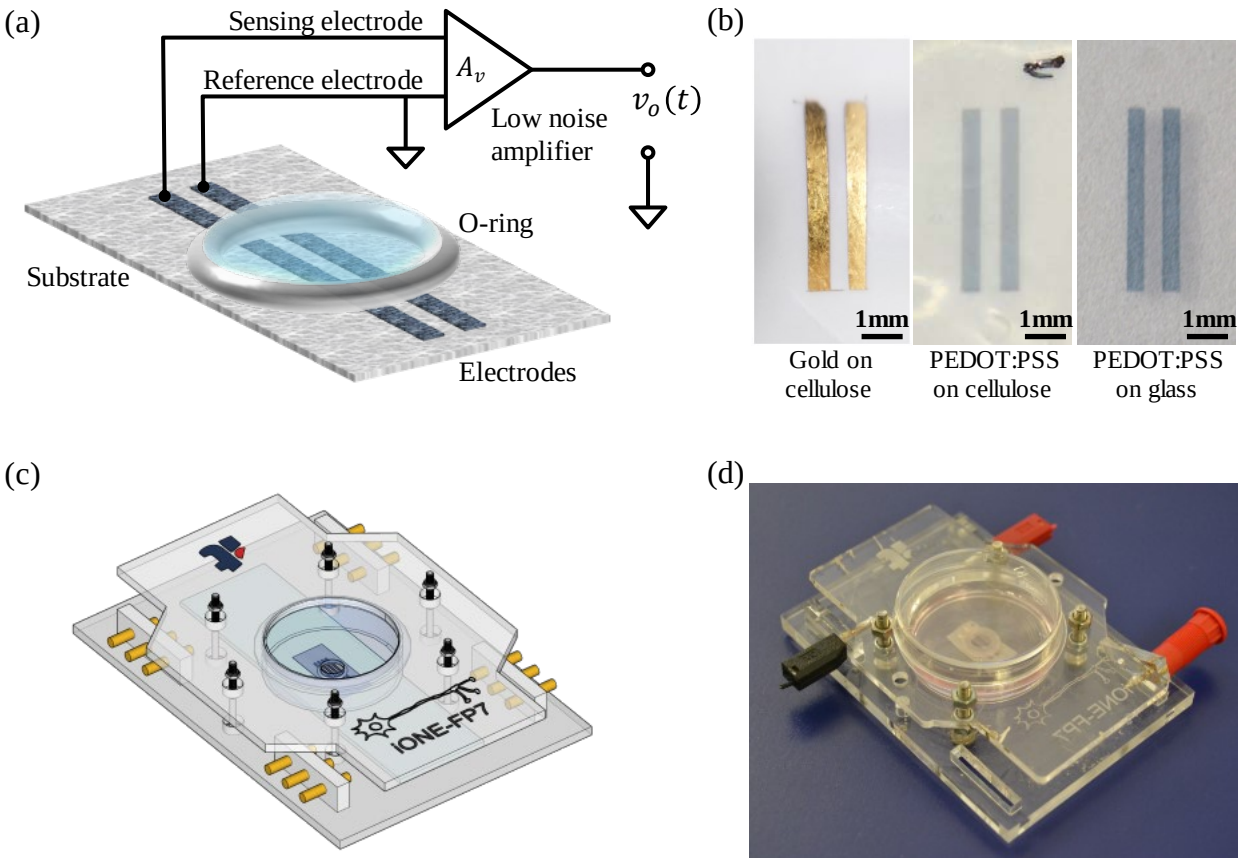


**Figure 6.1 –** Electrodes and sample holders. (**a**) Schematic diagram of the device and the electrical connections to the amplifier. (**b**) Photographs of the three types of electrodes fabricated. (**c**) Schematic model of the sensor in the sample holder. (**d**) Photograph of the fabricated prototype. Reproduced from reference [64] with permission from Elsevier, licence number 5506471207921 (Mar 12,2023).

of each preamplifier by applying uniform windows with unitary amplitude to the input signal, proceeded by an FFT to determine the spectral signal density ($S_n$). The output noise for the setup using the SR560 is given by $S_n(f) = (S_v(f)/A_V)^2$, where $S_v(f)$ is the r.m.s noise measured in V/√Hz for a given frequency, and $A_V$ is the gain of the amplifier.

The power spectral density was measured by dividing the full frequency range ($10^{-2}$ - $10^{-5}$ Hz) in several shorter ranges. The total smoothed power spectrum was obtained by joining the 15 shorter frequency bands i.e. 6.25 Hz, 12.5 Hz, 25 Hz, 50 Hz, 100 Hz, 200 Hz, 400 Hz, 800 Hz, 1.6 kHz, 3.2 kHz, 6.4 kHz, 12.8 kHz, 25.6 kHz, 51.2 kHz and 102.4 kHz. All frequency spans represent an average of at least 100 continuous recordings.

Due to redox reactions at the electrode-cell interface, DC voltage levels appear at the sensing electrodes. This DC offset causes a differential DC input signal that can saturate a high-gain DC-coupled differential amplifier [45]. The DC offset was removed by adjusting a tuning capacitance using the front-end offset potentiometer of the SR 560 amplifier.

3 or 4 pairs of sensing electrodes for each type of material and substrate were characterized. Although there is a small variability of the impedance and noise caused by the material processing, there is also variability caused by the mounting of the sample holder. Because it is difficult to discriminate both sources of variability, statistical analysis of electrical measurements was not carried out.

The bacterial cellulose surface was characterized by atomic force microscopy (AFM) using a NanoObserver from Concept Scientific Instruments (CSI). The sample morphology was analyzed in noncontact mode using silicon probes from APPNano with a radius smaller than 10 nm. The obtained images were processed and analyzed using Gwyddion software.

A Students *t*-test was used to evaluate the statistics of the signal-to-noise ratio and to estimate the significance level (*p*).

Histogram analysis was used to evaluate the recorded burst of ultra-low frequency signals generated by the Rat C6 glioma cells. The histogram uses bin distributed logarithmic in frequency.

### 6.2.4− Biological material

Rat glioma cells C6 (ATCC® CCL−107™) were cultured in F–12K nutrient medium supplemented with 15% fetal horse serum, 2.5% fetal bovine serum, and 1% penicillin and streptomycin. The cells were maintained in an aseptic environment at 37 °C in a $CO_2$ incubator (Thermo Scientific Midi 40) with a humidified atmosphere and 5% $CO_2$. The cells were harvested, and 50,000 cells were transferred to the sensing device in 400 μL of medium. The cell suspension generated a confluent monolayer of cells that covered the entire device surface. A zebrafish heart, when kept in a suitable environment, can beat in a reproducible way for a period as long as 8 h. This is enough time to move the heart to different electrodes and record the corresponding cardiac signal. Three experiments with three different zebrafish hearts were carried out. However, the data presented here refers to a single heart, the strongest beating one. The dependence of SNR on the electrode material was identical in all hearts tested. Zebrafish were anesthetized and sacrificed by immersion in water with an overdose of 300 mg $L^{-1}$ ethyl-3-aminobenzoate methane sulfonate salt (MS222). The hearts from the zebrafish were surgically extracted and placed in Krebs solution (400 μL) at 24 °C. Under these conditions the hearts kept beating for up to 24 h. The size of the zebrafish heart is about 1 mm and it beats about twice a second. Fish care and experimentation complied with the national legislation for the use of laboratory animals under a Group-1 license issued by the Veterinary General Directorate of the Ministry of Agriculture, Rural Development and Fisheries of Portugal.

# 6.3– Results

The goal of this study was to demonstrate the two-fold role of the electrical double-layer (EDL) resistance on the quality of the recorded part is focused on the role of the EDL resistance in minimizing the thermal noise. The electrode performance is demonstrated in the high frequency region (kHz) by measuring the beating of a zebrafish heart. The second part demonstrates the role of the EDL resistance on the shape of the signal. Finally, in the third part, by measuring signals in populations of glioma cells, we demonstrate the performance of the electrodes in the ultra-low frequency region ($f$ < 0.1 Hz).

## 6.3.1− Small signal impedance of the sensing electrodes

We [46] and other authors [16,47–50] have previously described the electrical coupling between cells and sensing electrodes and, for this reason, only a brief summary of the essential features needed to understand the data analysis is provided. The sensing layer is the electrical double-layer (EDL), which, in a simplistic way, is described by an equivalent parallel RC circuit network, as shown in the inset of Figure 6.2 (a). EDL is modeled by the parallel network comprised of the double layer capacitance ($C_D$) and resistance ($R_D$), also known as charge transfer resistance or ionic resistance of the double layer. The EDL is in series with the bulk electrolyte layer. The bulk electrolyte layer is formed by the parallel network comprised by the bulk resistance ($R_E$) and capacitance ($C_E$). We also include a series resistance ($R_S$), due to the electrode. $R_S$ is very small for metallic electrodes, but it cannot be neglected when PEDOT:PSS electrodes are used.

The impedance analyzer measures the overall parallel components $R_P$ and $C_P$. The impedance of the system is strongly frequency dependent. The frequency dependence arises from the fact that $C_D$ is higher than the capacitance of the series bulk electrolyte solution ($C_E$). The electrode in contact with a liquid behaves as two-layers in series, in addition $C_D$ and $R_D$ are also frequency dependent. Figure 6.2 (a) shows the measured parallel capacitance ($C_P$) and the parallel resistance ($R_P$) expressed as loss ($L_P$). $L_P = 1/(2.\pi.f.R_P)$, where $f$ is the frequency of the ac probing signal. $L_P$ has a relaxation called the Maxwell-Wagner relaxation [51]. This relaxation occurs at the frequency at which the high interfacial capacitance begins to be short-circuited as the frequency of the signal increases.

The power spectral density of the electrical noise in voltage ($S_V$) measured for the gold/electrolyte interface is shown in Figure 6.2 (b). The gold electrode was deposited on a thermally oxidized silicon substrate and the electrolyte was the cell culture medium. The electrode design is presented in Figure 6.1 (b). For frequencies below 1 Hz, the noise evolves approximately as $1/f^2$. This type of noise is known as pink noise and is common in EDLs [52]. In general terms, this type of noise has power spectra following a $1/f^{\alpha}$ (with $0.5 \lesssim \alpha \lesssim 1.5$) behavior at low frequencies. It has been observed in a

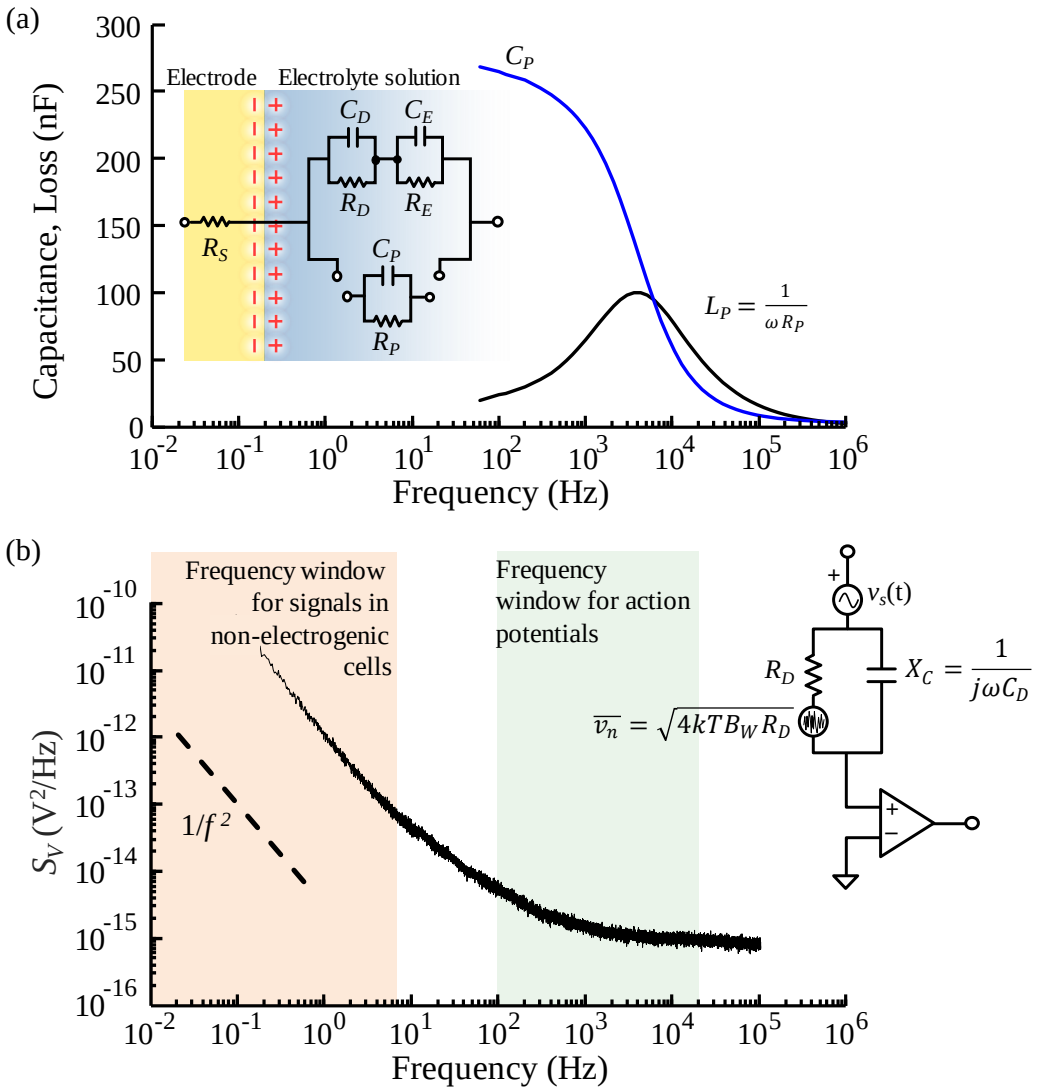


**Figure 6.2 –** Electrical double-layers, equivalent circuit and the thermal noise. (**a**) Frequency response of a gold/electrolyte system in a thermally oxidized silicon substrate. The inset scheme represents the simplified equivalent circuit of the EDL in series with the bulk electrolyte. (**b**) Noise ($S_V$) power spectrum density for the electrode with the impedance presented in (a). The inset circuit represents the thermal noise due to $R_D$. Reproduced from reference [64] with permission from Elsevier, licence number 5506471207921 (Mar 12,2023).

large variety of areas, including, physics, biology and music. However, no general physical explanation of $1/f$ noise has been proposed and its physical origin remains unsolved.

The pink noise in electrode/electrolyte systems was analyzed in detail in a study by Hassid et al. [52]. This reference on the noise of electrode/electrolyte systems shows that in the absence of electrochemical reactions at the electrode interface, the system should only exhibit thermal noise. The observation of excess noise is only expected when charge transfer occurs at the interface. The shape of the noise spectrum depends then on the nature of the charge transfer process: (i) if the mass transfer at the interface is dominated by electric fields, then noise spectra possess a $1/f$ type dependency; (ii) if the charge relocation is dominated by diffusion, the dependency will be of $1/f^2$ type.

For frequencies above 1 kHz the noise becomes frequency independent (white noise). This noise is caused by thermal noise generated by the resistance associated with the electrode/electrolyte interface. In contrast to the pink noise, thermal noise is well understood and quantitatively explained. The equivalent circuit in the inset of Figure 6.2 (b) shows the noiseless resistor ($R_D$) in series with the corresponding thermal noise source ($v_n$).

The frequency regions relevant for two types of electrophysiological processes, action potentials and slow oscillations are also highlighted in Figure 6.2 (b). The recording of action potentials requires a bandwidth of a few kilohertz (300 Hz − 5 kHz) [53], while bioelectrical oscillations generated by non-electrogenic cells require a frequency window from mHz up to 1 Hz. This milli-hertz spectral region is dominated by pink noise as shown in Figure 6.2 (b). When the goal is to develop devices to measure non-electrogenic cells, the lowering of the interfacial resistance is a critical issue. A low interfacial resistance minimizes the intrinsic electrode noise, and PEDOT:PSS-based electrodes on bacterial cellulose substrates offer the lowest interfacial resistance and, therefore, the lowest intrinsic noise. To show that PEDOT:PSS has the performance required to measure non-electrogenic cells, the PEDOT:PSS impedance was compared with the impedance of a metal electrode (gold) and how the morphology of the substrate modifies the impedance of the sensing surface is also demonstrated. The impedance of several electrode/electrolyte interfaces is shown below. The frequency dependence of the parallel capacitance ($C_P$) is presented in Figure 6.3 (a) and the corresponding parallel loss ($L_P$) in

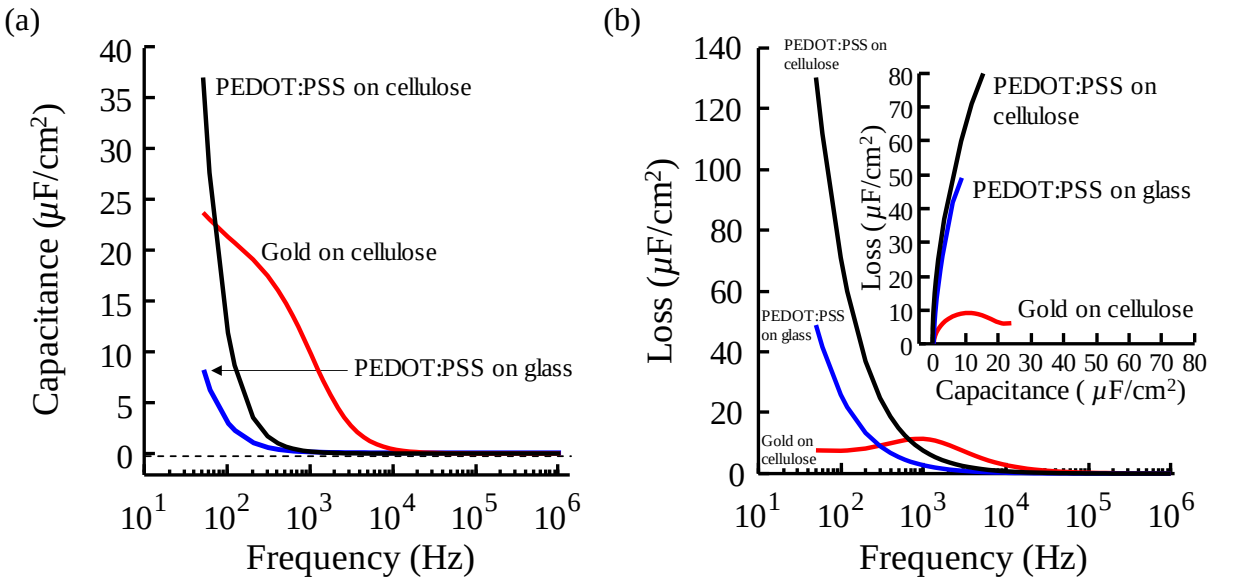


**Figure 6.3 –** Comparison between the impedance parameters, capacitance and resistance of printed PEDOT:PSS and gold electrodes on cellulose or glass substrates. (**a**) Frequency dependence of capacitance ($C_P$) and in (**b**) frequency dependence of loss ($L_P$). The inset shows $C_P$ and $L_P$ in a Cole-Cole representation. All plots were normalized by the total sensing electrode area, A = 2 mm$^2$. Reproduced from reference [64] with permission from Elsevier, licence number 5506471207921 (Mar 12,2023).

Figure 6.3 (b). This individual representation of capacitive and resistive components discriminates better their individual contributions to the impedance of the electrodes and the substrate. In agreement with previous reports, PEDOT:PSS offers a remarkably low impedance when compared with gold electrodes. Interestingly, the analysis of the individual impedance components, $C_P$ and $R_P$, reveals that, for frequencies above 1 kHz, the lowering of the impedance is essentially due to a lower interfacial resistance of the PEDOT:PSS electrodes. This low resistance is particularly important for lowering the intrinsic thermal noise.

Figure 6.3 (b) compares the loss as a function of frequency, for the three electrodes under study. The loss of the PEDOT:PSS measured at the frequency of 60 Hz is approximately 14 times higher than the loss of the gold-based electrode. Since loss is inversely proportional to the resistance, the PEDOT:PSS has 14 times lower resistance than the gold electrode. The difference in resistance between the PEDOT:PSS electrode printed on glass and on cellulose is due to the higher effective surface area of the cellulose nanofibers.

The inset in Figure 6.3 (b) shows $C_P$ and $L_P$ in a Cole-Cole representation. In this type of plot, a resistor is simply a dot while an ideal capacitor is a horizontal straight line.

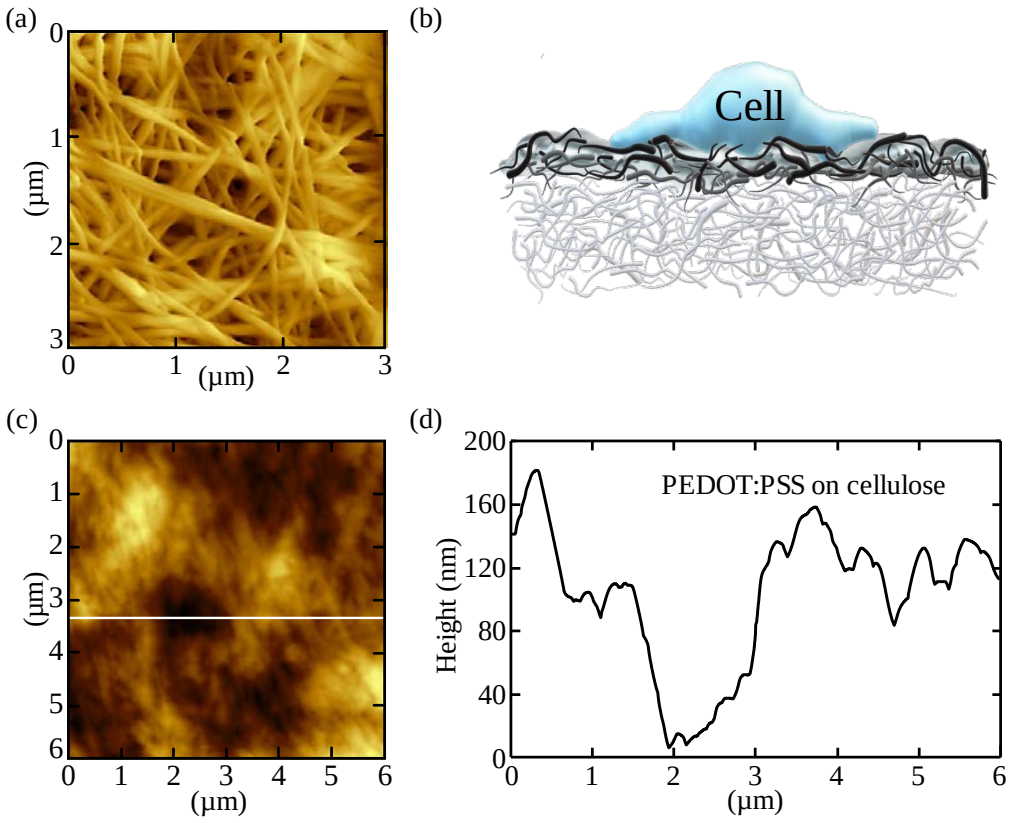


**Figure 6.4 –** Morphology of the bacterial cellulose substrate. (**a**) Topography AFM image with a scan area of 3 × 3 µm$^2$ of the surface of the bacterial cellulose showing nano-fibrillar structures. (**b**) Schematic representation of the PEDOT:PSS sensing electrode with cells on the bacterial cellulose substrate. (**c**) Topography AFM image of inkjet-printed PEDOT:PSS on bacterial cellulose. (**d**) Profile view of the PEDOT:PSS/bacterial cellulose electrode. Reproduced from reference [64] with permission from Elsevier, licence number 5506471207921 (Mar 12,2023).

The low impedance of PEDOT:PSS on bacterial cellulose (BC) is related to the morphological structure of the BC membrane as shown in Figure 6.4 (a). Bacterial cellulose is formed by an entangled mesh of nanofibers, approximately 100 nm thick and several microns long. Living cells seeded on these substrates encounter a 3D-like surface, as schematically represented in Figure 6.4 (b), that better mimics the extracellular matrix. Figure 6.4 (c) shows an AFM topography image of the cellulose coated with a PEDOT:PSS thin film. The corresponding profile view is shown in Figure 6.4 (d). The roughness of cellulose means it has valleys that can reach 180 nm deep. When the PEDOT:PSS ink impregnates the upper cellulose fibers, it enhances the active area of the electrode. The frequency dependence of the noise ($S_V$) for the four types of electrodes under study is compared in Figure 6.5. The amplifier noise ($S_V = 10^{-17}$ V$^2$/Hz for a bandwidth higher than 300 Hz) is well below the noise generated by the electrodes and all extrinsic noise sources have been minimized by appropriate shielding and grounding as described in the experimental section. The gold electrode, deposited either on glass or on cellulose, has the highest noise. The higher noise of the gold electrode is in line with the higher interfacial resistance. The lowest thermal noise ($S_V$ = 6 nV r.m.s) is observed for frequencies above 100 Hz and this noise is achieved when PEDOT:PSS is printed on bacterial cellulose, in agreement with the lowest interfacial resistance. The noise power spectral density analysis also shows that, for frequencies above 10 Hz, the noise of PEDOT:PSS on bacterial cellulose is one order of magnitude lower than the noise generated by a gold electrode on cellulose (Figure 6.5). The extremely

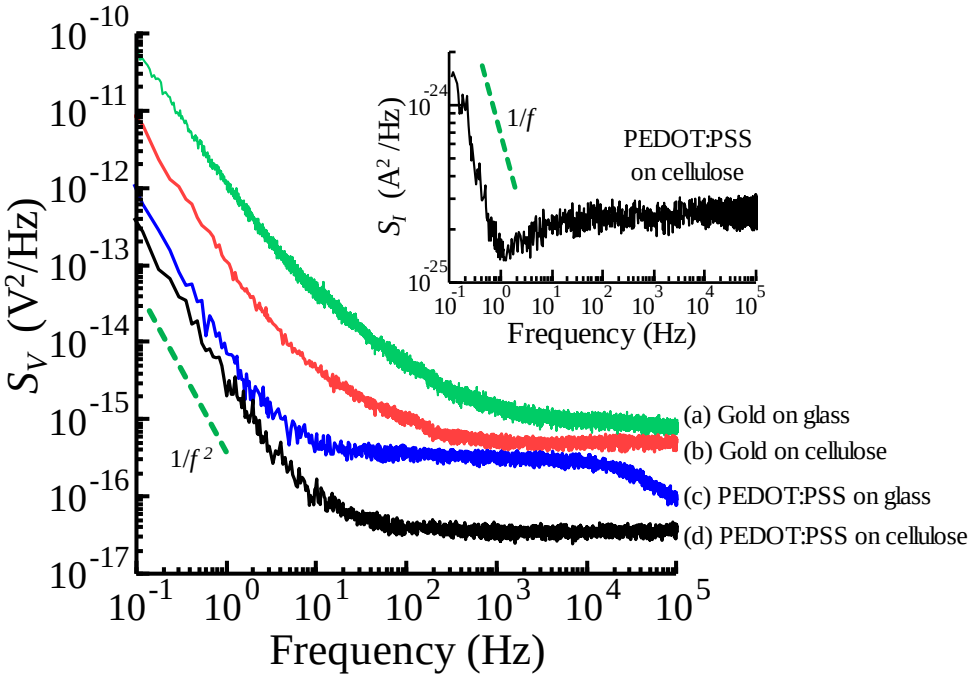


**Figure 6.5 –** Noise power spectral density ($S_V$) for the four different types of electrodes (gold and PEDOT:PSS, deposited on glass or on bacterial cellulose) evaluated in this study. (a)-green, gold on glass; (b)-red, gold on bacterial cellulose; (c)-blue, PEDOT:PSS on glass and (d)-black, PEDOT:PSS on cellulose. The inset shows the noise of the PEDOT:PSS on cellulose electrode when measured as current. Reproduced from reference [64] with permission from Elsevier, licence number 5506471207921 (Mar 12,2023).

low noise of the PEDOT:PSS-based electrodes extend up to frequencies as high as 100 kHz, also covering the frequency band used to measure action potentials. Although this work has focused on the recording of low frequency signals, where noise is a critical issue, in reality PEDOT:PSS electrodes are advantageous over the full frequency range used to measure electrophysiological signals. The pink noise ($1/f^2$ dependence) is common to all electrodes. With the exception of the curve corresponding to the PEDOT:PSS on glass, all the other curves shown in Figure 6.5 run parallel to each other. This independence of the $1/f$ noise on the electrode material may shed some light into the physical origin of this type of noise in electrode/electrolyte systems.

The spectral dependence of the noise measured in current for a PEDOT:PSS-based electrode on a cellulose substrate is shown in the inset of Figure 6.5. The noise in current shows two distinct spectral regions separated by a valley centered at 1 Hz. Below 1 Hz, the noise increases following the $1/f$ dependence. In contrast, above 1 Hz the noise increases until a plateau is reached at a frequency of 100 Hz. When measured in current detection method, the noise of the PEDOT:PSS electrode on cellulose has two relevant features; (i) it follows a $1/f$ dependency, which is a smoother rise than the $1/f^2$ dependence observed in voltage detection mode and, (ii) the onset of the $1/f$ tail begins one decade lower in frequency than the $1/f^2$ tail. These two aspects of the current detection mode are beneficial for low frequency measurements because they contribute to increase the SNR. Having characterized the intrinsic noise of the electrodes, we now proceed to show how the noise affects the quality of the recorded signal. The best way to evaluate the relative performance of our sensing electrodes is to use a well-defined bioelectrical signal source and perform comparative recordings with all the electrodes. For this purpose, a surgically extracted zebrafish heart was placed on top of the sensing electrode. To assure that the signal strength was identical in all experiments, the same zebrafish heart was moved between devices and used for all the electrodes under study. This procedure was used as proof of concept, assuring that the signal strength was equal in all the experiments. The relative quality of the signals recorded by the different electrodes was compared and is shown in Figure 6.6 (a) and (b). The highest SNR of 55 (in voltage detection mode) was obtained using PEDOT:PSS on bacterial cellulose and the poorest recordings (SNR = 10) were obtained with a gold electrode on the cellulose substrate. As described above, the high signal quality obtained using PEDOT:PSS on bacterial cellulose is due to the lower noise and to the higher interfacial capacitance. The relative values of the SNR are shown in the bar plot in Figure 6.6 (c) for both voltage and current detection modes. The comparative effect of detecting signals in voltage or in current has been addressed in our previous works [26].

### 6.3.2− Effect of the electrode/electrolyte interfacial resistance on the signal shape

The low interfacial resistance of the PEDOT:PSS/electrolyte interface minimizes the thermal noise, and the recorded signal shape is such that it improves the SNR. In order to understand the role of the resistance and capacitance in the definition of the signal shape, we need to analyze the current flowing through the equivalent circuit that describes the electrode/electrolyte interface, as shown in Figure 6.7 (a). In this analysis, the bulk electrolyte layer is described by the resistance $R_E$. In the equivalent circuit represented in Figure 6.2 $C_E$ was ignored because it is relatively small when compared with $C_D$. When a single square voltage pulse is applied to the device, the current $i_S(t)$ that flows through the system consists of two components, one is the displacement current through $C_D$, and the other is a steady state current flowing through $R_D$:

$$i_S(t) = C_D \frac{dv_C(t)}{dt} + \frac{v_C(t)}{R_D} \tag{6.1}$$

To calculate $i_s(t)$ the differential Equation (6.1) for the voltage, $v_C$ $(t)$, across the capacitor $C_D$ has to be solved [46]. The analytical solution is given in terms of the time constant $\tau$,

$$\tau = \frac{R_D R_E C_D}{R_D + R_E} \tag{6.2}$$

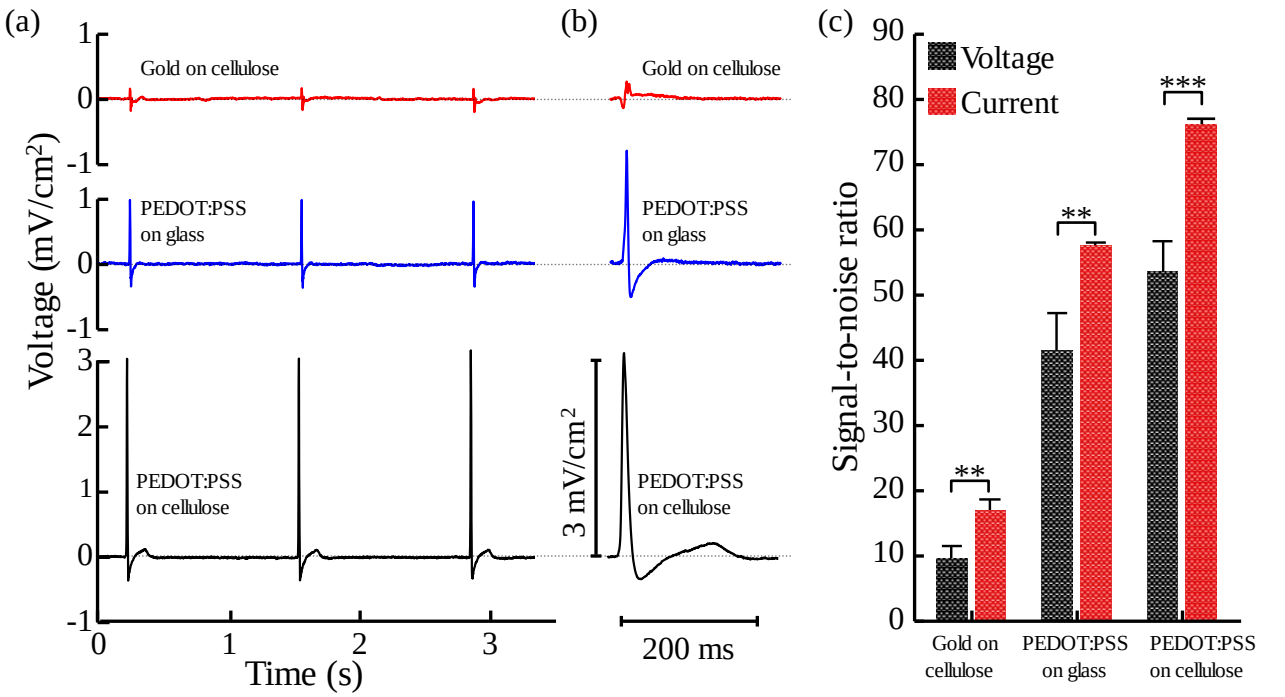


**Figure 6.6 –** Comparison of the signal quality obtained using different types of electrodes. (**a**) Three consecutive zebrafish heart beat. (**b**) Detailed view of individual signals. (**c**) Signal-to-noise ratio measured both in current and voltage detection mode in different types of electrodes. Signals were generated by placing the same zebrafish heart on top of each of the electrodes. ** and *** denote significant differences between SNR values detected in voltage and current modes of $p < 0.01$ and $p < 0.001$ (Student *t*-test), respectively. Reproduced from reference [64] with permission from Elsevier, licence number 5506471207921 (Mar 12,2023).

τ in Equation (6.2) is the time constant of an RC circuit with an effective resistance consisting of two in-parallel resistors ($R_D$ and $R_E$).

To visualize how the circuit time constant affects the shape of the signal, an experiment was performed in which a well-defined square-like signal from a signal generator was applied to the counter electrode. The flow of signal through the EDL was recorded as current signal on the sensing electrode.

The signal shapes recorded in current upon the application of an input voltage pulse of 100 μV for 2 s is presented in Figure 6.7 (b). When the signal was recorded with a gold electrode (see red curve in Figure 6.7 (b)), the corresponding signal in current was comprised of two current spikes, one upward at the rising edge and another downward at the falling edge of the voltage pulse, which are displacement currents. When the voltage was constant, the current fell rapidly to zero because the gold/electrolyte interface behaved almost as a purely capacitive interface. The application of an identical voltage pulse to a PEDOT:PSS-cellulose/ electrolyte interface causes a slightly different response of the current signal, (see black curve in Figure 6.7 (b)).

The output current signal also contains the current displacement spikes, but now the current takes nearly 2 s to decay to a steady state. Figure 6.7 (c) shows that the current decay is not a pure exponential as predicted by the simple equivalent circuit but is comprised of a fast component ($\tau_1$ = 0.25 s) followed by a slower component ($\tau_2$ = 0.64 s). We will show that these times constants are one order of magnitude higher than the predicted time constant based on Equation (6.2).

To obtain τ using Equation (6.2) we need to know the quasi-static values of $C_D$, $R_D$ and $R_E$. However both $C_D$ and $R_D$ are frequency dependent, and the lowest frequency of our impedance analyzer is 60 Hz. To obtain the quasi-static values we measured a series of current-voltage ($I$–$V$) loops with voltage

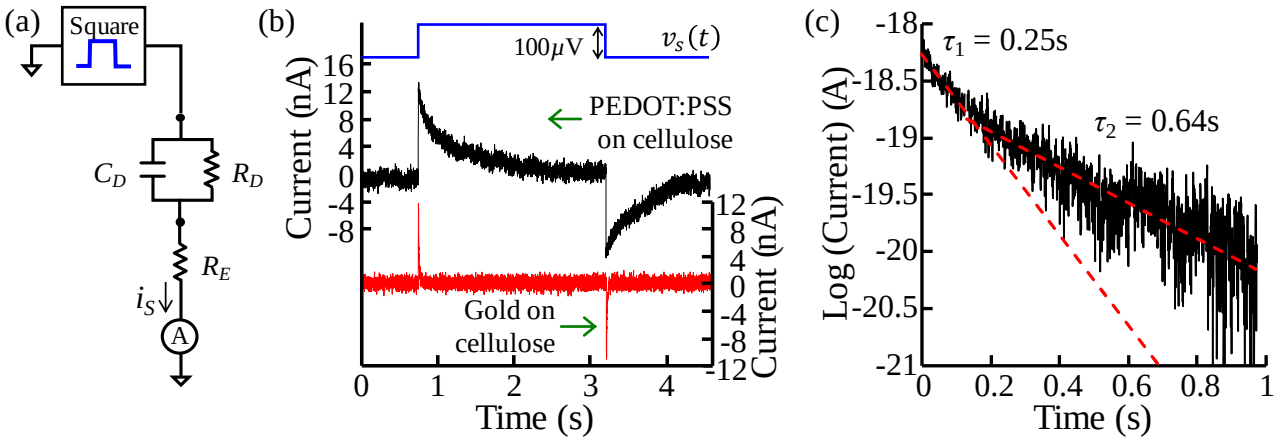


**Figure 6.7 –** The electrical signal recorded on different electrodes upon the application of a square voltage pulse. (**a**) Equivalent circuit used to interpret the transient response to a voltage pulse. (**b**) Comparison of the response of a gold-based electrode with the response of a PEDOT:PSS electrode printed on a bacterial cellulose substrate. (**c**) semi-logarithmic plot of the current decay across the PEDOT/electrolyte interface on cellulose after the application of a voltage step of 100 μV. The dashed lines are fits to the fast ($\tau_1$ = 0.25s) and slow decay components ($\tau_2$ = 0.64 s). Reproduced from reference [64] with permission from Elsevier, licence number 5506471207921 (Mar 12,2023).

ramps with a scanning speed of 20–30 mV/s (not shown). The voltage range was limited to only 100 mV to minimize charging effects and redox reactions. From the hysteresis in the *I–V* loops, we extracted the displacement component that is related with the quasi-static capacitance, ($C_D$ = 100 μF) and from the DC component we extracted the quasi-static resistance ($R_D$ = 12.5 kΩ). The quasi-static capacitance is 134 times higher than the capacitance measured at 60 Hz ($C_D$ = 742 nF) and the quasi-static resistance is 10 times higher than the resistance measured at 60 Hz ($R_D$ = 1.2 kΩ). Using the quasi-static impedance values in Eq. (6.2) we estimate a $\tau$ of 34 ms, a value that is one order of magnitude lower than the values of 250 ms or 640 ms experimentally recorded.

We propose that the slow response of the PEDOT:PSS/electrolyte interface upon the application of a voltage step is caused by a charging effect on the PEDOT:PSS electrode. The application of a voltage step on the PEDOT:PSS electrodes causes outflow or inflow (depending on the voltage sign) of ionic species at the PEDOT:PSS electrode, moving the interface out of equilibrium. At the outer interface with the electrolyte, ion diffusion occurs at a fast time-scale; the non-equilibrium state generated by the voltage pulses is then rapidly re-equilibrated. However, ions that were pushed deeper into the PEDOT:PSS by the external field will face not only a constricted environment but also longer pathways to diffuse out to the free electrolyte. The consequence is that a longer time is needed for the system to re-attain again equilibrium once it has been displaced from it upon a voltage pulse. In summary, the shape of the current transient suggests that it is the redistribution of the ionic charges that governs the transient response time and not the RC time constant as estimated by simple equivalent circuit modeling. These results are in agreement with the reported transient response of organic electrochemical transistors, where it is claimed that the ion redistribution in the film determines the transient response [51,52], and in neuromorphic devices [54]. For example, it is known that protons, ($H^+$), can easily be transported via the water molecules within the PEDOT PSS film through Grotthuss mechanism where protons will be transported from one water molecule to another through hydrogen bonding [53].

### 6.3.3− Detection of signals in non-electrogenic cell populations

The optimized ultra-low noise PEDOT:PSS/bacterial cellulose electrodes were used to measure electrical fluctuations generated by populations of C6 glioma cells. Glioma cells synchronize their activity to generate cooperative oscillations. These oscillations travel across the cell network at speeds of 10–30 μm/s and often become quasi-periodic. Details about this bioelectrical phenomenon have previously been reported [30,55–58]. When the traveling oscillation hits the electrode, cells on top of the electrode synchronize and generate a voltage signal proportional to the width of the sensing

electrode. Glioma cells are a robust model to evaluate the detection limits and the performance of our PEDOT:PSS-based electrodes. This is because glioma cells generate long-lasting signals fitting well in the class of signals generated by non-electrogenic cells, for instance astrocytes [25,31] and prostate cancer cells [29]. A time-trace in current of quasi-periodic bursts of activity of C6 glioma cells is shown in Figure 6.8 (a). The pattern of activity is described in four spans: (i) silent region (green color); (ii) quasi-periodic signals, representing early synchronization of C6 cells (blue color); (iii) synchronized activity of C6 cells (black color); and (iv) weak and unsynchronized activity (red color). To identify the major signal frequencies, the inter-spike time intervals were analyzed and distributed into corresponding frequency bins to build the histogram in Figure 6.8 (b). This procedure was adopted

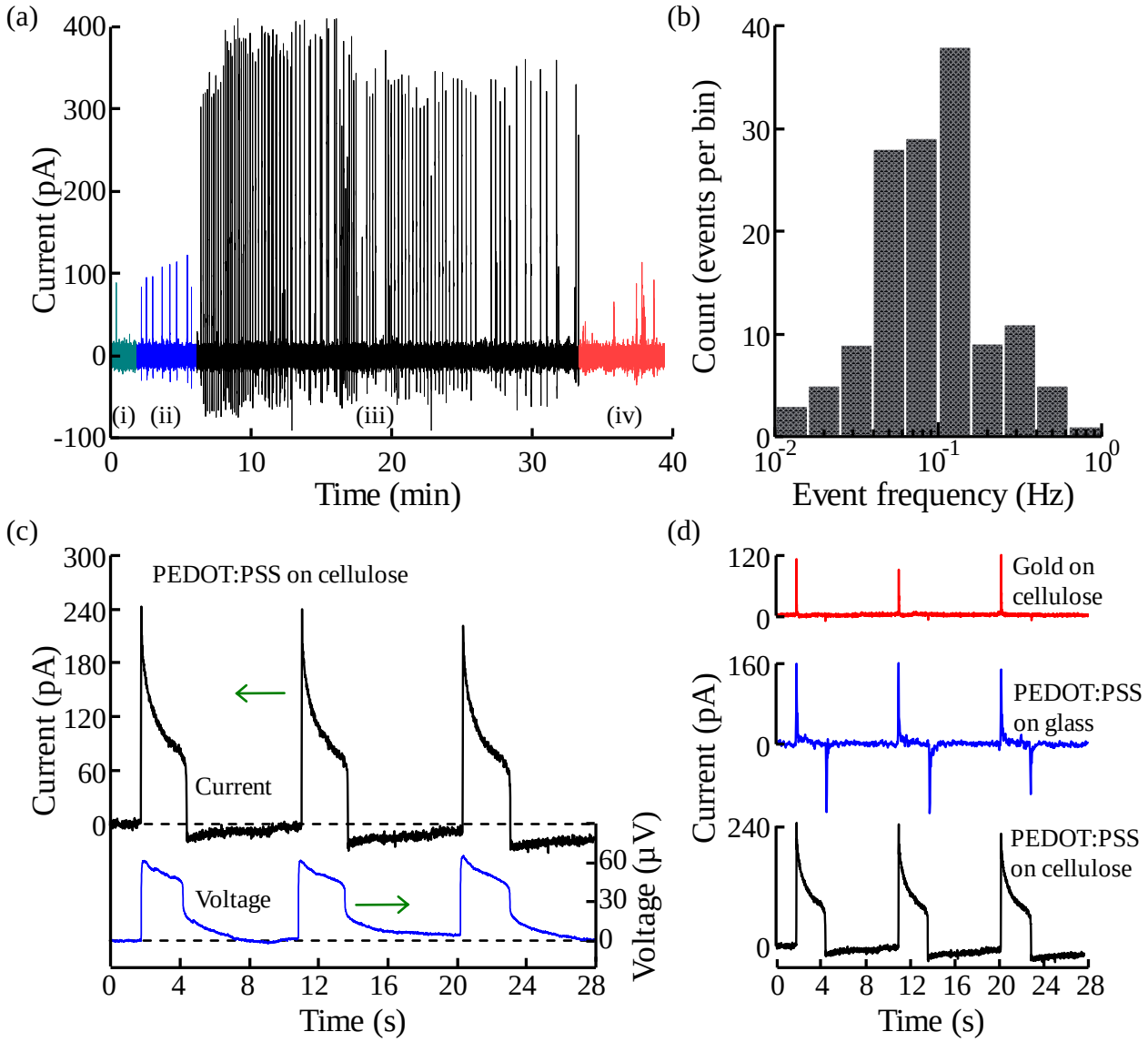


**Figure 6.8 –** (**a**) Time trace of current signals recorded in glioma cells using PEDOT:PSS-based electrodes in BC. (**b**) Histogram of the number of signals distributed into frequency slots. (**c**) Detailed view of the voltage and current signals recorded from a glioma population using a PEDOT:PSS/bacterial cellulose electrode. (**d**) Comparison of the signals recorded from a glioma cell population using different types of electrodes. Reproduced from reference [64] with permission from Elsevier, licence number 5506471207921 (Mar 12,2023).

because the signals were not periodic and had a broad distribution in frequency. For clarity, the bins on the histogram were distributed in a logarithmic frequency scale with 5 bins per interval of 10. The histogram shows that the dominant signal frequency is 0.126 ± 0.011 Hz. A detailed view of 3 consecutive individual signals, measured both as a current and voltage signal is shown in Figure 6.8 (c). The signal in voltage has a square-like shape of about 60 μV in amplitude and lasted for 2 s with an approximately 8 s periodicity and the corresponding signal in current followed the trend presented above. Displacement current spikes dominated the recorded signal edges. When the bioelectrical signal was measured as a current, both displacement currents and the dc contribution added together to strengthen the recorded bioelectrical signal.

To illustrate the dramatic effect of the electrode material on real recorded bioelectrical signals, three signals recorded for glioma cells are shown in Figure 6.8 (d). In gold-based electrodes, the displacement spikes dominate the signal. In PEDOT:PSS based electrodes, the slow relaxing component becomes pronounced, and the overall power of the signal is higher. As a consequence, there is a striking difference between the signal quality measured using bacterial cellulose and the other types of electrodes. The signals recorded using PEDOT:PSS/bacterial cellulose electrodes reach a SNR of 140, while the SNR is only 89 for PEDOT:PSS on glass. The improvement in signal quality, is due, to the high capacitance, to a lower noise, and also to a charging effect on the PEDOT:PSS.

It is important to emphasize that, in addition to the minimization of the thermal noise, charging effects on the PEDOT:PSS are also crucial in re-shaping the measured bioelectrical signal and in improving the SNR. As shown in Figure 6.7 (b), the slow decay in current upon the application of a voltage pulse introduces a slow component, which we attribute to a charge redistribution within the polymer. This charging effect should also occur in the PEDOT:PSS, when exposed to small ionic fluctuations generated by the cells. Figure 6.8 (c) shows clearly that the biosignal in voltage has a square-like component. This shape is expected because the native biosignal is a traveling wave crossing an electrode of a defined width as described in our previous publication [57]. However, the square voltage shape is followed by a slow component with a $\tau$ between 1.2 and 1.5 s. This slow relaxing phenomenon is in agreement with our previous analysis carried out using the simulated signal described in Figure 6.7. It is plausible that this slow decay of the biosignal is due to charges slowly relaxing back to equilibrium after the oscillation has passed through the electrode.

The voltage signal generated by the cell population may not be a symmetric signal, which means that the amplitude of the rising edge is not necessarily equal to the amplitude of the falling edge. This asymmetry becomes more pronounced when the signal is measured in current, because the

displacement spike is proportional to d$v$/d$t$ as shown in Equation (6.1). This feature may explain why the signal recorded using the gold electrode (in Figure 6.8 (d)) is strongly asymmetric.

### 6.3.4– Challenges in measuring populations of non-electrogenic cells using large area electrodes

A time trace of discrete and quasi-periodic discrete signals was presented above in Section 6.3.3, Figure 6.8. This signal behavior was used to highlight the improvement of the SNR when PEDOT:PSS based electrodes are used compared to gold electrodes.

Although, quasi-periodic behavior such as that shown in Figure 6.8 can often be recorded, a typical electrophysiological time trace usually consists of extended regions where discrete signals occur in a random manner and some regions may even resemble noise. Figure 6.9 shows two typical time traces for C6 glioma cell activity without quasi-periodic discrete signals. Figure 6.9 (a) is a representative example of activity recorded with PEDOT:PSS on bacterial cellulose, and Figure 6.9 (c) is an example of activity recorded with a gold electrode. The PSD of each time trace is shown in Figure 6.9 (b) and (d).

The time traces in Figure 6.9 show the onset of C6 bioelectrical activity after cell seeding at $t$ = 0 s. At the beginning, only the electrode noise can be observed. As time progresses, the signals become more frequent and have higher amplitude and duration (higher power). The increase in signal frequency and power suggests that the measured cell population forms a connected population and that some cells can synchronize their activity to generate signals with relatively high power. To illustrate how the signal frequency evolves with time, Figure 6.9 (b,d) shows the noise spectral density for different time points along the time trace (labeled regions (i), (ii) and (iii)). The black curves represent the electrode noise (see region (i)). As time progresses, the PSD increases in magnitude. This increase is particularly noticeable at frequencies below 20 Hz. The blue curves represent the early stages of C6 glioma cell activity (see region (ii)), but no discrete signals are observed, only a growth modulation of the noise amplitude. On the other hand, in the last hour of the two time traces showing the bioelectrical activity of the C6 cells in Figure 6.9 (a,c), the activity of the C6 cells is detected, but well defined discrete signals with a quasi-periodic behavior as the ones shown in Figure 6.8 are not observed.

The electrophysiological time trace of non-electrogenic cell populations often appears as a chaotic distribution of discrete signals with an ill-defined shape, randomly distributed in time and varying greatly in amplitude, as shown in
Figure 6.9. We hypothesize that this phenomenon occurs due to the lack of synchronization among the cells in the population.

Strong signals in the trace are possible generated by temporary synchronization of cells within clusters. However, these clusters only involve a small fraction of the entire cell population. It is also possible that there is a distribution of cell clusters that generates a corresponding distribution of signals.

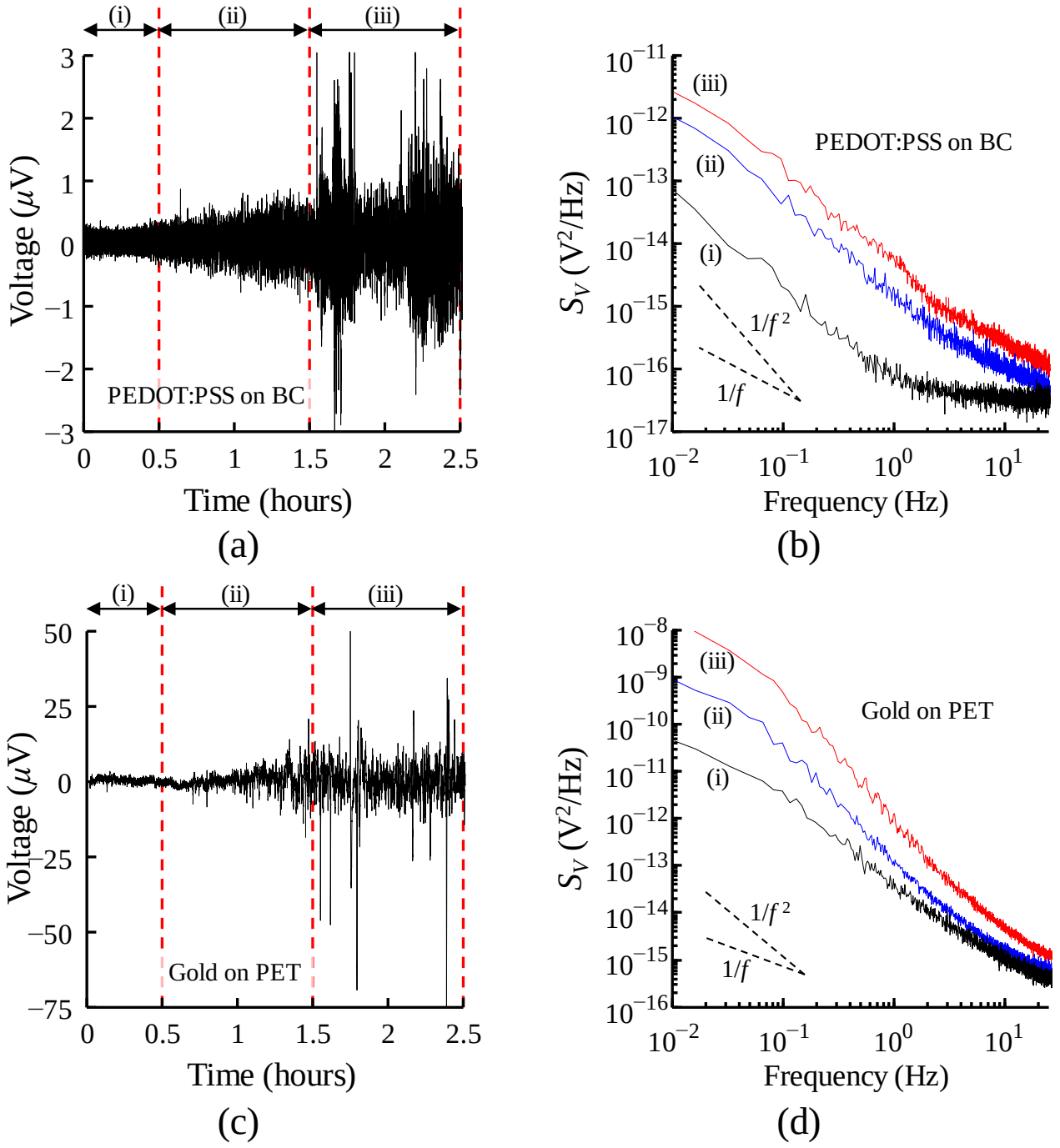


**Figure 6.9 –** Two different electrode types (PEDOT:PSS on BC and gold on PET) investigated in this study to optimise electrode geometry and area for measuring populations of glioma cells. (**a,c**) Time trace of voltage signals recorded in populations of glioma cells. (**b,d**) Noise power spectral density ($S_V$). Regions (i) to (iii) always represent the background noise without cell activity, and the early stage and established pattern of spontaneous cooperative activity.

Observing these signals as discrete and well-defined is challenging because simultaneous clusters may operate slightly out of phase, leading to partially superimposed signals.

Interestingly, we have observed that the higher the signal amplitude, the longer the signal duration, suggesting that larger cell clusters have a longer synchronization lifetime. Therefore, we conclude that the cell population is possible composed of a random distribution of cell clusters, with varying sizes and lifetimes of synchronization.

To fully understand the random behavior observed in Figure 6.9, we must assume that the cell populations are comprised of an ensemble of clusters. Each cluster is made of a small population of cells that can temporarily synchronize.

In summary, the variability in signal shapes, amplitudes, and duration is likely due to the presence of cell clusters with varying sizes and synchronization lifetimes within the non-electrogenic cell population.

## 6.4− Discussion and conclusions

The PEDOT:PSS/electrolyte interface has a very low intrinsic thermal noise in the frequency range from 0.1 Hz up to 100 kHz. In this frequency range, the noise of the PEDOT:PSS electrode is one order of magnitude lower than that noise generated by the gold electrode. The low intrinsic thermal noise maximizes the SNR ratio and makes the PEDOT:PSS-based electrodes ideally suited to measure a variety of electrophysiological signals, including action potentials and long-lasting oscillations generated by non-excitable cells.

In comparison with flat hard substrates, the use of bacterial cellulose as the substrate lowers the PEDOT:PSS impedance. The findings reported here suggest that the cellulose fibrous structure creates a micro-porosity that enhances the effective area of the electrical double-layers formed between the two phases of the PEDOT:PSS, the nanoscale PEDOT-rich and PSS-rich interconnected grains. Therefore, the bacterial cellulose substrate takes full advantage of the electronic properties related with the two-phase structure of PEDOT:PSS.

Moreover, we showed the influence of PEDOT:PSS charging effects on shaping the biosignal decay. We demonstrated that, when the signals are long lasting (a few seconds long), the slow relaxation of the charge distribution to equilibrium state contributes to enhance the SNR.

Because noise is critical at low frequencies, this study is focused on the electrode requirements that must be satisfied to record low-frequency signals from non-electrogenic cells. The interfacial resistance between the electrode and the electrolyte solution plays a crucial role because it controls the intrinsic noise generated by the electrode and also the long relaxation time to a steady component that

influences the recorded signal shape. Using electrodes based on PEDOT:PSS deposited on glass and on bacterial cellulose substrates, we experimentally evaluated the electrode performance in the recording of extracellular action potentials from zebrafish hearts and ultra-slow (0.1 Hz) oscillations from glioma cell populations.

To detect long lasting signals, the bottleneck that determines the detection limit is the $1/f^2$ noise. Here, we show that the low EDL resistance of the PEDOT:PSS printed on bacterial cellulose provides a way to minimize the deleterious effects of the $1/f^2$ noise.

These findings should be of value in configuring *in vitro* and *in vivo* extracellular electrode arrays for recording non-electrogenic cells in various applications. Particularly interesting research fields are astrocyte-neuron communications [59–61] and cancer research [27,62, 63]. In addition to the advantage of low intrinsic thermal noise, bacterial cellulose substrates are soft, biocompatible and low cost. Furthermore, bacterial cellulose-based electrodes do not represent a future environmental hazard.

# References

[1] E. Zeglio, A.L. Rutz, T.E. Winkler, G.G. Malliaras, A. Herland, Conjugated polymers for assessing and controlling biological functions, Adv. Mater. 31 (2019), 1806712.

[2] Z. Aqrawe, J. Montgomery, J. Travas-Sejdic, D. Svirskis, Conducting polymers as electrode coatings for neuronal multi-electrode arrays, Trends Biotechnol. 35 (2017), 93‑95.

[3] L.D. Garma, L.M. Ferrari, P. Scognamiglio, F. Greco, F. Santoro, Inkjet-printed PEDOT:PSS multi-electrode arrays for low-cost: in vitro electrophysiology, Lab Chip 19 (2019) 3776‑3786.

[4] J. Rivnay, R.M. Owens, G.G. Malliaras, The rise of organic bioelectronics, Chem. Mater. 26 (2014), 679‑685.

[5] M. Di Lauro, S. Benaglia, M. Berto, C.A. Bortolotti, M. Zoli, F. Biscarini, Exploiting interfacial phenomena in organic bioelectronics: conformable devices for bidirectional communication with living systems, Colloids Surf. B Biointerfaces 168 (2018), 143‑147.

[6] D.A. Koutsouras, A. Hama, J. Pas, P. Gkoupidenis, E.N. Supérieure, PEDOT : PSS Microelectrode Arrays for Hippocampal Cell Culture Electrophysiological Recordings, vol. 7, 2018, pp. 259‑265.

[7] M. Sessolo, D. Khodagholy, J. Rivnay, F. Maddalena, M. Gleyzes, E. Steidl, B. Buisson, G.G. Malliaras, Easy-to-Fabricate conducting polymer microelectrode arrays, Adv. Mater. 25 (2013),

2135‑2139.

[8] R.A. Green, N.H. Lovell, G.G. Wallace, L.A. Poole-Warren, Conducting polymers for neural interfaces: challenges in developing an effective long-term implant, Biomaterials 29 (2008), 3393‑3399.

[9] S. Inal, J. Rivnay, A.-O. Suiu, G.G. Malliaras, I. McCulloch, Conjugated polymers in bioelectronics, Acc. Chem. Res. 51 (2018), 1368‑1376.

[10] M. Berggren, A. Richter-Dahlfors, Organic bioelectronics, Adv. Mater. 19 (2007), 3201‑3213.

[11] F. Hempel, J.K. Law, T. Chien, W. Munief, X. Lu, Biosensors and Bioelectronics PEDOT : PSS organic electrochemical transistor arrays for extracellular electrophysiological sensing of cardiac cells, Biosens. Bioelectron. 93 (2017), 132‑138.

[12] A. Jonsson, S. Inal, I. Uguz, A.J. Williamson, L. Kergoat, J. Rivnay, D. Khodagholy, M. Berggren, C. Bernard, G.G. Malliaras, D.T. Simon, Bioelectronic Neural Pixel : Chemical Stimulation and Electrical Sensing at the Same Site, vol. 113, 2016, pp. 9440‑9445.

[13] T. Nyberg, A. Shimada, K. Torimitsu, Ion conducting polymer microelectrodes for interfacing with neural networks, J. Neurosci. Methods 160 (2007), 16‑25.

[14] E. Bihar, T. Roberts, M. Saadaoui, T. Hervé, De Graaf, J. B, G.G. Malliaras, Inkjet printed PEDOT:PSS electrodes on paper for electrocardiography, Adv. Healthc. Mater. 6 (2017), 1601167.

[15] P.M.C. Inácio, A.L.G. Mestre, M.D.C.R. De Medeiros, S. Asgarifar, Y. Elamine, J. Canudo, J.M.A. Santos, J. Bragança, J. Morgado, F. Biscarini, et al., Bioelectrical signal detection using conducting polymer electrodes and the displacement current method, IEEE Sensor. J. 17 (2017), 3961‑3966.

[16] M.E. Spira, A. Hai, Multi-electrode array technologies for neuroscience and cardiology, Nat. Nanotechnol. 8 (2013), 83‑94.

[17] M. Ganji, E. Kaestner, J. Hermiz, N. Rogers, A. Tanaka, D. Cleary, S.H. Lee, J. Snider, M. Halgren, G.R. Cosgrove, et al., Development and translation of PEDOT:PSS microelectrodes for intraoperative monitoring, Adv. Funct. Mater. 28 (2018), 1700232.

[18] D. Qi, Z. Liu, Y. Liu, Y. Jiang, W.R. Leow, M. Pal, S. Pan, H. Yang, Y. Wang, X. Zhang, et al., Highly stretchable, compliant, polymeric microelectrode arrays for in vivo electrophysiological interfacing, Adv. Mater. 29 (2017), 1‑10.

[19] J. Rivnay, P. Leleux, M. Ferro, M. Sessolo, A. Williamson, D.A. Koutsouras, D. Khodagholy, M. Ramuz, X. Strakosas, R.M. Owens, et al., High-performance transistors for bioelectronics through

tuning of channel thickness, Sci. Adv. 1 (2015), 1‑6.

[20] C.M. Proctor, J. Rivnay, G.G. Malliaras, Understanding volumetric capacitance in conducting polymers, J. Polym. Sci., Part B: Polym. Phys. 54 (2016), 1433‑1436.

[21] A.V. Volkov, K. Wijeratne, E. Mitraka, U. Ail, D. Zhao, K. Tybrandt, J. W. Andreasen, M. Berggren, X. Crispin, I.V. Zozoulenko, Understanding the capacitance of PEDOT:PSS, Adv. Funct. Mater. 27 (2017), 1700329.

[22] E. Milotti, 1/F Noise: a Pedagogical Review, 2002.

[23] J. Parkash, K. Asotra, Calcium wave signaling in cancer cells, Life Sci. 87 (2010), 587‑595.

[24] W. Kolch, M. Halasz, M. Granovskaya, B.N. Kholodenko, The dynamic control of signal transduction networks in cancer cells, Nat. Publ. Gr. 15 (2015), 515‑527.

[25] A.L.G. Mestre, M. Cerquido, P.M.C. Inácio, S. Asgarifar, A.S. Lourenço, M.L. S. Cristiano, P. Aguiar, M.C.R. Medeiros, I.M. Araújo, J. Ventura, et al., Ultrasensitive gold micro-structured electrodes enabling the detection of extracellular long-lasting potentials in astrocytes populations, Sci. Rep. 7 (2017), 14284.

[26] A.L.G. Mestre, P.M.C. Inácio, Y. Elamine, S. Asgarifar, A.S. Lourenço, M.L. S. Cristiano, P. Aguiar, M.C.R. Medeiros, I.M. Araújo, J. Ventura, et al., Extracellular electrophysiological measurements of cooperative signals in astrocytes populations, Front. Neural Circ. 11 (2017), 1‑9.

[27] P.R.F. Rocha, M.C.R. Medeiros, U. Kintzel, J. Vogt, I.M. Araújo, A.L.G. Mestre, V. Mail€ander, P. Schlett, M. Dr€oge, L. Schneider, et al., Extracellular electrical recording of pH-triggered bursts in C6 glioma cell populations, Sci. Adv. 2 (2016), e1600516.

[28] S. Asgarifar, A.L.G. Mestre, R.C. Félix, P.M.C. Inácio, M.L.S. Cristiano, M.C. R. Medeiros, I.M. Araújo, D.M. Power, H.L. Gomes, Extracellular electrophysiological based sensor to monitor cancer cells cooperative migration and cell-cell connections, Biosens. Bioelectron. 145 (2019), 111708.

[29] M. Cabello, H. Ge, C. Aracil, D. Moschou, P. Estrela, J.M. Quero, S.I. Pascu, P.R. F. Rocha, Extracellular electrophysiology in the prostate cancer cell model PC-3, Sensors 19 (2019), 1‑11.

[30] A.I. Borrachero-Conejo, E. Saracino, M. Natali, F. Prescimone, S. Karges, S. Bonetti, G.P. Nicchia, F. Formaggio, M. Caprini, R. Zamboni, et al., Electrical stimulation by an organic transistor architecture induces calcium signaling in nonexcitable brain cells, Adv. Healthc. Mater. 8 (2019), 1‑12.

[31] E. Saracino, L. Maiolo, D. Polese, M. Semprini, A.I. Borrachero-Conejo, J. Gasparetto, S. Murtagh, M. Sola, L. Tomasi, F. Valle, et al., A glial-silicon nanowire electrode junction enabling

differentiation and noninvasive recording of slow oscillations from primary astrocytes, Adv. Biosyst. 1900264 (2020), 1900264.

[32] D. Klemm, E.D. Cranston, D. Fischer, M. Gama, S.A. Kedzior, D. Kralisch, F. Kramer, T. Kondo, T. Lindstr€om, S. Nietzsche, et al., Nanocellulose as a natural source for groundbreaking applications in materials science: today’s state. *Mater*, Today 21 (2018), 720‑748.

[33] C.R. Rambo, D.O.S. Recouvreux, C.A. Carminatti, A.K. Pitlovanciv, R.V. Ant^onio, L. M. Porto, Template assisted synthesis of porous nanofibrous cellulose membranes for tissue engineering, Mater. Sci. Eng. C 28 (2008), 549‑554.

[34] N. Petersen, P. Gatenholm, Bacterial cellulose-based materials and medical devices: current state and perspectives, Appl. Microbiol. Biotechnol. 91 (2011), 1277‑1286.

[35] X. Lv, J. Yang, C. Feng, Z. Li, S. Chen, M. Xie, J. Huang, H. Li, H. Wang, Y. Xu, Bacterial cellulose-based biomimetic nanofibrous scaffold with muscle cells for hollow organ tissue engineering, ACS Biomater. Sci. Eng. 2 (2015), 19‑29.

[36] A. Meftahi, D. Nasrolahi, V. Babaeipour, S. Alibakhshi, S. Shahbazi, Investigation of nano bacterial cellulose coated by sesamum oil for wound dressing application, Procedia Mater. Sci. 11 (2015), 212‑216.

[37] J. Kim, S.W. Kim, S. Park, K.T. Lim, H. Seonwoo, Y. Kim, B.H. Hong, Y.H. Choung, J.H. Chung, Bacterial cellulose nanofibrillar patch as a wound healing platform of tympanic membrane perforation, Adv. Healthc. Mater. 2 (2013), 1525‑1531.

[38] A.J.D. Silvestre, C.S.R. Freire, C.P. Neto, Do bacterial cellulose membranes have potential in drug-delivery systems? Expet Opin. Drug Deliv. 11 (2014), 1113‑1124.

[39] N.H.C.S. Silva, I. Drumond, I.F. Almeida, P. Costa, C.F. Rosado, C.P. Neto, C.S. R. Freire, A.J.D. Silvestre, Topical caffeine delivery using biocellulose membranes: a potential innovative system for cellulite treatment, Cellulose 21 (2013), 665‑674.

[40] E. Trovatti, C.S.R. Freire, P.C. Pinto, I.F. Almeida, P. Costa, A.J.D. Silvestre, C. P. Neto, C. Rosado, Bacterial cellulose membranes applied in topical and transdermal delivery of lidocaine hydrochloride and ibuprofen: in vitro diffusion studies, Int. J. Pharm. 435 (2012), 83‑87.

[41] I.F. Almeida, T. Pereira, N.H.C.S. Silva, F.P. Gomes, A.J.D. Silvestre, C.S.R. Freire, J.M. Sousa Lobo, P.C. Costa, Bacterial cellulose membranes as drug delivery systems: an in vivo skin compatibility study, Eur. J. Pharm. Biopharm. 86 (2014), 332‑336.

[42] T. Carvalho, G. Guedes, F.L. Sousa, C.S.R. Freire, H.A. Santos, Latest advances on bacterial cellulose-based materials for wound healing, delivery systems, and tissue engineering, Biotechnol.

J. 14 (2019), 1‑19.

[43] N.H.C.S. Silva, J.P. Mota, T.S. de Almeida, J.P.F. Carvalho, A.J.D. Silvestre, C. Vilela, C. Rosado, C.S.R. Freire, Topical drug delivery systems based on bacterial nanocellulose: accelerated stability testing, Int. J. Mol. Sci. 21 (2020), 1262.

[44] E. Trovatti, L.S. Serafim, C.S.R. Freire, A.J.D. Silvestre, C.P. Neto, Gluconacetobacter sacchari: an efficient bacterial cellulose cell-factory, Carbohydr. Polym. 86 (2011), 1417‑1420.

[45] A. Bagheri, M.T. Salam, J.L.P. Velazquez, R. Genov, Low-frequency noise and offset rejection in DC-coupled neural amplifiers: a review and digitally-assisted design tutorial, IEEE Trans. Biomed. Circuits Syst. 11 (2017), 161‑176.

[46] M.C.R. Medeiros, A. Mestre, P. Inácio, S. Asgarif, I.M. Araújo, P.C. Hubbard, Z. Velez, M.L. Cancela, P.R.F. Rocha, D.M. de Leeuw, et al., An electrical method to measure low-frequency collective and synchronized cell activity using extracellular electrodes, Sens. Bio-Sensing Res. 10 (2016), 1‑8.

[47] M. Brittinger, P. Fromherz, Field-effect transistor with recombinant potassium channels: fast and slow response by electrical and chemical interactions, Appl. Phys. Mater. Sci. Process 81 (2005), 439‑447.

[48] P.R.F.F. Rocha, P. Schlett, U. Kintzel, V. Mail€ander, L.K.J.J. Vandamme, G. Zeck, H. L. Gomes, F. Biscarini, D.M. de Leeuw, Electrochemical noise and impedance of Au electrode/electrolyte interfaces enabling extracellular detection of glioma cell populations, Sci. Rep. 6 (2016), 34843.

[49] G. Massobrio, S. Martinoia, P. Massobrio, Equivalent circuit of the neuro-electronic junction for signal recordings from planar and engulfed micro-nano-electrodes, IEEE Trans. Biomed. Circuits Syst. (2017), 1‑10.

[50] Jing Guo, Jie Yuan, Mansun chan modeling of the cell-electrode interface noise for microelectrode arrays, IEEE Trans. Biomed. Circuits Syst. 6 (2012), 605‑613.

[51] W. Franks, I. Schenker, P. Schmutz, A. Hierlemann, Impedance characterization and modeling of electrodes for biomedical applications, IEEE Trans. Biomed. Eng. 52 (2005), 1295‑1302.

[52] A. Hassibi, R. Navid, R.W. Dutton, T.H. Lee, Comprehensive study of noise processes in electrode electrolyte interfaces, J. Appl. Phys. 96 (2004), 1074‑1082.

[53] V. Viswam, M.E.J. Obien, F. Franke, U. Frey, A. Hierlemann, Optimal electrode size for multi-scale extracellular-potential recording from neuronal assemblies, Front. Neurosci. 13 (2019), 1‑23.

[54] M. Giordani, M. Sensi, M. Berto, M. Di Lauro, C.A. Bortolotti, H.L. Gomes, M. Zoli, F. Zerbetto,

L. Fadiga, F. Biscarini, Neuromorphic organic devices that specifically discriminate dopamine from its metabolites by nonspecific interactions, Adv. Funct. Mater. 2002141 (2020), 1‑13.

[55] S. Asgarifar, P.M.C. Inácio, A.L.G. Mestre, H.L. Gomes, Ultrasensitive bioelectronic devices based on conducting polymers for electrophysiology studies, Chem. Pap. 72 (2018), 1597‑1603.

[56] A.C. Charles, C.C. Naus, D. Zhu, G.M. Kidder, E.R. Dirksen, M.J. Sanderson, Intercellular calcium signaling via gap junctions in glioma cells, J. Cell Biol. 118 (1992), 195‑201.

[57] N. Kuga, T. Sasaki, Y. Takahara, N. Matsuki, Y. Ikegaya, Large-scale calcium waves traveling through astrocytic networks in vivo, J. Neurosci. 31 (2011), 2607‑2614.

[58] A. Verkhratsky, R.K. Orkand, H. Kettenmann, Glial calcium: homeostasis and signaling function, Physiol. Rev. 78 (1998), 99‑141.

[59] D.S. Adams, M. Levin, Endogenous voltage gradients as mediators of cell-cell communication: strategies for investigating bioelectrical signals during pattern formation, Cell Tissue Res. 352 (2013), 95‑122.

[60] R. Balaji, C. Bielmeier, H. Harz, J. Bates, C. Stadler, A. Hildebrand, A.-K. Classen, Calcium spikes, waves and oscillations in a large, patterned epithelial tissue, Sci. Rep. 7 (2017), 42786.

[61] A. Volterra, J. Meldolesi, Astrocytes, from brain glue to communication elements: the revolution continues, Nat. Rev. Neurosci. 6 (2005), 626‑640.

[62] E. Jung, J. Alfonso, M. Osswald, H. Monyer, W. Wick, F. Winkler, Emerging intersections between neuroscience and glioma biology, Nat. Neurosci. 22 (2019), 1951‑1960.

[63] A. Maklad, A. Sharma, I. Azimi, Calcium signaling in brain cancers: roles and therapeutic targeting, Cancers 11 (2019), 145.

[64] P.M.C. Inácio, M.C.R. Medeiros, T. Carvalho, R.C. Félix, A. Mestre, P.C. Hubbard, Q. Ferreira, J. Morgado, A. Charas, C.S.R. Freire, F. Biscarini, D.M. Power, H.L. Gomes, Ultra-low noise PEDOT:PSS electrodes on bacterial cellulose: A sensor to access bioelectrical signals in non-electrogenic cells, Org. Electron. 85 (2020) 105882. https://doi.org/10.1016/j.orgel.2020.105882.

# Chapter 7

# Conclusions and further work

In this chapter, the primary contributions of the work presented in this thesis to the field of bioelectronics are summarized. The key issues that require further investigation are highlighted, and experiments are suggested to address the unresolved questions. Additionally, this chapter proposes the application of the results obtained from this study in future biomedical devices and cell-based sensing technologies.

## 7.1 – Summary of the main findings

The main goal of this thesis was to investigate the electrical coupling of extracellular signals generated by electrogenic and non-electrogenic cells using novel sensing electrodes. The electrodes were fabricated using conductive polymers and bacterial cellulose as scaffold materials. The electrical characterization was carried out using (i) small-signal impedance measurements, (ii) electrical noise, and (iii) transient response to voltage pulses. The electrical behaviour was interpreted using equivalent circuits to model the interface between cells and the electrodes. This approach proved beneficial in assessing the sensing capabilities of the electrodes. Furthermore, a comprehensive toolkit of experimental protocols for controlling, measuring, and processing data was also developed.

This work has made several significant contributions to the research area of electrophysiological devices and computer tools for bioelectrical signal processing. The following sections provide an overview of the main contributions.

### 7.1.1– Ultra-low noise sensing electrodes

In this study, electrophysiological sensing electrodes were fabricated by combining nanofibrous bacterial cellulose (BC) as a substrate with poly(3,4-ethylenedioxythiophene): Polystyrene sulfonate (PEDOT:PSS) as a conductive sensing electrode. The use of these materials provided a low impedance interface between the cells and the sensing surface, which is essential for achieving a high signal-to-noise ratio (SNR). Using these sensing electrodes, extracellular signals from populations of non-electrogenic cells were measured with an impressive SNR of up to 140.

It is worth noting that in previous studies, the high SNR of polymer-based surfaces has often been attributed to the high interfacial capacitance (low impedance) brought about by the polymer. However, it is known that the interfacial resistance also plays a detrimental role in the SNR, as it is responsible for electrical noise. A low resistance minimizes the intrinsic thermal noise and improves the detection limit of electrophysiological sensing devices. This thesis has shown that when comparing a classical gold/electrolyte interface with a PEDOT:PSS/electrolyte interface, the main difference between the two interfaces lies in the interfacial resistance. The low resistance associated with the electrical-double layers formed by the PEDOT:PSS/electrolyte interface, reduces electrical noise, making it the primary element responsible for an improved SNR.

The low impedance of PEDOT:PSS on BC is attributed to the morphological structure of the BC membrane. Atomic force microscopy (AFM) analysis revealed that the BC membrane is composed of a randomly intertwined nanofiber structure. The deposition of PEDOT:PSS from aqueous solutions enabled the conductive polymer to deeply penetrate the BC structure and create an electrode with a large sensing area.

The material combination of PEDOT:PSS and BC is biocompatible and favorable for cell attachment and proliferation. Additionally, the excellent adhesion properties of PEDOT:PSS to bacterial cellulose are worth noting. In comparison, when PEDOT:PSS is printed onto flat surfaces such as glass and silicon, the polymer tends to delaminate in the presence of electrolyte solutions.

The functionalization of the bacterial cellulose to make it biodegradable or resorbable is very interesting for implantable bioelectrical devices and an interesting area to purse the research.

In this thesis, PEDOT:PSS/BC sensing electrodes were successfully used for in vitro and ex vivo extracellular and impedance measurements with a wide range of cell types, including embryonic bodies (EBs), small organs, and high-grade primary tissue samples. The robust nature of these electrodes provides a reliable platform for electrophysiological measurements, making them ideal for long-term studies and potential applications in implantable medical devices.

### 7.1.2– Framework for understanding the utility of recording bioelectric signals using current detection method

We conducted electrical characterization of PEDOT:PSS electrodes with different sensing areas to record cardiac signals in embryonic bodies. Signal recording was performed in both voltage and current detection modes. Surprisingly, we found that the signals measured in current detection mode had a higher signal-to-noise ratio (SNR) than those measured in voltage detection mode. This is because, when considering the frequency bandwidth, the noise behavior in current and voltage

detection modes is opposite. In current detection, the thermal noise increases with bandwidth, while in voltage detection, the noise decreases with bandwidth. Therefore, for high bandwidths, we expected a better SNR ratio in voltage detection mode.

However, we found that the dominant noise source in the low-frequency region was the pink noise, which follows a $1/f^{\alpha}$ noise dependence. Our experimental data presented in chapter 5 showed that the current detection mode had an advantage because the power dependence ($\alpha$) of the polymer-electrolyte interface noise tended to be unity ($\alpha = 1$) when the noise was measured as current, while the voltage measurements followed a power of two ($\alpha = 2$). This means that the contribution of $1/f$ noise resulted in a signal attenuation of 20 dB/dec for voltage detection, as opposed to 5 dB/dec for current detection.

Furthermore, we found that interfacial capacitance played an important role in achieving a high SNR when the signal was detected as a current. In the current detection mode, the peak value of the detected current signal ($i_s$) is the displacement current and therefore proportional to the product of the first derivative of the voltage signal ($dv_s/dt$) and the interfacial capacitance.

### 7.1.3 − Effect of the electrode/electrolyte interfacial resistance on the signal shape

When measuring extracellular signals using extracellular electrodes it is important to ask how the electrode (material, geometry and area) affects or controls the shape of the signal recorded. In the case of chemical traveling waves it is known that the width of the extracellular signal is expected to be defined by the width of the sensing electrode. However, assuming that the bioelectrical signal is a local oscillation can different electrodes pick different signal shapes? If the electrodes are fabricated using conducting polymers such as the PEDOT:PSS electrodes, the answer to this question is yes, the type of the electrode used can indeed modify the shape of the measured signal. This was demonstrated in chapter 6, and it is summarized below.

This thesis has shown that the electrode/electrolyte interfacial resistance contributes to the reshaping of the recorded signal, particularly visible when using PEDOT:PSS electrodes. The current flowing through the entire electrode-electrolyte interface was analysed when 100 μV voltage pulses were applied. For the gold electrodes, only the displacement current peaks were observed on the rising and falling edges of the voltage pulse, consistent with a purely capacitive interface. In contrast, the PEDOT:PSS electrodes' transient response to a voltage pulse shows a slightly different behavior. In addition to the displacement current peaks, a decay process that takes about 2 seconds for the interface to reach equilibrium was observed. We hypothesize that this slow response is due to the charging of ionic species deep inside the PEDOT:PSS electrodes, and the signal shape is controlled by the redistribution of ionic charges that determine the settling time of the current transient.

In summary, the type of electrode used can modify the shape of the measured bioelectrical signal. The slow response of the PEDOT:PSS electrodes to voltage pulses possible due to the charging of ionic species deep inside the electrodes, which can result in a small distortion of the signal shape when comparing with the signal shape measured by a gold electrode. Understanding the contribution of electrode/electrolyte interfacial resistance to signal reshaping can guide the development of accurate bioelectrical recording systems.

## 7.2 – Suggestions for further work

The electrical characterization of the transducer devices developed in this work has revealed several other areas worthy of further investigation. Some of these aspects are briefly commented on below.

### 7.2.1 – Optimization of the electrode geometry and area to measure populations of non-electrogenic cells

In chapter 6 of this thesis, populations of non-electrogenic cells were measured using electrophysiological techniques. These measurements revealed that certain time traces of bioelectrical activity consist of well-defined discrete signals, indicating that cells adherent to the sensing electrode are forming cell-cell connections and behaving as an organized tissue that can act cooperatively or in a synchronized manner. However, other time traces may be less well-defined, as seen in Figure 6.9 of chapter 6, with signals varying in amplitude, duration, and temporal distribution, suggesting that the entire cell population being measured is not fully synchronized. Instead, there is a distribution of synchronized cell clusters. These cell clusters can be oscillating in phase or out of phase.

This view of cells organized into synchronized clusters raises several interesting questions. What is the minimum number of cells required to generate a discrete signal?, what is the maximum spatial extent of a synchronized cluster?, whether the signal is a local oscillation or a traveling wave, and how long it takes for synchronization mechanisms to occur?

To answer the above questions, it is essential to know how many cells are being probed by the sensing electrodes. Therefore, the area of the sensing electrode and its geometry are crucial parameters for extracting relevant and quantitative information from the biological process. If the electrode is too small, it may fail to detect the full power of the signal, while an electrode that is too large may record

an ensemble of synchronized cell clusters operating out of phase, resulting in a noisy electrophysiological time trace similar the one shown in Figure 6.9.

The electrode geometry is also a critical parameter in measuring non-electrogenic cell populations. A proper design can allow us to distinguish a local oscillation from a traveling wave. While the shape and geometry of the sensing electrodes are not relevant for detecting local oscillations, they are crucial for detecting traveling oscillations. For instance, a traveling wave passing through an array of parallel fingers with different widths and equally spaced in space generates quasi-periodic signals with a width proportional to the width of the finger which is crossing. By designing an array of fingers with increasingly larger widths, a train of signals with increasing duration can be generated. The signal pattern (signal duration) should be proportional to the pattern of the finger's widths. Therefore, as a suggestion for further work it is proposed that arrays of finger type electrodes are fabricated and measured.

### 7.2.2 – Strategies to bring down the 1/*f* noise of the electrical double-layer

The 1/*f* noise presents a significant limitation in devices used to measure the bioelectrical activity of non-electrogenic cells. The 1/*f* type of noise dominates the millihertz frequency range and determines the detection limit for low-frequency weak signals. Therefore, minimizing the 1/*f* noise is crucial for fabricating devices that can detect signals from non-electrogenic cells.

Chapter 6 reports that measuring the signal in the current detection mode is more effective than in voltage mode because the $\alpha$ parameter, which determines the magnitude of the 1/*f* noise, is lower in the former. Therefore, it is suggested to explore the measuring method of a variety of sensing materials and electrode geometries.

The low-frequency noise usually follows a law of the type the $1/f^{\alpha}$ where the $\alpha$ parameter is usually between 1 and 2. In chapter 6 it was reported that measuring the signal in the current detection mode is more effective than in voltage mode because the $\alpha$ parameter, is lower in current detection mode than in voltage detection. The physics behind this result remains elusive. It also found that the $\alpha$ parameter depends on the material used to fabricate the sensing electrode. In addition, it also found that the electrode geometry is affecting the value of the $\alpha$ parameter. Co-planar electrode configurations have a lower $\alpha$ parameter than perpendicular electrode arrangements such as when a vertical Ag/AgCl electrode perpendicular to the sensing electrode surface is used.

To further investigate the reduction of 1/*f* noise, it is proposed to characterize the 1/*f* noise for a variety of conducting coatings to explore the role of the material in minimizing the 1/*f* noise. Additionally, different geometries for the sensing electrodes can be experimented with to determine

how electrode arrangements affect the value of the $\alpha$ parameter. Overall, these insights provide a foundation for developing strategies to lower the $1/f$ noise and improve the detection limits for sensing electrodes.

### 7.2.3 − Data analysis tools to extract meaningful information from electrophysiological time traces

Even assuming that signals are a result of a synchronization process, it is unlikely that the entire cell population is synchronized. Therefore, a sensing electrode may collect a variety of signals which are produced by a distribution of cells clusters. On top of this variability on the population, the clusters may be oscillating in phase or out of phase adding further complexity to the overall electrophysiological time trace. Assuming this complex scenario, how can we extract meaningful biological information from an electrophysiological time trace that measures a large population of cells? To answer this question, we must use artificial intelligence tools capable to recognize signal patters embed into a matrix of complex signals. We propose that some signal patterns are identified first manually and then use these well-defined patterns to train an algorithm that can detect these partners in a complex time trace.

As a starting point it will be very interesting to inspect if some of the electrophysiological time traces can be explained by the co-existence of two trains of quasi-periodic signals out of phase. If this happen then we would expect that the overall signal recording, shows first an increasing in frequency when the superposition occurs followed by a frequency decrease when the superposition fades away. An electrophysiological recording possible fitting into this behavior is show in Figure 7.1.

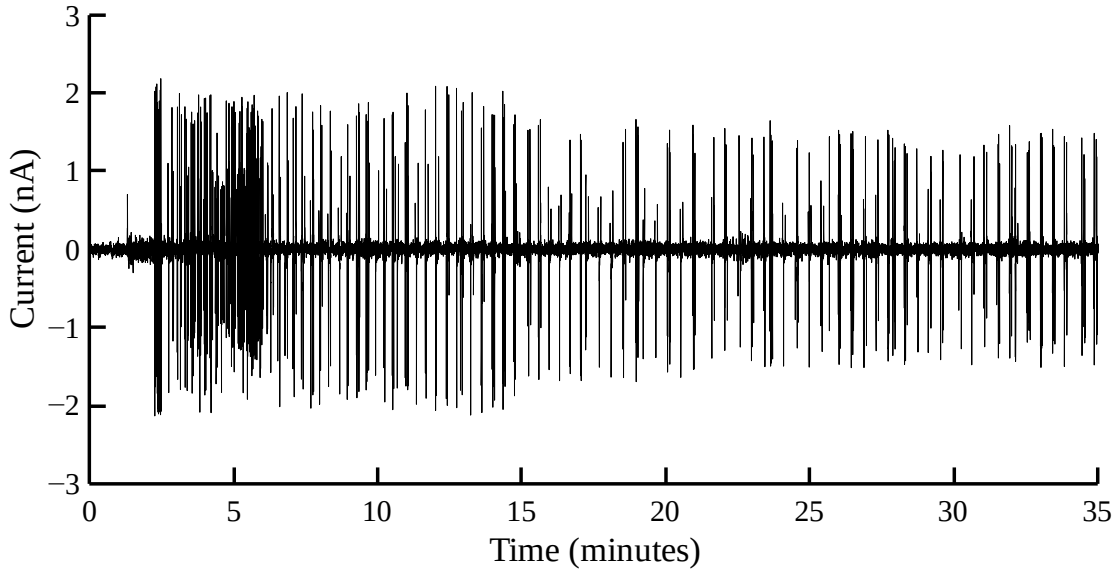


**Figure 7.1 –** Electrophysiological time trace that possible can be explained by the superposition of several quasi-peridoc burst occurring simultaneously.

### 7.2.4 − Bidirectional communication between cell and the sensing electrode: exploitation as therapeutic devices

In Chapter 6, it was shown that the developed electrode-based technology provides access to detect discrete signals generated by C6 glioma cells. Although C6 glioma cells are derived from rat brain tumors, this technology can be further extended to detect signals from glioma cells in human glioblastoma multiform (hGBM) tumors. hGBM tumors are currently an incurable disease that is resistant to surgery, radio- and chemotherapy, as well as treatments with anti-cancer drugs, because the blood-brain barrier is not permeable enough to allow therapeutic drug concentrations to accumulate in the brain.

As part of our thesis work, we have access to surgically removed tissues from a human glioblastoma (hGBM) generously provided by the Centro Hospitalar Universitario do Algarve (CHUA). We prepared the tissues for measurement using our sensing electrodes shortly after their extraction.

Based on our previous research, we were aware that C6 cells could react to the acidification of their surrounding medium. When exposed to lactic acid, the C6 cell population produced bursts of quasi-periodic signals. We discussed this finding in the context of patients with glioblastoma who often suffer from epileptic seizures. We hypothesized that the acidification caused by the tumor might trigger bioelectrical activity, which then leads to epileptic seizures.

To test our hypothesis, we exposed the human glioblastomas to lactic acid and monitored their response. Figure 7.2 illustrates the bioelectrical response of a tissue sample obtained from the outer layer of a hGBM tumor after exposure to the acidification of the surrounding medium.

We observed that the tumor generated electrophysiological signals in response to a pH change from 7.4 to 6.5. However, the activity was not sustained in a constant acidic environment (pH 6.5) and faded within a few minutes. Nonetheless, the addition of fresh medium partially or completely restored the pH medium and triggered electrophysiological activity as shown in Figure 7.2.

Following acid exposure, the tumors displayed discrete quasi-periodic signals in the frequency range of a few mHz. This bioelectrical behavior is consistent with a cell synchronization mechanism, indicating that the tumor behaves as a unit rather than a collection of individuals or uncorrelated cells.

Notably, we observed millihertz biphasic signals in GBM tumors, like those recorded in a 2D cell population. This is a highly significant finding, as it indicates that our *in vitro* approach, which relies on immortal cell lines, provides valuable information. We emphasize this point because there is a prevalent belief that only 3D biological models can yield valuable information about the bioelectrical communication between cells.

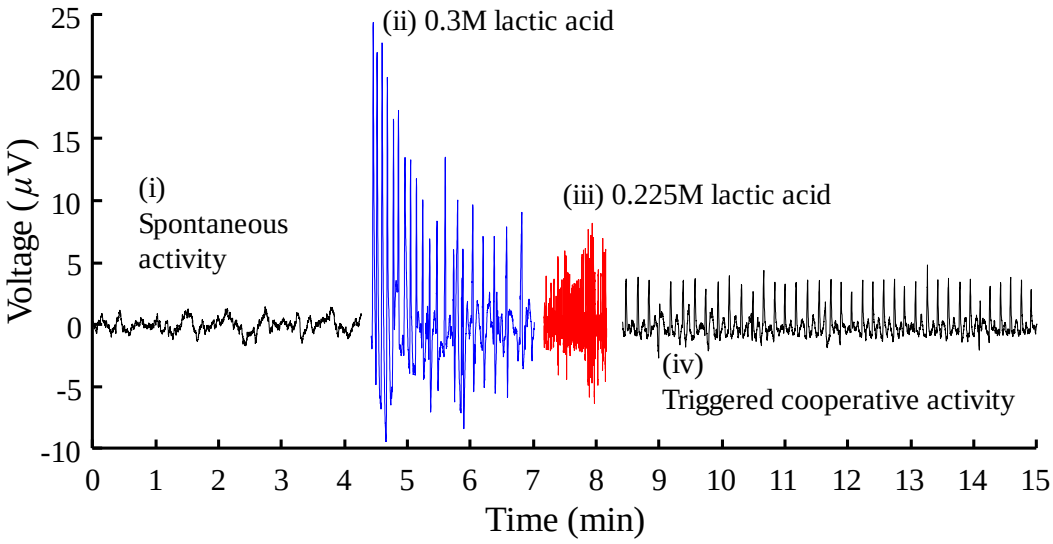


**Figure 7.2 –** Time trace of recorded discrete voltage signals generated from an hGBM tumor using PEDOT:PSS/bacterial cellulose electrodes. Areas (i) show spontaneous activity, (ii) and (iii) triggered activity upon exposure to 0.3M and 0.225M lactic acid, and (iv) triggered cooperative activity after washing with fresh medium.

We conducted extensive measurements in several GBM tumors, but unfortunately, the results were not analyzed in time to be included in this thesis. However, our preliminary data analysis suggested several avenues for further research.

One direction involves the use of sensing electrodes as therapeutic devices, or electroceutical devices, as they are now commonly named. The underlying hypothesis for this approach is that

diseases arise from faulty cell-cell communication, or crosstalk, within a tissue. If the proper functional cell-cell communication can be restored, it may be possible to reverse the disease state.

Our research group is convinced that our electrode-based technology offers an effective means of recording the signal patterns generated by populations of communicating cells. In theory, a "dictionary" of these signal patterns can be created, which may help us to decipher the language of cell-cell communication. If we can decode the cell-cell communication language, the sensing electrodes may be used to send instructions back to the cell population. Hopefully, cells may perceive these signals as instructions and respond to. Ultimately, our devices could be used to overdrive malfunctioning cell signaling and correct it, leading to an entire new generation of therapeutic devices.

### 7.2.5 − Applications as cell sensor devices

As demonstrated along this thesis, cells release into the extracellular space chemical messengers that change the ionic concentration and the electrical potential at the interface between the cells and a sensing electrode where the cell adhere. These electrochemical bursts can be detected as small voltage signals. This bioelectrical activity is strongly dependent on the health state of the cells or microorganisms. When exposed to toxic agents or drugs, it is plausible the bioelectrical activity is dramatically affected and modified.

The methods and the electrodes presented here can be explored as sensing devices that rely on the bioelectrical activity of cells or other microorganisms to sense exposure to toxic substances. The devices can be explored to monitor the environment, namely in oceans and in lakes for high precision and real-time pollutants detection, in the pharmaceutical industry as a drug screening platform and also in a laboratory for research purposes.

# Appendix A

## *rcSoftware*: A MATLAB-based application for control of an electrophysiological system – signal acquisition, storage, and processing

*rcSoftware* is a comprehensive toolkit designed for signal acquisition, collection, and processing in an ultra-low electrophysiological system setup. While it was specifically developed for this system, the data collection and processing tools can be adapted for use with different recording instrumentation. The program was developed using MATLAB, with the core module designed for control of the instrumentation while providing real-time access to signal processing tools. The *rcSoftware* has functions for performing time series and statistical analyses. Time series analysis offers the possibility to calculate average periodograms using a conventional arithmetic method or the Bartlett method. Statistical analysis is provided in two forms, the time-weighted average method, and the histogram method, each of which can be used to analyze signal morphological parameters (amplitude, area, length, inter-signal length, frequency, noise level, and SNR). Minimal background knowledge is required to operate and process data using high-level tools, making it an accessible option for researchers interested in the field of electrophysiology. Since the release of the first version, the *rcSoftware* has been used in a variety of published work by our research group, and its user base has grown considerably.

## A.1 − Introduction

Performing real-time electrophysiological experiments usually requires an expensive set-up. In many cases, the apparatus consists of a combination of different instrumentation that requires an autonomous management system. In such scenarios, there are two common options available. The first is to use the software provided by the manufacturer, which often requires a license fee. The second option is to use an open-source toolkit that is already available for the specific setup [1–5]. However, it can be challenging to find commercially available software that is tailored to the specific needs of a particular instrumentation setup. This can be especially difficult for academic research and development groups who may have limited resources.

The *rcSoftware* was designed specifically for control, data management, and signal processing. However, it is worth considering the possibility that Keysight Technologies instruments [6] (the manufacturer of the (DSA instrument could offer comparable solutions through a partnership width Eggplant software [7] or through the Keysight VEE Pro software [8]. As mentioned in reference [8], it should be noted that both solutions require software development and licensing fees, which are typically several thousand dollars or more.

While the 35670A Data Link software [9] can be download for free at the Keysight Technologies website and does not require a license, it should be noted that it is only useful for experienced users with extensive training. To use the software, users must become familiar with the equipment and be able to repeatedly perform the same measurements and store data protocols in the equipment's internal memory buffers. The software is also limited in that it requires full-time human supervision and can only be used to transfer data to a local PC. Additionally, it does not provide access to visualize or process raw data.

Similar to many customized in-house solutions [10–12], the *rcSoftware* was developed as part of this Ph.D. thesis. Given the time required to develop an entire application using a low-level programming language, as well as the graphical user interface (GUI), the solution for developing the *rcSoftware* was to use high-level programming platforms, also known as application programming interfaces (APIs). APIs are common in the development of research and development of software tools. Examples of such platforms are the LabVIEW [13–16], Python [17–20] and MATLAB [21–26]. These platforms are preferable to facilitate the programming time efficiency and avoid large scripts.

After evaluating the pros and cons of various high-level platforms, the MATLAB was chosen for the development of *rcSoftware* for the following reasons: (i) familiarity and expertise with the language; (ii) ease of deployment to any operating system (OS) without requiring the target platform to install the MATLAB, yet at a cost of a MATLAB (through a commercial license to use the deploy tool); (iii) Robust support for creating a user-friendly graphical user interface (GUI); (iv) use of the proprietary binary file format (.mat file extension) for loading and saving large datasets of recorded data,; (v) an extensive library of functions that are required for data and signal processing.

Given these advantages described above, the *rcSoftware* was developed with a simple and intuitive GUI providing all necessary tool for autonomous control of the Keysight 35670A (DSA) and for real-time data collection and processing.

The main purpose of *rcSoftware* is to include autonomous control and processing tools, thereby avoiding permanent human super-vision, highly qualified technical expertise, and programing skills. This results in a significant improvement in the time-efficiency to conduct experiments and leading to quicker publication of data. The following sections provide detailed descriptions the acquisition,

collection and processing toolboxes, including the system specifications, GUIs, operation instructions and data handling procedures.

## A.2 − System specifications

The ultra-low-noise electrophysiological setup consists of a low-noise preamplifier (LNA) connected to a digital signal analyzer (DSA). The Stanford SR560 voltage LNA (Stanford Research Systems, Sunnyvale, USA) [27] is used for voltage measurements, while a Stanford SR570 current LNA (Stanford Research Systems, Sunnyvale, USA) [28] is used for current measurements. The Agilent 35670A FFT DSA (currently owned by Keysight Technologies, Santa Rosa, USA) [29] with 2-channel is used. A Keysight 82357B USB/GPIB Interface High-Speed USB 2.0 (Keysight Technologies, Santa Rosa, USA) [30] was used to provide the physical interface between the DSA and a local PC. As for the LNA, a generic USB/RS-232 adapter is used for the physical interface. Note that

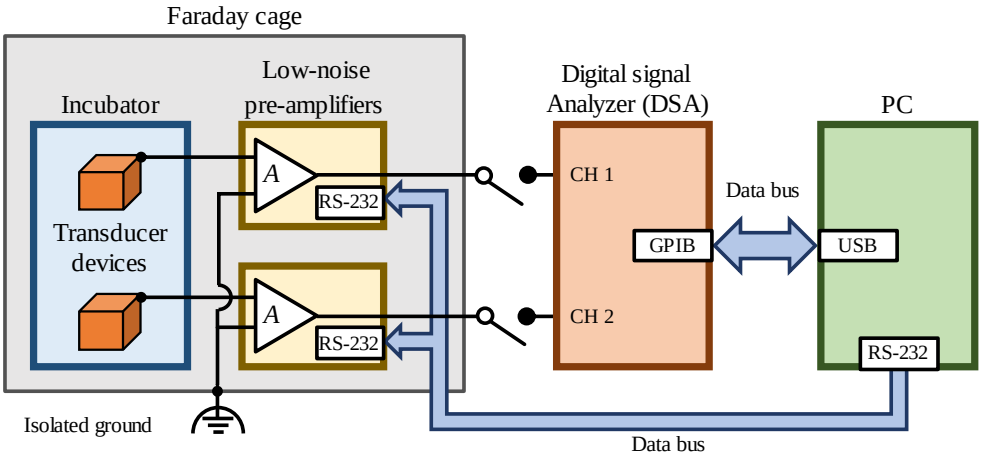


(a)

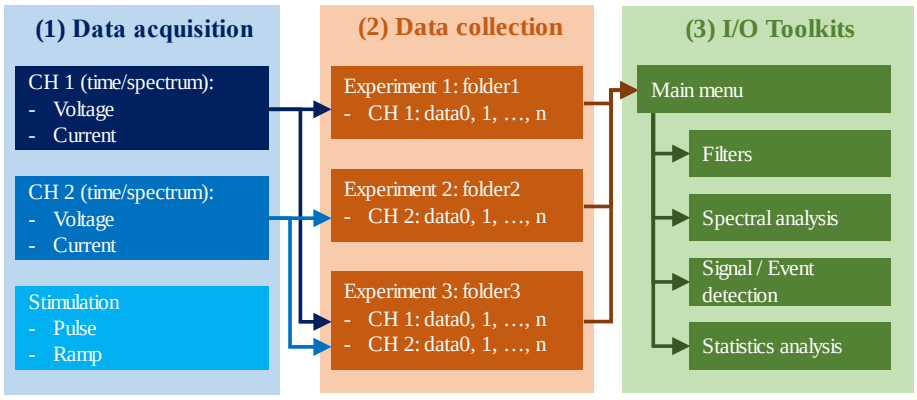


(b)

**Figure A.1 –** (**a**) Schematic diagram of the ultra-low noise electrophysiological recording system. (**b**) Workflow of the rcSoftware: (1) The data acquisition module allows the user to select the type of data recording, either by manual or autonomous control of the instrumentation; (2) The data acquisition module allows the user to select the data location; (3) The I/O toolkit module allows the user to process the stored data in real time and provides access to various processing tools.

the RS -232 interface of the LNAs allows listen-only communication, so the *rcSoftware* is not able to provide fully autonomous control of the instruments.

The *rcSoftware* requires a local PC, running MATLAB version 2014b [31] or later, and a version of a Virtual Instrument Software Architecture (VISA) installed on the local PC to allow MATLAB to access the physical layers of the GPIB interface. Installing Keysight IO libraries suite software with version 17.0 or later automatically installs and sets up all required drivers, VISA and the USB/GPIB interface. The Keysight IO libraries suite can be viewed and downloaded from the Keysight website [32]. For debugging device communication, it is recommended to install the Keysight Command Expert utility. The generic USB/RS-232 adapter on Windows® computers running Windows 8.0 or later and the generic OS drivers are sufficient. On Macintosh or Linux OS distributions, the user must make sure to find a working driver if OS cannot assign a generic driver. Figure A.1 (a) shows a schematic diagram of low-noise electrophysiological instrumentation.

## A.3 − *rcSoftware* overview

The rcSoftware operates based on the workflow diagram shown in Figure A.1 (b), numbered (1) through (3) and summarized below. First, module (1) represents the data acquisition phase and is executed by the data acquisition toolbox shown in Figure A.2 (a) (DAT). DAT performs live experiments to record electrophysiological signals, which also includes a beta version of an electrical pulse stimulation toolbox (ST). The second module (2) refers to the data acquisition options required to assemble the raw data into organized structural arrays. While DAT is running, data from live experiments are immediately available and can be used with the data processing toolbox shown in Figure A.2 (c) (DPT). However, for offline work, the data collection toolbox (DCT) shown in Figure A.2 (b) was developed to facilitate the processing scripts required to organize raw data files into structural arrays of data. Third, module (3) consists of the Data Processing Toolbox (DPT) shown in Figure A.2 (c), which contains a set of tools for preprocessing data, such as the use of filters, and for visualizing the recorded data.

## A.4 − Data acquisition toolbox (DAT)

The Data Acquisition Toolbox graphical user interface (DAT), shown in Figure A.2 (a), consists of two main windows labeled Real-Time Measurements (window (1)) and Instrument (window (2)). The options outside of windows (1) and (2) are part of the outer panel options described later in section A.1. Figure A.2 (a) shows all the default settings. Note that in the connection field inside the main field (2), the non-editable text field shows the physical GPIB address, e.g. ‘GPIB0::11::INSTR’. If no physical connection to the DSA is detected, the string ‘simulate’ is displayed, and as soon as DAT

opens the GUI, periodic warnings about a faulty connection or detection of the DSA are issued. By default, DAT always starts offline for security reasons and forces the user to initiate the physical connection. This process is required for security reasons to ensure that the user heeds all displayed warnings.


(a)

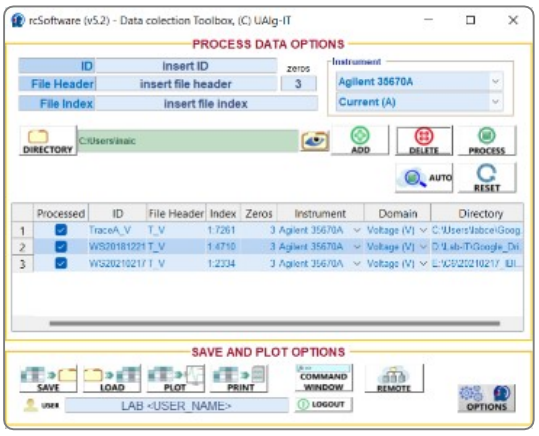


(b)

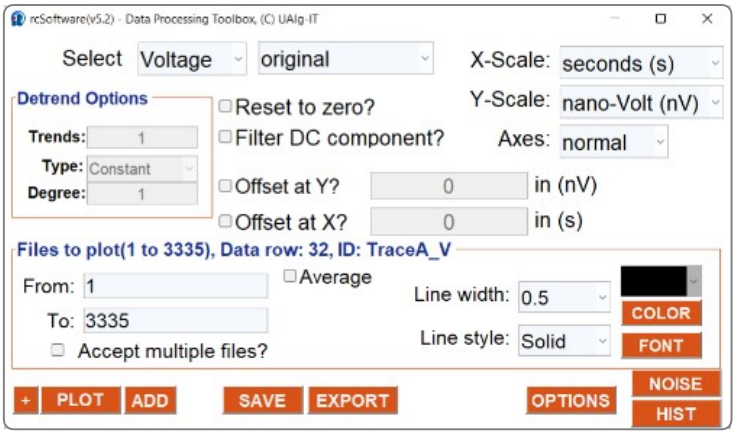


(c)

**Figure A.2 –** Layouts of the graphical user interface (GUI) of the *rcSoftware* toolkits. (a) Data acquisition toolkit (DAT). (b) Data collection toolkit (DCT). (c) Data processing toolkit (DPT).

### A.4.1 − Outer panel options

On the graphical user interface of DAT, you will find three pushbuttons labeled Clock, Keyboard, and Sound, as well as an option button labeled Remote to display the system clock on the graphical user interface, use keyboard shortcuts to change settings on the graphical user interface, issue audible alerts about new data availability, warnings, or errors, and enable remote access to DAT. Pressing the 'h' or 'H' key opens a help menu that summarizes all available keyboard shortcuts. Appendix B contains all the instructions, descriptions, and commands for using the remote-control options.

### A.4.2 − Panel (1): Real-time measurements

Within panel (1) there are two panels, Trace A and Trace B, both of which provide access to identical functions: (i) an output axis for visualizing the recorded data; (ii) highlighting the recording channel; (iii) a button for displaying $1/f$ and $1/f^2$ plot lines (for spectral data only); (iv) two dedicated pushbuttons named LIN or LOG for switching the X and Y axes between linear and logarithmic scales; (v) one pushbutton labeled FIG to open the same data displayed in the panel axes in an external MATLAB figure; (vi) three pushbuttons labeled VIEW, NOISE, and HIST to open the Data Processing Toolbox (DPT), the Noise Data Processing Toolbox (NDPT), or the Statistical Data Processing Toolbox (SDPT), respectively. The following sections describe each toolbox.

The axes in the Trace A and B panels in Figure A.2 (a) use the same default font, line, and color settings, the MATLAB plot function [33] to enter the plotted data into the axes, and the MATLAB axis function [34] to automatically set the X-Y axis boundaries. Occasionally, the axes are over-scaled, as in the case of the axes of Trace B in Figure A.2 (a). To provide the user with some degree of customization, seven adjustment boxes have been provided on the right side of the Trace B axes via the 'Trace B' button in the options menu in Figure A.3 (e), allowing you to quickly change the width of the major and minor grid lines and transparency settings, change the axis scaling between tight and automatic, or manually set the maximum and minimum Y-axis scaling values via two editable boxes.

### A.4.3 − Panel (2): Instrumentation

As the name Panel (2) implies, Panel (2) refers to the remote control of instruments. For security reasons, Panel (2) is built in a secure mode that disables all editable fields on the GUI when one of the following conditions is met: (i) the connection to the DSA is offline or (ii) while recording live data.

As mentioned in section A.1, DAT is always started in offline mode, case (i). Thus, to unlock the GUI options of the panel (2), the user must press the ON /OFF button in the connection panel to connect to the DSA. When the connection is successfully established (online), the color and label of the pushbutton will change and the 'Interface Status' checkbox will be automatically checked to highlight the online connection status. After enabling the control panel options (2), the user must set up the DSA via the graphical user interface of DAT. To perform live and standard electrophysiological recordings, the essential functions such as the acquisition, data, and storage options shown schematically in Figure


**Figure A.3 –** Programmable options and additional features provided through the DAT user interface to perform live and standard data logging. (**a**) Schematic representation of the main programmable options. Pulse options are delineated by a black dashed line to indicate that it's an optional feature. (**b**–**e**) GUI of the menus for adding and viewing the capture table options, the Pulse Stimulation Toolbox (PST), and the options menu DAT, respectively. The PST is still under development (a beta version).

A.3 (a) must be programmed. However, Figure A.3 (a) lists additional functions beyond the options required for standard recordings, namely the pulse options that can be used to simultaneously apply voltage pulses and record the response. DAT also contains optional functions that are described in more detail in the subsections of section A.4.

### A.4.3.1 − Capture options

The acquisition options include all the functions required to set up DAT for autonomous control of the acquisition sequence, i.e., the recording loop (RL) sequence. The size of the RL sequence ($L_n$) can be easily changed using the selection menu in the Loop panel: ‘Manual’, ‘Auto. Limit’ and ‘Automatic’. The ‘Manual’ mode is useful for making single measurements by setting $L_n = 1$. The mode ‘Auto. Limit’ is useful for short-term autonomous control of the RL, where the user can enter a number ($N_{RL}$) in the text box on the right side of the RL selection menu to set Ln = $N_{RL}$. The ‘Automatic’ mode is useful for long-term autonomous control of the RL by setting $L_n \rightarrow \infty$.

The combination of the different settings in the acquisition options determines the behavior of the RL sequence, i.e. the measurement resolution, the delay time ($\Delta T_d$) before the start of the RL sequence and the timer ($\Delta T_t$) between successive measurements can be programmed. By default, $\Delta T_d$ and $\Delta T_t$ are zero, but can be changed by entering a number in the text boxes in the Delay and Timer fields. As with the measurement resolution, the duration of the recording window ($\Delta T_w$) and the number of samples per window ($N_w$) must be set in the resolution window using the two selection menus. When using the protocol described above, the autonomous control of the RL sequence is limited to always using the same acquisition option settings to perform live acquisition of electrophysiological data. Thus, to use different acquisition options within the RL sequence, the acquisition table options located in the upper right corner of the panel (2) must be used to program a sequence of acquisition options by pressing the ON /OFF button within the acquisition table. Immediately after the capture options are activated, a dialog box opens corresponding to the dialog box shown in Figure A.3 (b), named "Add Menu". The "Add" menu" allows adding a set of capture options to be used in RL at the last position (last row) of the table of capture options. The capture options table can be viewed by pressing the "View" button in the capture options table, which opens a "View Menu" as shown in Figure A.3 (c). In addition to displaying the Capture Options Table, the "View Menu" has three buttons: one to access the "Add Menu", another to delete the rows in the Capture Options Table where the DEL field is checked, and another to update the table. Note that the RL sequence uses only the capture options defined in the capture field or table. In both cases, the capture options include an additional feature that allows the frequency range to be used. The start and stop frequency range can be set manually,

but the values entered require hardware validation. If the entered values are not validated, DSA will determine and return the closest valid values to the entered values. Thus, when the user sets the start and maximum frequencies on the capture panel, DAT immediately performs hardware queries to validate the entered values, while the values in the capture options table are not monitored and may not be the values used by the RL sequence.

Other capture options relate to the number of DSA input channels and the input overload suppression mode. Regarding DSA input channels, *rcSoftware* is designed to record only two input channels simultaneously, although there are some Keysight 35670A DSAs that are equipped with four input channels (also known as the AY6 option). When single-channel mode is enabled, the RL sequence allows simultaneous recording of transient and frequency responses using Trace A and Trace B panels, respectively. Note that single-channel mode applies only to recording the first input channel (CH 1). When using the two- channel mode (CH 1 and CH 2), only the transient or frequency response per recording channel can be measured. It is important to note that by recording the transient, spectral analysis can be performed later, but the reverse is not possible. On the other hand, the overload suppression mode is a useful option when the behavior of the sample to be measured from oscillations with amplitudes that require calibration (tuning) of the measurable input voltage range is known in advance or predicted. Otherwise, if there is an input overload in one of the recording input channels, the data will be lost, and the user will have to wait for another window period ($\Delta T_w$) to be recorded. Appendix C contains a table describing the typical values of the DSA frequency range as a function of the recording window period ($\Delta T_w$) and the number of samples ($N_w$).

By default, DAT synchronizes the RL sequence to the DSA Operation Status Register (OSR). While using the OSR has advantages, e.g., to avoid adjusting the time between successive measurements when averaging, on the other hand, the measurement can be fraught with problems due to the lack of automatic detection of the input range (if enabled). To force the RL sequence to always perform the transient and range measurement between successive measurements (and not during averaging), the RL sequence uses the ABORt command to interrupt the measurement, which immediately terminates the measurement in progress and resets the trigger system. To avoid using the ABORt command, DAT provides a button called "Status of Abort flag after each file" in the options menu shown in Figure A.3 (e) ‘to enable/disable the use of the ABORt command.

DSA also allows you to capture data remotely in a fully manual mode by using the two Start and Pause pushbuttons in box (2) below the Capture Options table. The Start and Pause buttons mimic the buttons of the same name in the DSA front end. When the Start button is pressed, the current measurement is paused, the DSA is configured with the capture options defined in DAT, and a new measurement is started. The Pause button simply forces the interruption of the current acquisition and,

importantly, keeps the last recorded data available in the DSA screen and memory so that the recorded data can be saved manually by simply pressing the Save button to the right of the Pause button.

### A.4.3.2 − Data options

The Trace A and B fields within box (2) provide access to the data options. The main characteristics to be specified are the recording channel, the range of the X and Y axes, and the unit. For the range of the X-axis the options Transient or Frequency Response are available, for the Y-axis Voltage or Current. To change the Y-axis domain, the pushbutton must be pressed in the Trace A and B fields. Changing the Y domain also determines which LNA options affect the recorded data, specifically the LNA voltage gain ($A_v$) or current sensitivity ($A_i$) in the Stanford SR560 and SR570 fields. Therefore, for transient measurements, the Y-Data field provides only a single option for recording voltage in volts (V) or current in amps (A). For voltage measurements, the DAT determines the recorded input voltage ($v_{in}$) of the SR560 LNA as:

$$v_{in}(t) = A_v v_{meas}(t) \tag{4.1}$$

where $A_v$ is the gain of the preamplifier and $v_{meas}$ is the voltage recorded by the DSA, where $v_{meas}$ is the output voltage ($v_{out}$) of the LNA, $v_{meas} = v_{out}$. By default, all input channels are set to measure the rms value of the voltage ($v_{rms}$), so $v_{meas} = v_{rms}$. For current measurements, DAT determines the sensed input current ($i_{in}$) of the SR570 LNA as follows:

$$i_{in}(t) = A_i v_{meas}(t) \tag{4.2}$$

where $A_i$ is the sensitivity of the preamplifier in amps per volt (A/V) and $v_{meas}$ is the voltage recorded by the DSA. Note that the Stanford SR570 LNA is a transimpedance amplifier that allows $i_{in}$ to be converted to a voltage signal, i.e., the output voltage ($v_{out}$) of the LNA, where $v_{meas} = v_{out}$.

If spectral measurements are used, the same spectral units are available to perform spectral analysis of voltage and current, where different types of spectra can be analyzed: linear spectrum (LS) with unit of measurement [V] or [A], power spectrum (PS) [$V^2$] or [$A^2$], root of power spectral density (RTPSD) [V/√Hz] or [A/√Hz], power spectral density (PSD) [$V^2$/Hz] or [$A^2$/Hz], and energy spectral density (ESD) [$V^2$·s/Hz] or [$A^2$·s/Hz]. By default, the spectral analysis is calculated by the DSA, so DAT must perform a unit conversion according to the gain or sensitivity of the LNA. A solution for the unit conversion was proposed by R. Tinti [27] and is as follows:

$$S_{in}(f) = \left(A_n S_{meas}(f)\right)^2 \tag{4.3}$$

where $A_n$ is either $A_i$ or $A_v$, depending on whether the measurement is in current or voltage, $S_{meas}$ is the measured spectrum, and Sin is the input noise spectrum of the LNA. However, equation (4.3) only

applies to the unit conversion of LS and RTPSD. For PS, PSD and ESD, equation (4.3) can be estimated as:

$$S_{\text{in}}(f) = \left(A_{\text{n}}\sqrt{S_{\text{meas}}(f)}\right)^2 \tag{4.4}$$

where the root square of the $S_{\text{meas}}$ converts the square unit, e.g. $V^2$, to the root unit V.

In addition, the Trace A and B fields provide the ability to change the X and Y axis display to a linear or logarithmic scale, set the channel coupling to AC or DC, set the window function to Uniform, Flattop, or Hanning, and set the input channel shielding to floating or ground.

### A.4.3.3 – Data storage options

The core function of *rcSoftware* data storage options is to allow the user to make decisions about how and where live recorded data is stored. The file management method implemented in DAT for data storage requires a destination location (directory) to store a raw data file with a unique (non-existent) file name. To change the location or specify a new location, the Change Directory button must be pressed. A folder selection dialog [28] opens where the user can select either a storage location on a local or a cloud-based drive. After closing the folder dialog, the selected location is displayed in the "Current Directory" window. As for the file name structure, all raw data files are saved with a file name that uses the same file name header followed by an index number that forces the index number to be saved with three leading zeros, e.g. "VOLTAGE001.m" or "VOLTAGE100.m". Two editable text fields are available in the "Insert File Name" field to change the file name header and index number. If the user selects an existing filename in the current directory (combination of filename header and index number entered in the GUI text fields), a dialog box [29] is displayed where the user must select how the next raw data file should look like: (i) overwrite an existing raw data file or (ii) increase the index number of the file until the first non-existing filename and index number combination is found. In the case of overwriting, only the first file with the same filename at the destination will be overwritten. All subsequence raw data files are automatically traversed until the first non-existent combination of filename and index number. To improve the usability of the user interface, the two editable text fields for changing the filename and index number are built into a background color scheme: Green indicates that the filename doesn't exist in the current directory; Orange indicates that the filename already exists in the current directory and the index number of the next recorded raw data file will be incremented; Yellow indicates that the user has requested that a particular filename be overwritten; Blue indicates that a new filename has been created with fresh data.

All raw data files are always stored in a MATLAB script file (.m). Each file always contains a text header followed by arrays of recorded raw data and a short script that visualizes the raw data stored in

the file. The text header stored in each file always contains the date and time of data acquisition; the LNA options used (gain and gain mode for voltage recordings and sensitivity and gain mode for current recordings); the measurement resolution options of the DSA ($\Delta T_w$ and $N_w$); a comment line that can provide an insightful description of the recorded data, e.g. E.g., name and identification number of the instrument (ID) and name of the cell line and cell culture medium used; and finally, the data options (windowing, coupling, shielding, and range) for each recording track A and B. The arrays of recorded data consist of two columns, where the first column always contains the time or frequency values, and the second column contains the recorded voltage or current values of the transient or spectrum data.

### A.4.3.4 − DSA optional features

The Keysight 35670A DSA has several optional features, some of which are included in DAT. For example, the DSA's graphic outputs, which allow the instrument display and an external monitor connected to the VGA port to be used simultaneously. DAT includes two pushbuttons in the display panel to control the graphic outputs, one assigned to the instrument display and the other to the external monitor. Another feature of DAT is the self-calibration of the instrument, which is displayed in the calibration panel. Two options are available to perform the front-end self-calibration preprogrammed by the manufacturer. One option allows a one-time self-calibration by pressing the calibration button. The other option allows a timer to be programmed to perform the self-calibration at regular intervals. To set up the calibration timer, the user must select the "Automatic" check box and enter the duration of the timer in units of minutes in the text box.

The other optional features of the DSA at DAT are dynamic range control and automatic axis scaling. By default, the dynamic range of the DSA is set to automatic, while automatic axis scaling is disabled. Therefore, to change the dynamic range to DAT, the user must uncheck the "Auto" checkbox in the range. Then a sliding menu will be displayed under the "auto" bullet, allowing the range to be set to a constant value ($W_R$), which will be displayed in the title of the range field $W_R$. If a fixed range is used, all signals with a higher amplitude than the selected range will be cut off. The automatic axis scaling of DSA can be activated or deactivated on DAT via the "Auto Scaling" button under the option field of the acquisition table.

### A.4.3.5 − DAT additional features

Some functions of DAT are considered additional functions because they aren't essential for recording electrophysiological signals. However, the Pulse Stimulation Toolbox (PST) shown in Figure A.3 (d) is provided with DAT to apply and record the response to voltage pulses. PST is still a

beta version that has numerous bugs that require thorough rework for some processes. Nevertheless, the version of PST presented here is shown as a proof of concept. The main features of PST are synchronization with the RL sequence and options to specify pulse shape (square, ramp, triangle), amplitude (- 5 V to 5 V and step size of 1.22 mV), frequency and duty cycle. All the above pulse settings depend on software control routines of the SR570 LNA input power supply, resulting in discrete pulse shapes (as when programming a pulse shape with a digital-to-analog converter (DAC)). Note that the pulse shapes depend heavily on the baud rate of the communication protocol and on the assumption that all messages sent to the LNA via the serial communication protocol (RS -232) are listened to and processed in time. Therefore, PST is far from being a robust alternative to voltage pulse stimulation but is useful for measurements that don't require high precision of pulse shape. To start the PST, the user must press the designated pulse button.

The other additional features of DAT are the listing of recorded data, the data export tool, and the options menu. The data export tool allows all recorded data to be saved to a MATLAB binary file (.mat). Later, in section A.5, the structure of data stored in MATLAB binary files will be described. To export the recorded data, the "Export" button must be pressed, which opens a dialog box for saving files [30]. For data listing, a specially developed dialog box is used with a table listing all data recorded so far. In the worst case, four dialog boxes are created listing the trace A and B recordings with transient and spectrum data.

Finally, the options menu shown in Figure A.3 (e) can be opened using the Options button of the same name. Essentially, the options menus provide access to numerous settings of the DAT. The most important settings are the physical addresses of the RS -232 and GPIB interfaces. For voltage and current LNAs, the RS -232 port number can be set individually. Since the SR560 and SR570 LNAs are listen-only communication protocol devices, there is no guarantee that the connected device is the SR560 or SR570 LNA, even if the connection status indicates that the connection is active. For the physical address of the GPIB interface used to connect to the Keysight 35670A DSA, there are two fields for entering the GPIB board index and primary address, as well as a button named "find" that uses the MATLAB function *instrfind* [31] to search for whether an Agilent or Keysight device is registered in the device registers of OS and available for connection establishment.

Other settings in the options menu include debug, diary, and report modes. In debug mode, any problems that cause the system to malfunction are printed out and sent via email. The printout is done in the MATLAB command window and the email is sent to the email address specified in the corresponding text box. Diary mode uses the MATLAB diary feature [32] and is useful for debugging purposes. Note that DAT prints the commands sent to the DSA and other information about the RL

sequence in the MATLAB command window. In report mode, a log of all recorded data is saved to a text file.

The remaining settings provided by the options menu are the print and performance options. The print options allow you to change the print format of the raw data files. The default format of the raw data files has already been described in the last paragraph of section A.4.3.2. If you prefer a different format, you can upload a text file containing a script that is compatible with the main variables of the *rcSoftware* and can print the raw data in the desired format. In the print options, there is a check box to specify the download and capture times between DAT and DSA in the header of the raw data file, and a text box to specify the printing accuracy of the raw data in text form. The performance options consist of calculation methods that allow the timeline and spectrum data to be determined instead of querying the DSA to obtain the same parameters. These options can be beneficial to avoid a small latency between each recorded file. The Timeout field in the Performance Options sets the amount of time DAT will automatically close all alarm and warning dialog boxes triggered by DAT.

# A.5 − Data Collection Toolbox (DCT)

The Data Collection Toolbox (DCT), shown in Figure A.2 (b), is designed to provide (i) an intuitive and interactive user interface for managing large raw data sets; (ii) automatic data compilation tools for organizing raw data files into one-dimensional arrays; (iii) offline access to the Data Process Toolbox (DPT). In essence, DCT is an abstract layer between the user and the raw data, providing less experienced users with efficient methods for accessing the raw data. Nevertheless, it's of utmost importance that users understand how the raw data is assembled into arrays.

First, the basic knowledge that any user should have in order to understand how DCT works is that data stored in files recorded with DAT is supported by DCT's compilation routine (CR) unless the files have been manipulated in some way. Also, each data file recorded with DAT always contains a file header and raw *x*,*y*−data fields of length (*k*), where the file header is needed to preserve the original printed date and time information (*T*). Second, CR assumes that multiple files (*N*) can be input, which also means that an equal number of raw data fields $x1, \ldots, xn$ and $y1, \ldots, yn$ are input, as shown in Figure A.4 (a). It is worth nothing that $x1, \ldots, x$n always starts at zero, i.e., $xn[1] = 0$, where *n* represents the index number of the file name. Third, all raw *x*,*y*−data series in the files recorded by DAT were hard printed with respect to the gain ($A_v$) or sensitivity ($A_i$) of the LNA, regardless of whether the measurement was made in voltage or current.

The core of CR is to sequentially store the raw *x*,*y*−data fields according to the incremental order of *n* into one-dimensional numerical array data structures (NADS), as shown in Figure A.4 (b). The CR uses the concatenation method to concatenate the raw *x*,*y* data fields into NADS, namely the *y*,

$x_{M1}$, $x_{M2}$, $x_{M3}$−NADS, through a for-loop large enough to perform $L$ iterations, i.e., $i$ = 1 to $L$, where $L$ is the length of $n$ and $i$ is the iteration index. To keep track of the indexing addresses of the $x$,$y$−data fields in the NADS, both the value of $i$ and the first ($F_n$) and last ($E_n$) address indexes used to find the $x$,$y$−data fields in the NADS are stored in the iteration field ($I$) and the indexing address fields ($F$ and $E$), respectively (see Figure A.4 (c)). To later access the $x$,$y$−data fields stored in the NADS, users only need to specify the iteration index value i, which corresponds to a filename index $n[i]$ and a data address (DA) specified by DA = $F[i]$ to $E[i]$.

The reason why CR performs the concatenation of the raw $x$−data arrays into three different NADSs, namely the $x_{M1}$, $x_{M2}$, $x_{M3}$ NADSs, is because of the use of the three different methods for organizing the timeline shown in Figure A.4 (d). Method 1 ($x_{M1}$) organizes the $x$−data fields according to the printed date and time information ($T$) retrieved from the file headers; method 2 ($x_{M2}$) according to the sampling period ($T_s$) of the last concatenated $x$−data field, where $T_s$ is simply given by the difference between two data samples; and method 3 ($x_{M3}$) according to a constant offset period ($T_c$) between each $x$−data field. $x_{M1}$ ensures that the original time axis is maintained, while $x_{M2}$ ensures that the connections between successive recorded raw data files are visually perceived as if they had been recorded continuously. In the worst case, $T_s$ is half a second ($f_s$ = 0.5 s), which can be determined from Table C.1 in Appendix C for recording windows of 2048 s with a total of 4096 samples per window. As with $x_{M3}$, the idea behind the structure of the timeline is to avoid large interruptions, e.g., DAT the typical latency ($\Delta t$) is estimated to be four seconds ($\Delta t \geq 4$ s) in the best case, where $\Delta t$ depends on the execution time of the routines that continuously check the DSA OSR, the data transfer time over the GPIB interface to the local PC, and the time required for matching and checking the input signal range. By default, $T_c$ is five seconds ($T_c$ = 5 s) and cannot be changed (hard-coded). The $x_{M3}$-NADS will likely be removed in future versions as it consumes memory resources, increases processing time, and has not produced useful results in practice to date. The pseudocode for CR is described in Figure A.4 (e).

Input data from CR must be entered by users into the Experiment Data Table (EDT), which is included in the DCT graphical user interface, as shown in Figure A.2 (b). Each row of the EDT represents a different experiment, and each experiment consists of a status, ID, a file header, an index, zeros, an instrument, a domain, and directory values. The experiment parameters described previously can be added to the EDT by manual and automatic methods or by simply loading experiment data stored in MATLAB binary (.mat) files. Note that the source of the (.mat) files containing the experimental data can be either the DCT or DAT. Saving and loading experimental data is the recommended procedure for the DCT because it saves time to quickly refill the DCT workspace with experimental data, and if the experimental data has already been compiled (with the EDT status value

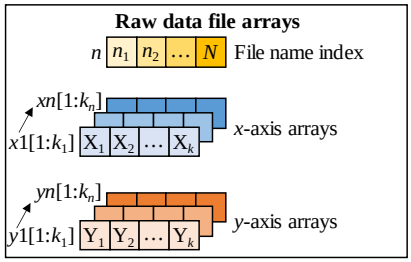


(a)

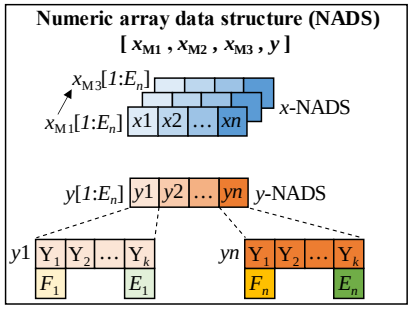


(b)

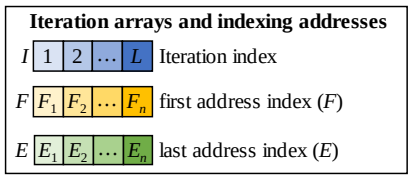


(c)

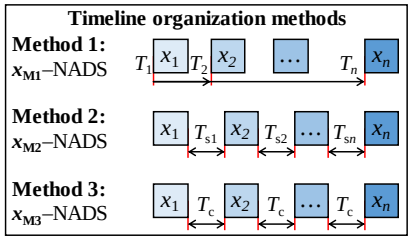


(d)

**Pseudo-code:** Compilation routine (CR)

**Input:** $n$ – index of the raw data file arrays
$T_c$ – constant offset interval between consecutive raw data files ( $T_c$ = 5 s)

**Data:** Raw data file arrays and the acquisition time and date interval
$y(1)[1{:}k_1]$ , … , $y(n)[1{:}k_n]$ ; $x(1)[1{:}k_1]$ , … , $x(n)[1{:}k_n]$ ; $T(1)$ , … , $T(n)$

**Result:** $y[\,]$ , $x_{M1}[\,]$ , $x_{M2}[\,]$ , $x_{M3}[\,]$ – NADS
$I[\,]$ , $F[\,]$ , $E[\,]$ – file and position indexing arrays

$N$ = length( $n$ ); // Total number of raw data files
**// Create file and indexing arrays**
$I = 1 : N$ ; // one index per each raw data file array ( $n$)
$F(I) = 0$ ; // Create $F$[] same size as $I$ and equalize all values to zero
$E(I) = 0$ ; // Create $E$[] same size as $I$ and equalize all values to zero
**// Create empty NADS**
$y = [\,]$ ; $x_{M1} = [\,]$ ; $x_{M2} = [\,]$ ; $x_{M3} = [\,]$ ; $F = [\,]$ ; $E = [\,]$ ;
$L = 0$ ; // buffer variable to store the length of $y$–NADS
$T_s = 0$ ; // buffer variable to store the sampling time of $x(n)$
**for** $i = I$
**// Concatenate*y*(*i*) to *y*–NADS**
$y = [\,y\,, y(i)[\,]\,]$ ;
**// Compilation method 1: concatenate*x*(*i*) to $x_{M1}$–NADS**
$T = T(i) - T(1)$ ; // Elapsed time between $T_1$ and $T_i$
$x_{M1} = [\,x_{M1}\,, (\,x(i)[\,] + T\,)\,]$ ;
**// Compilation method 2: concatenate*x*(*i*) to $x_{M2}$–NADS**
$x_{M2} = [\,x_{M2}\,, (\,x(i)[\,] + x_{M2}[end] + T_s\,)\,]$ ;
$T_s = x(i)[2] - x(i)[1]$ ; // Sampling time: difference between two consecutive samples
**// Compilation method 3: concatenate*x*(*i*) to $x_{M3}$–NADS**
$x_{M3} = [\,x_{M3}\,, (\,x(i)[\,] + x_{M2}[end] + T_c\,)\,]$ ;
**// Save file and position indexes**
$F = [\,F\,, (\,L + 1\,)\,]$ ; // First position is the previous saved last position + 1
$L$ = length( $y$ ) ; // Update length of $y$-NADS
$E = [\,E\,, L\,]$ ; // Last position is equal to the length of $y$–NADS
**end**

(e)

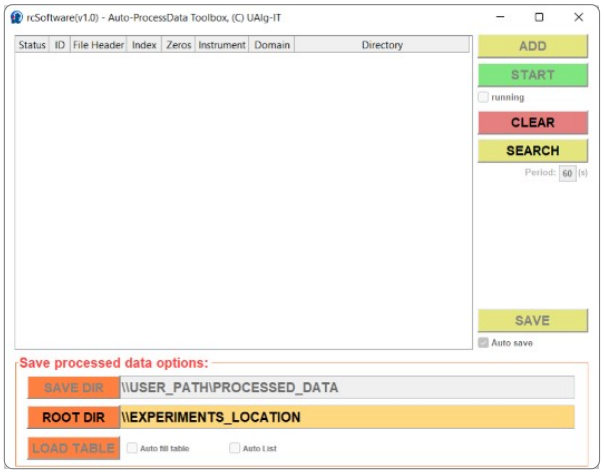


(f)

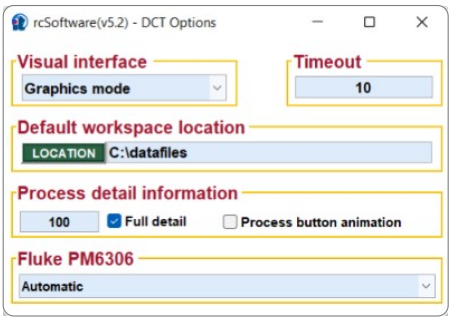


(g)

**Figure A.4 –** Arrays, methods, and tools for data collection. (**a**–**c**) Schematic representation of the arrays of the x,y raw data file, the numerical array data structure (NADS), and the iteration arrays or indexing addresses. (**d**) Data compilation methods for transient data. (**e**) Pseudocode of the compilation routine (CR) of raw data arrays in NADS. (**f**–**g**) GUI of the Auto Process Data Toolbox (APDT) and the DCT options menu, respectively.

enabled), it eliminates the time-consuming task of running CR. Both the manual and automatic methods require the user to interact with the DCT and be familiar with the procedures described in section A.5.2 for including the raw data in the EDT.

## A.5.1 − Secure workspace mode

The DCT is protected by a security system that requires authentication. Only registered users can access all DCT functions. However, a demo version is available for guest users. The DCT functions provided in the graphical user interface are locked when the DCT is launched and require login credentials to unlock them. If the login fails or the password dialog box closes, there is a button in the save and plot options to reopen the password dialog box.

DCT recognizes three types of users: administrator, regular users, and guest users. The only difference between administrator and regular users is the abstraction level of all debug lines output to the MATLAB command window. Guest users are limited to testing the DCT interface and can only run simulations of the CR. Regular users are always identified by their OS user account name, regardless of the OS installed, and the user password is provided.

The password dialog is based on the original code developed by Komarov [33]. Nevertheless, significant changes have been made to handle sensitive data encrypted with a Rivest-Shamir-Adleman (RSA) cipher key and to establish synchronization with the DCT.

## A.5.2 − DCT Panel (1): Process data options

Panel (1) provides access to manual and automatic compilation methods. In the manual method, the user must manually fill in all editable fields needed to identify all raw data files for each experiment performed with DAT, e.g., experiment identification string (ID), file name header and index number, leading zeros (with respect to the file index number), recording device, y−axis range (voltage or current), and file location (directory). After all settings are made, the user can either compile the raw data into NADS immediately using the "Process" button or add the new experiment information to the EDT using the "Add" button. The "Add" function is helpful to automate the CR with multiple experiments in the EDT so that the user must fill in all editable fields again for each experiment. Note that immediate compilation of the raw data into NADS is only possible if the EDT is empty, otherwise the experiment information entered into the editable fields will be neglected. The automatic method is implemented by the Auto Process Data Toolbox (APDT) shown in Figure A.4 (f), which provides a search engine for collecting the experiment information needed to compile the raw data from multiple experiments into NADS. The APDT is accessed by clicking the button AUTO. When the APDT is

started, a dialog box [28] is launched to select the root directory of the search engine, i.e., the search engine collects information from all folders above the root directory. Note that the search engine scan may take a long time depending on the number of files and folders to be analyzed. Therefore, it's advisable to use narrow root directories and repeat the process to change and check different root directories. The root directory can be changed using the "Root Directory" button in the "Save Processed Data" radio button and the search routine can be started using the "List" button. While the search engine is collecting information, the APDT is locked until the inspection routine is finished. Only then is the collected information automatically included in the EDT of the APDT. The APDT provides an option to clear the EDT via the "Clear" button. Note that the only procedure provided to transfer the EDT from the APDT to the DCT requires closing the APDT window. This aspect will need to be fixed in a future release.

Regardless of whether the DCT EDT is filled out manually or automatically, the CR must be executed using the "Process" button. The processing time for compiling the entire EDT varies depending on the local PC hardware and the large number of raw data files to be processed. Note that CR automatically skips any experiments in the EDT that are already marked as compiled (status field in the first column is checked). If an error occurs during processing, for example if the data file is corrupted or incompatible, a popup window will be displayed with a detailed error message. Once CR completes processing the EDT, the status field for all successfully completed experiments is activated and a file selection dialog [30] opens, prompting the user to specify a directory and file name to save the compiled data to a MATLAB binary (.mat) file, as recommended.

All fields in the EDT are editable. Any change in an EDT field has no immediate effect but requires deselecting the status fields and re-running CR via the process button. The EDT has a delete button and a reset button. The delete button allows you to exclude experiments (rows) from the EDT via a dialog box with a list of all experiments and three buttons: one button provides the option to exclude all experiments from the EDT; the second button excludes only the experiments selected in the dialog box list; and the third button allows you to cancel the delete operation and close the dialog box . The "Reset" button resets the DCT to the default values and empties the EDT.

### A.5.3 − Panel (2): Save and plot options

The save and load buttons allow you to use MATLAB's interactive folder and file selection box [28,30] to save and load the EDT from MATLAB binary files (.mat). The source of the binaries can be from either the DAT or the DCT. The loading process can be run multiple times, allowing an extensive library of experiments to be included in the DCT workspace.

The "Plot" button opens the Data Processing Toolbox (DPT) shown in Figure A.2 (c) with all the data collected in the EDT of the DCT. Note that the DPT runs independently of the DCT. Therefore, changes in the EDT won't take effect until you press the Plot button.

The print button is useful for obtaining text files (.txt) for each experiment listed in the EDT, detailing the experiment file by file. After pressing the pushbutton, a file selection dialog [30] opens, prompting the user to specify a directory and file name for saving the report files. After selecting the file name and location, a dialog box opens with a list of all experiments, where the user has the option to print the report files of all or the selected experiments as well as to cancel the printing process.

The command window print button is for troubleshooting purposes only and is accessible only to the administrator. It provides a high-level method that mimics the MATLAB command window, but in a very limited form. The Command Window button will likely be removed or made inaccessible in a future release.

### A.5.4 − DCT built as an autonomous server machine for raw data compilation

The remote-control button opens the APDT shown in Figure A.4 (f), but all buttons and editable fields in the user interface are unlocked and enabled for immediate use. The unlocked features in the remote options allow the setup of a server-like local PC, which periodically runs a search engine in a root directory to collect raw data files and compile them into NADS. All remote options still correspond to a beta version, presented here as a proof-of-concept. More work is needed to develop a stable version.

The use of the remote server offers users time savings by giving them immediate access to experimental data already compiled and ready to use at DPT, thus avoiding the longtime of collecting and compiling experimental data. However, Internet speed or cloud server access time may also impose time constraints. The size of a MATLAB binary file (.mat) containing an experiment with about 3800 raw data files compiled into NADS using DCT is about 122 MB. Therefore, in a cloud-based storage system, it'll take an upload and download time of 122 MB for the data to become available. Compared to the 564 MB, which occupies the same uncompressed 3800 raw data on the local drive or cloud storage space, the compiled form of the raw data in NADS stored in .mat files allows 4.5 times compression and instant access to the data via the DCT. Remote access is via the mechanism described in Appendix B, which is also used at DAT. It's advisable to use a different location for the user requests, otherwise the server is likely to behave unexpectedly.

## A.5.5 − DCT options menu

The DCT contains an options menu that allows the user to make some adjustments to the DCT functions. The DCT options menu is shown in Figure A.4 (g) and is accessed by pressing the options key. One of the options provided is the popup menu, which can be used to switch the visual interface of all pushbuttons in the graphical user interface between graphic and text modes. In graphics mode, the DCT sets the background of all buttons with images, while in text mode it uses the built-in MATLAB button properties to set the background color and text. Another setting in the options menu is the timeout period (in seconds), which allows you to set the amount of time after which popup warning windows will automatically close.

By default, the DCT working folder (similar to the MATLAB workspace location) is set by the MATLAB *userpath* [34] function. However, if the user pretends to change the location where all folder or filename selection dialog boxes are open, they can use the ‘location’ button to specify a new location by using a folder selection dialog box [28] or by simply typing a string with a valid (existing) location in the text box.

While CR is running, the DCT graphical user interface displays a series of text boxes with iteration status information, namely the line number of the EDT that identifies the experiment in progress, the iteration index, the number of the file being compiled, the total number of files, the percentage, and the estimated time to complete CR for the experiment in progress. In the detail view of the process, located in the DCT options menu, the user can change the frequency of updating the detail information, the level of detail, and the use of graphical animations during the execution of CR. The detail level number entered in the first text box determines the number of iterations until the detail information is updated. If the Full Details button is disabled, only the percentage and estimated time to complete CR will be updated.

The remaining setting in the DCT options menu applies to raw data files recorded with in-house software called RCL, which remotely controls a Fluke PM6306 impedance analyzer (Fluke Corporation, Everett, USA). The RCL software runs on legacy Microsoft computers (DOS). Therefore, all recorded files extracted to modern OS need additional editing to change the file extension capital letters from ‘.M’ to ‘.m’, otherwise the files cannot be run in MATLAB. Also, for some files, the missing impedance values recorded at the frequency of 50 Hz need to be repaired, resulting in run errors. Therefore, the DCT options menu provides a popup menu to toggle the automation of CR according to the file repair and file extension change described earlier. By default, the "Automatic" mode is set, i.e. CR first checks the file extension and only then corrects the 50 Hz impedance data line if necessary. If the file has no error (even if the 50 Hz line doesn't exist), the routine to correct the

50 Hz line is skipped. There is also "Manual", "Yes, all" and "Skip all" modes. In the "Manual" mode, the user must decide for each file whether to change the file extension and fix the error. The "Yes, All" mode forces the change and fix of all operations; the "Skip All" mode ignores the change and fix of all operations.

# A.6 − Data Processing Toolbox (DPT)

The Data Processing Toolbox graphical user interface (DPT), shown in Figure A.2 (c), was developed to provide a set of tools and functions that allow visual access to data recorded with DAT through MATLAB figure windows. The procedures for handling, processing, and visually accessing the data are described in section A.6.1. The additional features of DPT are then described, such as the in-figure tools, the options menu DPT, the Noise Data Processing Toolbox (NDPT), and the Statistical Data Processing Toolbox (SDPT).

## A.6.1 − Handling, process, and visual access of the data

To visualize data, you must use one of the three available buttons in the lower left corner, labeled "+", "Plot" and "Add". The "+" button always creates a new mapping window to visualize the selected data, while the "Plot" button displays the selected data in the last mapping window created with DPT. By default, both the "+" and "Plot" buttons replace the data previously displayed in the figure unless the MATLAB *hold* function [35] has been enabled by the user. The "Add" button allows multiple plots to be inserted into the same figure window via an interactive options menu that allows the user to select one of the currently available figure windows.

Although by default the data is plotted immediately into a MATLAB imaging window when one of the three pushbuttons described above is pressed, the DCT provides the option to first select the experimental data ($y$−NADS) from either DAT or the DCT and then select one of the three $x_{M1}$, $x_{M2}$, $x_{M3}$−NADS available for each experiment using the two side-by-side drop-down menus in the upper left corner of DPT. $y$−NADS are unique to each experiment, but can relate to either voltage or current data. For this reason, the selection menu on the left displays the text string "Voltage" or "Current" for each experiment loaded into the DPT workspace in the following order in the title of the file panel: File Index Number (e.g., 1 to 100); EDT Line Number; and Experiment ID. If the DAT was used to open the DPT instead, the line number is omitted, and the experiment ID is recording track A or B. The drop-down menu on the right replaces the three $x_{M1}$, $x_{M2}$, $x_{M3}$−NADS variable names with the text strings "Original", "Join", and "Constant offset", respectively.

In the upper right corner of the user interface additional settings are offered to adjust the scales of the X-Y units, to enter an offset value for the X-Y data and to make the X-axis data start at zero ($x[1] = 0$) regardless of the logged time in NADS.

### A.6.1.1 − Files Panel

The file panel contains two editable text fields, namely the 'from' and 'to' fields, which allow scaling of the data address (DA) displayed only with the values of the iteration index ($i$), where $i_F$ and $i_T$ are the numerical value entered in the 'from' and 'to' fields, respectively. Normally, the iteration index is equal to the index of the file name ($n$), $i = n[i]$, which means that the selected experiment in the NADS compiles the $x$,$y$−data fields since $n[1] = 1$ and beyond in a natural and increasing order ($\mathbb{N}$). In cases where $n[1] \neq 1$ or $n \notin \mathbb{N}$, $i \neq n[i]$. In these cases, it's advisable to print a report file of the selected experiment on the DCT to get a list of NADS organization by $i$ and $n$. By default, $i_F$ and $i_T$ are forced by DPT to be a text string containing a natural number, namely the DA given by: DA = $F[i_F]$ to $E[i_T]$. However, if the "Accept multiple files?" button is enabled, DPT accepts that $i_F$ and $i_T$ are a series of natural numbers. In this case, non-sequential data sets can be visualized, e.g., if $n[i]$ = [1 2 3 4 5 6], then $i = n$, and to visualize all data except $i = 2$ and $i = 4$, the $i_F$ and $i_T$ values must be defined as $i_F$ = “1 3 5” and $i_T$ = “1 3 6”, where DA is given by,

$$\text{DA} = \left[F\left[i_F[1]\right] \text{ to } E\left[i_T[1]\right], F\left[i_F[2]\right] \text{ to } E\left[i_T[2]\right], F\left[i_F[3]\right] \text{ to } E\left[i_T[3]\right]\right]$$

### A.6.1.2 − *x*,*y*−axes font and plot lines parameters

The parameters for the x and y-axis, the font and the plot lines can be changed with the two push buttons and the three selection menus in the file control panel. The "Font" and "Color" buttons can be used to format the font, font style, and font size parameters for the x and y axes using the MATLAB font selection dialog box [44] or the font color using the interactive MATLAB color tool [45]. In the plot line parameters, users can change the line thickness from 0.5 to 12 points (points are MATLAB's default unit), the line style (solid, dashed, dotted, and dashed-dotted), and the line color in one of the 31 predefined color palettes in the three dropdown menus. Note that changes to the font and line parameters take effect only for new figures created using the methods of DPT described earlier in section A.6.1.

## A.6.1.3 − Detrend options panel

Detrend analysis supported by DPT is useful for removing the DC component from transient data. However, it should be used with caution, especially by inexperienced users who cannot account for signal distortion due to the filtering process. Note that the detrend analysis used by DPT isn't the same as the MATLAB *detrend* function [36], but is a programmed function called *itdetrend* that has the same properties as [36] to analyze either the total magnitude or the trend of a data set by removing interpolating polynomials of different orders, as well as a function to filter the entire data set with a Savitzky-Golay (S-G) filter. The S-G filter uses convolution to fit successive frames (such as fixed-size trends) with least-squares polynomials of different orders, a method often used for data smoothing [37]. Detrend analysis and the S-G filter use the polynomials to fit the trends of a data set, with the main difference between the two methods being the trend size (number of samples) being analyzed. The *itdetrend* function allows the use of trends with full, fixed, or even different sizes, as shown in Figure A.5 (a−e). Figure A.5 (a) shows the case where the *itdetrend* function is unique compared to the MATLAB *detrend* function [36]: when the trend size is set to zero, the *itdetrend* function

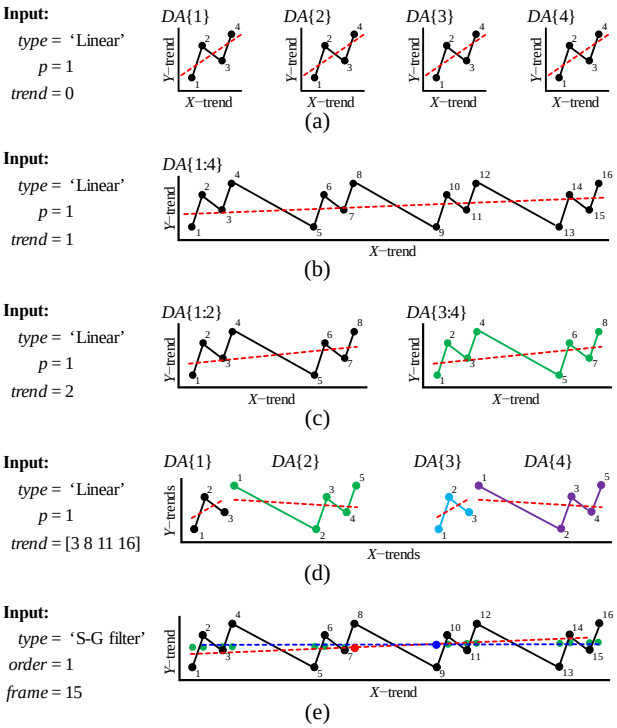


**Pseudo-code:** *itdetrend* routine

**Input:** *type* – type of interpolation method
*p* **or** *order* – polynomial degree (order), $p \geq 0 \wedge p \in \mathbb{N}$
*trend* **or** *frame* – trend size or frame length
**Data:** *x*[1:*K*] **and** *y*[1:*K*] – datasets of the original $x_{Mn}$ and *y*-NADS
**Result:** $y_F$[ ] – NADS, where $y_F$ is the filtered NADS

**// Select detrend method**
**if** type = 'Constant' **or** type = 'Linear' **or** type = 'Polynomial'
  **// Get data addresses (DAs)**
  *DA* = getDataAddress( *x* , *y* , *trend* ) ; // DA is a cell array structure
  *N* = length( *DA* ); // Each cell contains the DA to each trend
  **// Create empty NADS**
  $y_F$ = [ ] ;
  **for** *k* = 1 : *N*
    *Y* = *y*[ *DA*{*k*} ]; // Get *Y*-trend
    *X* = *x*[ *DA*{*k*} ]; // Get *X*-trend
    $P_p$ = *polyfit*( *X* , *Y* , *p* ); // Get the interpolating polynomial coefficients
    *P* = *polyval*( $P_p$ , *X* ); // Get the interpolating polynomial samples
    $y_F$ = [ $y_F$ , *Y* − *P* ] ; // Subtract the interpolating polynomial
  **end**
**else** // type = 'S-G filter'
  $y_F$ = *y* − *sgolayfilter*( *y* , *p* , *trend* ); // Subtract the interpolating S-G filter
**end**

(f)

**Figure A.5 –** Examples of detrend analysis performed with the *itdetrend* function considering the use of NADS, which stores four data samples per raw data file. (**a−d**) Using interpolating 1st order polynomials, degree (*p*) = 1, and different trend sizes (*trend*). (**e**) Using an S-G filter with 1st order polynomials (*order* = 1) and fixed frame length (*frame* = 15 samples), corresponding to a total of 16 trends, i.e., *DA* = { 1:8 , 1:9 , 1:10 , 1:11 , 1:12 , 1:13 , 1:14 , 1:15 , 2:16 , 3:16 , 4:16 , 5:16 , 6:16 , 7:16 , 8:16 , 9:16}. The red and blue dashed lines and solid examples are the only interpolating polynomials that span the full image length for *DA* = {1:15} and *DA* = {2:16}, respectively. (**f**) Pseudocode of the *itdetrend* routine.

automatically detrends the *y*−NADS dataset into trends that match the original, i.e. detrend file-by-file or equal detrend *i*-by-*i* index value. Figure A.5 (e) shows the only example in which the S-G filter is used. For simplicity, only the fitting lines with a frame length of fifteen data samples (frame = 15) are shown. The remaining frames include fewer data samples (frame < 15) and showing fourteen more lines in Figure A.5 (e) would degrade the visibility of the data.

To use Detrend Analysis, users must check the "Filter DC component?" box on the DPT graphical user interface to unlock the "Trend", "Degree", and "Type" fields. The Type field is a drop-down menu that lets users switch the detrended analysis method between Constant, Linear, Polynomial, and S-G filters. The Constant and Linear options are an extension of the Polynomial method, where the polynomial degree (*p*) is fixed at zero and one, respectively, regardless of the number entered in the "Degree" field. In the "Trend" field, users can specify the trend quantities, as shown in the examples in Figure A.5 (a−e). When the "Type" is changed to S-G filter, the names of the "Trend" and "Degree" fields change to "Frame" and "Sequence" respectively.

The pseudocode for the *itdetrend* routine is described in Figure A.5 (f). It consists of using the MATLAB functions *polyfit* [38], *polyval*[39], and *sgolayfilter* [40] to perform the detrend analysis. The *getDataAddress* function is a programmed function that returns a cell array structure containing the data addresses (DA) relative to the input trend value, as described in section A.6.1.1.

### A.6.1.4 − Time series analysis (Average options)

Through the graphical user interface of DPT, users can quickly estimate the average power spectral density (ΔPSD or $|S(f)|^2$) of the selected data files by simply activating the "Average" button. By default, DPT estimates the one-sided PSD ($|S_n(f)|^2$) using the MATLAB *periodogram* function [41] convolved with a uniform rectangular window for each raw data segment (transient raw data per file), yielding the average of *N* periodograms ($|S(f)|^2$) given by,

$$|S(f)|^2 = \frac{1}{N}\sum_{n=0}^{N}|S_n(f)|^2 \tag{4.5}$$

where *n* is the index of the raw data segment. To calculate and visualize the ΔPSD, users must press one of the three assigned pushbuttons to display the data. If a single data file is used and the Average option is enabled, the PSD obtained isn't an average, but the estimated one-sided PSD, as also obtained from live recordings of transient data using the DSA.

Along with the average options, two other settings are provided. One is a drop-down menu that allows users to change the window function used to estimate the PSD: Rectangular, Hamming, Gaussian, Flat Top, Kaiser, Blackman, Chebyshev, Hanning, Taylor, and Tukey [42–51]. The other

setting is a numerically editable field only (hereafter denoted *M*) that allows estimate ΔPSD using the Bartllet's method [52,53] to reduce the variance of the periodogram in exchange for a reduction of the frequency resolution ($f_s$). Bartllet's method consists of split the original data segment with a total of $N_{ODS}$ samples into *K* (non-overlapping) data segments with equal numbers of samples *L*, so that $K = N_{ODS} / M$, where *M* is simply a divisor. Next, the periodogram of each data segment is calculated and averaged, resulting in a reduced variance periodogram (ΔPSD).

There are three possible scenarios for estimating the ΔPSD as a function of the *M* value: (i) when $M = 1$ (the default value), (ii) when $M > 1$ and (iii) when $M < 1$.

**(i) −** When $M = 1$, the averaged periodogram (ΔPSD) is calculated without using the Barllet method. Thus, each iteration of equation (4.5) consists of averaging periodograms, each resulting from a segment of data stored in the NADS that corresponds to the original raw data from a recorded file.

**(ii) −** When $M > 1$, the Barllet's method is used, and in turn, the original data segment which has a length of $N_{ODS}$ samples is split into *K* data segments of *L* samples. Since $M > 1$, *K* is necessarily smaller than the length $L_n$ of a data segment stored in the NADS corresponding to the original raw data from a recorded file, i.e., $K = N_{ODS} / M \wedge L > L_n$. In this case, $f_s$ increases because a wider time window (with more samples per data segment) is used. For example, when $M = 2$, each iteration of equation (4.5) consists of averaging periodograms, each resulting from merging two data segments of length $L_n$ stored in NADS, thus doubling the window period without changing the sampling time. Under these circumstances, each data segment $K_{[n]}$ used to calculate the periodogram has a length of *L* samples of $2 \times L_n$, resulting in an estimated average periodogram that doubles the frequency resolution ($f_s$) compared to the standard $f_s$ obtained when $M = 1$.

**(iii) −** When $M < 1$, the Barllet's method is used, and in turn, the original data segment which has a length of $N_{ODS}$ samples is split into *K* data segments of *L* samples. Since $M < 1$, *K* is necessarily greater than the length $L_n$ of a data segment stored in the NADS corresponding to the original raw data from a recorded file, i.e., $K = N_{ODS} / M \wedge L < L_n$. In this case, $f_s$ decreases because a smaller time window (with less samples per data segment) is used. For example, when $M = 0.5$, each iteration of equation (4.5) consists of averaging periodograms, each resulting from halving one data segments of length $L_n$ stored in NADS, thus halving the window period without changing the sampling time. Under these circumstances, each data segment $K_{[n]}$ used to

calculate the periodogram has a length of $L$ samples of $0.5\times L_n$, resulting in an estimated average periodogram that halves the frequency resolution ($f_s$) compared to the standard $f_s$ obtained when $M = 1$.

It is worth noting that the algorithm for averaging periodograms for data recorded at different periods and resolutions is unsupervised, and in turn, users are advised to have caution using the periodogram averaging technique. Therefore, is users' responsibility to use only data segments from files with the same sampling time to perform spectral averaging correctly.

Moreover, if the Bartllet method is used ($M \neq 1$), data samples can be neglected. For example, if $M = 3$ and the data segment to be divided into $K$ segments consists of contiguous data segments with $4\times L_n$ samples, the averaged periodogram results from a single iteration ($n = N = 1$) of equation (4.5) considering the length $L$ of the data segment $K_{[n]}$ with $3\times L_n$, again neglecting the last $L_n$ samples. One way to avoid neglecting data segments is to use overlays (overlapping samples), as proposed by the well-known Welch method [54]. This option is not yet available, although a beta version has been implemented for experimental purposes only.

## A.6.2 − In-figure toolbar tools

In addition to MATLAB's own in-figure tools, a total of sixteen additional tools have been developed and appear in the toolbar of all MATLAB figure windows created by DPT. Table A.1 describes the sixteen additional tools and identifies them with a tool number (1 − 16). The tool number is arranged in the same visual order from left to right in the figure toolbar as shown in Figure A.6 (a,b).

Tools 1, 8, 9, 10, and 14 are used to quickly save the figure window to image or data files. The filename and save location are displayed in the balloon when users hold the mouse pointer over the tool icon for about 2 seconds. To change the file name or location, users must use the options menu described in section A.6.3 or the Figure option Toolbox (FOT), which users can access just by pressing the tool icon 15.

Tool 2 measures the maximum horizontal ($\Delta x$) and vertical ($\Delta y$) Euclidean distances between two or three cursor datatips and displays the $\Delta x$ and $\Delta y$ distances in a text box located on the far right of the figure axes (see Figure A.6 (a)). The $\Delta x$ and $\Delta y$ dimensions are automatically calculated when one of the cursors datatips is moved.

Tool 14 is recommended to store relevant information about the signals. It provides a simple but manual tool to export datatips information to a MATLAB script file (*.m) that users can later use to perform the desired analysis.

**Table A.1.** List and description of in-figure tools included in the toolbar of all MATLAB figure windows created with DPT.

| Tool | Icon | Description | |
|---|---|---|---|
| 1 |  | Save the axes of the figure in a Portable Network Graphic (*.png) image file. | |
| 2 |  | Measures the maximum horizontal ($\Delta x$) and vertical ($\Delta y$) Euclidean distances between two or three cursor datatips. | |
| 3 |  | Copy the axes of the figures to the clipboard area. Only on Windows® computers the metadata is copied as well. | |
| 4 |  | Changes the axes of the figure between normal and square elongation. | |
| 5 |  | Decreases line width by 0.5 points per click. | (i) If there is only one axis and one line in the figure's axes, the line settings are changed in the only line present.<br><br>(ii) If there are two or more axes or two or more lines in the same axes, users must insert a new or move the last inserted cursor datatip to select the line to change the settings. |
| 6 |  | Increases line width by 0.5 points per click. | |
| 7 |  | Change the line color between black, blue, red, magenta, and green. | |
| 8 |  | Save all data on the axes of the figure to a MATLAB binary file (*.mat). Also create a MATLAB script file (*.m) that contains a short code to load and plot the data stored in the *.mat file. | |
| 9 |  | Save all data on the axes of the figure to a MATLAB script file (*.m) and include at the end of the file a short code to plot the variables printed in the *.m file. | |
| 10 |  | Save all data on the axes of the figure to a MATLAB script file (*.m) using ASCII format. | |
| 11 |  | Enable/disable the horizontal and vertical axes grid lines visibility. If logarithmic scale is used, it also enables minor grid lines. | |
| 12 |  | Enable/disable the figure axes contour line visibility. | |
| 13 |  | Join multiple data lines into a single data line. It requires insert at least one cursor data tip per each line to join. | |
| 14 |  | Save the displayed information on all cursor data tips into a MATLAB script file (*.m) file. | |
| 15 |  | Open the Figure Options Toolbox (FOT), which lets users quickly edit the properties of a MATLAB figure window, axes, and $x$,$y$−axis, sum or multiply a given $x$,$y$−data row by a constant value, and change the filename and location of files created with the in-figure tools. | |
| 16 |  | Measures the signal area ($\Delta A$), length ($\Delta X$), and amplitude ($\Delta Y$) parameters between two cursor datatips. Also measures the positive ($^+$) and negative ($^-$) portions of the signal parameters. Note that the baseline must be always set to $y = 0$. | |

Tool 15 opens the Figure options toolbox (FOT) shown in Figure A.6 (d). The FOT provides quick and easy access to format or change the properties of MATLAB figure windows, axes, and the $x$− and $y$−axes, similar to the MATLAB Property Inspector menu but with additional features, such as interactive drop-down menus for selecting the figure handle to edit and the subsequent axes and data handles. In the upper left corner of the user interface, users can use the 'Figure Handle button to update the list of drop-down menus on the right to include all figure and subsequent axis handles. So if a figure has multiple axes, say 4 axes, there will be 4 handles available for editing in the selection menu.

Similarly, the data handles are updated using the ‘Figure Data button to update the selection menu on the right side of the button with all the data handles within the selected figure handle.

FOT is divided into fields and each field is labeled according to the specified properties, except for the font properties, which users can access via a separate button, and the background color of the figure, which users can select via a drop-down menu below the field for the y-axis. In the $x-$ and $y-$axis fields, users can change the axis boundaries using the editable "Start" and "End" text boxes, which correspond to MATLAB's *xlim* and *ylim* [55,56] functions. Users can also specify the tick period or size (depending on the context) with a single number or a sequence of numbers, change the axis scale between linear and logarithmic, and change the axis color. Using the axis properties, users can change the background color of the axes, set the graphical aspect ratio of the axes between normal and square, turn on the visibility of the axis contour lines as in the MATLAB *box* function [57], turn on and off the function to keep the plot as in the MATLAB *hold* function [35], edit the axis and title labels, set the length and direction of the small and large axis ticks, change the line width, and finally use a unique feature that allows users to quickly multiply the length of the axis ticks by a number.

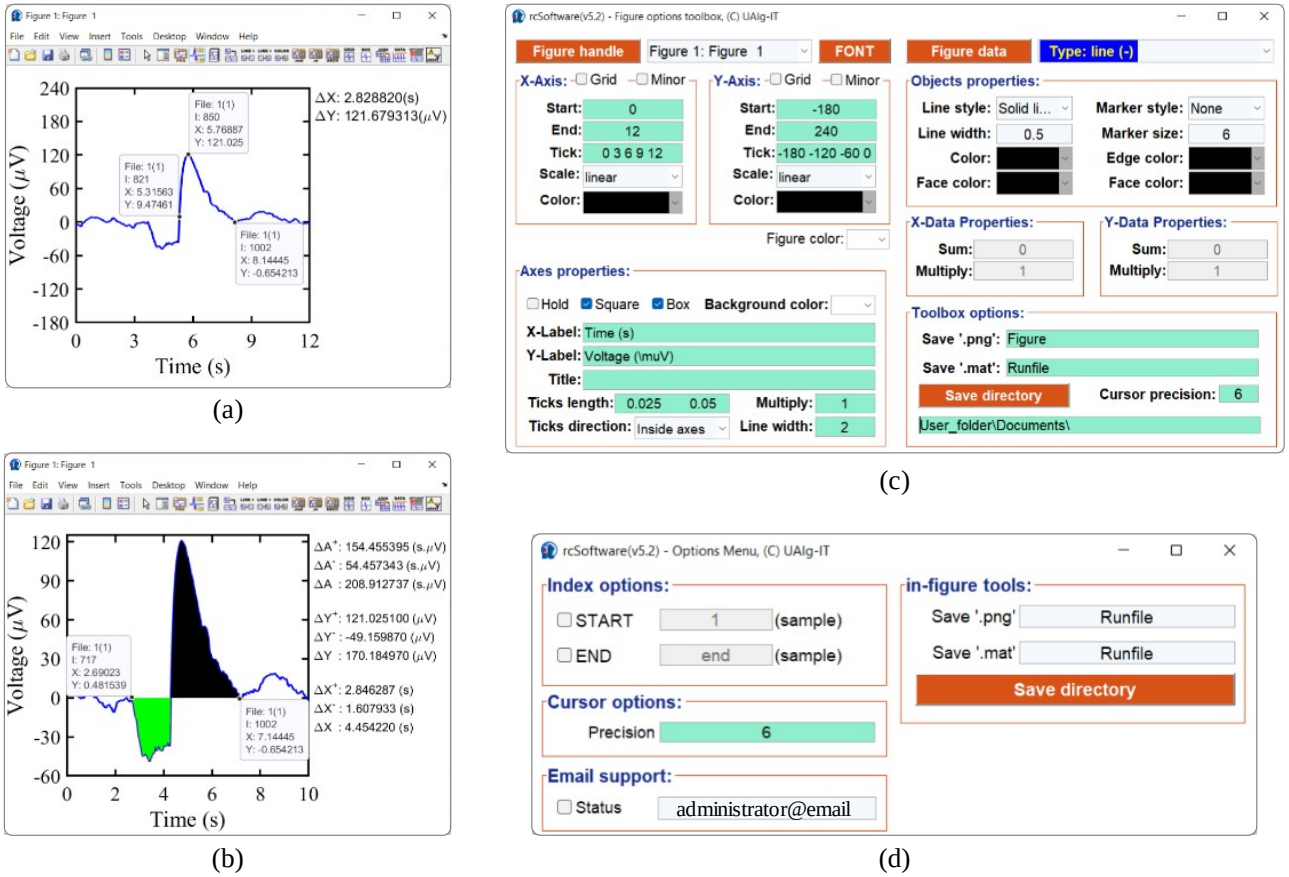


**Figure A.6 –** DPT additional settings and tools. (**a**) Example of using tool 2 (Euclidean ruler) to measure maximum horizontal ($\Delta x$) and vertical ($\Delta y$) Euclidean distances between three cursor datatips. (**b**) Example of using Tool 16 to measure the signal area ($\Delta A$), length ($\Delta X$), and amplitude ($\Delta Y$) parameters between two cursor data tips. (**c**) Figure Options Toolbox (FOT) user interface. (**d**) User interface of the options menu DPT.

Object properties let users access the properties of the data handles, such as the width, style, and color of the line and marker. The X,Y−Data property box allows users to sum or multiply the selected X,Y data by a number. This option is very useful when users combine it with the tool 16 to quickly level the signal baseline to $y = 0$. In the tool options users can change the file names and location of the images, MATLAB binary (*.mat) and script (*.m) files used by tools 1, 8, 9, 10 and 14. The Save Directory button opens a dialog box [28] where the location can be changed. To avoid overwriting files, the background process analyzes the headers of the input files and automatically iterates the file name with an index number to the first non-existent file name in the selected location. In the option field of the toolbox users can change the decimal precision of the cursor data type numbers.

Tool 16 measures the signal area ($\Delta A$), length ($\Delta X$), and amplitude ($\Delta Y$) parameters between two cursor datatips as shown in Figure A.6 (b). Also, the total positive (+) and negative (−) components of the signal are displayed, namely $\Delta A^+$, $\Delta A^-$, $\Delta X^+$, $\Delta X^-$, $\Delta Y^+$ and $\Delta Y^-$. All values are printed in a text box located on the far right of the axes of the figure. When one of the datatips is moved, all signal parameters are automatically iterated. Note that depending on the number of samples to be analyzed, it may take a long time to perform a single iteration, mainly because of the large number of blocks printed to mark both the positive (black) and negative (green) areas. The signal area is determined assuming that the baseline lies on the ordinate, $y = 0$, and is the sum of all areas between two consecutive data samples, $P_0 = (x_0,y_0)$ and $P_1 = (x_1,y_1)$, assuming that there are three cases: case 1, both ordinates of $P_0$ and $P_1$ are greater than or equal to zero, $y_0 \geq 0$ and $y_1 \geq 0$; case 2, both ordinates of $P_0$ and $P_1$ are less than or equal to zero, $y_0 \leq 0$ and $y_1 \leq 0$; and case 3, one of the ordinates of $P_0$ and $P_1$ is positive and the other is negative. Thus, for cases 1 and 2, when $y_0 = 0 \vee y_1 = 0$, the total area ($\Delta A$) is given by,

$$\Delta A = \frac{\Delta P\{x_0, x_1\} \times \Delta P\{y_0, y_1\}}{2} \tag{4.6}$$

where $\Delta A$ is simply a triangular surface. If $y_0 \neq 0 \wedge y_1 \neq 0$, then $\Delta A$ is the sum of a rectangular and a triangular surface, where the height of the rectangle is the lowest ordinate, $\min\{y_0,y_1\}$, and the height of the triangle is the difference between $\max\{y_0,y_1\}$ and $\min\{y_0,y_1\}$, and is given by,

$$\Delta A = \Delta P\{x_0, x_1\}\left(\min\{y_0, y_1\} + \frac{\max\{y_0, y_1\} - \min\{y_0, y_1\}}{2}\right) \tag{4.7}$$

In case 3, $\Delta A$ is the sum of two triangular areas, but requires determining the coordinate of the intersection with the ordinate axis, $P_i = (x_i,y_i) = (x_i,0)$. $x_i$ is found by solving linear equations and is equal to $x_i = -b / m$, where $m = \Delta P(y_0,y_1) / \Delta P(x_0,x_1)$ and $b = y_1 - m \times x_1$. Thus, $\Delta A$ is the sum of the positive ($\Delta A^+$) and negative ($\Delta A^-$) triangular areas, respectively, given by equation (4.6) considering the samples $[P_0,P_i]$ and $[P_i,P_1]$.

## A.6.3 − DPT Options menu

DPT contains an options menu where the user can make settings related to the functions of DPT. The user interface of the DPT options menu is shown in Figure A.6 (d) and is accessed by clicking the "Option" button in the bottom corner. The options menu of DPT is divided into several sections, namely Index, Cursor, Email, and In-Figure Tools.

In general, the data management and processing routine (DMPR) implemented by DPT automatically uses the DA to collect data segments from a NADS, as described in section A.6.1.1. To allow users to select only a portion of the defined data segment by the $i_F$ and $i_T$ values through the data address (DA) on the DPT, the index panel provides two editable text fields in the DPT options menu, namely the "start" and "end" fields, to change the first ($i_s$) and last ($i_e$) indexing values of the data segment, respectively. For security reasons, the "$i_s$" and "$i_e$" fields are locked for indexing by default, so the supervised values of DA defined on the DPT page must be used. Otherwise, the unsupervised values $i_s$ and $i_e$ are used, which must be within the range of $i_s \geq 1$ and $i_e \leq$ length( data segment). To allow users to select the index relative to the last position of the data segment, the keyword "end" is accepted in the text fields, similar to the use of the MATLAB function *end* [58] in the context of an object indexing expression.

The DCT options menu includes an email panel that allows the user to enable or disable background email support for the administrator. When email support is enabled, with the user's permission, the DCT sends supporting emails to the administrator listing errors and the user's profile (OS and MATLAB versions, local username, work, and home directories).

The remaining options relate to tools and functions to be used in MATLAB figure windows. One function is to replace the generic MATLAB cursor datatips [59] with a customized version that displays: the filename index ($n$) and iteration index ($i$) in circular brackets, i.e., $n(i)$; the index value ($I$) relative to the data segment plotted in the figure axes; the $x$,$y$ coordinates of the tip position with programmable floating-point precision via the DCT Options menu Cursor Panel.

The In-Figure Tools panel can be used to change the file names used by the in-figure tools to quickly save the figures as Portable Network Graphic (.png) images or as MATLAB binary (.mat) and script (.m) files, as described in section A.6.2.

## A.6.4 − Save and export tools

To save and export data displayed in a MATLAB figure, two buttons are provided in the GUI of the DPT, respectively. The save button requires user to first select the MATLAB figure to save through

a dialog box listing all figures, and only then opens the MATLAB *saveas* function [60] restricting to save the MATLAB figure in the following formats: MATLAB Figures (*.fig), Portable Network Graphics (*.png), JPEG image (*.jpg), TIFF image (*tif), Windows® BITMAP (*.bmp), MATLAB Program file (*.m) and MATLAB binary file (*.mat). As for the export button opens a file selection dialog box [30] that allows gather the data plotted in a selected MATLAB figure and save MATLAB binary file (*.m) and MATLAB Program file (*.m). Despite the file formats are the same as the files created with the MATLAB *saveas* function previously described, the data is first stored in *x*,*y*-like data arrays and only then saved or printed in the *.mat and *.m files, i.e., each dataset is saved in *.mat files as $x_1$, $x_2$, …, $x_n$ and $y_1$, $y_2$, …, $y_n$ variables for the abscissa and ordinate data gathered from the selected figure axes; or case *.m files is used, the datasets are printed in different variables as $k_1 = [x_1,y_1]$, $k_2$, …, $k_n = [x_n,y_n]$. At the end of the *.m file, a brief MATLAB script is printed to plot all printed data. All files exported to *.mat files are also paired with *.m file with the same name of the *.mat file and containing a brief MATLAB script that allows loading and plot all data saved in the *.mat file. Note that the in-figure Tool 8 and 9 described on section A.3 are an extension of the export figure tool, just differing of the automatic or manual insertion of the file name and directory.

### A.6.5 − Noise Data Processing Toolbox (NDPT)

The Noise Data Processing Toolbox (NDPT), shown in Figure A.7 (a), is specifically designed for processing signals embedded in noise and allows either the peak amplitudes of the signal ($\Delta P_a$) and the noise ($\Delta N_a$) to be estimated, but not necessarily simultaneously. When both $\Delta P_a$ and $\Delta N_n$ are estimated simultaneously, NDPT also provides an option to estimate the signal-to-noise ratio (SNR), which is SNR = $\Delta P_a$ / $\Delta N_n$. Note that ΔPa is simply the sum of the maximum and minimum absolute values of the data vector relative to the filtered data set ($\Delta y$) represented by the blue curve in Figure A.7 (b), i.e., $\Delta P_a = |\max\{\Delta y\}| + |\min\{\Delta y\}|$, which limits the use of this function to narrow observation windows, as otherwise no useful application is envisaged for estimating $\Delta P_a$ and hence SNR. For this reason, a check box has been included in the NDPT to allow the estimation of each parameter. $\Delta N_n$ is estimated using a combined method that first performs a histogram analysis of $\Delta y$, where the number of bins (histogram bars) can be specified in the NDPT, and then fits a normal distribution to the histogram to estimate the confidence interval ($\Delta\sigma$) (see Figure A.7 (b)), where $\Delta\sigma$ is the estimated noise amplitude considering the deviation error ($\sigma_e$) specified in the NDPT. Both the histogram and the fitted distribution are obtained using the MATLAB function *histfit* [61]. To determine Δσ, the fitted distribution line must be normalized and the number of samples greater than $\Delta\sigma$ counted, i.e., $\Delta\sigma = 1 - \sigma_e$. The blue circular markers in Figure A.7 (b) highlight the first and last samples where $\Delta\sigma = 1 - \sigma_e$.

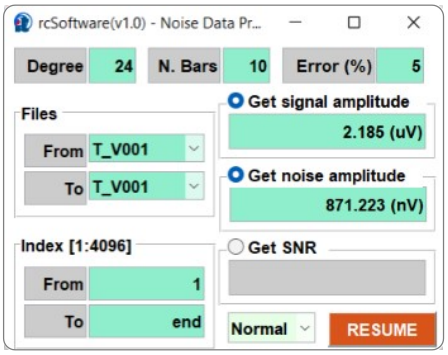


(a)

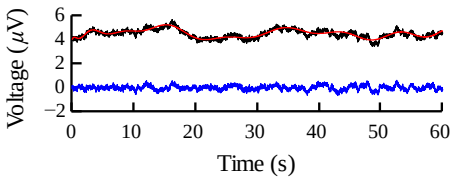


(b)

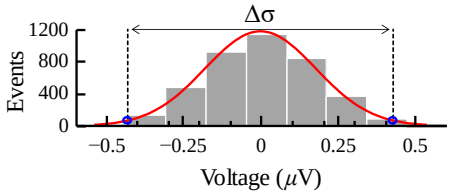


(c)

**Pseudo-code: Estimate signal peak amplitude ($\Delta P_a$), noise ($\Delta N_n$) and, signal-to-noise ratio (SNR) routine**

**Input:** *perror* – confidence interval error ( $\sigma_e$), $0 \leq perror \leq 1$
*nbars* – Number of histogram bars (bins)

**Data:** $x[1{:}K]$ **and** $y[1{:}K]$ – datasets of the original $x_{Mn}$ and *y*-NADS

**Result:** *noise* ($\Delta N_n$) ; *signal* ($\Delta P_a$) ; *snr* (SNR)

**// Perform the histogram with a distribution fit analysis**

[ *histdata* , *fitline* ] = *histfit*( *y* , *nbars* , '*normal*' );

*X* = *fitline.xdata;* // Get fitted *x*-data array

*Y* = *fitline.ydata;* // Get fitted *y*-data array

**// Normalize *y*-data array (*Ynorm*)**

*Ynorm* = *Y* / *max*( *Y* );

**// find the indices of all *Ynorm* array greaterthan $\sigma_e$**

*I* = *find*( *Ynorm* ≥ *perror* );

**// Determine the sampling rate of the fitted distribution line**

*Xs* = *X*[*nbars*] − *X*[*nbars* − 1];

**// Result: *Nn*, noise amplitude ($\Delta N_n$)**

*noise* = *length*( *I* ) * *Xs*;

**// Result: *Pa*, signal peak amplitude ($\Delta P_a$)**

*signal* = *abs*( *max*( *y* ) ) + *abs*( *min*( *y* ) );

**// Result: *SNR*, signal-to-noise ratio (SNR)**

*snr* = *signal* / *noise*;

(d)

**Figure A.7 –** Noise Data Processing Toolbox (NDPT). (**a**) Layout of the graphical user interface (GUI). (**b,c**) The graphical output of NDPT each time the resume button is pressed. (**b**) The black line always represents the *x*,*y*−data fields selected in the NDPT file window, the red line is the polynomial fitting curve, and the blue line is the filtered *x*,*y*−data fields. (**c**) Histogram and normal distribution fitting curve of the filtered *x*,*y*−data series. $\Delta\sigma$ is the confidence interval. (**d**) Pseudocode of the routine for estimating signal peaks ($\Delta P_a$), noise ($\Delta N_n$), and signal-to-noise ratio (SNR).

The pseudocode for estimating the peak signal amplitude ($\Delta P_a$), noise ($\Delta N_a$), and signal-to-noise ratio (SNR) is described in Figure A.7 (d).

NDPT enforces the filtering of the data and only through the polynomial interpolation method applied to the entire dataset, offering the user only the possibility to adjust the polynomial degree value. To avoid filtering, it's advisable to set the polynomial degree to zero (*degree* = 0). This only removes a constant value from the entire data set, moves the data closer to the origin of the ordinate axis ($y = 0$), and doesn't remove any frequency component. Figure A.7 (b) shows an example of the filtering process performed by NDPT. The black line is the original data set ($y$) selected in the file panel, the red line is the interpolated polynomial ($p^n$) corresponding to the degree value specified in the NDPT degree text box, and the blue line is the filtered data set ($\Delta y$) obtained by $\Delta y = y - p^n$.

The NDPT also provides the option to select either $x_{M1}$ or $x_{M2}$ NADS by using the drop-down menu next to the "Resume" button. Note that the *y*−NADS used by the NDPT is passed as an input argument by either the DAT or the DPT.

Also, in the index panel there is an option to set the indexing address of the dataset, which can be useful to limit the noise analysis to a specific area of the original dataset. The indexing of the data address (DA) is the same as described in section A.6.3 to adjust the values $i_s$ and $i_e$.

## A.6.6 − Statistical Data Processing Toolbox (SDPT)

The Statistical Data Processing Toolbox (SDPT), shown in Figure A.8 (a), is specifically designed for processing and statistical analysis of *y*−NADS passed as input arguments from either DAT or DPT. Nevertheless, SDPT provides an alternative option to override the primary use of *y*−NADS with data from any MATLAB window. When the External Data option is enabled, a drop-down menu is displayed in the graphical user interface below the filter field, allowing the user to select the data to be processed. In addition, the preprocessing routines of DPT and SDPT differ only in the peak detection function, which allows the user to specify six input arguments for the MATLAB function *findpeaks* [62], namely the minimum peak height, minimum peak spacing, minimum peak expression, peak threshold, minimum peak width, and maximum peak width. By default, the MATLAB *findpeaks* function does not support the detection of negative local maxima. However, the user interface includes a slider menu near the title of the *findpeaks* options that can be used to switch the method of detecting local maxima between positive peaks only, negative peaks only, and either positive or negative peaks. The method for detecting local maxima with negative polarity consists of centering and mirroring the analyzed data set along the abscissa axis. This method does not corrupt the data and is used only to overcome the limitation of the *findpeaks* function. Note that the processing routine for detecting positive and negative peaks matches the option of detecting peaks with positive and negative polarization simultaneously, regardless of the signal polarization specified in the slider menu, i.e., the *findpeaks* function must be executed twice. Figure A.8 (b) shows a detailed view of the recorded bioelectrical signals in the flow of an embryonic body (EB) composed of at least 50% cardiac muscle cells stored in the *y*−NADS, where the red solid dots are the output of the peak detection routine. To perform the preprocessing functions and visualize the processed data, one of the two adjacent buttons must be used, namely the "Get Data" and "New" buttons. The only difference between the "Get Data" and "New" buttons is that the "New" button always creates a new MATLAB window, while the "Get Data" button reuses the last MATLAB window created by SDPT to replace the previously recorded data.

When the check box above the Histogram Analysis Options title is checked, SDPT provides the ability to use various histogram analysis algorithms (HAA) through a drop-down menu, namely the "Type" menu, and to perform the statistical analysis through one of two side-by-side buttons, "Get

Histogram" and "New", whose functions are the same as those previously described for the "Get Data" and "New" buttons. All HAA are based on counting or averaging the number of events within a bin period ($B_T$). By default, $B_T$ corresponds to the size of the *x*–NADS unit users selected in the drop-down menus above the "New" and "Get Data" buttons, i.e. $B_T$ = 1 second, minute, hour, day, or year. To use different bin sizes, users can change $B_T$ to correspond to a fixed number of bins ($B_N$) or a fixed bin width ($B_F$) in the selection menu to the left of the "Get Data" button. If $B_N$ is selected, the size of each bin is automatically iterated and is given by $B_T = T_T / B_N$, where $T_T$ is the window period of the data set. If $B_N$ or $B_F$ is selected, a text box will appear in the Histogram Analysis options for the user to specify the value $B_N$ or $B_F$.

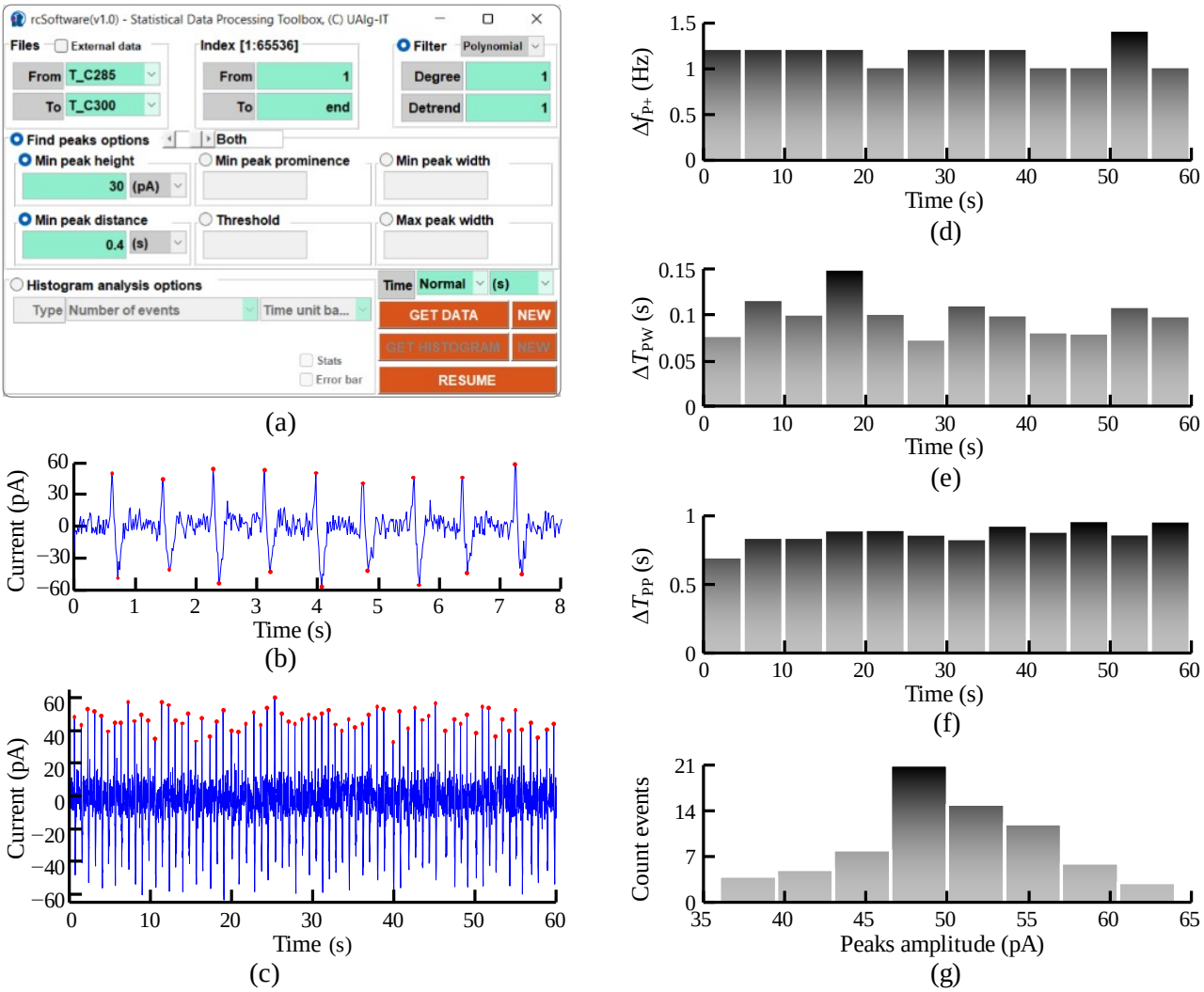


**Figure A.8 –** Statistical Data Processing Toolbox (SDPT). (**a**) Layout of the graphical user interface (GUI). (**b**) Detail view of the recorded bioelectrical activity of an embryoid body (EB) of cardiomyocyte cells. The red solid represents the output of both positive and negative peak detection function. (**c**) Larger dataset of the recorded bioelectrical activity and the output of the positive peak detection function used in the histograms plots (**d**–**g**) obtained with the signal frequency ($\Delta f_P$), average peak width ($\Delta T_{PW}$), and average inter-peak interval ($\Delta T_{PP}$) HAAs using $B_T$ = 10 s, and the amplitude analysis HAA using fix number of bars, $B_T$ = 8, respectively.

The "Type" drop-down menu provides access to ten HAA, namely the number of events ($\Delta N_C$), average peak width ($\Delta T_{PW}$), average peak amplitude ($\Delta P_A$), average inter-peak interval ($\Delta T_{PP}$), average prominence ($\Delta P_P$), inter-peak interval ($H_{PP}$), amplitude analysis ($H_{PA}$), prominence analysis ($H_P$), histogram, and signal frequency ($\Delta f_P$). However, some algorithms are only useful if the input data ($x_{in}$ and $y_{in}$) are equal to the peak width, amplitude, prominence, or inter-peak interval values returned by the MATLAB *findpeaks* function; otherwise, all samples in the data set are used, i.e., $x_{in}$ and $y_{in}$ are the $x$,$y$−data fields collected by NADS, causing HAA to interpret peak width as equal to $x_{in}$ samples, inter-peak interval as the inter-sample interval, peak amplitude as equal to sample amplitude ($y_{in}$), and prominence as the inter-sample amplitude difference. When the "Error bars" checkbox is selected, MATLAB error bars [63] are displayed along with the histogram bins after running any HAA, with the width of the error bar centered on the bin value ± standard deviation (SD) [64]. $H_{PP}$, $H_{PA}$, and $H_P$ HAA use the MATLAB function *histogram* plot [65] to analyze $x_{in}$ and $y_{in}$, while the histogram HAA uses the MATLAB function *histfit* [61], which performs the same histogram analysis but includes a distribution fitting curve, e.g., normal, log-normal, logistic, logistic, Poisson, Weibull, exponential, and others.

Figure A.8 (c-g) illustrates the typical use of SDPT. Figure A.8 (c) shows images of the contractile beat of cardiomyocytes and red circles representing the output of the peak detection function, i.e., the $x_{in}$ and $y_{in}$ data sets used by HAA. For example, Figure A.8 (d−e) shows the HAAs output of signal frequency ($\Delta f_P$), average peak width ($\Delta T_{PW}$), and average inter-peak interval ($\Delta T_{PP}$) using $B_T$ = 10 s. Figure A.8 (g) shows the HAA output of the amplitude analysis using the fixed number of bars, $B_T$ = 8.

# A.7 − Discussion

The *rcSoftware* is an all-in-one (AiO) toolkit specifically designed for the acquisition, collection, and processing of electrophysiological data recorded with a dedicated ultra-low-noise instrumentation that is able to record various samples and characterize their basic noise sources, namely pink noise (1/$f$), generation and recombination noise (G-R noise), random telegraph noise (RTN), and shot noise, as well as perform signal processing. In addition, the *rcSoftware* supports both real-time and offline data processing programs and allows remote access to live recordings. The data processing tools provide access to large datasets through an intuitive and user-friendly GUI that allows data to be quickly and easily obtained for publication. For example, previous work has been published using earlier and unpublished versions of the *rcSoftware* to record and process the bioelectrical activity of astrocyte cells [66,67], glioma cells [68,69], EBs of cardiomyocytes [70,71], and small organs [72], and to characterize the charge dynamics near the three-dimensional electrode surfaces [73].

Nevertheless, improvements are still needed to increase the temporal acquisition delay of the *rcSoftware* between successive windows. So far, the implementation based on monitoring the OSR of the DSA has proven to be the main failure, reaching delay times of at least 4 seconds between successive measurements. A more robust approach has been to combine the DSA capability with BASIC routines to take live recordings of data into an internal memory buffer of the DSA and use the DAT to read and clean the buffer. This approach has been initiated but is not yet complete, as developers still need to establish robust triggering mechanisms to synchronize DAT and the DSA internal routines.

The data acquisition and processing tools provided with the *rcSoftware* have proven to be versatile. Data files originating from various instruments and recorded with proprietary software packages specifically designed to control and perform data acquisition are now supported by CR of the DCT for data acquisition into NADS and further use with the DPT. Supported data files include data recorded with the in-house RCL software used to control and record data from a Fluke PM6306 RCL impedance analyzer (Fluke Corporation, Everett, USA); in-house TKTRONIX software that can acquire data from a Tektronix TR210, TDS220, and TDS224 digital oscilloscopes (Tektronix Inc., Beaverton, Oregon, USA); and in-house FET software that allows control and recording of data from multiple instruments. For example, transient recordings of current or voltage using a Keithley 487 picoammeter or a Keithley 2182a nanovoltmeter (Keithley Instruments Inc, Cleveland, Ohio, USA); the current−voltage (I−V) characteristics using the Keithley 487 as a picoammeter and the Keithley 6487 as a voltage source (Keithley Instruments Inc., Cleveland, Ohio, USA). Therefore, both DCT and DPT can be further developed with special routines to interpret and support data files from external systems.

# References

[1] J.S. Rothman, R.A. Silver, Neuromatic: An integrated open-source software toolkit for acquisition, analysis and simulation of electrophysiological data, Front. Neuroinform. 12 (2018) 14. https://doi.org/10.3389/FNINF.2018.00014/BIBTEX.

[2] K. Imfeld, S. Neukom, A. Maccione, Y. Bornat, S. Martinoia, P.A. Farine, M. Koudelka-Hep, L. Berdondini, Large-scale, high-resolution data acquisition system for extracellular recording of electrophysiological activity, IEEE Trans. Biomed. Eng. 55 (2008) 2064–2073. https://doi.org/10.1109/TBME.2008.919139.

[3] J. Putzeys, B.C. Raducanu, A. Carton, J. De Ceulaer, B. Karsh, J.H. Siegle, N. Van Helleputte, T.D. Harris, B. Dutta, S. Musa, C. Mora Lopez, Neuropixels Data-Acquisition System: A Scalable Platform for Parallel Recording of 10 000+ Electrophysiological Signals, IEEE Trans.

Biomed. Circuits Syst. 13 (2019) 1635–1644. https://doi.org/10.1109/TBCAS.2019.2943077.

[4] K.S. Mannatunga, S.H.M. Ali, M.L. Crespo, A. Cicuttin, J.G. Samarawikrama, High Performance 128-Channel Acquisition System for Electrophysiological Signals, IEEE Access. 8 (2020) 122366–122383. https://doi.org/10.1109/ACCESS.2020.3007082.

[5] B.A. Suter, T. O'Connor, V. Iyer, L.T. Petreanu, B.M. Hooks, T. Kiritani, K. Svoboda, G.M.G. Shepherd, Ephus: Multipurpose data acquisition software for neuroscience experiments, Front. Neural Circuits. 4 (2010) 100. https://doi.org/10.3389/FNCIR.2010.00100/BIBTEX.

[6] Keysight Technologies., Electronic design, test automation & measurement equipment | Keysight., (n.d.). https://www.keysight.com/zz/en/home.html (accessed March 16, 2022).

[7] Eggplant software., Eggplant Homepage., (n.d.). https://www.eggplantsoftware.com/ (accessed March 16, 2022).

[8] Keysight Technologies., Keysight VEE Pro 9.32., (n.d.). https://www.meilhaus.de/en/vee-pro.htm (accessed March 19, 2022).

[9] Keysight Technologies., 35670A DataLink | Keysight., (n.d.). https://www.keysight.com/zz/en/lib/software-detail/computer-software/35670a-datalink-1425653.html (accessed March 16, 2022).

[10] G.B. Grant, F.S. Werblin, Low-cost data acquisition and analysis programs for electrophysiology, J. Neurosci. Methods. 55 (1994) 89–98. https://doi.org/10.1016/0165-0270(94)90044-2.

[11] M. Pratt, The Pros and Cons of Developing Your Own Software Versus Outsourcing., Business.Org. (2013). https://www.business.org/software/apps/the-pros-and-cons-of-developing-your-own-software-versus-outsourcing/ (accessed January 19, 2022).

[12] N. Ustinov, Building An In-House Solution Vs. Buying Software: Pros And Cons To Consider, Forbes Technol. Counc. (2021). https://www.forbes.com/sites/forbestechcouncil/2021/07/29/building-an-in-house-solution-vs-buying-software-pros-and-cons-to-consider/ (accessed January 19, 2022).

[13] S. Wang, H. Han, K. Gao, Z. Wang, C. Zhang, M. Yang, Z. Wu, Z. Wu, A user-friendly LabVIEW software platform for grating based X-ray phase-contrast imaging, J. Xray. Sci. Technol. 23 (2015) 189–199. https://doi.org/10.3233/XST-150480.

[14] D.H. Morse, A.J. Antolak, G.S. Bench, M.L. Roberts, A flexible LabVIEW$^{TM}$-based data acquisition and analysis system for scanning microscopy, Nucl. Instruments Methods Phys. Res. Sect. B Beam Interact. with Mater. Atoms. 158 (1999) 146–152. https://doi.org/10.1016/S0168-583X(99)00507-8.

[15] I.W. Kirkman, P.A. Buksh, Data acquisition and control using National Instruments'

"LabVIEW" software, Rev. Sci. Instrum. 63 (1992) 869–872. https://doi.org/10.1063/1.1142631.

[16] M.A. Muyskens, S. V. Glass, T.W. Wietsma, T.M. Gray, Data Acquisition in the Chemistry Laboratory Using LabVIEW Software, J. Chem. Educ. 73 (1996) 1112. https://doi.org/10.1021/ed073p1112.

[17] T. Akam, M.E. Walton, pyPhotometry: Open source Python based hardware and software for fiber photometry data acquisition, Sci. Rep. 9 (2019) 3521. https://doi.org/10.1038/s41598-019-39724-y.

[18] S.J. Weber, PyMoDAQ: An open-source Python-based software for modular data acquisition, Rev. Sci. Instrum. 92 (2021). https://doi.org/10.1063/5.0032116.

[19] L.J. Koerner, T.A. Caswell, D.B. Allan, S.I. Campbell, A Python Instrument Control and Data Acquisition Suite for Reproducible Research, IEEE Trans. Instrum. Meas. 69 (2020) 1698–1707. https://doi.org/10.1109/TIM.2019.2914711.

[20] A. Neto, H. Fernandes, A. Duarte, B.B. Carvalho, J. Sousa, D.F. Valcárcel, M. Hron, C.A.F. Varandas, FireSignal-Data acquisition and control system software, Fusion Eng. Des. 82 (2007) 1359–1364. https://doi.org/10.1016/j.fusengdes.2007.02.016.

[21] S. Nickell, F. Förster, A. Linaroudis, W. Del Net, F. Beck, R. Hegerl, W. Baumeister, J.M. Plitzko, TOM software toolbox: Acquisition and analysis for electron tomography, J. Struct. Biol. 149 (2005) 227–234. https://doi.org/10.1016/j.jsb.2004.10.006.

[22] U. Egert, T. Knott, C. Schwarz, M. Nawrot, A. Brandt, S. Rotter, M. Diesmann, MEA-Tools: An open source toolbox for the analysis of multi-electrode data with MATLAB, J. Neurosci. Methods. 117 (2002) 33–42. https://doi.org/10.1016/S0165-0270(02)00045-6.

[23] K. Sieczkowski, T. Sondej, A method for real-time data acquisition using Matlab software, Proc. 23rd Int. Conf. Mix. Des. Integr. Circuits Syst. Mix. 2016. (2016) 437–442. https://doi.org/10.1109/MIXDES.2016.7529782.

[24] A. V. Uppuluri, R.J. Jost, MATLAB-based ERS SAR data acquisition and processing software for classroom use, IEEE Natl. Radar Conf. - Proc. (2004) 524–528. https://doi.org/10.1109/nrc.2004.1316480.

[25] R.C. Schultz, R.W. Ives, Biometric data acquisition using MATLAB GUIs, Proc. - Front. Educ. Conf. FIE. 2005 (2005) 1–5. https://doi.org/10.1109/fie.2005.1612189.

[26] W.F. Asaad, E.N. Eskandar, A flexible software tool for temporally-precise behavioral control in Matlab, J. Neurosci. Methods. 174 (2008) 245–258. https://doi.org/10.1016/j.jneumeth.2008.07.014.

[27] R. Tinti, F. Sischka, C. Morton, Proposed System Solution for 1 / f Noise Parameter Extraction,

(n.d.) 1–7.

[28] The MathWorks Inc., Open folder selection dialog box - MATLAB uigetdir., (n.d.). https://www.mathworks.com/help/matlab/ref/uigetdir.html (accessed March 20, 2022).

[29] The MathWorks Inc., Create question dialog box - MATLAB questdlg., (n.d.). https://www.mathworks.com/help/matlab/ref/questdlg.html (accessed March 20, 2022).

[30] The MathWorks Inc., Open dialog box for saving files - MATLAB uiputfile., (n.d.). https://www.mathworks.com/help/matlab/ref/uiputfile.html (accessed March 20, 2022).

[31] The MathWorks Inc., (To be removed) Read serial port objects from memory to MATLAB workspace - MATLAB instrfind., (n.d.). https://www.mathworks.com/help/matlab/ref/instrfind.html (accessed March 21, 2022).

[32] The MathWorks Inc., Log Command Window text to file - MATLAB diary., (n.d.). https://www.mathworks.com/help/matlab/ref/diary.html (accessed March 21, 2022).

[33] O. Komarov, okomarov/passfield - GitHub., 2014. (2022). https://github.com/okomarov/passfield (accessed April 4, 2022).

[34] The MathWorks Inc., View or change default user work folder - MATLAB userpath., (n.d.). https://www.mathworks.com/help/matlab/ref/userpath.html (accessed March 27, 2022).

[35] The MathWorks Inc., Retain current plot when adding new plots - MATLAB hold., (n.d.). https://www.mathworks.com/help/matlab/ref/hold.html (accessed March 27, 2022).

[36] The MathWorks Inc., Remove polynomial trend - MATLAB detrend., (n.d.). https://www.mathworks.com/help/matlab/ref/detrend.html?searchHighlight=detrend&s_tid=srchtitle_detrend_1 (accessed March 9, 2022).

[37] R. Schafer, What Is a Savitzky-Golay Filter? [Lecture Notes], IEEE Signal Process. Mag. 28 (2011) 111–117. https://doi.org/10.1109/MSP.2011.941097.

[38] The MathWorks Inc., Polynomial curve fitting - MATLAB polyfit., (n.d.). https://www.mathworks.com/help/matlab/ref/polyfit.html?searchHighlight=polyfit&s_tid=srchtitle_polyfit_1 (accessed March 9, 2022).

[39] The MathWorks Inc., Polynomial evaluation - MATLAB polyval., (n.d.). https://www.mathworks.com/help/matlab/ref/polyval.html?searchHighlight=polyval&s_tid=srchtitle_polyval_1 (accessed March 9, 2022).

[40] The MathWorks Inc., Savitzky-Golay filtering - MATLAB sgolayfilt, (n.d.). https://www.mathworks.com/help/signal/ref/sgolayfilt.html?searchHighlight=sgolayfilter&s_tid=srchtitle_sgolayfilter_1 (accessed March 9, 2022).

[41] The MathWorks Inc., Periodogram power spectral density estimate - MATLAB periodogram, (n.d.). https://www.mathworks.com/help/signal/ref/periodogram.html?s_tid=doc_ta (accessed

March 9, 2022).

[42] The MathWorks Inc., Rectangular window - MATLAB rectwin., (n.d.). https://www.mathworks.com/help/signal/ref/rectwin.html (accessed March 28, 2022).

[43] The MathWorks Inc., Hamming window - MATLAB hamming., (n.d.). https://www.mathworks.com/help/signal/ref/hamming.html (accessed March 28, 2022).

[44] The MathWorks Inc., Gaussian window - MATLAB gausswin., (n.d.). https://www.mathworks.com/help/signal/ref/gausswin.html?searchHighlight=gaussian window&s_tid=srchtitle_gaussian window_2 (accessed March 28, 2022).

[45] The MathWorks Inc., Flat top weighted window - MATLAB flattopwin., (n.d.). https://www.mathworks.com/help/signal/ref/flattopwin.html (accessed March 28, 2022).

[46] The MathWorks Inc., Kaiser window - MATLAB kaiser., (n.d.). https://www.mathworks.com/help/signal/ref/kaiser.html?s_tid=doc_ta (accessed March 28, 2022).

[47] The MathWorks Inc., Blackman window - MATLAB blackman., (n.d.). https://www.mathworks.com/help/signal/ref/blackman.html (accessed March 28, 2022).

[48] The MathWorks Inc., Chebyshev window - MATLAB chebwin., (n.d.). https://www.mathworks.com/help/signal/ref/chebwin.html?s_tid=doc_ta (accessed March 28, 2022).

[49] The MathWorks Inc., Hann (Hanning) window - MATLAB hann., (n.d.). https://www.mathworks.com/help/signal/ref/hann.html (accessed March 28, 2022).

[50] The MathWorks Inc., Taylor window - MATLAB taylorwin., (n.d.). https://www.mathworks.com/help/signal/ref/taylorwin.html?s_tid=doc_ta (accessed March 28, 2022).

[51] The MathWorks Inc., Tukey (tapered cosine) window - MATLAB tukeywin., (n.d.). https://www.mathworks.com/help/signal/ref/tukeywin.html?s_tid=doc_ta (accessed March 28, 2022).

[52] M.S. Bartlett, Smoothing Periodograms from Time-Series with Continuous Spectra, Nature. 161 (1948) 686–687. https://doi.org/10.1038/161686a0.

[53] M.S. BARTLETT, PERIODOGRAM ANALYSIS AND CONTINUOUS SPECTRA, Biometrika. 37 (1950) 1–16. https://doi.org/10.1093/biomet/37.1-2.1.

[54] P. Welch, The use of fast Fourier transform for the estimation of power spectra: A method based on time averaging over short, modified periodograms, IEEE Trans. Audio Electroacoust. 15 (1967) 70–73. https://doi.org/10.1109/TAU.1967.1161901.

[55] The MathWorks Inc., Set or query x-axis limits - MATLAB xlim., (n.d.).

https://www.mathworks.com/help/matlab/ref/xlim.html (accessed April 7, 2022).

[56] The MathWorks Inc., Set or query y-axis limits - MATLAB ylim., (n.d.). https://www.mathworks.com/help/matlab/ref/ylim.html (accessed April 7, 2022).

[57] The MathWorks Inc., Display axes outline - MATLAB box., (n.d.). https://www.mathworks.com/help/matlab/ref/box.html?s_tid=doc_ta (accessed April 7, 2022).

[58] The MathWorks Inc., Terminate block of code or indicate last array index - MATLAB end., (n.d.). https://www.mathworks.com/help/matlab/ref/end.html (accessed March 30, 2022).

[59] The MathWorks Inc., Create data tip - MATLAB., (n.d.). https://www.mathworks.com/help/matlab/ref/matlab.graphics.datatip.datatip.html (accessed March 30, 2022).

[60] The MathWorks Inc., Save figure to specific file format - MATLAB saveas, (n.d.). https://www.mathworks.com/help/matlab/ref/saveas.html?searchHighlight=saveas&s_tid=srchtitle_saveas_1 (accessed March 9, 2022).

[61] The MathWorks Inc., Histogram with a distribution fit - MATLAB histfit., (n.d.). https://www.mathworks.com/help/stats/histfit.html?s_tid=doc_ta (accessed March 12, 2022).

[62] The MathWorks Inc., Find local maxima - MATLAB findpeaks., (n.d.). https://www.mathworks.com/help/signal/ref/findpeaks.html (accessed March 9, 2022).

[63] The MathWorks Inc., Line plot with error bars - MATLAB errorbar., (n.d.). https://www.mathworks.com/help/matlab/ref/errorbar.html (accessed March 14, 2022).

[64] The MathWorks Inc., Standard deviation - MATLAB std., (n.d.). https://www.mathworks.com/help/matlab/ref/std.html?s_tid=doc_ta (accessed March 14, 2022).

[65] The MathWorks Inc., Histogram plot - MATLAB., (n.d.). https://www.mathworks.com/help/matlab/ref/matlab.graphics.chart.primitive.histogram.html (accessed April 11, 2022).

[66] A.L.G. Mestre, M. Cerquido, P.M.C. Inácio, S. Asgarifar, A.S. Lourenço, M.L.S. Cristiano, P. Aguiar, M.C.R. Medeiros, I.M. Araújo, J. Ventura, H.L. Gomes, Ultrasensitive gold micro-structured electrodes enabling the detection of extra-cellular long-lasting potentials in astrocytes populations, Sci. Rep. 7 (2017) 1–11. https://doi.org/10.1038/s41598-017-14697-y.

[67] A.L.G. Mestre, P.M.C. Inácio, Y. Elamine, S. Asgarifar, A.S. Lourenço, M.L.S. Cristiano, P. Aguiar, M.C.R. Medeiros, I.M. Araújo, J. Ventura, H.L. Gomes, Extracellular Electrophysiological Measurements of Cooperative Signals in Astrocytes Populations, Front. Neural Circuits. 11 (2017) 1–9. https://doi.org/10.3389/fncir.2017.00080.

[68] S. Asgarifar, A.L.G. Mestre, R.C. Félix, P.M.C. Inácio, M.L.S. Cristiano, M.C.R. Medeiros,

I.M. Araújo, D.M. Power, H.L. Gomes, Extracellular electrophysiological based sensor to monitor cancer cells cooperative migration and cell-cell connections, Biosens. Bioelectron. 145 (2019). https://doi.org/10.1016/j.bios.2019.111708.

[69] M.C.R. Medeiros, A. Mestre, P. Inácio, S. Asgarif, I.M. Araújo, P.C. Hubbard, Z. Velez, M.L. Cancela, P.R.F. Rocha, D.M. de Leeuw, F. Biscarini, H.L. Gomes, An electrical method to measure low-frequency collective and synchronized cell activity using extracellular electrodes, Sens. Bio-Sensing Res. 10 (2016) 1–8. https://doi.org/10.1016/j.sbsr.2016.06.002.

[70] M.C.R.M.C.R. Medeiros, A.L.G.A.L.G. Mestre, P.M.C.P.M.C. Inácio, J.M.L.J.M.L. Santos, I.M.I.M. Araujo, J. Bragança, F. Biscarini, H.L.H.L. Gomes, J. Bragancą, F. Biscarini, H.L.H.L. Gomes, Performance assessment of polymer based electrodes for *in vitro* electrophysiological sensing: the role of the electrode impedance, Proc. SPIE - Int. Soc. Opt. Eng. 9944 (2016) 994404. https://doi.org/10.1117/12.2237659.

[71] P.M.C. Inacio, A.L.G. Mestre, M.D.C.R. De Medeiros, S. Asgarifar, Y. Elamine, J. Canudo, J.M.A. Santos, J. Braganca, J. Morgado, F. Biscarini, H.L. Gomes, Bioelectrical Signal Detection Using Conducting Polymer Electrodes and the Displacement Current Method, IEEE Sens. J. 17 (2017) 3961–3966. https://doi.org/10.1109/JSEN.2017.2703834.

[72] P.M.C. Inácio, M.C.R. Medeiros, T. Carvalho, R.C. Félix, A. Mestre, P.C. Hubbard, Q. Ferreira, J. Morgado, A. Charas, C.S.R. Freire, F. Biscarini, D.M. Power, H.L. Gomes, Ultra-low noise PEDOT:PSS electrodes on bacterial cellulose: A sensor to access bioelectrical signals in non-electrogenic cells, Org. Electron. 85 (2020) 105882. https://doi.org/10.1016/j.orgel.2020.105882.

[73] J.A. Reis, M.C.R. Medeiros, P.M. Inácio, M. Cerquido, J. Ventura, H.L. Gomes, Transient electrical behavior of an electrode/electrolyte interface based on a surface micro-structured with gold mushroom shapes, J. Appl. Phys. 124 (2018) 214902. https://doi.org/10.1063/1.5042712.

# Appendix B

The remote access is limited to attend user requests for data, thus requiring internet access and a personal cloud space (e.g., Google Drive, or similar) to be installed in the local-PC. The communication protocol is based in a simple text file. To perform a data request, first user is required to set on DAT the current directory path or on the ADPT the root directory path with read/write permissions, and both paths must be created in the cloud space. Then user must create a file with the exact name '*getdata.txt*' to send commands to DAT or DAPT. If the command is accepted by the DAT or ADPT, the file '*getdata.txt*' is rewritten with an acknowledge text message "ACK". Table B.1 lists and describes all available commands. The ADPT only accept requests for NADS, i.e. the commands '*s*' and '*l*'. To download only a specific data file from the EDT, the command '*s*' can be combined with a number as '*s n*', where '*n*' is the row number of the EDT. Long wait times are expected for data to be available in the cloud space, even if an "ACK" was received.

**Table B.1** − List of commands for requesting data remotely. Note that previous returned files are not replaced, instead, the same file name header is used and the last number in file name is incremented.

| Command | Description | Output |
|---|---|---|
| a | Request all data recorded on MATLAB binary file (*.mat) and pre-formatted to be plotted through a script file (*.m). | **TRACE A, voltage:** runmatAllDataAV1.m, runmatAllDataAV1.mat |
| ai | Same as 'a' but restricted to data recorded in current. | **TRACE A, current:** runmatAllDataAI1.m, runmatAllDataAI1.mat |
| av | Same as 'a' but restricted to data recorded in voltage. | **TRACE B, voltage:** runmatAllDataBV1.m, runmatAllDataBV1.mat |
| | | **TRACE B, current:** runmatAllDataBI1.m, runmatAllDataBI1.mat |
| s | Request all NADS saved on a MATLAB binary file (*.mat) to load in the DCT. | TRACE A, voltage: structAV1.mat |
| si | Same as 's' but restricted to data recorded in current. | TRACE A, current: structAI1.mat |
| sv | Same as 's' but restricted to data recorded in voltage. | TRACE B, voltage: structBV1.mat |
| | | TRACE B, current: structBI1.mat |
| l | Request report file (.txt) listing all data recorded (including instrument settings per each recorded file). | TRACE A, voltage: listAV1.txt |
| li | Request only data recorded in current. | TRACE A, current: listAI1.txt |
| lv | Request only data recorded in voltage. | TRACE B, voltage: listBV1.txt |
| | | TRACE B, current: listBI1.txt |

# Appendix C

The Agilent 35670A DSA is an FFT-based spectrum/network analyzer with an effective frequency range from 122 μHz to 102.4 kHz. The input recorded voltage per each channel is converted with a 16-bit ADC. The time capture functions are related to the FFT analysis to ensure all recorded data respects the Nyquist theorem, such that, regardless of the defined window period ($T$), the number of samples of time capture window ($N_T$) is always 2.56 higher than the output FFT-based spectrum number of samples ($N_f$). The window period and the number of samples are pre-defined by the manufacturer. Table C.1 summarizes the frequency range in terms of maximum bandwidth ($B_W$) in function of the resolution (window period in function of the number of samples).

**Table C.1** − Typical values of the DSA frequency range in function of the recording window period and number of samples in time ($N_T$) and frequency ($N_f$) domain.

| | **Number of samples per time window ($N_T$)** | | | | |
|---|---|---|---|---|---|
| | 256 | 512 | 1024 | 2048 | 4096 |
| | **Number of samples per spectrum window ($N_f$)** | | | | |
| | 100 | 200 | 400 | 800 | 1600 |
| **Window period ($T$)** | **Bandwidth ($B_W$)** | | | | |
| 2048 s | 48.828125 mHz | 97.65625 mHz | 195.3125 mHz | 390.625 mHz | 781.25 mHz |
| 1024 s | 97.65625 mHz | 195.3125 mHz | 390.625 mHz | 781.25 mHz | 1.5625 Hz |
| 512 s | 195.3125 mHz | 390.625 mHz | 781.25 mHz | 1.5625 Hz | 3.125 Hz |
| 256 s | 390.625 mHz | 781.25 mHz | 1.5625 Hz | 3.125 Hz | 6.25 Hz |
| 128 s | 781.25 mHz | 1.5625 Hz | 3.125 Hz | 6.25 Hz | 12.5 Hz |
| 64 s | 1.5625 Hz | 3.125 Hz | 6.25 Hz | 12.5 Hz | 25 Hz |
| 32 s | 3.125 Hz | 6.25 Hz | 12.5 Hz | 25 Hz | 50 Hz |
| 16 s | 6.25 Hz | 12.5 Hz | 25 Hz | 50 Hz | 100 Hz |
| 8 s | 12.5 Hz | 25 Hz | 50 Hz | 100 Hz | 200 Hz |
| 4 s | 25 Hz | 50 Hz | 100 Hz | 200 Hz | 400 Hz |
| 2 s | 50 Hz | 100 Hz | 200 Hz | 400 Hz | 800 Hz |
| 1 s | 100 Hz | 200 Hz | 400 Hz | 800 Hz | 1.6 kHz |
| 500 ms | 200 Hz | 400 Hz | 800 Hz | 1.6 kHz | 3.2 kHz |
| 250 ms | 400 Hz | 800 Hz | 1.6 kHz | 3.2 kHz | 6.4 kHz |
| 125 ms | 800 Hz | 1.6 kHz | 3.2 kHz | 6.4 kHz | 12.8 kHz |
| 62.5 ms | 1.6 kHz | 3.2 kHz | 6.4 kHz | 12.8 kHz | 25.6 kHz |
| 31.25 ms | 3.2 kHz | 6.4 kHz | 12.8 kHz | 25.6 kHz | 51.2 kHz |
| 15.625 ms | 6.4 kHz | 12.8 kHz | 25.6 kHz | 51.2 kHz | 102.4 kHz |
| 7.8125 ms | 12.8 kHz | 25.6 kHz | 51.2 kHz | 102.4 kHz | |
| 3.90625 ms | 25.6 kHz | 51.2 kHz | 102.4 kHz | | |